THE UNIVERSITY OF QUEENSLAND

AUSTRALIA

On binary scaling and ground-to-flight extrapolation in high-enthalpy facilities

Guerric de Crombrugghe de Looringhe
BSc, MSc in Engineering
MRes in Aeronautics and Aerospace

A thesis submitted for the degree of Doctor of Philosophy at
The University of Queensland in 2016
School of Mechanical and Mining Engineering

Abstract

The binary scaling law is commonly used to study the aerothermodynamics of hypersonic vehicles in high-enthalpy facilities. It enables the duplication of the shock layer in the vicinity of the stagnation point, including binary chemistry and nonequilibrium processes, through the reproduction of the Péclet and wall Damköhler numbers. These are both conserved through the duplication of the composition of the gas, the free-stream enthalpy h_∞ and the product of a density and a length-scale of the flow ρL.

Binary scaling is built on the assumption of a flow devoid of radiation coupling and governed by binary reactions. These two conditions drastically narrow down the envelope of flows for which binary scaling can be used. Moreover, diffusive transport and wall chemistry have never been addressed although they can have an important impact on the wall heat flux.

The first part of this thesis consists in an effort to better understand the theoretical role and effect of the different assumptions done to build the binary scaling. It is first shown that diffusive transport and wall chemistry should scale appropriately. Second, that non-binary chemistry will cause the shock layer in the laboratory flow to be hotter and less dissociated. A methodology is proposed to identify clearly what free-stream conditions will affect the least the flow variables of interest. Lastly, that radiation coupling will be weaker in the laboratory flow than in flight, causing the enthalpy contained in the shock layer to be greater in the laboratory flow.

These findings are verified in the second part with two experiments.

The first experiment was performed in the Plasmatron plasma wind tunnel at the von Karman Institute, Belgium. Binary scaled boundary layers were obtained for flows where diffusion and wall chemistry contribute significantly to the heat flux. The stagnation point heat fluxes were measured and exhibit a good agreement with the theoretical scaling law. This also validates the use of the binary scaling law in subsonic high-enthalpy facilities.

The second experiment was performed in the X2 expansion tube at the Centre for Hypersonics, Australia. Three flows were obtained over cylinders of different radii, adapting the free-stream density according to the binary scaling law. The free-stream conditions were determined in order to ensure a significant radiative coupling. Its effect could clearly be identified through measurements of the shock standoff distance, stagnation point heat flux, and shock layer radiation. A new method, based on a mix of experiments, computational fluid dynamics, and informed use of engineering correlations is proposed to perform ground to flight extrapolation for cases for which the radiative coupling is non-negligible.

Declaration by author

This thesis is composed of my original work, and contains no material previously published or written by another person except where due reference has been made in the text. I have clearly stated the contribution by others to jointly-authored works that I have included in my thesis.

I have clearly stated the contribution of others to my thesis as a whole, including statistical assistance, survey design, data analysis, significant technical procedures, professional editorial advice, and any other original research work used or reported in my thesis. The content of my thesis is the result of work I have carried out since the commencement of my research higher degree candidature and does not include a substantial part of work that has been submitted to qualify for the award of any other degree or diploma in any university or other tertiary institution. I have clearly stated which parts of my thesis, if any, have been submitted to qualify for another award.

I acknowledge that an electronic copy of my thesis must be lodged with the University Library and, subject to the policy and procedures of The University of Queensland, the thesis be made available for research and study in accordance with the Copyright Act 1968 unless a period of embargo has been approved by the Dean of the Graduate School.

I acknowledge that copyright of all material contained in my thesis resides with the copyright holder(s) of that material. Where appropriate I have obtained copyright permission from the copyright holder to reproduce material in this thesis.

Publications during candidature

Journal Papers

de Crombrugghe, Morgan, R. G., and Chazot, O."Theoretical Approach and Experimental Verification of the Role of Diffusive Transport under Binary Scaling Conditions", *International Journal of Heat and Mass Transfer*, 97:675-682, June 2016.

Reviewed Conference Papers

de Crombrugghe, G., Gildfind, D., Zander, F., McIntyre, T. J., and Morgan, R. G., "Design of Test Flows to Investigate Binary Scaling in High Enthalpy $CO_2 - N_2$ Mixtures", *19th Australasian Fluid Mechanics Conference, December, Melbourne, Australia*, 2014.

Conference Papers

de Crombrugghe, G., Morgan, R. G., McIntyre, T. J., and Zander, F., " Experimental Duplication of Venus Atmospheric Entry Flow", *11th NASA Venus Exploration Assessment Group (VEXAG) Meeting, November 19-21, Washington DC, U.S.A.*, 2013.

Alba, C., Lewis, L., de Crombrugghe, G., Eichmann, T., Morgan, R. G., and Greedyke, R., "Investigation of Surface Radiation in Earth Re-Entry Flows with Graphite Ablation", *6th Ablation Workshop, April 10-11 , Illinois, U.S.A.*, 2014.

Publications included in this thesis

de Crombrugghe, G., Gildfind, D., Zander, F., McIntyre, T. J., and Morgan, R. G., "Design of Test Flows to Investigate Binary Scaling in High Enthalpy $CO_2 - N_2$ Mixtures',' *19th Australasian Fluid Mechanics Conference, December, Melbourne, Australia*, 2014.

Content partly incorporated in chapter 6 and appendix G.

Contributor	Statement of contribution
de Crombrugghe, G. (Candidate)	Original idea (100%) Designed the experiments (90%) Wrote the paper (100%)
Gildfind, D.	Designed the experiments (10%) Provided expert advice (25%)
Zander, F.	Provided expert advice (25%) Reviewed the paper (25%)
McIntyre, T. J.	Reviewed the paper (25%)
Morgan, R. G.	Provided expert advice (50%) Reviewed the paper (50%)

de Crombrugghe, Morgan, R. G., and Chazot, O."Theoretical Approach and Experimental Verification of the Role of Diffusive Transport under Binary Scaling Conditions", *International Journal of Heat and Mass Transfer*, 97:675-682, June 2016.

Content partly incorporated in section 2.4 and chapter 5.

Contributor	Statement of contribution
de Crombrugghe, G. (Candidate)	Original idea (100%) Designed the experiments (90%) Wrote the paper (100%)
Morgan, R. G.	Provided expert advice (50%) Reviewed the paper (50%)
Chazot, O.	Designed the experiments (10%) Provided expert advice (50%) Reviewed the paper (50%)

Contributions by others to the thesis

No contribution by others

Statement of parts of the thesis submitted to qualify for the award of another degree

No contribution by others

Acknowledgment

These past few years have been full of new adventures and discoveries, both from the personal and professional point of view. The year 2013 started with an important step: moving down under. In 2014, I got married. In 2015, I received a dog and bought a house. In 2016, I am submitting my Ph.D. thesis.

First and foremost, I would like to thank my supervisors. Richard Morgan is not only an incredibly knowledgable (shall I say erudite?) professor, he is also a very kind and sympathetic person. Richard gave me the opportunity to explore my own research topics while remaining available if I needed guidance. Olivier Chazot is both a man of science and a humanist. He gave me the taste for the things beyond science, and our discussions about research often drifted away towards philosophy. Both Richard and Olivier proved to be extremely flexible when personal matters forced me to adapt my work. Last but not least, I would like to thank Tim McIntyre. Our weekly meetings encouraged me to have some structured progress in my work.

My deepest thanks then go to all these beautiful people I met at the Centre for Hypersonics. I will never forget my first day: no one knew a new student was arriving, there was no computer, no desk, nothing. A student wearing a T-shirt referring to a "Schnitzel run" (what could it possibly be?) gave me a pile of documents to read and wished me good luck. It was Fabian Zander. I immediately understood this was the start of my first friendship in Australia, many of which would follow. Students in the dungeon do not see the Sun very often and yet they cultivate a strong sense of cooperation and sharing. Allow me mention in particular those I spent the most time with: Elise Fahy, David Gilfind, Chris James, Steven Lewis, Hadas Porat, Jorge Sancho, Umar Sheikh, Pierpaolo Toniato, Han Wei, and Brad Wheatly. Then, there is the motorbike gang that took me out of the dungeon and made me discover the wonders of Queensland: Mathew Bricalli, Stefan Brieschenk, Dawid Preller, and Juanra Llobet. But I did not spend all my candidature in the dungeon. I must also thank the following people who contributed in one way or another to this work: Nikhil Banerji, Kevin Basore, David Buttsworth, Rowan Gollan, Bernd Helber, Peter Jacobs, Francesco Panerai, Isil Sakraker, Sandy Tirtey, Anabel del Val, Tristan Vanyai, and Dylan Wise. Finally, I would also like to express my warmest thanks to the technical staff for their amazing support during my experiments: Frans de Beurs and Keith Hitchcock at the University of Queensland, and Pascal Collin at the von Karman Institute.

Lastly, I want to acknowledge the continuous encouragements through thick and through thin of my wonderful wife, Ysaline, and my stupid dog, Colette.

Keywords

Hypersonics, fluid, entry, binary, scaling, similitude, high-enthalpy, high-temperature, ground-to-flight, Venus.

Australian and New Zealand Standard Research Classifications (ANZSRC)

ANZSRC code: 090107, Hypersonic Propulsion and Hypersonic Aerodynamics 100%

Field of Research (FoR) Classification

FoR code: 0901, Aerospace Engineering, 100%

Contents

List of Figures

List of Tables

List of Symbols

Notation conventions

q	quantity
$\dot{q}$	flux of quantity per unit area
$\overline{q} = q/q_{\text{ref}}$	dimensionless quantity
$\widehat{q}$	average of the measured quantity
$\sigma_{\text{meas}} q$	standard deviation on a single measurement of the quantity
$\sigma_{\text{set}} q$	standard deviation on a set of measurements of the quantity

Nondimensional numbers

Arr	Arrhénius parameter
Da_b	Damkhöler number of the bulk of a porous material (heterogenous)
Da_g	Damkhöler number of the gas-phase (homogenous)
Da_w	Damkhöler number of the wall (heterogenous)
K	hypersonic similarity parameter
Kn	Knudsen number
Le	Lewis number
Pe	Péclet number
Pr	Prandtl number
Re	Reynolds number
M	Mach number
γ	heat capacity ratio
Γ	Goulard number

Roman symbols

a	speed of sound	$\mathrm{m/s}$
a	acceleration	$\mathrm{m/s^2}$
a	thermal sensitvity	$\mu\mathrm{V/K}$
A	area	$\mathrm{m^2}$
A_{ul}	Einstein's spontaneous transition probability	$-$
B_{lu}	Einstein's absorption transition probability	$-$
B_{ul}	Einstein's stimulated emission probability	$-$
c_p	heat capacity at constant pressure	$\mathrm{J/K}$
c_v	heat capacity at constant volume	$\mathrm{J/K}$
D	diameter	m
D	diffusion coefficient	$\mathrm{m^2/s}$
e	specific energy	$\mathrm{J/kg}$
E	energy	J
g	specific Gibbs energy	$\mathrm{J/kg}$
g	degeneracy or statistical weight	$-$
h	specific enthalpy	$\mathrm{J/kg}$
I	irradiance *or* radiance	$\mathrm{W/m^2}$ *or* $\mathrm{W/m^2/sr}$
j	diffusion flux	$\mathrm{kg/m^2/s}$
k	thermal conductivity	$\mathrm{W/m/K}$
k	reaction rate of order n	$\mathrm{mol^{1-n}m^{n-1}/s}$
K_c	equilibrium constant	*context-dependent*
L	length	m
m	mass	kg
M	third-party (chemically neutral) chemical species	$-$
M_m	molar mass	$\mathrm{kg/m^3}$
N	number of items (e.g. measurements)	$-$
n	number density	$\mathrm{/m^3}$
p	pressure	Pa
q	heat flux	$\mathrm{W/m^2}$
Q	heat load	$\mathrm{J/m^2}$
R	radius	m
R	specific ideal gas constant	$\mathrm{J/kg/K}$
s	specific entropy	$\mathrm{J/K/kg}$
t	time	s
T	temperature	K
v	velocity	$\mathrm{m/s}$
V	volume	$\mathrm{m^3}$
$\dot{w}$	mass production	$\mathrm{kg/m^2/s}$ *or* $\mathrm{kg/m^3/s}$
x	mass fraction	$\mathrm{kg/kg}$
y	direction of space	m
Y and Y_2	arbitrary atomic and molecular species	$-$
Z	arbitrary atomic species	$-$

Greek symbols

α	dissociation fraction	$-$
α	absorbance	$-$
α	thermal diffusivity	$\mathrm{m^2/K/s}$
β	transversal velocity gradient	$/\mathrm{s}$
β	ballistic coefficient	$\mathrm{kg/m^2}$
γ	catalycity	$-$
γ_{entry}	entry angle	deg
δ	boundary layer thickness	m
Δ	shock stand-off distance	m
ϵ	emissivity	$-$
ϵ	porosity	$-$
ζ	oblique shock angle	deg
η	emission coefficient	$\mathrm{W/m^3}$
θ_a	activation temperature	K
ι	deflection angle	deg
κ	absorption coefficient	$/\mathrm{m}$
κ	quality of diffusive transport scaling	$-$
μ	dynamic viscosity	$\mathrm{kg/s/m}$
ν	frequency	Hz
ν	stoichiometric coefficient	$-$
Π	nondimensional / similarity parameter	$-$
ρ	density	$\mathrm{kg/m^3}$
σ	stress tensor	Pa
σ	extinction coefficient	$/\mathrm{m}$
σ	wavenumber	$/\mathrm{m}$
τ	thickness ratio	$-$
τ	time constant	s
τ	optical thickness	$-$
ϕ	line shape function	$-$
Φ	molar concentration	$\mathrm{mol/m^3}$
χ	scale factor	$-$
ψ	modified dissociation fraction	$\mathrm{mol/kg}$
ψ_w	modified wall dissociation fraction	$-$
ω	solid angle	sr

Sub- and Superscripts

ad	adiabatic
av	average
b	backward
c	convection
cd	conduction
d	dissociation
d	diffusion
dyn	dynamics
e	collision
e	edge of boundary layer
e	equivalent
el	electronic
entry	entry
eq	equilibrium
f	forward
flight	flow in flight (full-scale)
fr	frozen
i	direction of space (or j)
in	inward
inv	inviscid
k	energy mode
l	lower
lab	flow in the laboratory (down-scale)
m	(solid) material
out	outward
r	radiation
ref	reference
s	chemical species (or t)
s	sensible
stat	static
stag	stagnation point or line (implicit if not specified)
t	total
tr	translational
u	upper
vib	vibrational
w	wall
Y and Y_2	arbitrary atomic and molecular species
0	total (stagnation) conditions
3	ternary (i.e. related to three-body chemical reactions)
∞	free-stream

Constants

c	speed of light	$2.9979 \cdot 10^{8}$	$\mathrm{m/s}$
h	Planck constant	$6.6261 \cdot 10^{-34}$	$\mathrm{m^2kg/s}$
k_B	Boltzmann's constant	$1.3806 \cdot 10^{-23}$	$\mathrm{m^2kg/s^2/K}$
N_A	Avogadro constant	$6.0221 \cdot 10^{23}$	$\mathrm{/mol}$
R	ideal gas constant - air	8.3145	$\mathrm{J/mol/K}$
	ideal gas constant - Venus	8.3230	$\mathrm{J/mol/K}$
	specific ideal gas constant - air	287.06	$\mathrm{J/kg/K}$
	specific ideal gas constant - Venus	191.20	$\mathrm{J/kg/K}$
	specific ideal gas constant - CO_2	188.90	$\mathrm{J/kg/K}$
π	pi	3.1416	$-$
σ	Stefan-Boltzmann constant	5.6704	$\mathrm{W/m^2/K^4}$

List of Acronyms

CEA	Chemical Equilibrium with Applications
CFD	Computational Fluid Dynamics
CFCFD	Compressible Flow Computational Fluid Dynamics
CfH	Centre for Hypersonics
EAST	Electric Arc Shock Tube
EDL	Entry, Descent, Landing
ESA	European Space Agency
FWHM	Full Width at Half-Maximum
ICCD	Image-intensified Charge-Coupled Device
ICP	Inductive Coupled Plasma
IR	Infrared
LHTS	Local Heat Transfer Simulation
LTE	Local Thermodynamic Equilibrium
NASA	National Aeronautics and Space Administration
NEQAIR	Nonequilibrium Air Radiation
NIR	Near Infrared
NIST	National Institute of Standards and Technology
Oz	Australia
Poshax	Post-SHock relAXation solver
TPM	Thermal Protection Material
TPS	Thermal Protection System
UQ	University of Queensland
UV	Ultraviolet
Venus-GRAM	Venus Global Reference Atmospheric Model
VEXAG	Venus Exploration Advisory Group
VIRA	Venus International Reference Atmosphere
VKI	von Karman Institute
VUV	Vacuum Ultraviolet
X2	UQ expansion tube

"The more important fundamental laws and facts of physical science have all been discovered, and these are now so firmly established that the possibility of their ever being supplanted in consequence of new discoveries is exceedingly remote.

Nevertheless, it has been found that there are apparent exceptions to most of these laws, and this is particularly true when the observations are pushed to a limit, i.e., whenever the circumstances of experiment are such that extreme cases can be examined. [...]

As instances of such discoveries, which are in most cases due to the increasing order of accuracy made possible by improvements in measuring instruments, may be mentioned: first, the departure of actual gases from the simple laws of the so-called perfect gas."

- Albert A. Michelson, in *Light Waves and Their Uses* [122] (1903)

"Essentially, all models are wrong,
but some are useful."

- George E. P. Box, in *Empirical Model-Building and Response Surfaces* [18] (1987)

Chapter 1

Introduction

"I have often been impressed by the scanty attention paid even by original workers in physics to the great principle of similitude."

- Lord Rayleigh [157]

This thesis aims to present an in-depth study of similitude analysis applied to hypersonic flows. Similitude analysis is a fantastic mathematical tool which allows to obtain information about a system that is unavailable for whatever reason by studying another one that might be more accessible. In our case, the unavailable system is a hypersonic vehicle, such as a spacecraft plunging the atmosphere of some foreign planet at tremendous speed. The other one, more accessible, is a model of that spacecraft, installed in a hypersonic wind tunnel, in the (relative) comfort of a laboratory that offers both a controlled environment and repeatability.

With these few concepts, we can already shed some light on the title of this work. *Ground-to-flight extrapolation* is the process of studying a laboratory flow to learn about a vehicle in flight. *Binary scaling* is one of the methodologies to perform these extrapolations, that we will inspect in more details. Hypersonic wind tunnels, because of the enormous amount of energy the involve, are referred to as *high-enthalpy facilities*.

However, while similitude analysis is undoubtedly useful, it also has certain limitations. Emerging - or re-emerging - trends in the space industry, such as reusable vehicles and the multiplication of space debris, might result in a new interest for hypersonic technologies with the objective of developing cheaper, safer, and larger systems[1]. If so, proper understanding of every aspects of the design of hypersonic craft, including ground-to-flight extrapolation, will become increasingly necessary. In that context, the limitations of similitude analysis have therefore to be properly understood and, where possible, accounted for.

[1]The interested reader can find in appendix A a brief account of the central role of hypersonics for the aerospace industry in the medium-term future.

1.1 On the role and challenges of experimentation in hypersonics

The design of a system (atmospheric entry vehicle or other) is schematically executed in three steps, represented in figure 1.1. First, a feasibility study, which usually consists of a rough preliminary design built upon simple correlations. These can then serve as input to enter the design itself. This second step is an iterative process which is usually supported by intermediate testing and verification of key elements. Lastly, the final design has to go through a full validation prior to being accepted.

The design supporting activities of a hypersonic vehicle will require an extensive use of fluid dynamics. Because Navier-Stokes equations cannot be solved analytically[2], a solution has to be obtained either by acting on nature itself (i.e. performing an experiment) or using a computer to solve them numerically with computational fluid dynamics (CFD). It should be noted, as illustrated in figure 1.2, that CFD codes are built upon physical models which are themselves developed through experiments[3].

Computer simulations and experiments are thus used simultaneously during the design process. In some cases, such as for example subsonic aircraft design or automotive aerodynamics, CFD tools are so advanced that experiments are barely needed. In some others, such as turbomachinery or high-performance automotive, the level of accuracy aimed for requires to continuously improve the physical models that are fed to CFD with experiments.

One could thus be tempted to relegate experimental hypersonics to a technical role of validation for CFD, when it can be afforded, as it is already the case for most branches of fluid dynamics. However, unlike these other branches of fluid dynamics, the consolidation of hypersonic numerical codes with models versatile enough to provide accurate results over a wide range of flow conditions has not taken place yet. That is because of the very nature of the hypersonic challenge: first, conditions are harsh, and second, even in the simplest case there is a wide variety of strongly intertwined physical processes. As a result, current modern CFD tools are only judged reliable for spacecraft design in the case of low orbit re-entry: moderately low hypersonic flows characterized by low ionization and for which 5 air species models are sufficiently accurate.

Atmospheric entry vehicles are meant to ensure the survival of a payload through the critical phase of EDL. The hypersonic phase is usually limited for the entry portion. At high altitude, during the beginning of the entry phase, the flow is rarefied and the chemical processes are likely to be out of equilibrium in a significant portion of the shock layer. As the vehicle decelerates through the atmosphere, the aeroheating loads build up in the form of a complex combination of conductive, diffusive, and radiative heat fluxes. Aerodynamic forces also start to play a significant role, with

[2]There is an even more fundamental issue in that there is no demonstration for the existence of a smooth solution to Navier-Stokes equations. This issue became one of the seven Millennium Prize problems identified by the Clay Mathematics Institute, the assignment being to prove or give a counter-example of the following statement: *in three space dimensions and time, given an initial velocity field, there exists a vector velocity field and a scalar pressure field, which are both smooth and globally defined, that solve the Navier-Stokes equations.* It is rather amusing to consider that we fly airplanes using a set of equations of which our theoretical understanding is still incomplete.

[3]As Einstein puts it: *"Pure logical thinking cannot yield us any knowledge of the empirical world; all knowledge of reality starts from experience and ends in it."* [45]

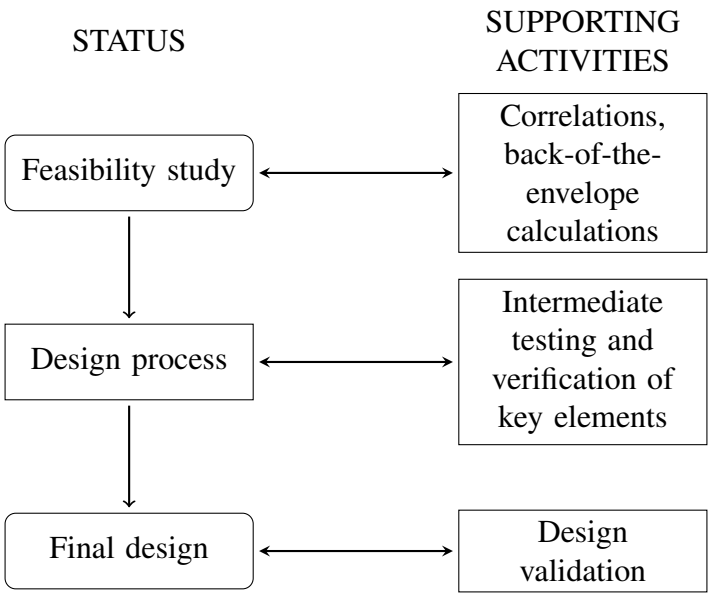

Figure 1.1: *Schematic high-level representation of the steps in the design of a system, and corresponding supporting activities.*

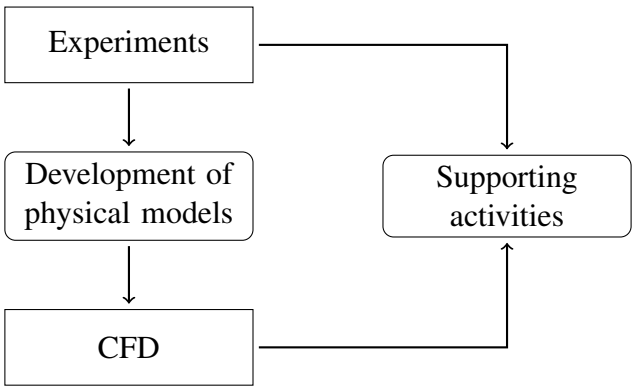

Figure 1.2: *The role of experiments and CFD in the design of systems involving fluid dynamics.*

questions of stability and possibly also control. These are particularly important as the flow around the vehicles transitions from a supersonic to a subsonic regime.

When examining a little closer the aeroheating phase, one realizes that the thermal stresses at the wall are a strong function of a wide range of flow properties such as the temperature of the shock layer, the chemical composition of the boundary layer (which may result in further recombination at the wall), the nature of radiative heat fluxes, or the laminar to turbulent transition. The use of ablative materials, considered as an appropriate solution to sustain important heat loads, further increase the complexity of the problem by blowing new species in the boundary layer, absorbing part of the radiative heat flux, and affecting turbulent transition. All these processes further influence other flow properties that come into play for the craft's design: pressure distribution, leeward radiation, shock standoff distance, etc. Moreover, the terms needed to close Navier-Stokes equations need to be modeled using other branches of science than fluid dynamics, such as chemistry, materials sciences, and even electromagnetism (if there is significant ionization) or quantum physics (to characterize radiation).

Nevertheless, the situation is not a dead-end, but rather an arduous task assigned to engineers and scientists. Let us thus begin with the beginning, and investigate what are the reasons why it is difficult to obtain experimental data of sufficient quality:

- First, one has to design a test set-up that untangles the flow processes so as to isolate as much as can be one particular flow process from the others. That is one of the reason why experimental hypersonics often focuses on very simple geometries (e.g. flat plates, spheres, normal shock front, etc.) or relies on bold assumptions (e.g. local thermal equilibrium, adiabatic flow, etc.).

- Second, the free-stream conditions are difficult to control and characterize. Indeed, the establishment of a test flow in hypersonic wind tunnels is generally a very complex problem on its own. While high-enthalpy facilities have been used for decades with a certain level of confidence, many questions remain unanswered and require thus to make strong assumption. For example, what fraction of the electric power is transferred to the flow in arcjets or inductively coupled plasma wind tunnels? Does the erosion of the electrode in arcjets have an influence of the macroscopic flow features? How does the boundary layer grow in the nozzle of expansion tubes? Moreover, the quantities of interest in the free-stream are either not directly accessible (e.g. enthalpy, density, etc.) or difficult to measure (e.g. dissociation fraction, flow contamination, etc.).

- Thirdly, measurements are performed in a challenging environment. For example, test durations in expansion tubes and shock tubes are typically in the order of a fraction of a millisecond, which implies that transient measurements techniques have to be used. Debris from the diaphragms, needed in those facilities, severely damage the test model, thereby changing its surface properties, and thus requiring to replace it frequently. Heat gauges in plasma wind tunnels are submitted to intense heating for long durations. Non-intrusive optical techniques need complex calibration procedures.

- Lastly, the tremendous amount of energy required to create hypersonic flows implies that the duplication of the flow encountered in flight in ground-based laboratories is only partial[4]. In other words: either only a portion of the flow is obtained (e.g. the boundary layer in the vicinity of the stagnation line in plasma wind tunnels, the inviscid portion of the flow immediately downstream of the shock in shock tubes, etc.), or the whole flow is obtained but over a smaller scale (figure 1.3). Coarser approaches are sometimes preferred, such as for thermal protection material (TPM) testing for which the wall heat flux is sometimes regarded as the only significant variable.

All these arguments demonstrate the importance to understand not only *how* we are testing (i.e. free-stream conditions, instrumentation, etc.) but also *what* we are testing. The process is slow[5], but moving forward as experimentalists gain a better acquaintance of their facilities, and as the dialogue with numericists and theorists is strengthened, improving the mutual understanding of the needs and difficulties of each party.

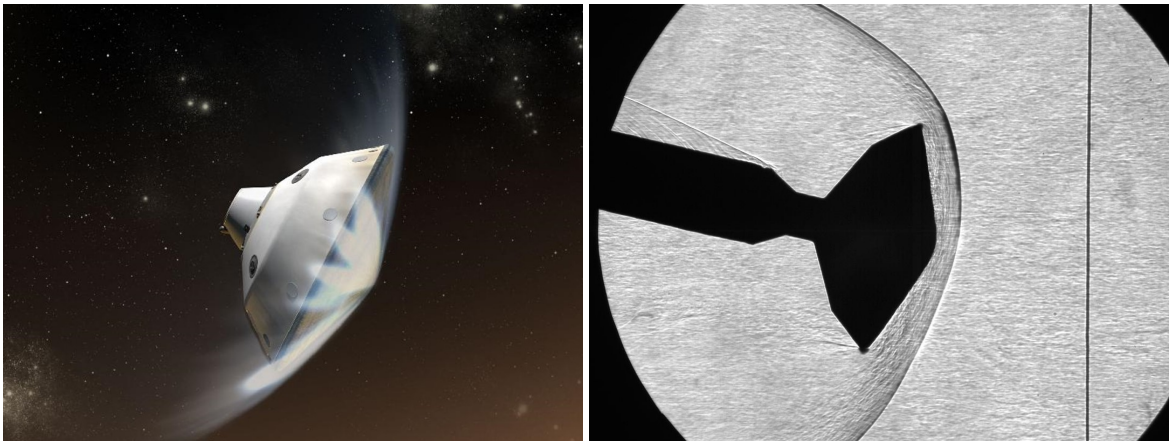

(a) (b)

Figure 1.3: *One of the aims of experimental hypersonics: achieving at least partial similarity between the flow encountered in flight and that obtained in ground-based wind tunnels. Here, and artist's rendering of MSL entering the martian atmosphere (a) and a Schlieren image of a* $1/30$ *scale model of the MSL aeroshell in the Hypersonic Tunnel* 9 *at the Arnold Engineering Development Complex (b). (Source: JPL and AEDC)*

1.2 Purpose of this thesis

In this thesis, we take a closer look at the correspondence between the flow in flight and its truncated version that can established in ground facilities. More specifically, we investigate one of such truncated experimental duplication, namely the binary scaling law.

The four research questions that are at stake are:

1. Which testing methodology can we apply for high-enthalpy ground-to-flight extrapolation?

[4]The different techniques used to obtain high-enthalpy flows will be discussed in section 2.3.

[5]We did not even touch upon the logistics of operating hypersonic facilities and their instrumentation, which are often insatiable in terms of time, man-power, and money.

2. Do all the flow features scale appropriately within a family of binary scaled flows?

3. If not, what macroscopic differences will these discrepancies cause?

4. Can we provide tools to account for these differences when performing ground-to-flight extrapolation?

With these, we hope to demonstrate that experimentation is and will remain a performing and relevant tool for aerospace design in general, and hypersonic fluid dynamics in particular.

1.3 Thesis outline

The investigations are divided in two parts. The first part consists in a state-of-the-art review of binary scaling, what is known about it, and how it is used. This base knowledge is extended with the help of physical modeling and elementary numerical simulations so as to define, from a theoretical point of view, the limits of binary scaling. The second part is focused on the experimental investigations that support and complement the conclusions of the first part.

The first part is divided into three chapters. The first one puts the binary scaling law into **context**. The different scaling laws used for super- and hypersonic fluid dynamics are briefly presented, gradually increasing the free-stream enthalpy and thus also the overall complexity of the flow. Although most of what is presented in this chapter is already largely known, it is insightful to systematically develop the binary scaling law. A major advantage of this approach is that it provides a solid base on which we will then be able to identify the shortcomings of that scaling law. Moreover, it allowed us to clarify the role of diffusive transport, which is properly scaled within a family of binary scaled flows. That result, while simple, was not known.

In the second chapter, we pinpoint which are the main **limitations** of the binary scaling. These are classified in four groups: simplifications in the chemistry model, loose definition of the scaling parameters, radiation coupling in the gas-phase, and off-stagnation line effects. Only the first three items are examined, the last one being out of the scope of the present work. A common approach is to restrict the use of binary scaling to flows with little radiation coupling and for which a significant fraction of the shock layer is in nonequilibrium, which justifies the use of a simplified chemistry model. In this chapter, we investigate how each of these hypotheses impact the quality of the scaling and how the error they introduce can be accounted for.

Once the binary scaling theory is laid out, the third chapter consists in a **practical example** of the logic to apply to perform ground-to-flight extrapolation of a certain quantity, i.e. how to derive the value of a variable in flight based on the measurement of that variable in a scaled laboratory flow. The quantity of interest is the stagnation point heat flux, which is interesting for two aspects. First, it is a crucial design parameter of atmospheric entry vehicle that is often at the centre of experimental campaigns. Second, it is a highly problematic flow variable regarding binary scaling as it does not scale in a linear fashion and is highly influenced by radiation coupling.

The second part consists in the description of two experiments from the test set-up to the discussion of the results. These two experiments constitute an assessment of the theory developed in the first part. Not only do they support the conclusions made regarding the applicability and limitations of binary scaling, but they also provide unique material to validate new methodologies to account for these limitations.

The **first experiment** is fully described in the fifth chapter (i.e. the first chapter of the second part). It was conducted in a subsonic facility, the Plasmatron plasma wind tunnel at the von Karman Institute (VKI), in Belgium. Its main purpose is to *demonstrate that diffusive transport scales appropriately* under binary scaling conditions (figure 5.2). As a side result, it also extend the use of binary scaling to subsonic flows, opening a new range of potential applications to experimentalists.

The **second experiment** is described over the four remaining chapters. It was conducted in a hypersonic facility, the X2 super-orbital expansion tube at the University of Queensland, in Australia. Its purpose is to **apply binary scaling in a controlled environment**. Tests are performed in three flows and three different models designed in such a way that the resulting shock layer are similar from the point of view of binary scaling, i.e. belong to the same family of binary scaling flows. The advantage of this approach is that all three test cases are investigated in the same wind tunnel, using the same instrumentation and the same post-processing techniques. Differences from one test case to another can thus not be attributed to uncertainties with specific test conditions.

The sixth chapter is a description of the **design test condition** methodology in the X2 expansion tube, and how it was applied for this specific test campaign. The importance to design test condition that would result in significant radiation coupling is stressed. It is indeed not only a pivotal element of this investigation of binary scaling, but also more generally a central question for future developments in hypersonics and for which more experimental data is needed [63].

Three elements are measured during this second experiment: the shock standoff distance, the stagnation point heat flux, and the shock layer radiation along the stagnation line.

The seventh chapter concerns the **shock standoff**. The main purpose of this measurement is to confirm that the three test conditions are indeed radiatively coupled and that this coupling increases with the length-scale of the flow (figure 7.3). Moreover, this data complements the small base of publicly available experimental data for the high-speed hypersonic regime [212].

The measurements related to the **stagnation point heat flux** are presented in the eighth chapter. The effect of non-binary chemistry and radiative coupling are clearly identified, corrupting any attempt to perform ground-to-flight extrapolation with the tools traditionally used. Nevertheless, a new extrapolation methodology is suggested and successfully validated (figure 8.8). It is based on experimental measurement, an informed use of correlations, and elementary CFD simulations. That novel method only requires from the experimentalist to measure the total heat flux on one test condition, from which he can then derive the convective and radiative heat flux for any flow of the same binary scaling family. The results are not only more accurate, but they can also be looked at with greater confidence.

Lastly, the measurement of the **spectral radiation along the stagnation line** primarily serves to support the overall conclusions made in the previous chapter and throughout the first part of the thesis.

Two regions of the spectrum are examined: a portion of the near-infrared, and part of the C_2 Swan system. As expected, it appears that radiation (i.e. temperature) is higher as the length-scale of the flow decreases, with stronger atomic lines and less molecular features.

More detailed data related to the experimental campaign can be found in appendix, as well as a literature review of **Venus atmospheric entry**: the rationale to research it, what is known, what remains to be discovered. Venus atmospheric entry is the topic of one of the two experiments described in the second part. It is a particularly relevant case for binary scaling with two regards. First, the Venusian atmosphere is thick, thus resulting in dense shock layers that favor chemical equilibrium. Second, it is rich in strong radiators and direct entry takes places at velocities in excess of $\sim 10\,\mathrm{km/s}$. These two elements contribute to a strong radiation in the shock layer, and thus a non-negligible radiative coupling. The duplication of Venus atmospheric entry flows is thus a binary scaling worst case scenario.

1.4 Contributions of this thesis to the discussion

The original contributions of this work are mainly:

1. A systematic and rigorous approach to the binary scaling law (chapter 2).
2. The theoretical demonstration and experimental assessment of the role of diffusive transport under binary scaling conditions (chapters 2 and 5).
3. The theoretical demonstration and experimental assessment of extension of the binary scaling law to subsonic flows (chapter 5).
4. The identification of non-binary chemistry and radiation coupling as the two main limitations to the application of binary scaling (chapter 3).
5. The experimental demonstration of the influence of these two limitations on macroscopic features of the flow such as shock standoff distance (chapter 7), stagnation point heat flux (chapters 4 and 8) and spectral radiation (chapter 9).
6. Experimental data relevant for Venus atmospheric entry regarding shock standoff distance (chapter 7), stagnation point heat flux (chapters 4 and 8) and spectral radiation (chapter 9).
7. The proposition and experimental validation of a new methodology to enhance the results of ground-to-flight extrapolation of the stagnation point heat flux (chapter 8).
8. The proposition and experimental validation of a methodology to obtain in expansion tubes different flows belonging to the same binary scaling family (chapter 6).

Part I

Literature review and theoretical developments

Chapter 2

Hypersonic Scaling Laws

"Undoubtedly, philosophers are in the right when they tell us that nothing is great or little otherwise than by comparison."

- Jonathan Swift, in *Gulliver's Travels* (1726)

This opening chapter serves as a gradual introduction to the binary scaling law. The purpose and specific vocabulary of similitude analysis is first briefly presented. Various scaling laws used for hypersonic flows are then progressively introduced, i.e. increasing the number of physical processes coming into play, and thus the number of flow variables and constituting equations.

The first section is devoted to the Reynolds-Mach scaling. It is used for moderate enthalpy flows, for which compressibility plays a role but not thermal effects. That scaling is widely used and well-known in aeronautical applications, it is based on the nondimensionalisation of the mass and momentum balance equations. Two dimensionless numbers are identified; the Reynolds and the Mach number

The section thereafter is devoted to flows for which the enthalpy is high enough to introduce thermal effects but not chemistry. Three additional dimensionless numbers are introduced: the specific heat ratio, the Prandtl number, and the dimensionless internal energy of the wall.

Increasing even further the free-stream enthalpy leads to chemical effects. While that causes a breakdown of the similitude analysis, some assumptions are made, allowing the development of the binary scaling law and obtention of partial similarity in some cases. Three more dimensionless numbers are introduced: the Damköhler numbers of the gas phase and of the wall, and the Péclet number. Using the Π theorem, we will demonstrate that there is only one degree of freedom left: the length scale of the flow.

Pushing the binary scaling to its utter limits and increasing even further the free-stream enthalpy, radiation becomes so intense that it starts coupling with the rest of the flowfield, cooling some regions and heating others. Vehicles encountering that type of flow are at the edge of human technology: interplanetary probes plumbing the atmosphere of the Earth, Venus, Mars, Titan, or the gas giants at speeds greater than $\sim 10\mathrm{km/s}$. In those extremely harsh environments, the similitude analysis finally

breaks down: there are no degrees of freedom left, and only full-scale duplication is possible for all parameters at once. Nonetheless, partial simulation of selected parameters is still possible and very useful.

Schematically speaking, the progressive increase of the free-stream enthalpy can indeed been seen as an increase of complexity. Indeed, for a flow out of equilibrium the change in enthalpy h can be expressed as:

$$dh = dg + Tds + sdT \tag{2.1}$$

where g is the specific Gibbs energy, s the specific entropy, and T the temperature. Considering an inflow at constant temperature and thermochemical equilibrium ($dg = 0$), an increase in enthalpy (i.e. velocity) corresponds thus to an increase in entropy. The latter is regarded as an expression of the degree of disorder or, in popular culture, complexity[1].

2.1 Similitude analysis

The purpose of *similitude analysis*, sometimes referred to in the literature as *inspectional analysis*, is to obtain information about a system (the flow around an airplane, a chemical reactor, or even a financial market) using a different time or spatial scale when the system of interest is too costly or technically impossible to reproduce in its original duration or dimensions, or simply unavailable. This is done by identifying and reproducing a series of reference quantities that we will call *similarity parameters* although they are also found in literature under the name *eigen-measure*. Ideally, simple quantitative relations can be derived between the experimental measurement and the variables of interest so as to avoid complicated mathematical modeling and computer time.

A very basic example would be the similarity that exists between geometrical figures of the same family[2]. For example, one knows that every triangle obeys the Al-Kashi theorem:

$$c^2 = a^2 + b^2 - 2ab\cos\gamma \tag{2.2}$$

Three similarity parameters can be identified in this case, for example: $\Pi_1 = a/b$, $\Pi_2 = \gamma$ and $\Pi_3 = c/b$. In other words, we divided every length (a, b, and c) by a reference length-scale (b).

[1] The free-stream in ground-based laboratories is often at higher temperature than in flight, and sometimes even out of equilibrium ($g > 0$). Therefore, if the enthalpy of the free-stream in the laboratory equals that of the flight, one can write:

$$s_{\text{lab}}/s_{\text{flight}} = g_{\text{lab}}/s_{\text{lab}}T_{\text{flight}} + T_{\text{lab}}/T_{\text{flight}} > 1$$

where the subscripts flight and lab stand respectively for flight and laboratory conditions. The entropy of the inflow is thus greater in flight than in the laboratory.

[2] The concept of similitude can be traced back to - and probably finds its origins in - the ideas of geometrical similarity and proportions developed by the Greeks. Later early users of dimensional analysis included Galileo, Mariotte, Newton, and Fourier, who first theorized its approach in terms of units. An interesting historical overview can be found in [15].

Al-Kashi's theorem can be expressed with those new parameters:

$$\Pi_3 = \Pi_1^2 + 1 - 2\Pi_1 \cos \Pi_2 \tag{2.3}$$

The value of Π_3 is thus the same for all triangles that share the same Π_1 and Π_2. While that relationship was easy to establish analytically, some other systems are much more complex and only allow for empirical or semi-empirical similarity parameters. This strategy has been applied with a certain degree of success to many fields of physics, its most famous application being most probably fluid dynamics.

Prior to applying *similitude analysis*, it is important to differentiate it from *dimensional analysis*. Dimensional analysis is built upon the Vaschy-Buckingham Π theorem. Attributed to an independent derivation of Vaschy in 1892 [203] and some years later Buckingham in 1914 with a more rigorous proof [23], it was actually first derived by Bertrand in 1878 [13]. The theorem states that if a problem has N variables and that P fundamental dimensions are required to describe them, then the physical relations between those variables can be expressed with $N - P$ nondimensional variables, each of those being a product of power of the original variables. The Π theorem is a mathematical theorem, and has thus absolute validity [15].

In our example with the triangles, we have four variables $N = 4$ (a, b, c, and γ) and one fundamental dimensions $P = 1$ (length in m, the angle behind expressed in rad which are length ratios). The number of nondimensional parameters is thus $N - P = 3$. These three parameters are obtained as:

$$\Pi = a^j b^k c^l \gamma^m \tag{2.4}$$

where we necessarily have that $j + k + l = 0$ and m can take any value so as to ensure that each Π is dimensionless. The combinations we obtained earlier was $j = 1$, $k = -1$, $l = m = 0$ for Π_1, $j = k = l = 0$, $m = 1$ for Π_2, and $k = -1$, $l = 1$, $j = m = 0$ for Π_3. However, any other combination that satisfies the two conditions on the exponents is valid.

This illustrates the essential difference between similitude and dimensional analysis. While for the former we worked on the Al-Kashi theorem (our model for triangles), for the later we simply identified the variables and dimensions of the problem. The advantage of dimensional analysis is thus that it does not require to know the constitutive equations of the problem, which makes it very attractive. However, there is a risk of losing some of the information contained in these, including the physical significance of the nondimensional groups. As expressed by Bridgman, the right set of parameters *"cannot be decided by the philosopher in his armchair"* [21].

Nevertheless, dimensional analysis is a powerful tool with extension in many branches of knowledge. Consider for example *allometry*, a discipline of life science. It states that similarities can be found between all mammals in the form of mass ratios: the mass of the heart to the mass of blood, the mass of the kidney to the mass of liver, etc. Knowing the mass of an extinct or newly discovered mammal allows thus to predict the mass of blood its body contains.

As such, similitude analysis can be considered as a particular case of dimensional analysis for which a more rigorous approach is taken. Indeed, it also satisfies the Vaschy-Buckingham Π theorem of dimensional analysis but relies on a physical understanding of the phenomena (through models) rather than on intuition or experiments.

2.2 Low to Medium Hypersonic Scaling Laws

2.2.1 Reynolds-Mach scaling

Let us first consider a simple case: a steady, viscous, compressible and isothermic flow. We assume that the body shape and angle of attack are duplicated for the entire family of scaled flows. Such a problem is solved with the Navier-Stokes equations for the balance of mass (equation 2.5), and momentum (equation 2.6 for $j = 1, 2, 3$):

$$\frac{\partial}{\partial y_i}(\rho v_i) = 0 \tag{2.5}$$

$$\frac{\partial}{\partial y_i}(\rho v_i v_j) = -\frac{\partial p}{\partial y_j} + \mu\left(\frac{\partial^2 v_i}{\partial^2 y_i} + \frac{1}{3}\frac{\partial^2 v_i}{\partial y_j \partial y_i}\right) \tag{2.6}$$

where ρ is the density, y_i direction of space, v the velocity, p the pressure, μ the dynamic viscosity. Note that Einstein's notation is used, and that we applied Stokes' hypothesis on the bulk viscosity in order to isolate the dynamic viscosity. An interpretation of the different terms can be found in any good (hypersonic) fluid dynamics text book, such as [7]. The solution to equation 2.5 is trivial, while the nondimensional form of equation 2.6 is:

$$\frac{\rho_\infty v_\infty^2}{L}\frac{\partial}{\partial \overline{y}_i}(\overline{\rho v}_i \overline{v}_j) = -\frac{p_\infty}{L}\frac{\partial \overline{p}}{\partial \overline{y}_j} + \frac{\mu v_\infty}{L^2}\overline{\mu}\left(\frac{\partial^2 \overline{v}_i}{\partial^2 \overline{y}_i} + \frac{1}{3}\frac{\partial^2 \overline{v}_i}{\partial \overline{y}_j \partial \overline{y}_i}\right) \tag{2.7}$$

where the overlined terms are dimensionless, for example $\overline{y} = y/L$ with L a typical length-scale of the flow or $\overline{\rho} = \rho/\rho_\infty$ with the subscript ∞ referring to the the free-stream. Note that the thermal effects are not accounted for at this stage. As a consequence, the viscosity μ does not vary with temperature, and the use of the subscript ∞ is thus superfluous. Dividing all terms by the group $\rho_\infty v_\infty^2/L$, one obtains:

$$\frac{\partial}{\partial \overline{y}_i}(\overline{\rho v}_i \overline{v}_j) = -\frac{p_\infty}{\rho_\infty v_\infty^2}\frac{\partial \overline{p}}{\partial \overline{y}_j} + \frac{\mu}{\rho_\infty L v_\infty}\overline{\mu}\left(\frac{\partial^2 \overline{v}_i}{\partial^2 \overline{y}_i} + \frac{1}{3}\frac{\partial^2 \overline{v}_i}{\partial \overline{y}_j \partial \overline{y}_i}\right) \tag{2.8}$$

The nondimensional group multiplying the second term on the right-hand side is the inverse of the free-stream Reynolds number Re_∞, and the group multiplying the first term on the right-hand side is the inverse of the product of the heat capacity ratio with the square of the free-stream Mach number $\gamma \mathrm{M}_\infty^2$. Indeed, using the ideal gas law $p/\rho = RT$ and the definition of the speed of sound $a^2 = \gamma RT$

one can write:

$$\frac{p_\infty/\rho_\infty}{v_\infty^2} = \frac{RT_\infty}{v_\infty^2} = \frac{1}{\gamma}\frac{\gamma RT_\infty}{v_\infty^2} = \frac{1}{\gamma \mathrm{M}_\infty^2} \tag{2.9}$$

Equation 2.8 ultimately becomes:

$$\frac{\partial}{\partial \overline{y}_i}(\overline{\rho v}_i \overline{v}_j) = -\frac{1}{\gamma_\infty \mathrm{M}_\infty^2}\frac{\partial \overline{p}}{\partial \overline{y}_j} + \frac{1}{\mathrm{Re}_\infty}\overline{\mu}\left(\frac{\partial^2 \overline{v}_i}{\partial^2 \overline{y}_i} + \frac{1}{3}\frac{\partial^2 \overline{v}_i}{\partial \overline{y}_j \partial \overline{y}_i}\right) \tag{2.10}$$

This is consistent with the Π theorem. In this case, $N = 5$ variables are needed to describe the problem: v_∞, ρ_∞, μ, a, and L. On the other hand, $P = 3$ dimensions are required to describe those variables: mass kg, time s and length m. The speed of sound was chosen for the sake of simplicity but, alternatively, it is possible to use the pressure p as both are linked through the definition of the speed of sound. There should therefore only be $N - P = 2$ similarity parameters.

Let us reflect on the beauty and simplicity of what has been derived in less than a page. There is a family of flows that are mathematically similar to one another; any variable in any of these flows is linked to all the others through simple mathematical relations. The condition to ensure that similarity is that they have to be characterized by the same object shape and angle of attack and the two following similarity parameters have to be duplicated:

$$\Pi_1 = \mathrm{Re}_\infty = \frac{\rho_\infty v_\infty L}{\mu} \propto \frac{\text{momentum forces}}{\text{viscous forces}} \tag{2.11}$$

$$\Pi_2 = \gamma \mathrm{M}_\infty^2 = \frac{v_\infty^2}{RT_\infty} \propto \frac{\text{kinetic energy}}{\text{internal energy}} \tag{2.12}$$

where Π_1 represents the viscosity of the flow and Π_2 for its compressibility. In other words, as long as the balance between momentum and viscous forces on the one hand and kinetic and internal energy on the other hand is maintained, the solution of the flow is the same. It should be noted that the same test gas is usually used, and therefore in most applications one can simplify the second similarity parameter to $\Pi_2 = \mathrm{M}_\infty$.

Incidentally, the Knudsen number is also duplicated through Π_1 and Π_2:

$$\mathrm{Kn} = \frac{\sqrt{\gamma \mathrm{M}^2}}{\mathrm{Re}}\sqrt{\frac{\pi}{2}} = \frac{k_B T}{\sqrt{2}\pi d^2 p L} \tag{2.13}$$

where k_B is Boltzmann's constant and d the particle hard shell diameter. This result is far from being anecdotical, as the Knudsen is used to determine whether statistical mechanics or continuum mechanics should be used. If the original flow is a continuum, so will be the scaled one, and the Navier-Stokes equations will remain applicable[3].

[3]Would it not have been the case, other techniques should have been used to account for rarefied regime [111] thus potentially breaking the similarity.

Since there are $N - P$ similarity parameters that have to be reproduced, and N variables to reproduce them, the number of dimensions P is in the present case also the number of degrees of freedom of the problem. Indeed, one could for example reduce the temperature of the flow, use a smaller-scale model, and a substitution gas (e.g. N_2 instead of air) thereby changing μ and R. By doing so, the adjustment in free-stream density is imposed through the Reynolds number, and that in velocity through the Mach number.

This approach is commonly used in aeronautics, and therefore also in low-enthalpy hypersonic. A typical application would be to lower the temperature of the flow so as to reach a certain Mach number at a lower velocity than what would be required at room temperature. Many facilities are therefore characterized in terms of the Mach and Reynolds numbers they can achieved (see for example figure 2.1). The upper limit of the wind tunnel's envelope is then imposed by the test gas' condensation temperature; past a certain Mach number the similarity does not hold anymore.

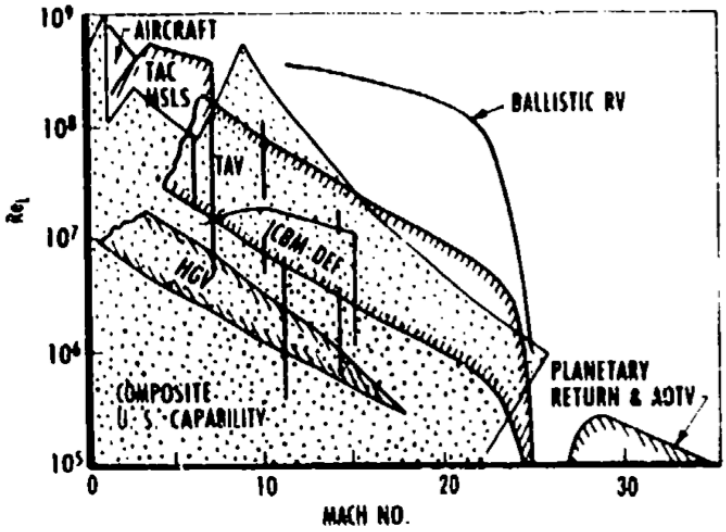

Figure 2.1: *Example of facility performance envelope definition as a function of Mach and Reynolds number. The U.S. capability in the early 90s is compared against typical hypersonic problems: hypersonic glide vehicles (HGV), trans-atmospheric vehicles (TAV), intercontinental ballistic missiles (ICBM), etc. Figure excerpted from [116].*

2.2.2 Hypersonic Similarity

Let us do a small side track and examine a special type of Reynolds-Mach scaling: the hypersonic similarity. It is used for flows with Mach numbers large enough to be technically challenging. It is, however, only applicable for slender bodies, i.e. bodies that generate weak shocks and thus limited thermal effects, if any.

Tsien demonstrated a method to duplicate these flows at even lower Mach number by modifying their geometry [196]. The slenderness of a body is quantified with its thickness ratio, defined as $\tau = D/L$ where D is the body's diameter and L its length. A body is considered as slender if $\tau \ll 1$. In that case, the shock layer is very thin and the flow can be considered as inviscid, i.e. it is mainly

the shock that determines the pressure distribution along the body's surface. The second term on the right-hand side of equation 2.10 is thus ignored and only M_∞ has to be duplicated. The equation can then be further simplified using the small-disturbance theory, and Π_2 becomes:

$$\Pi_2 = K = M_\infty \tau \tag{2.14}$$

where K is known as the hypersonic similarity parameter. Increasing the thickness ratio of the slender body allows thus to work at lower Mach numbers.

Hayes and Probstein further extended that analysis for flows with non-negligible viscous layers (i.e. with a certain bluntness) [74], which is the case of many hypersonic vehicles. For such bodies, the boundary layer is thick and has an influence on the pressure distribution, which in turn has an effect on the thickness of the boundary layer itself; there is viscid-inviscid coupling. They introduced a viscous-inviscid interaction parameter χ, which characterizes the ratio with which the boundary layer grows:

$$\Pi_1 = \chi = M_\infty^3 \sqrt{\frac{C}{Re_\infty}} \tag{2.15}$$

where:

$$C = \frac{\mu_w T_\infty}{\mu_\infty T_w} \tag{2.16}$$

where the subscript w stands for the wall.

2.2.3 Reynolds-Mach scaling with thermal effect

Increasing the free-stream enthalpy, the temperature of the shock layer will rise and thermal effects will have to be taken into account. In other words, the Navier-Stokes equation for the conservation of energy has to be solved as well. We remain here under the hypothesis of a chemically inert and adiabatic flow[4]. The conservation of energy is then expressed as:

$$\frac{\partial}{\partial y_i}\left[\rho v_i \left(e + \frac{v_i^2}{2}\right)\right] = -\frac{\partial q_i}{\partial y_i} + \frac{\partial}{\partial y_j}(\sigma_{ij} v_i) - \frac{\partial}{\partial y_i}(v_i p) \tag{2.17}$$

where $e = c_p dT$ is the thermal energy, with c_p the heat capacity at constant pressure, $q_i = k\partial T/\partial y_i$ is the conductive heat flux with $k(T)$ the thermal conductivity, σ_{ij} is the stress tensor, that we choose not to express fully as we did in equation 2.6 for the sake of simplicity. For moderate free-stream enthalpy, the gas can be treated as a calorically perfect gas, i.e. c_p and c_v are constant. As the enthalpy increases, it has to be treated as a thermally perfect gas, i.e. flow properties such as $c_p(T)$ and $c_v(T)$ are now variable with temperature.

[4]In the rest of this thesis, we will refer to an *adiabatic flow* as a flow for which the gas phase is adiabatic. A non-adiabatic flow is then a flow for which certain fractions of the flow are cooled down or heated up by radiation.

Going through the same exercise that led us to the Mach-Reynolds scaling, one obtains the following nondimensional form for the conservation of energy:

$$\begin{aligned}&\overline{\rho v_i}\frac{\partial \overline{e}}{\partial \overline{y}_i} + \frac{\gamma(\gamma-1)}{2}\mathrm{M}_\infty^2 \frac{\partial}{\partial \overline{y}_i}\left(\overline{v}_i^2\right) \\ &= \frac{\gamma}{\mathrm{Pr}_\infty \mathrm{Re}_\infty}\frac{\partial}{\partial \overline{y}_i}\left(\overline{k}\frac{\partial \overline{T}}{\partial \overline{y}_i}\right) + \gamma(\gamma-1)\frac{\mathrm{M}_\infty^2}{\mathrm{Re}_\infty}\frac{\partial}{\partial \overline{y}_i}(\overline{\sigma}_{ij}\overline{v}_i) - (\gamma-1)\frac{\partial}{\partial \overline{y}_j}(\overline{p v}_i)\end{aligned} \tag{2.18}$$

The additional similarity parameters are thus the free-stream specific heat ratio, γ_∞, and the free-stream Prandtl number Pr_∞:

$$\Pi_3 = \gamma_\infty = \frac{c_{p,\infty}}{c_{v,\infty}} \propto \frac{\text{fluid's capacity to store mechanical energy}}{\text{fluid's capacity to store thermal energy}} \tag{2.19}$$

$$\Pi_4 = \mathrm{Pr}_\infty = \frac{c_{p,\infty}\mu_\infty}{k_\infty} \propto \frac{\text{energy dissipated by friction}}{\text{energy transported by conduction}} \tag{2.20}$$

where Π_3 stands for the fluid's thermal properties, and Π_4 stands for heat dissipation.

The boundary condition for the temperature at the wall has to be included since it is required to close the problem. Performing a similar inspection on the equation describing the energy exchanges between the fluid and the wall requires the introduction of a fifth similarity parameter Π_5, which stands for the thermal gradients. It is defined as the dimensionless internal energy of the wall:

$$\Pi_5 = \overline{e}_w = \frac{c_{p,w}T_w}{c_{p,\infty}T_\infty} \simeq \frac{T_w}{T_\infty} \propto \frac{\text{internal energy of the wall}}{\text{internal energy of the free-stream}} \tag{2.21}$$

This fifth similarity parameter is needed to account for heat conduction in the wall[5]. The thickness of the boundary layer, for example, depends on the thermal gradient at the wall and impacts turbulent transition, heat transfer, pressure distribution, etc.

Furthermore, now that the fluid's properties are allowed to vary with temperature, and that γ is a parameter on its own, Π_1 and Π_2 become:

$$\Pi_1 = \mathrm{Re}_\infty = \frac{\rho_\infty v_\infty L}{\mu_\infty} \tag{2.22}$$

$$\Pi_2 = \mathrm{M}_\infty = \frac{v_\infty}{a_\infty} \tag{2.23}$$

[5]Unfortunately, the same cannot be said about catalycity. All investigations of surface catalycity tend to demonstrate that, in one way or another, it depends on the temperature of the wall. However, to the author's knowledge, this dependency is not identified in the form of the ratio T_w/T_∞. These considerations will be further elaborated upon in section 2.4.3.

Let us note that the use of the subscript ∞ can be misleading as the reference quantities have to be defined related to the flow of interest. In the case of a blunt body creating a strong detached shock, for example, there is a significant amount of real gas effects occurring downstream of the shock. Therefore, the reference is not the free-stream but could for example be the frozen post-shock conditions[6].

These developments to include the thermal effects are consistent with the Π theorem. The additional variables describing the problem are the free-stream temperature T_∞, the body's surface temperature T_w, the gas' heat capacity at constant pressure $c_{p,\infty}$ and constant volume $c_{v,\infty}$, and its thermal conductivity k_∞. Using these, the speed of sound becomes redundant as the pressure can be derived from the ideal gas law, and therefore $N = 9$. One more dimension is required, the temperature K, and thus $P = 4$. This leads to $N - P = 5$ similarity parameters.

The inattentive reader could conclude that we have thus now 4 degrees of freedom in the design of our scaling. However, with a few notable exceptions, these additional similarity parameters require the use of the same gas mixture in scaled flows as in the original one. Therefore, all fluid properties (k, c_p, c_v, and μ) can actually be represented by a single variable, and the number of free variables reduces to $N' = 6$, leading to only $N' - (N - P) = 1$ degree of freedom. For non-reacting gases, the flow properties that we have identified depend solely on temperature. The values of Π_3 to Π_5 are thus fixed, as well as that of Π_2 since the temperature needs to be duplicated. Using a smaller-scale model implies to adapt the density ρ_∞, both being linked through the Reynolds and Mach numbers.

Nevertheless, it should be noted that the advantage of similitude analysis is that it allows identification of the driving processes of a flow. It is thus possibly to refine our analysis and try to identify key assumptions that would allow us to further exploit these results.

As an illustration, consider that in most instances the kinetic energy contained in the free-stream is considerably higher than the thermal energy of the wall, leading to very large Π_5. The exact duplication of T_w is then not always as critical for some processes, and a sufficiently low wall temperature will be considered as a satisfying duplication. Unless, of course, there are other wall processes that depend on temperature and have an effect on the macroscopic features of the flow.

Another example of such simplification is the *Oswatitsch Mach number independence principle*. It states that for large Mach numbers (above $\mathrm{M}_\infty \approx 4 - 6$), some of the aerodynamic quantities of interest in their dimensionless form (pressure coefficient, etc.) and the flowfield structure (shock wave shapes, etc.) become essentially independent of its actual value [138]. That principle can be derived mathematically and has been observed experimentally and numerically for flows with minimal real gas effects (see for example [63, 96, 193]). This allow one more degree of freedom, often necessary when performing experiments[7].

[6] As it will be demonstrated later for the binary scaling, for example, the post-shock Reynolds number is properly duplicated although that of the free-stream is incorrect. It is thus important to understand what portion of the flow is being duplicated, and how the similarity parameters are defined.

[7] While the Mach number independence principle is commonly accepted and used, it should be noted that it was developed under the assumption of inviscid flows and calorically perfect gas. Its applicability to flows involving chemically reacting mixtures of perfect gases or non-adiabatic effects is still discussed (see for example [79] and [96]).

2.3 High-enthalpy flows

As the enthalpy increases, the temperature downstream of the shock will eventually be sufficient to induce chemistry and the development of a thermochemical nonequilibrium layer, as illustrated in figure 2.2. This flow regime is sometimes referred to as *high-hypersonic*. Most of the free-stream's kinetic energy is converted in translational energy as the particles slow down while encountering the high-pressure gas downstream the shock. The other energy modes subsequently get excited through collisions while the translational energy modes start to relax. The translational-rotational energy transfer is very quick, in the order of tens of collisions, while it takes longer for vibrational energy to equalize - thousands of collisions. The amount of vibrational energy stored up by molecules might overcome the nuclear bound and cause dissociation. Further downstream, excitation of bound electrons and de-excitation through electromagnetic radiation at different rates leads to nonequilibrium electronic population distribution[8].

Examples of such flows are atmospheric entry capsules during the aeroheating phase of their descent, when they cruise at velocities in excess of $5\ \mathrm{km/s}$. As a point of comparison, the onset of molecular oxygen dissociation is around $h_\infty \simeq 10\ \mathrm{MJ/kg}$ ($v_\infty \simeq 4.5\ \mathrm{km/s}$), shortly followed by molecular nitrogen.

With the inclusion of chemistry, the mass balance (equation 2.5) becomes:

$$\frac{\partial}{\partial y_i}(\rho v_i + j_{s,i}) = \dot{w}_s \tag{2.24}$$

where the subscript s denotes a chemical species, and the terms j and $\dot{w}$ are respectively the diffusion and mass production source terms. That equation has thus to be solved for every species simultaneously (i.e. for $s = 1, \cdots, n$ with n the number of species).

As illustrated in figure 2.3, two experimental strategies are used to study these flows depending on what features are to be studied. These traditionally correspond to the two types of high-enthalpy facilities: impulse and continuous.

Impulse facilities such as expansion tubes or ballistic ranges are typically limited both in terms of model size and flow duration because they produce a relatively small test flow. However, they also enable very large free-stream velocities, and thus also Mach number. These two constraints make it an appropriate candidate to apply the *binary scaling*, explored in section 2.4. Binary scaling has the advantage of duplicating the entire shock layer in the vicinity of the stagnation line, from the free-stream to the wall. The drawback is uses a scaled geometry and, as we will demonstrate throughout this work, a full similarity with all flow parameters is not possible. Appropriate modeling is therefore

[8]This view, however, is somewhat outdated. Nonequilibrium processes and the associated modes of energy storage involved have been an important research topic for the last 40 years. A popular approach is the two-temperatures model, which postulates that the rotational and translational modes can be represented by one temperature, and the vibrational and electronic modes by a second. That model, however, is increasingly being questioned with the availability of more accurate experimental measurements. Significant differences between all four modes are, in some situations, evident. One of the major challenges of hypersonics today is to incorporate more physically representative models (such as vibrationally specific kinetic models) into tractable CFD codes.

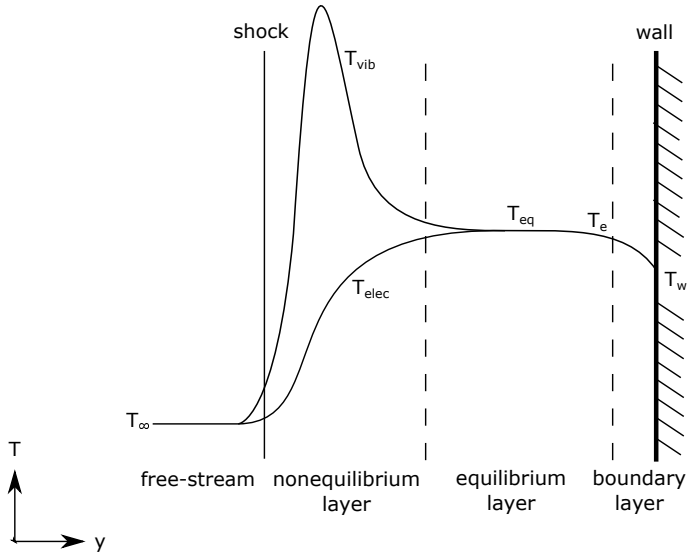

Figure 2.2: *Sucint description and nomenclature used in this report to describe the different regions of the shock layer, illustrated with the temperature profile. Downstream of the shock, the free-stream temperature T_∞ abruptly increases as the the flow's kinetic energy is converted in translational energy. There is a region of thermal and chemical nonequilibrium, followed by a region where the equilibrium properties are reached T_{eq}, and finally the boundary layer close to the wall.*

necessary to correctly understand how to interpret the data. Moreover, tests are performed over very short durations, in the order of micro- to milliseconds.

While impulse facilities obtain the required free-stream enthalpy by inputing kinetic energy to the flow[9], continuous facilities do so by inputing it thermal energy. The free-stream Mach number being moderate, binary scaling can not be applied for the entire flowfield. Another technique is therefore used: the *Local Heat Transfer Simulation* (LHTS), examined in section 2.5. It only reproduces the boundary layer in the vicinity of the stagnation line. However, unlike the binary scaling which as its name implies is a scaling, the LHTS is an exact (i.e. full scale) duplication of a region of the flow. Moreover, test times in the order of seconds and even minutes can be achieved. This enables to study features that are typically out of the reach of binary scaled flows such as gas-surface interactions, material response, etc.

Nonetheless, these two strategies can be applied in any kind of facility. The LHTS has been used in impulse facilities (see for example [160, 159] for shock tubes) and the binary scaling has succesfully been used in a plasma wind tunnel (see chapter 5).

[9]The process, however, can involve thermal energy. In shock tubes, for example, thermal energy is first added to the flow which is then expanded from stagnation through a nozzle. Similarly, as we will see in chapter 6.1.1, a non-negligible fraction of the enthalpy of the flows obtained in the expansion tubes operated at the University of Queensland is actually thermal.

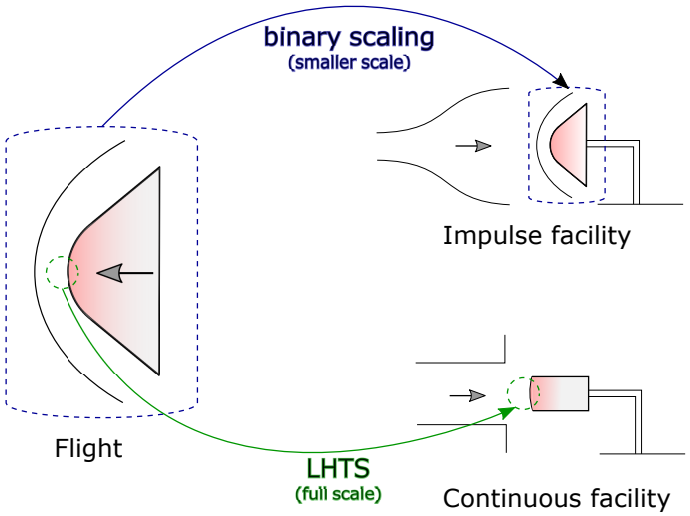

Figure 2.3: *The test section in impulse facilities limits the size of the models that can be used. Binary scaling is therefore used as it allows to duplicate the flowfield around a smaller scale version of the probe in flight. LHTS, traditionally used in continuous facilities, only enables to obtain the boundary layer in the vicinity of the stagnation point, but withouth scaling.*

2.4 Binary scaling

2.4.1 State of the art

The traditional derivation for the binary scaling as it can be found in reference papers such as [60] or [82] is as follows. Assuming that the flow is governed by binary (i.e. dissociation) reactions, the chemical reaction rate expressed in terms of fractional composition can be represented as:

$$\frac{\partial x_Y}{\partial t} = \rho f(x_Y, T) \tag{2.25}$$

where x_Y is the fraction of dissociated gas. Provided that the dissociation fraction and temperature are duplicated, the time-scale of the chemistry will thus be expressed as $\tau = 1/\rho$. The convective time-scale (time of residence), in turn, can be defined as $\tau = \Delta/v$, with Δ the shock standoff. The Damköhler number, which describes the ratio of those two time scales, is thus:

$$\mathrm{Da} = \frac{\rho\Delta}{v} f(x_Y, T) \tag{2.26}$$

Therefore, if the product $\rho\Delta$ is constant, then chemical reactions will occur over the same relative length-scale. The post-shock temperature is automatically conserved if the free-stream velocity is duplicated. Indeed, as a first approximation, the free-stream sensible enthalpy and post-shock kinetic enthalpy are both negligible. Therefore, one can write:

$$\frac{v_\infty^2}{2} \simeq h(T) \tag{2.27}$$

The mass flow ρv being constant across a normal shock, the post-shock velocity is also obtained for sufficiently high Mach numbers. Provided that the dissociation fraction, viscosity and thermal

properties of the gas only depends on temperature, the Reynolds, Mach, and Prandtl number are also duplicated.

These considerations on the chemical nonequilibrium can be extended to the thermal nonequilibrium. Indeed, the rate at which each energy mode e_k reaches equilibrium can be expressed as:

$$\frac{de_k}{dt} = \frac{1}{\tau_i}(e_k^{\text{eq}} - e_k) \tag{2.28}$$

where τ is the relaxation time, and the equilibrium value for each energy mode are:

$$e^{\text{eq}} = \underbrace{\frac{3}{2}RT}_{\textit{translational}} + \underbrace{RT}_{\textit{rotational}} + \underbrace{\frac{h\nu/k_BT}{e^{h\nu/k_BT}-1}RT}_{\textit{vibrational}} + \underbrace{e^{\text{el}}}_{\textit{electronic}} \tag{2.29}$$

where h is Planck's constant and ν the frequency. The relaxation for a certain energy mode time depends on the transition probability for that particular energy mode, which is an intrinsic property of the species considered, and the collision frequency ν_c, which relates to the pressure and temperature through:

$$\nu_c \propto \frac{p}{\sqrt{T}} \tag{2.30}$$

The relaxation time for a certain species s therefore also a function of temperature and pressure $\tau_s = \tau_s(p, T)$. For diatomic gases, for example, a commonly used model is:

$$\tau = \frac{c_1}{p}\exp\left[(c_2/T)^{1/3}\right] \tag{2.31}$$

where the coefficients c_1 and c_2 are intrinsic properties of the species considered, and can be determined experimentally. Although there is a considerable amount of scatter in their reported values, notably because of the high uncertainty associated with that type of measurement, reasonable values can be found in literature (see for example [205]).

The relaxation time should scale in the same fashion as a convective time-scale of the flow, thereby guaranteeing that the dimensionless characteristic length scale for the nonequilibrium processes remains the same. Using the convective time-scale obtained earlier, the Damköhler number of thermal nonequilibrium is:

$$\text{Da} = \frac{\Delta p}{v c_1 \exp\left[(c_2/T)^{1/3}\right]} \tag{2.32}$$

As a first approximation, one can consider that pressure is proportional to density, and the scaling parameters are thus the same as for chemical nonequilibrium: ρL, where L is a characteristic length-scale of the flow, and $h_\infty \simeq v_\infty^2/2$.

In reality, when considering an experimental facility such as an expansion tube or a shock tube[10], best practice is to use duplicate h_∞ instead of v_∞:

$$h_\infty = \frac{v_\infty^2}{2} + h_\infty(T) \simeq h(T) \tag{2.33}$$

Indeed, the major contribution to the free-stream enthalpy is from the gas' kinetic enthalpy but there is a small yet non-negligible contribution in the form of sensible enthalpy[11].

According to our knowledge, Birkhoff is the first author to mention what he then calls a binary scaling modeling in 1951. He notes that *"the transformation of distance and density in reciprocal ratios, with conservation of velocity and temperature, has extraordinary properties.* $[\cdots]$ *It has the great advantage of enabling one to reproduce to scale many aerothermodynamic effects of the upper atmosphere, by small scale model tests performed near the Earth's surface "* [15]. He mentions three of such properties. First, the Mach number is conserved for calorically perfect gas. Second, if only binary molecular collisions need to be considered, the Reynolds, Prandtl, and Knudsen number are also conserved. Finally, it preserves second-order reactions of chemical kinetics. Birkhoff, however, does not investigate further than these high-level considerations.

Intuitively, the binary scaling applies better to high altitude rarefied flows for which three-body collisions are rare (i.e. and thus a large portion of the shock layer is out of equilibrium). The rate processes for lower altitude flows may be governed by three-body collisions, which prevents from using scaling laws. Cheng indeed showed that for a sufficiently high free-stream density the chemical concentrations could not be scaled [34]. Based on these considerations, Gibson demonstrated the applicability of binary scaling to flight conditions of practical interest [57]. He particularly pointed out the role of the Knudsen number to determine the shock-layer chemical state. Hall et al. later noticed that binary scaling should apply to vibrational and electronic relaxation processes, thus allowing for the scaling of the shock-layer radiation [72].

More specific investigations on the range of applicability of binary scaling were then performed by Gibson, Marrone, and Sowyrda [58, 61, 59] and summarized in a chapter written for the AGARD meeting on The High Temperature Aspect of Hypersonic Flows, held at VKI in April 1962 [60]. In that chapter, they develop an analytical method based on the shock-mapping technique to determine the chemical state of shock layers around hypersonic blunt bodies. They then show how that method can be used to assess the quality of the scaling in terms of atomic concentrations in the shock-layer and shock standoff depending on the altitude, nose radius and velocity. One of such practical example is shown in figure 2.4.

The flow conditions for which they consider binary scaling to be applicable are mostly contained at altitudes higher than $30\ \mathrm{km}$. For example, a velocity and free-stream density of respectively 7 $\mathrm{km/s}$ and $1.8 \cdot 10^{-12}\ \mathrm{kg/m^{-3}}$ will require $\rho_\infty R < 10^{-12}\ \mathrm{kg/m^{-2}}$ [60]. They further note that error

[10]The case of flows with a significantly lower contribution from kinetic enthalpy will be explored in chapter 5, with the practical example of subsonic test flows in a plasma wind tunnel.

[11]In flight, the sensible enthalpy is usually negligible. If 10% of the test flow's free-stream enthalpy consists out of sensible enthalpy, then the velocity of the test flow is 95% of what it is in flight. The impact of the post-shock velocity in the vicinity is thus considered as minor.

on the concentration of nitric oxide and electrons increases towards the stagnation point [60], which is normal given their concentration depend on a three-body reactions.

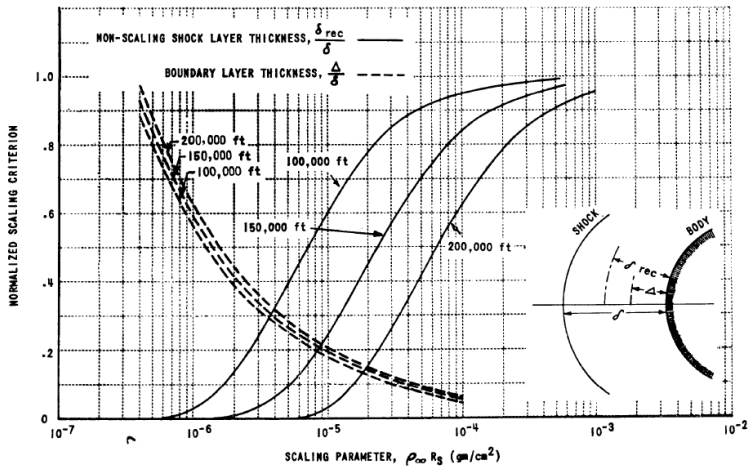

Figure 2.4: *Example of the figures that can be built with the method of Gibson and Marrone, in this case for $v_\infty = 7$ km/s. The evolution of the boundary layer thickness with the altitude is represented with the dashed lines (i.e. smaller model implies a slightly thicker stagnation point boundary layer) and the evolution of the "recombination layer" in which the binary scaling does not apply is represented with the continuous lines. Figure excerpted from [60].*

Since these early investigations, the amount of research performed on binary scaling reduced. Inger showed that binary scaling could be extended to slender bodies with a blunt nose and affinely related bodies (equation 2.14) if the gas is completely frozen [85]. Ellington also suggested a refined method to take the interdependence of those limits into account in a more streamlined fashion [46]. Hornung discussed questions related to the wall temperature and the free-stream dissociation in wind tunnel flows [82]. Stalker later referred to the binary scaling as an extension of the Mach-number principle in the realm of similitude laws [177].

Despite its limitations, binary scaling is commonly used as a scaling parameter for experimental studies in impulse facilities (i.e. such as expansion tubes). Some examples can be found the following references: [29, 30, 73, 113, 127].

A form of the binary scaling is also widely used for scramjet testing. Indeed, for a hydrogen-air model, the ignition time depends on radical formation reactions, which are binary[12]. When studying two scramjet models with a length ratio of $1:5$, Pulsonetti and Stalker noticed that the characteristic length for the mixing at molecular level was proportional to the inverse of the pressure [199]. A similar dependence was found for the boundary layer development, and thus also for wall friction and heat transfer [199]. The resulting *pressure-length scaling* is obviously the same as the *binary scaling* provided that the temperature and mixture composition is the same (in the hypothesis of an equilibrium flow). However, the final combustion reactions towards the formation of stable products

[12] Although most empirical delay time correlations indicate that reaction rates are more appropriately modeled with a reaction order of 1.8 rather than 2.

(e.g. H_2O) are not binary. Some authors suggest therefore to use a power n of the pressure rather than the pressure itself, depending on the flight regime that is being simulated [166].

Let us also mention the studies on radiation performed by Park. He noted that for a non-absorbing medium radiation is intrinsically proportional to density, while the distance on which thermal and chemical properties reach equilibrium is inversely proportional to density (equation 2.28). Because the radiative heat flux mainly depends on the integration of the former over the latter, it is independent of density. He further extended that property to the equilibrium region and refers to it as the *binary scaling relationship* [147]. While it is not the same as our binary scaling law, it provides an interesting insight in that the radiative heat flux does not scale (i.e. is exactly duplicated) within a family of binary scaled flows. Based upon the results presented in [145] for Fire and [144] for shock tube experiments, Park notes that this property may prove to be wrong at high altitudes because of a collision-limiting phenomena [147].

2.4.2 Gas Phase

Let us now take a more systematic approach to demonstrate that early result. The starting point of binary scaling is the nondimensionalization of equation 2.24. The mass production and diffusion terms need therefore to be expressed as a function of the flow variables.

Mass production

The mass production of a certain species s can be expressed as a function of its molarity per unit of volume Φ_s as:

$$\dot{w}_s = M_{m,s}\frac{\partial \Phi_s}{\partial t} \tag{2.34}$$

where $M_{m,s}$ is the species' molar mass.

Determining the changes in molarity of a certain species over time requires to explore its chemistry. Any chemical reaction can be written in its general form as:

$$\sum_{s=1}^{n} \nu_s' Y_s \underset{k_b}{\overset{k_f}{\rightleftharpoons}} \sum_{s=1}^{n} \nu_s'' Y_s \tag{2.35}$$

where Y_s are the chemical species involved in the reaction, ν_s' and ν_s'' are the stoichiometric coefficients of the reactants and products, and k_f and k_b are the forward and backward reaction rate coefficients. These are measured experimentally and fitted to a pre-existing model. For high temperature applications, it is usually modeled with an generalized form of Arrhenius' law:

$$k = cT^n e^{-\theta_a/T} \tag{2.36}$$

where c and n are fitting parameters and θ_a the activation temperature. In the thermal nonequilibrium region, a common approach is to consider two or more temperatures, for each of the energy modes. The same expression 2.36 is used, but with an average temperature $T_{\text{av}} = \sqrt{T_{\text{tr}} T_{\text{vib}}}$ where the subscripts tr and vib respectively stand for the translational and vibrational temperatures. According to the law of mass action [71], the net rate of formation of one of the species Y_s is then expressed as:

$$\frac{\partial \Phi_s}{\partial t} = (\nu_s'' - \nu_s') \left\{ k_f \prod_s \Phi_s^{\nu_s'} - k_b \prod_s \Phi_s^{\nu_s''} \right\} \tag{2.37}$$

The left-hand side in the brackets is the forward reaction rate and the right-hand side the backward reaction rate.

For an ideal dissociating gas such as described by Lighthill and Freeman [54, 107] composed of one species Y_2 and its dissociated counterpart Y, the only chemical reaction is:

$$Y_2 + M \underset{k_b}{\overset{k_f}{\rightleftharpoons}} 2Y + M \tag{2.38}$$

where M is a third-party species, which could be either Y or Y_2. Applying equation 2.37, to that simplified chemical model, one obtains:

$$\frac{\partial}{\partial t} \Phi_Y = 2\big(k_{f,1} \Phi_{Y_2} \Phi_Y + k_{f,2} \Phi_{Y_2}^2\big) - 2\big(k_{b,1} \Phi_Y^3 + k_{b,2} \Phi_Y^2 \Phi_{Y_2}\big) \tag{2.39}$$

Defining the molarity of Y and Y_2 in terms of the dissociated gas mass fraction:

$$\Phi_Y = \frac{\rho x_Y}{M_{m,Y}} \qquad\qquad \Phi_{Y_2} = \frac{\rho(1 - x_Y)}{2M_{m,Y}} \tag{2.40}$$

Inserting the result in equation 2.34, the mass production is finally expressed as:

$$\begin{aligned} \dot{w}_s &= 2\left(\frac{k_{f,1} \rho^2 x_Y (1 - x_Y)}{2M_{m,Y}} + \frac{k_{f,2} \rho^2 (1 - x_Y)^2}{4M_{m,Y}} \right) - 2\left(\frac{k_{b,1} \rho^3 x_Y^3}{M_{m,Y}^2} + \frac{k_{b,2} \rho^3 x_Y^2 (1 - x_Y)}{2M_{m,Y}^2} \right) \\ &= \frac{k_f \rho^2 (1 - x_Y^2)}{2M_{m,Y}} - \frac{k_b \rho^3 (x_Y^3 + x_Y^2)}{M_{m,Y}^2} \end{aligned} \tag{2.41}$$

where for the sake of clarity if was assumed that $k_f = k_{f,1} = k_{f,2}$ and $k_b = k_{b,1} = k_{b,2}$. One of the underlying assumptions of binary scaling is that the flow is driven by binary reactions (dissociation and ionization). It is the case in the nonequilibrium layer immediately downstream of the shock which, for sufficiently high-enthalpy, can extend to a large fraction of the shock layer. Under these conditions, the second term on the right-hand side of equation 2.41 is ignored.

The dissociation presented in equation 2.38 is only one of the schemes to be expected in high-temperature gas. Other schemes include[13]:

$$\begin{aligned} \text{Neutral exchange: } & Y + Y_2 \rightleftharpoons Y_2 + Y \\ \text{Associative ionisation: } & Y + Y \rightleftharpoons Y_2^+ + e^- \\ \text{Charge exchange: } & Y^+ + Y_2 \rightleftharpoons Y + Y_2^+ \\ \text{Electron-impact ionisation: } & Y + e^- \rightleftharpoons Y^+ + 2e^- \end{aligned} \tag{2.42}$$

Neutral exchange, associative ionisation, and charge exchange are binary both in the forward and backward direction. Dissociation and electron-impact ionisation are binary in the forward direction but ternary in the backward direction.

Diffusion

The diffusion of a certain species s in a certain direction of space i can be modeled using Fick's first law:

$$j_{s,i} = -D_s M_{m,s} \frac{\partial \Phi_s}{\partial y_i} \tag{2.43}$$

where D is the diffusion coefficient with units of m^2/s. Using expressions 2.40, it can be expressed for a Lighthill-Freeman gas as:

$$j_{s,Y} = -D_Y \frac{\partial(\rho x_Y)}{\partial y_i} \qquad\qquad j_{s,Y_2} = -\frac{D_{Y_2}}{2} \frac{\partial[\rho(1-x_Y)]}{\partial y_i} \tag{2.44}$$

The only differences between those equations are a factor 2 and the expression of the fraction of dissociated gas, both of which are nondimensional. We can thus safely work only on the diffusion of Y without loosing generality on the conclusions for the nondimensional form of equation 2.24.

For a multi-component mixture, the diffusion coefficient is averaged from the binary diffusion coefficients with the Wilke mixture rule [208]:

$$D_s = \frac{1 - x_s}{\sum_{t \neq s} \frac{x_t}{D_{s,t}}} \tag{2.45}$$

where the subscripts s and t stand for two different species. From Chapman-Enskog kinetic theory [134], each binary diffusion coefficient is defined as:

$$D_{s,t} = \frac{3}{16} \frac{1}{n \overline{Q}^{(1,1)_{s,t}}} \sqrt{\frac{2\pi k_B N_A T (M_{m,s} + M_{m,t})}{M_{m,s} M_{m,t}}} \tag{2.46}$$

where N_A is the Avogadro constant, $n = p/(k_B T)$ is the number density with p the pressure, and $\overline{Q}^{(i,j)} = \Omega^{(i,j)} \pi$ is the diffusion cross-section. The collision integral Ω is obtained from correlation of

[13] Reactions that include the interaction with photons will be discussed in appendix D and are described in equations D.5 and D.12.

the form:

$$\Omega^{(i,j)} = \frac{a_1 + a_2 T^{a_3}}{a_4 + a_5 T^{a_6}} \tag{2.47}$$

where the parameters a are fitted experimentally (see for example [27] for air). One can thus identify the contribution of the pressure to the diffusion coefficient such as being:

$$D = \frac{1}{p} f(T, x_1, \cdots, x_n) \tag{2.48}$$

Final form

Using equations 2.41 and 2.44, the dimensionless form of equation 2.24 becomes:

$$\frac{\rho v}{\Delta} \frac{\partial(\overline{\rho v_i})}{\partial \overline{y_i}} - \frac{D_Y \rho}{\Delta^2} \frac{\partial^2(\overline{\rho} x_Y)}{\partial^2 \overline{y_i}} = k_f \rho^2 \frac{(1 - x_Y^2)}{2 M_{m,Y}} \tag{2.49}$$

where all the terms have been nondimensionalized as for example $\overline{y} = y/\Delta$, with Δ the shock standoff distance in the streamwise direction, a characteristic length-scale for the region of interest. Rearranging the terms:

$$\frac{\partial(\overline{\rho v_i})}{\partial \overline{y_i}} - \frac{D_Y}{\Delta v} \frac{\partial^2(\overline{\rho} x_Y)}{\partial^2 \overline{y_i}} = \frac{\Delta}{v} \rho k_f \psi \tag{2.50}$$

where we defined the modified dissociation fraction ψ as $psi = (1 - x_Y^2)/2M_{m,Y}$. The reaction constant k_f as it is expressed in equation 2.36 has the units of $\mathrm{m}^3/\mathrm{mol}/\mathrm{s}$.

The group on the right-hand side of the equation is therefore a nondimensional number, identified as a Damköhler number Da_g for the gas-phase[14]:

$$\Pi_6 = \mathrm{Da}_g = \frac{\Delta}{v} \rho k_f \psi \propto \frac{\text{chemistry}}{\text{mass convection}} \tag{2.52}$$

It characterizes the degree of chemical nonequilibrium, and can be interpreted as the ratio between two characteristic time-scales: one for convection $\tau = \Delta/v$ and the other for chemistry $\tau = 1/\rho k_f \psi$. For $\mathrm{Da}_g = \infty$ the flow is in equilibrium: the time-scale characteristic of the chemical processes is negligible compared to that of convection and the chemistry can thus be viewed as instantaneous. Inversely, for $\mathrm{Da}_g = 0$, the flow is frozen: the gas is chemically inert.

Provided the gas mixture is duplicated, k_s is a function of temperature only while ψ is a strong

[14] It has the same signification as the binary scaling parameter χ derived by Gibson and Marrone [60]. Using our nomenclature, their parameter reads as:

$$\chi = \frac{k_f}{M_m} \int_0^y \frac{\rho dy}{v} \tag{2.51}$$

While Da_g is defined locally, this parameter is defined over an arbitrary length-scale y. This allows to obtain analytical solutions over any portion of streamline. That additional layer of complexity, however, is not necessary in the present analysis.

function of temperature but also weakly depends on density. Let us assume for the time being that both terms are a function of temperature only. As a first approximation, the free-stream sensible enthalpy and post-shock kinetic enthalpy are both negligible. Therefore, one can write $v_\infty^2/2 = h(T)$, and the post-shock temperature is achieved by reproducing the correct free-stream velocity. The product ρv being constant across a normal shock, the post-shock velocity is also obtained for high Mach numbers.

The last group to duplicate, $\Delta\rho$, raises two issues. First, the exact value of Δ cannot be known prior to the test and has thus to be estimated through numerical simulations or using correlations. Second, the post-shock density ρ is not constant but will along the stagnation line due to changes in the chemical composition of the flow [81, 86, 87, 207]. Alternatively, another expression, easier to handle than $\rho\Delta$, is $\rho_\infty L$, where L is a transverse length-scale of the hypersonic vehicle, such as the nose radius. Several empirical or semi-empirical correlations do indeed demonstrate a linear relation between those two groups (see for example [75, 110, 201] or more recently [212] for the high velocity range).

Similarly, the group multiplying the diffusion term is the Péclet number for mass transport:

$$\Pi_7 = \text{Pe} = \frac{\Delta v}{D} \propto \frac{\text{mass convection}}{\text{mass diffusion}} \tag{2.53}$$

It can be regarded as the ratio of a mechanical length, Δ, to a diffusion length D/v. Alternatively, it could also be interpreted as the ratio of a mechanical velocity v and a diffusion velocity D/Δ. As for the other similarity parameters, while the processes coming into play can be clearly identified, their identification is open.

Using equation 2.54 in equation 2.53, and subsequently applying the perfect gas equation (the temperature and mixture composition being duplicated):

$$\text{Pe} = \frac{\rho\Delta v}{f(T, x_1, \cdots, x_n)} \tag{2.54}$$

where the dependance on temperature and perfect gas constant of the density was inserted in the function f of temperature and mixture composition. It is thus only when expressing the diffusion coefficient and its dependance on pressure that the applicability of the binary scaling to chemically reacting flows appears; in the laboratory, the diffusion coefficient decreases in inverse proportion to the increase in density (or pressure) thereby compensating the effect of the smaller length scale on the diffusive transport.

Some authors also mention the Arrhénius parameter Arr in the form:

$$\Pi = \text{Arr} = \frac{\theta_a}{T} = \frac{e_a}{RT} \tag{2.55}$$

We consider, however, that the complexity of the problem prevents the use of substitution gases (at least for those who are reacting, there are some example of substitution of inert gases). Therefore, the Arrhénius parameter is implicitly duplicated.

The dimensionless form of the mass balance equation presented in equation 2.24 is thus:

$$\frac{\partial(\overline{\rho v_i})}{\partial \overline{y_i}} - \frac{1}{\mathrm{Pe}} \frac{\partial^2(\overline{\rho} x_Y)}{\partial^2 \overline{y_i}} = \mathrm{Da}_g \tag{2.56}$$

That equation and the importance of the Damköhler and Péclet numbers is well-known to in chemical engineering [161], and is of particular interest when studying reactive flows in complex geometries such as capillary tube or porous media.

2.4.3 Gas-Surface Interaction

Mass production defined in the context of wall recombination is per unit of surface rather than per unit of volume as it was the case in the gas-phase chemistry. Therefore, one ought not to balance it with the gradient of the diffusive mass flux but rather with the diffusive mass flux itself. The mass balance equation expressed at the wall is thus:

$$j_{s,i} = \dot{w}_s \tag{2.57}$$

where $\dot{w}_s$ has the units of $\mathrm{kg/m^2 s}$.

Recombination at the wall is often considered to be a first order reaction. Indeed, in that context equation 2.38 would thus be written:

$$Y + Y \rightarrow Y_2 \tag{2.58}$$

where the backward reaction is largely negligible, the wall being colder than the flow. Equation 2.41 is then expressed as:

$$\dot{w}_{s,w} = k_{s,w} \rho_w \frac{M_{m,s}}{M_m} x_{s,w} \tag{2.59}$$

where the subscript w is for the wall, and $k_{s,w}$ is the catalytic speed for the species s, with the dimension of $\mathrm{m/s}$. It is thus different in its definition to a reaction rate as defined in equation 2.36. Assuming a Maxwellian distribution for the species s at the wall with a Chapman-Enskog perturbation to account for the presence of the wall, it can be expressed as:

$$k_{s,w} = \frac{2\gamma_s}{2 - \gamma_s} \sqrt{\frac{k_B N_A T_w}{2\pi M_{m,s}}} \tag{2.60}$$

where the catalycity γ is defined as a recombination probability, i.e. the ratio between the number flux of particles of species s impinging the surface and the number flux of particles of species s leaving the surface. We assume that $\gamma(T_w)$ is an intrinsic property of the constituting material of the wall, and is thus conserved through binary scaling as long as the same wall material is used. That approach has been used with some degree of success by numerous authors (see for example [41, 69, 178]). Recent experiments, however, have demonstrated that the catalycity may also depend on the environment of

the wall, and in particular the pressure at the outer edge of the boundary layer [33, 143].

Rigorous nondimensionalization of the wall mass balance equation results in the obtention of a Damköhler number for the wall Da_w:

$$\Pi_8 = \mathrm{Da}_w = \frac{\Delta}{D_w} k_w \psi_w \propto \frac{\text{chemistry}}{\text{mass diffusion}} \tag{2.61}$$

with the modified dissociation fraction at the wall $\psi_w = x_{Y,w} M_{m,Y} / M_m$. As observed for the gas-phase, there is one time-scale for diffusion $\tau = \Delta^2 / D_{Y,w}$ and the other for chemistry $\tau = \Delta / k_{Y,w} \psi_w$. Using the dependance of the diffusion coefficient on pressure, identified in equation 2.54, we observe thus that Da_w is duplicated as well through the binary scaling.

2.4.4 Scaling parameters

In summary, the requirements of the binary scaling are:

1. The test model has to have the same geometry and angle of attack as the hypersonic vehicle, and the test flow has to have the same nature as the flow encountered in flight;

2. The product $\rho_\infty L$ and the free-stream velocity v_∞ (or more generally free-stream enthalpy h_∞, as expressed in equation 2.33) have to be duplicated. These will be referred to as scaling parameters rather than similarity parameters. The former are dimensional numbers which ensure that the latter, which are dimensionless, are duplicated.

Or, m As a result, the post-shock temperature and velocity - and therefore also the Da_g, Pe, and Da_w - are duplicated, at least in the vicinity of the stagnation line. This ensures that the same solution to equations 2.24 and 2.57 are obtained in the laboratory as in flight.

Incidentally, the other similarity parameters are also duplicated for the post-shock flow. Indeed, downstream of the shock the flow is a chemically reacting mixture of perfect gases. The gas properties such as γ, Pr, or μ depend on the temperature and on the mixture composition. In the nonequilibrium region, the mixture composition has to be directly determined from the population (number of particles) in each different energy state for each different species, which also depends on the history of the flow. In the equilibrium region, mixture composition can be simply determined from two state variables, say temperature and pressure.

The very purpose of binary scaling, however, is to duplicate a certain type of chemistry (that which is governed by binary reaction) which is expected to play the most significant role in the shock layer. Moreover, numerous authors have shown that the chemical state of the flow (i.e. wether it is frozen or in equilibrium) is a driving force in the evolution of the gas properties (see for example [76]). In the present case, the state of the flow is governed by the gas-phase Damköhler number, which is one of our similarity parameters. As a first order approximation, we can thus reasonably assume that the gas properties are duplicated.

In that case, γ (Π_3) and Pr (Π_4) are automatically duplicated. The post-shock velocity being duplicated, M (Π_2) is also obtained. Conveniently, Re (Π_1) is also duplicated since ρL is one of our key scaling parameter, as thus also Kn as stated in equation 2.13. Finally, a sufficiently low T_w

will often lead to an acceptable (Π_5). If most of the flow is governed by binary reactions, all the macroscopic features of the flow should thus theoretically be duplicated.

In order to construct the binary scaling, we have thus added three similarity parameters per species: one Da_g, one Da_w, and one Pe. Along the way we have also added an abundance of variables: reaction rate constants, diffusion coefficients, and catalycities. With the help of a few clever assumptions, however, we were able distill the quintessence of that complex situation and obtain these four simple conditions: same geometry and test gas, same h_∞, same ρL, and large enough Mach number. That leaves us thus with one degree of freedom, and a definition of how it can be applied.

2.5 Local Heat Transfer Simulation

The purpose of the LHTS is to provide in the laboratory the same (i.e. without scaling) boundary layer at the stagnation point as in flight. The concept was formulated by Kolesnikov [98, 100]. He later applied and validated it to extrapolate from test to flight conditions [99], and numerous examples for successful applications can be found in literature (see for example [11]).

His analysis is based on the boundary layer theory for reacting gases. The convective heat flux at the stagnation point of a hypersonic blunt body with a fully catalytic surface and a frozen boundary layer can be expressed with the Fay and Riddel formula [50]:

$$q_w = 0.763\mathrm{Pr}^{-0.6}(\rho_e\mu_e)^{0.4}(\rho_w\mu_w)^{0.1}\,\beta_e^{0.5}(h_{0,e}-h_w)\left[1+(\mathrm{Le}^{\alpha}-1)\,\frac{h_{d,e}}{h_{0,e}}\right] \tag{2.62}$$

where the subscripts e refers to the edge of the boundary layer, w to the wall, and 0 to total conditions, Le is the Lewis numbers, β the transversal velocity gradient, and h_d is the dissociation enthalpy, i.e. the weighted sum of the dissociation enthalpy of the constituents:

$$h_d = \sum_{s=1}^{n} x_s h_{d,s} \tag{2.63}$$

The Lewis number is expressed as:

$$\mathrm{Le} = \frac{k}{\rho c_p D} \propto \frac{\text{thermal diffusion}}{\text{mass diffusion}} \tag{2.64}$$

The exponent α is equal to 0.52 for an equilibrium boundary layer, and 0.63 for a frozen one. Another formulation for the stagnation heat flux is given by Goulard for a frozen flow over a surface of arbitrary catalycity [69]:

$$q_w = 0.664\mathrm{Pr}^{-2/3}(\rho_e\mu_e)^{0.5}\,\beta_e^{0.5}h_{0,e}\left[1+\left(Le^{2/3}\Phi-1\right)\frac{h_{d,e}(x_e-x_w)}{h_{0,e}-h_w}\right] \tag{2.65}$$

where Φ is a term that accounts for the catalycity.

Upon closer inspection of these relations reveals that the heat flux is controlled by three indepen-

dent factors: $(h_{0,e} - h_w)$, ρ_e, and β_e. Providing the outer edge of the boundary layer is in equilibrium, two variables are sufficient to characterize the thermodynamic state of the flow. One can thus write $\rho_e = f(h_e, p_e)$. Furthermore, Goulard shows that the wall enthalpy is completely determined by the outer edge parameters and the wall temperatures $h_w = f(h_e, p_e, \beta_e, T_w)$ [69]. Finally, the three parameters to duplicate are the enthalpy, pressure, and velocity gradient at the outer edge of the boundary layer.

The LHTS has the obvious disadvantage that it only allows for a partial duplication of the flow. However, the stagnation point is in many cases the one submitted to the most stringent thermal stress and therefore also a good benchmark for a conservative validation of numerical simulations or analytical analysis.

Moreover, the LHTS is not a scaling but a direct (i.e. full-scale) reproduction of the flow. As such, it allows to investigate the material response, which cannot be done in a scaled flow[15].

Today, the general trend for ground testing is to use the LHTS for the boundary layer and thermal protection material (TPM) characterization and validation. The later being characterized by time-scales much larger than what can be achieved in a high-enthalpy facility, it is mostly used in plasma wind tunnels. However, it could very well also be applied in impulse facilities. Shortly after Fay and Riddel published their theory, and long before Kolesnikov theorized the LHTS, Rose and Stark applied the same methodology, which they called *stagnation point simulation*, in an electric arc-driven shock tube [160, 159].

On the other hand, binary scaling is used to study the shock layer and the shock shape, and has been so far only applied in high enthalpy facilities. In the frame of this work, it was applied to a subsonic flow in an attempt to generalize the binary scaling theory. The experiment and its (successful) results are described in chapter 5.

[15] This statement will be investigate in more details in section 4.3.

Chapter 3

Assumptions and limitations driving the binary scaling

"Science may be described as the art of systematic over-simplification - the art of discerning what we may with advantage omit."

- Karl Popper, in *The Open Universe : An Argument for Indeterminism* [153]

Much of our work in the previous chapter has been an application of the first half of the definition of science as given by Popper: systematic over-simplification. Obtaining an elegant an simple set of scaling parameters has indeed forced us to ignore many flow features and skip some formalities. These can be classified in three groups:

1. Issues related to the simplified **chemistry** model:

   - The more complex chemistry associated with gases that do not behave as predicted by the Lighthill-Freeman model. In air, for example, there are not only molecular species (i.e. O_2, N_2) and their dissociated counterpart (O, N), but also a product of their joint recombination (i.e. NO, NO_2). Third-party species involved in the dissociation exemplified in equation 2.38 may be any atom or molecule present in the mixture, resulting in a variety of possible reaction rate constants rather than just the oversimplified unique one. Moreover, ionization was not touched upon although it does play a significant role at high-enthalpies. The same goes for the diffusion coefficient.
   - Even in the Lighthill-Freeman hypothesis, the role of non-binary (unitary, ternary, or higher-order) reactions was neglected, assuming binary scaling is only applied to flows where a significant fraction of the shock layer is in nonequilibrium. This is a very restrictive requirement that excludes many interesting high-enthalpy flows from the range of application of binary scaling. Moreover, there is no clear definition of what "a significant fraction" is.
   - Similarly, the dependence of gas properties with pressure was assumed to be small enough. This is only a first order approximation, which might prove to result in significant differ-

ences, especially if the flow is only partially dissociated (i.e. in temperature ranges where the variation of gas properties with pressure is larger).

2. The **scaling parameter** ρL is loosely defined. We assumed that the length-scale of the flow would be the shock standoff distance, but is it so? Is it equivalent to using the nose radius of the blunt body? The same goes for the density: is using the free-stream density really the same as using the post-shock density? Besides, which post-shock density are we referring to?

3. The flow was assumed to be **adiabatic**, i.e. the enthalpy was considered constant along a streamline. As the free-stream enthalpy increases, radiative heating couples with the rest of the flowfield, causing certain portions of the flow to heat up and some other to cool down. This has some obvious consequences on the macroscopic features of the flow, and might therefore alter the quality of the scaling.

4. We focused on the **stagnation line** and its immediate vicinity. While this is an important region of the flow, it is important to understand how the rest of the flowfield is affected by a change in length-scale.

It would be no surprise if the blind application of our binary scaling rule lead to erroneous results, without any tool to interpret what may have gone wrong. Our role, as scientists, is to go through the second part of Popper's definition and discern *what we may with advantage omit*[153].

In this chapter, we explore both what are the effects of some of the shortcomings listed above. The consequences for the stagnation point heat fluxes, including ablation, will be discussed separately in chapter 4. The theoretical findings will be verified with computational fluid dynamics (CFD). These simulations will be performed with air rather than a Lighthill-Freeman gas, thus enabling to validate the use of that simplified model to derive our theory.

First, we go through the effect of ternary and higher-order chemical reactions. This will allow to pinpoint how binary scaling affects the equilibrium composition of the flow, and provide tools to draw the limit of its applicability.

Second, we will look at the different definitions of density that can be used by examining how it evolves along the stagnation line downstream of the shock. The two main effects coming into play will be distinguished: chemistry, and viscid-inviscid interactions.

Only adiabatic gases will be considered up to that point. The effect of radiation and radiative coupling will thus be thoroughly discussed from the theoretical point of view. No numerical simulations will be performed at this stage, as the findings will be verified experimentally in the following chapters.

Finally, some hints for the extension of the binary scaling theory to off-stagnation regions will be given. That last section is, however, not as comprehensive as the previous ones as it is somewhat out of the scope of this work.

3.1 Non-binary chemistry

In this section, we will examine the effect of non-binary chemistry along two axes. First, we perform a theoretical analysis of the effects incurred by ternary and higher order reactions on the change in the distribution of the chemical state along a streamline (i.e. nonequilibrium). Second, we will focus more specifically on how the non-binary chemistry affects the equilibrium properties.

It results from this analysis that the binary scaling duplicates properly the nonequilibrium region, where the chemistry is mostly governed by binary reactions. Moreover, under certain conditions, binary scaling also results in a satisfying duplication in the equilibrium layer. These conditions are that the binary mass production rate has to be significantly larger than the ternary mass production rate. Second, the change in density in the equilibrium region should not incur a change in dissociation fraction larger than a certain threshold. Both these conditions can be verified prior to the experiment with well established gas properties tables.

3.1.1 Validity of the binary chemistry hypothesis

Higher-order Damköhler number

Let us start our analysis with the Lighthill-Freeman dissociating gas hypothesis. In equation 2.41, the second term on the right-hand side was assumed to be negligible. This implies:

$$\frac{2\rho}{M_{m,Y}}\frac{(x_Y^3+x_Y^2)}{(1-x_Y^2)}\frac{k_b}{k_f} \ll 1 \tag{3.1}$$

Or, expressing the ratio of the Arrhenius rates in the form of the equilibrium constant $K_c = K_c(T)$, which is an intrinsic property of the gas that only depends on temperature, we can identify the different contributions as:

$$\underbrace{\frac{2}{M_{m,Y}}\frac{1}{K_c(T)}}_{\textit{temperature + gas nature}} \underbrace{\rho}_{\textit{density}} \underbrace{\frac{(x_Y^3+x_Y^2)}{(1-x_Y^2)}}_{\textit{dissociation fraction}} \ll 1 \tag{3.2}$$

For dissociation reactions, K_c increases monotonously with temperature. Therefore, the applicability of binary scaling is favored by high temperatures (i.e. high free-stream enthalpy) and low density. This illustrates the condition proposed by Gibson [57] that binary scaling should be restricted to high altitude flows.

The role of dissociation fraction is illustrated in figure 3.1, where the ordinate are in a logarithmic scale. Weak dissociation (i.e. up to $x_Y = 0.1$) plays in favor of binary scaling by drastically reducing the ratio. This explains why binary scaling performs particularly well in the nonequilibrium region, where the level of dissociation is still low while the temperature is very high. There is then an intermediate region where dissociation has a limited effect on the ratio, from $x_Y = 0.4$ to $x_Y = 0.8$. It is only when dissociation is very strong (i.e. larger than $x_Y = 0.9$) that it affects negatively the applicability of binary scaling. Flow chemistry, however, is not limited to a single binary-ternary reaction as simplified in this analysis. An increase in enthalpy will not result in a saturation in dissociated species

Y causing $x_Y = 1$ but rather in its ionization into Y^+, another binary-ternary reaction.

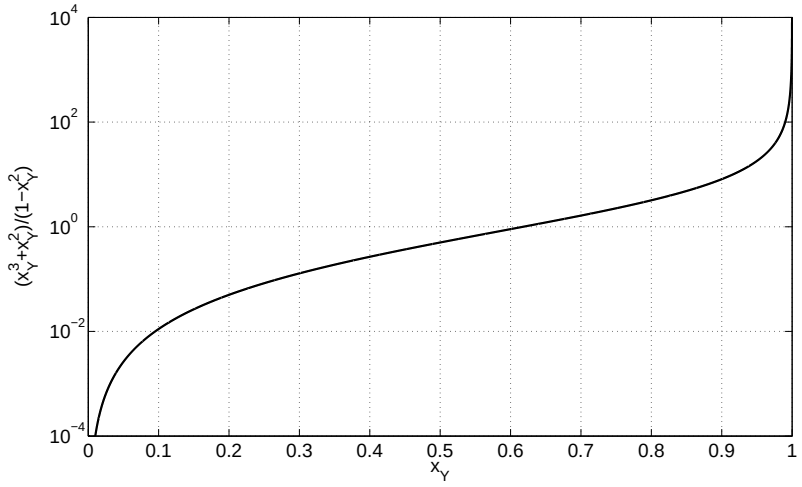

Figure 3.1: *Role of the dissociation fraction on the ratio between ternary and binary reactions for a Lighthill-Freeman gas.*

To investigate the regions of the flow where equation 3.2 is not verified,we first introduce the scale of a model χ is defined as:

$$\chi = \frac{R_{\text{lab}}}{R} = \frac{\rho}{\rho_{\text{lab}}} < 1 \tag{3.3}$$

The gas-phase Damköhler number for ternary reactions is:

$$\text{Da}_3 = \frac{\Delta}{v}\rho^2 k_b \psi_3 \tag{3.4}$$

with $\psi_3 = \psi_3(x_Y)$. A change in length-scale will thus result in a change in Da_3 such that:

$$\frac{\text{Da}_{3,\text{lab}}}{\rho_{\text{lab}}} = \frac{\text{Da}_3}{\rho} \quad \Rightarrow \quad \text{Da}_{3,\text{lab}} = \frac{1}{\chi}\text{Da}_3 \tag{3.5}$$

The ternary Damköhler number is thus larger for the scaled flow. In other words, ternary reactions are taking place over a relatively shorter length-scale in the laboratory than in flight. As illustrated in equation 2.38 and equations 2.42, all relevant reaction schemes taking place in the shock layer are either binary or ternary. For other reaction schemes of order n, that relation can be generalized to:

$$\text{Da}_{n,\text{lab}} = \chi^{(2-n)}\text{Da}_n \tag{3.6}$$

Numerical investigation for a normal shock

Numerical simulations were performed with the Post-SHock relAXation solver (Poshax), originally developed by R. Gollan [66, 154]. Poshax is part of a compressible flow CFD (CFCFD) code collection developed at the University of Queensland (UQ) [92]. It solves the one-dimensional variations

of the inviscid flow properties behind a normal shock[1]. Examples of succesful applications or experimental validations can be found in [68, 29, 104]

The simulation were done with Park's eleven species air model [147, 148], with electronic energy exchange from Gnoffo [64], and two temperatures [146]. The baseline case is for a free-stream static pressure of $22.0\ \mathrm{Pa}$, which corresponds to an altitude somewhat higher than $60\ \mathrm{km}$, well above the lower limit recommended by Gibson and Marrone [60]. The free-stream temperature is $247\ \mathrm{K}$, with a composition of 78% of N_2 and 22% of O_2. Three free-stream velocities were investigated, $7\ \mathrm{km/s}$, $10\ \mathrm{km/s}$ and $14\ \mathrm{km/s}$, and four model sizes (values of χ), 1, $1/2$, $1/4$, and $1/8$[2].

The free-stream velocities considered account for different types of atmospheric entry: from a low Earth orbit at $7\ \mathrm{km/s}$ up to a far solar system return at $14\ \mathrm{km/s}$. The corresponding points are illustrated in a velocity-density (e.g. velocity-altitude) map in figure 3.11 against the trajectory of the Shuttle, Apollo, and Hayabusa. Free-stream velocities far outside that range would be irrelevant for the application of binary scaling. Moreover, it will be shown in figure 3.11 that these velocities correspond to three equilibrium chemistry regimes: dominated by dissociation, peak in concentration of dissociated species, and dominated by ionization.

The temperatures (vibrational and electronic) and concentration of dissociated nitrogen N are depicted in figures 3.3 and 3.4, and the scaled density profiles are depicted in figure 3.5. The nondimensionalization was performed as follows:

$$\overline{y} = \frac{y}{\chi R} \qquad \overline{\rho} = \frac{\chi \rho}{\rho_\infty} \qquad \overline{T} = \frac{T}{\theta_{N_2}} = \frac{TR}{e_a} \tag{3.7}$$

where with x the direction normal to the shock and $\overline{T}$ is the Arrhénius parameter encountered in equation 2.55. The parameters selected were $R = 1.362\mathrm{m}$, which is the nose radius of an equivalent axisymmetric body used to model the windward centerline of the Space Shuttle at high angle of attack [171], and $\theta_{N_2} = 1.132 \cdot 10^5 \mathrm{K}$ is the equivalent temperature for the dissociation of N_2, with $e_a = 941.2\mathrm{kJ/mol}$ [147, 148].

In the nonequilibrium layer, the overall agreement between the scaled profiles and the original one remains good for temperature (figures 3.3) and the concentration of atomic nitrogen (figures 3.4) Scaled density profiles are also in excellent agreement immediately downstream of the shock although the scaled flows are more rarefied than what they should be, and more so as the free-stream velocity increases (figure 3.5).

At low free-stream velocity the scaled thermal and chemical nonequilibrium layers shrink as the size of the model decreases, but the tendency reverses as the free-stream velocity increases. From equation 3.6, we know the recombination Damköhler number is larger over a scaled than over the original one. Intuitively, equilibrium should thus be reached faster in scaled shock layers (through

[1] Although a normal shock is only representative of the region around the stagnation line, it can be extended to the rest of a blunt-body flow using shock mapping theory [58].

[2] The conclusions drawn for the baseline case of $60\ \mathrm{km}$ can be extended to lower altitudes as there is a constant ratio of $1/2$ between each of them. The different χ correspond then respectively to altitudes of approximately $60\ \mathrm{km}$, $55\ \mathrm{km}$, $50\ \mathrm{km}$ and $45\ \mathrm{km}$.

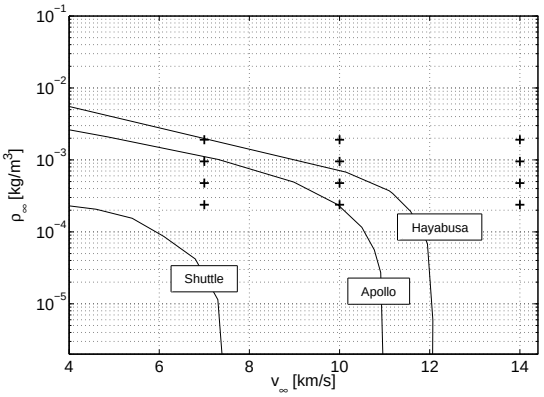

Figure 3.2: *Free-stream conditions investigated with Poshax against the trajectory of the Shuttle, Apollo, and Hayabusa.*

faster recombination). It is indeed what is observed at low velocity in figures 3.3 (a) and (b), but not for the other velocities.

A likely explanation comes from the reference density chosen to define the scale factor χ, which was here ρ_∞. As velocity goes up, it becomes larger than what it should be if it was based on the equilibrium density and therefore it artificially inflates the nonequilibrium layer, compensating the effect of enhanced recombination. To confirm this hypothesis, figures 3.3 (c) and 3.4 (c) were redrawn for the smallest model scale, using two scale factors; one based on free-stream values $\chi_\infty = \rho_\infty/\rho_{\infty,\text{lab}} = 1/8$, and one based on the equilibrium values $\chi_{\text{eq}} = \rho_{\text{eq}}/\rho_{\text{eq,lab}} = 1/7.2$. The results are shown in figure 3.6. The equilibrium scale factor does indeed yield the correct nonequilibrium thickness. However, its agreement with the original curves in the nonequilibrium layer itself is poorer than the theoretical scale factor, as the density ratio is not exactly matched there.

The issue at stake is thus that *the density field does not scale as a whole*. Depending on what reference density is chosen, different regions of the flow are thus properly duplicated. Nevertheless, the error induced in the other regions of the flow is negligible and the overall agreement between the scaled and original flow remains excellent. The role of the reference density will be further discussed in section 3.2.

3.1.2 Effect of non-binary reactions on the equilibrium chemistry

Theoretical developments

Regardless of the chemical dynamics, the larger density also has an effect on the equilibrium concentration. Indeed, the equilibrium constant K_c for a general chemical reaction such as the one exemplified in equation 2.35 is defined as:

$$K_c(T) = \frac{\prod_s \Phi_s^{\nu_s''}}{\prod_s \Phi_s^{\nu_s'}} \tag{3.8}$$

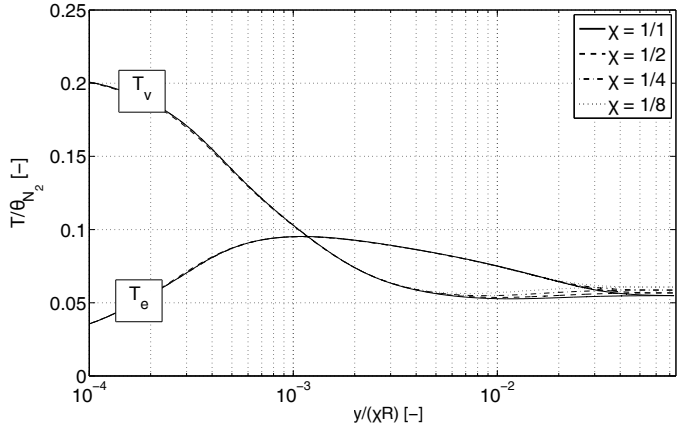

(a)

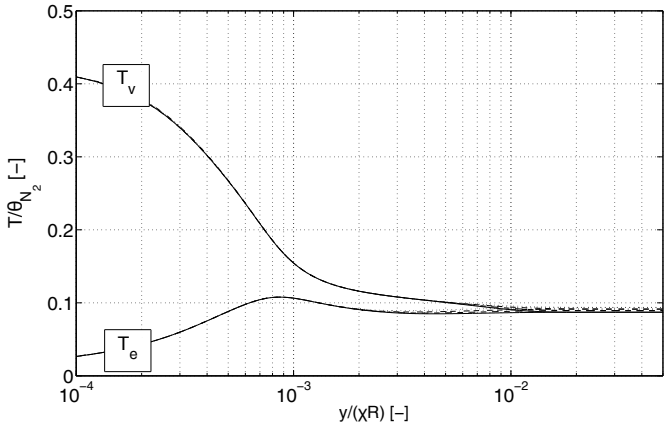

(b)

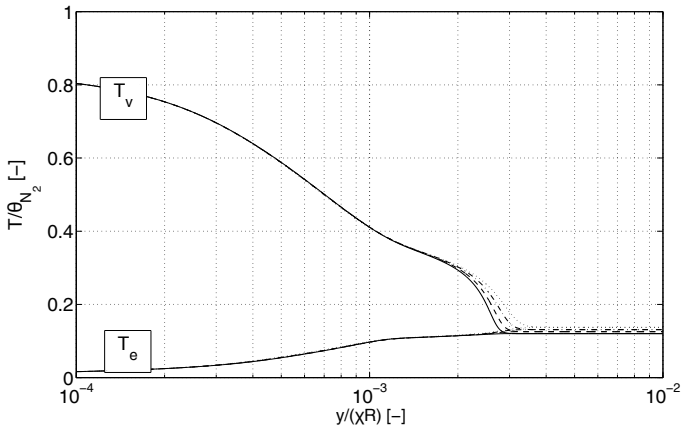

(c)

Figure 3.3: *Post-shock nonequilibrium temperature different scalings and velocities of* $7\ \mathrm{km/s}$ *(a),* $10\ \mathrm{km/s}$ *(b) and* $14\ \mathrm{km/s}$ *(c). The normal distance from the shock was divided by the scale factor* χ*, in accordance with the binary scaling theory.*

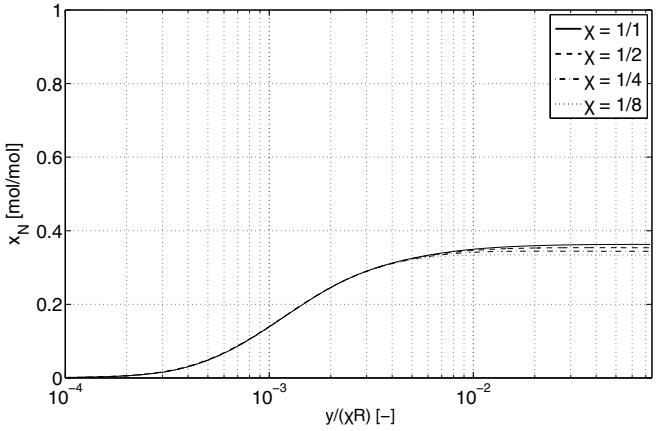

(a)

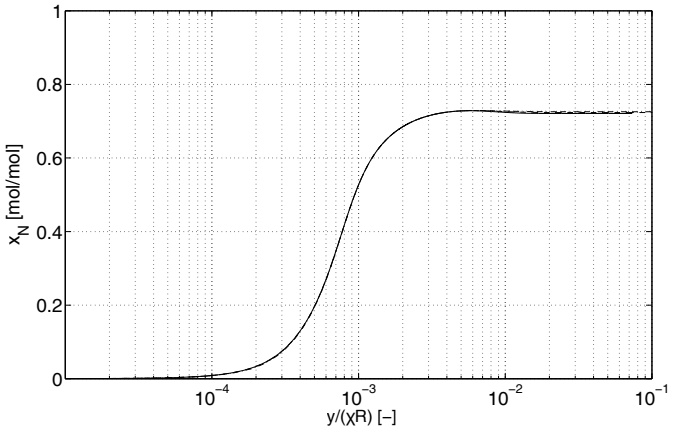

(b)

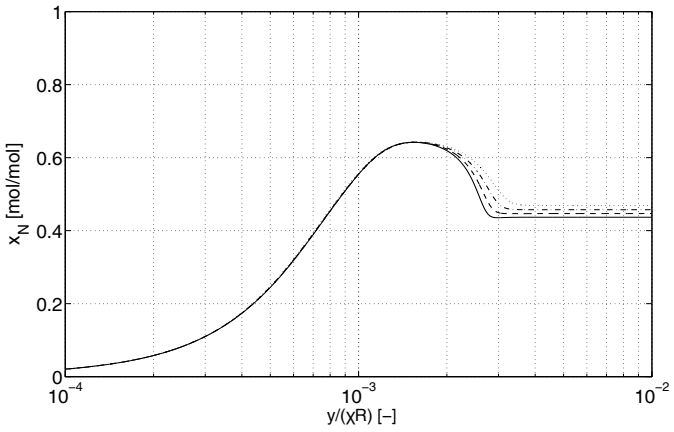

(c)

Figure 3.4: *Post-shock concentration of dissociated nitrogen for different scalings and velocities of* $7\ \mathrm{km/s}$ *(a),* $10\ \mathrm{km/s}$ *(b) and* $14\ \mathrm{km/s}$ *(c). The normal distance from the shock was divided by the scale factor* χ*, in accordance with the binary scaling theory.*

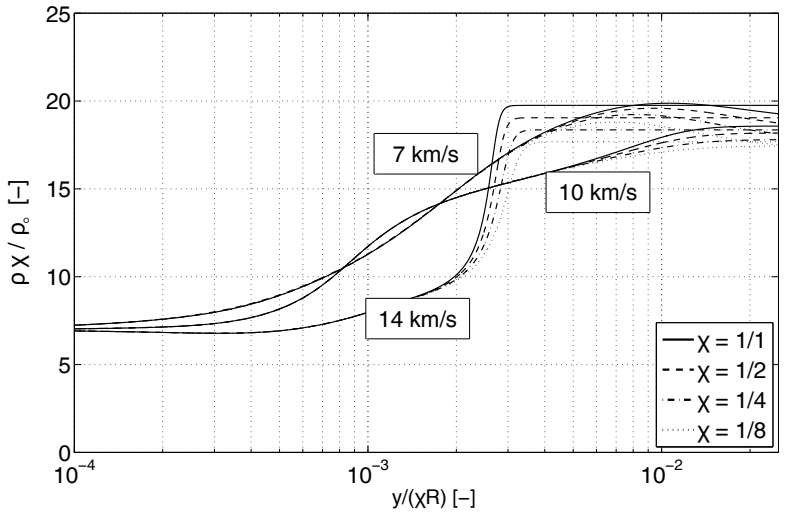

Figure 3.5: *Scaled post-shock density for different scalings at different velocities. The normal distance from the shock was divided by the scale factor χ and the density multiplied by the same factor, in accordance with the binary scaling theory. The scaling factor yields accurate results close to the shock but not towards the equilibrium layer.*

Using the Lighthill-Freeman model exposed earlier (equation 2.38), and using equations 2.40:

$$K_c(T) = \frac{2\rho}{M_{m,Y}} \frac{x_Y^2}{(1 - x_Y)} \tag{3.9}$$

As for the non-binary Damköhler (equation 3.6), the equilibrium constant is not scaled properly due to the presence of density. As it is a function of temperature only, the higher density over the scaled model can only be compensated by a decrease in the fraction of dissociated gas.

While the density changes, the enthalpy remains constant as it is one of the scaling parameter. It is defined as:

$$h = \underbrace{\frac{v^2}{2}}_{kinetic} + \underbrace{\int c_p dT + x_Y e_a}_{sensible} + \underbrace{\int \frac{p}{d\rho}}_{work} \tag{3.10}$$

The contribution of the work is negligible compared to the kinetic enthalpy in the free-stream or the sensible enthalpy downstream of the shock. Closer inspection of the sensible term reveals that a decrease of dissociated species x_Y is balanced by an increase in temperature. In other words: dissociation being endothermic, if it does not occur as much then less heat is absorbed in chemical reactions. Intuitively, the laboratory flow is thus expected to be less dissociated and hotter, which then further impacts other flow properties.

Numerical investigation for a Lighthill-Freeman gas

That simple observation is verified using with Chemical Equilibrium with Applications (CEA), a software tool developed at the NASA Lewis Research Centre [119] which allows to obtain the frozen or equilibrium flow properties. To begin with, the gas simulated is a reasonable Lighthill-Freeman

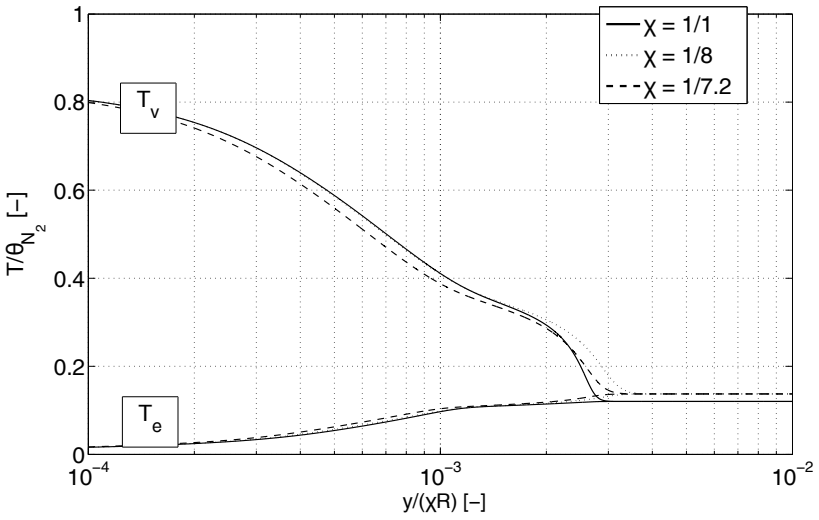

(a)

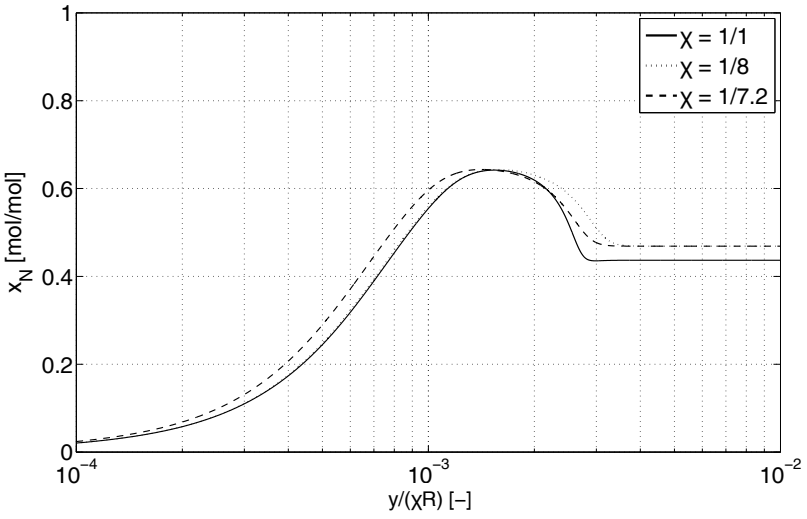

(b)

Figure 3.6: *Comparison of the results obtained with the theoretical and equilibrium scaling on the post-shock nonequilibrium temperature (a) and concentration of dissociated nitrogen (b) for a scale factor of* $1/8$*. The theoretical and equilibrium scalings gives respectively better results in the nonequilibrium and equilibrium regions. The normal distance from the shock was divided by the scale factor* χ*, in accordance with the binary scaling theory.*

approximation for air: pure N_2, with no ionization allowed. The only chemical reaction allowed is thus:

$$N_2 + M \underset{k_b}{\overset{k_f}{\rightleftharpoons}} 2N + M \tag{3.11}$$

with M being either N_2 or N. That reaction is indeed of the same form as equation 2.38.

The temperature and pressure are set as input parameters. The results are shown on a velocity-density (i.e. velocity-altitude) map, in order to visualize the practical effect of the scaling on the trajectory of an atmospheric entry probe. The free-stream velocity and density are retrieved as: The temperature and pressure are set as input parameters. The results are plotted on a velocity-density map, in order to visualize the practical effect of scaling on the trajectory of an atmospheric entry probe. The free-stream velocity is obtained with equation 2.27:

$$h = \frac{v_\infty^2}{2} \quad \Rightarrow \quad v_\infty \simeq \sqrt{2h} \tag{3.12}$$

And the stagnation pressure is derived using Newtonian theory:

$$p_{\text{eq}} = p_\infty + 2\frac{\rho_\infty v_\infty^2}{2} \simeq \rho_\infty v_\infty^2 \quad \Rightarrow \quad \rho_\infty \simeq \frac{p_{\text{eq}}}{v_\infty^2} \tag{3.13}$$

The results are depicted in figures 3.7. The trajectory of the Hayabusa probe, retrieved from [197], is also plotted conjointly with the corresponding flow conditions obtained for a $1/10$ scale model (the original capsule being $40\ \mathrm{cm}$ in diameter, that corresponds to a model of $4\ \mathrm{cm}$ in diameter which can easily be accommodated in most high enthalpy facilities).

Three regions can be identified: below $\sim 4\ \mathrm{km/s}$ the enthalpy is not large enough to cause dissociation, above $\sim 10\ \mathrm{km/s}$ the flow is fully dissociated, and in between dissociation progressively occurs. Only the region in between is relevant to our analysis; in the two other regions an increase of density at constant enthalpy would not cause any change in the chemical composition and the binary scaling is thus ideally applied.

Ideally, all isolines should be vertical so that the flow properties of interest remain constant no matter what the scale of the model is. This is not the case. As expected, in the region of interest ($4 - 10\ \mathrm{km/s}$) the scaled flow is both less dissociated and hotter. These changes further impact other flow properties such as the viscosity (i.e. the Reynolds number, one of our similarity parameters, is thus smaller for the scaled flow).

Numerical investigation for air

The same exercise is repeated with air instead of pure nitrogen. The equivalent of figures 3.7 are depicted in figures 3.8. The contour map for the concentration of atomic oxygen, free electrons, and nitrogen oxide are depicted in figures 3.9. The contour map for the speed of sound, Prandtl number, and density are depicted in figures 3.10.

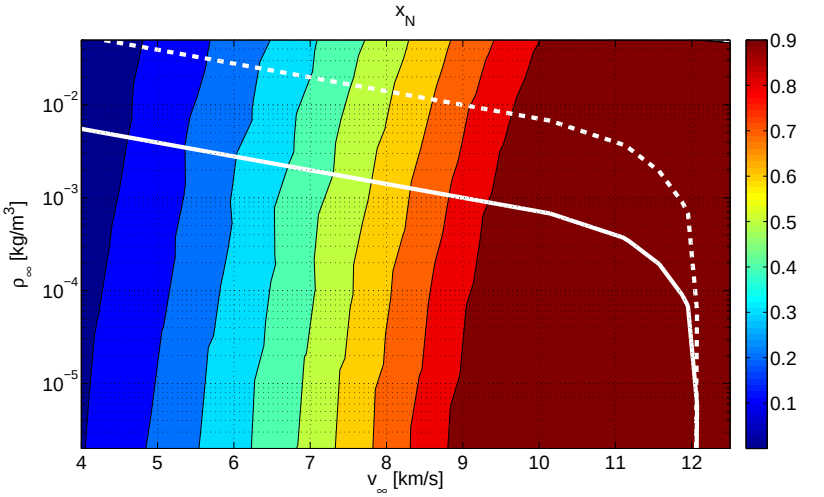

(a)

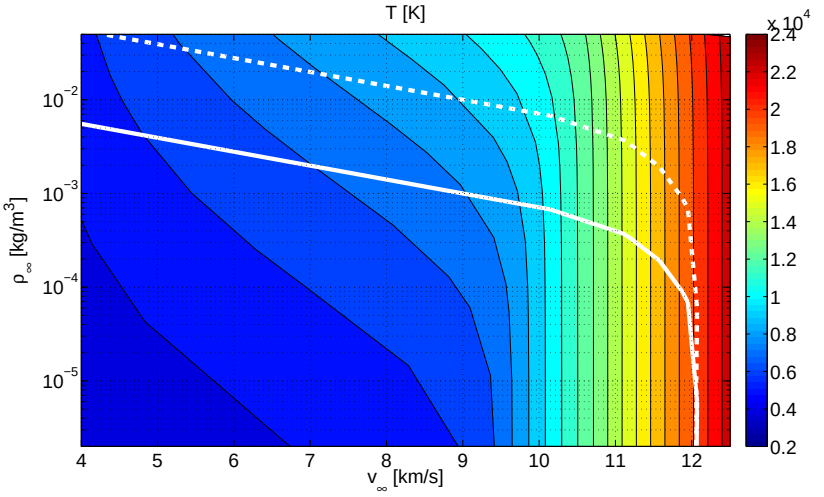

(b)

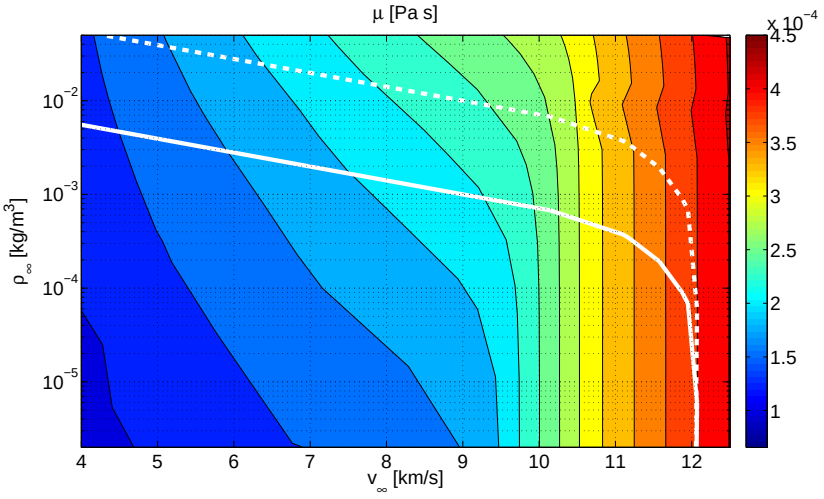

(c)

Figure 3.7: *Velocity-density map of the equilibrium dissociation mass fraction (a), temperature (b), and viscosity (c) obtained with CEA for a pure N_2 mixture. Each level correspond a change of* $0.1\ \mathrm{kg/kg}$, $1000\ \mathrm{K}$ *and* $0.25 \cdot 10^{-4}$ Pas *respectively in figure (a), (b) and (c). Binary scaling does indeed cause the scaled flow to be hotter and less dissociated than the original one.*

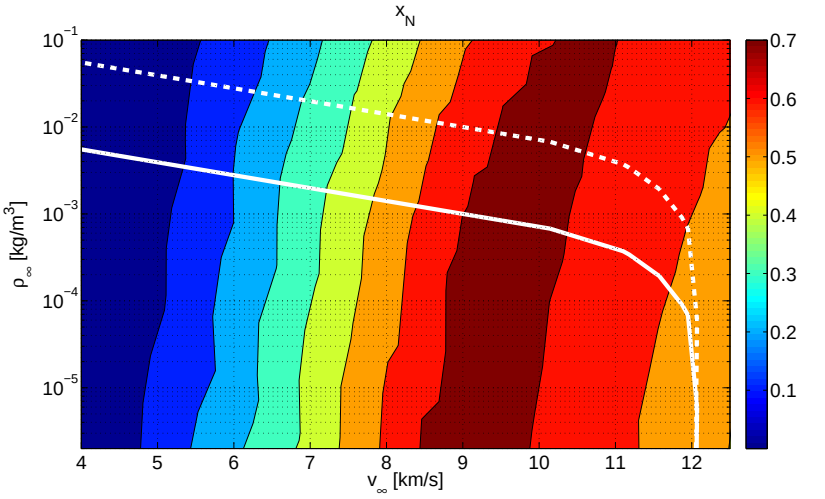

(a)

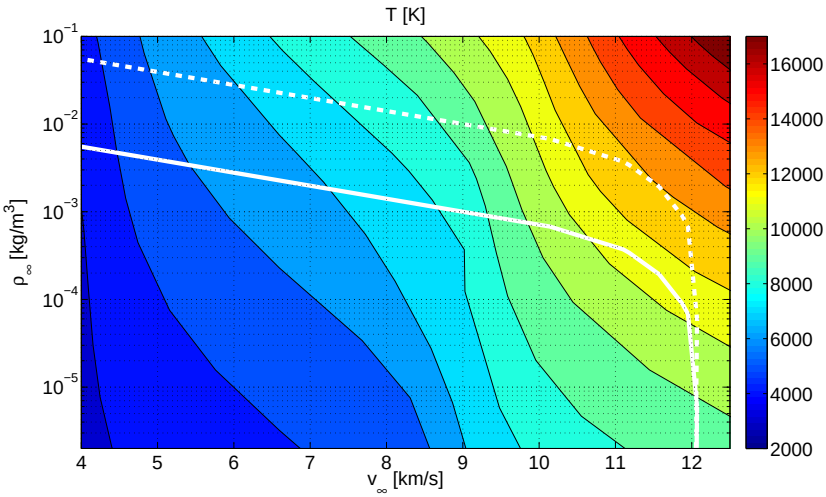

(b)

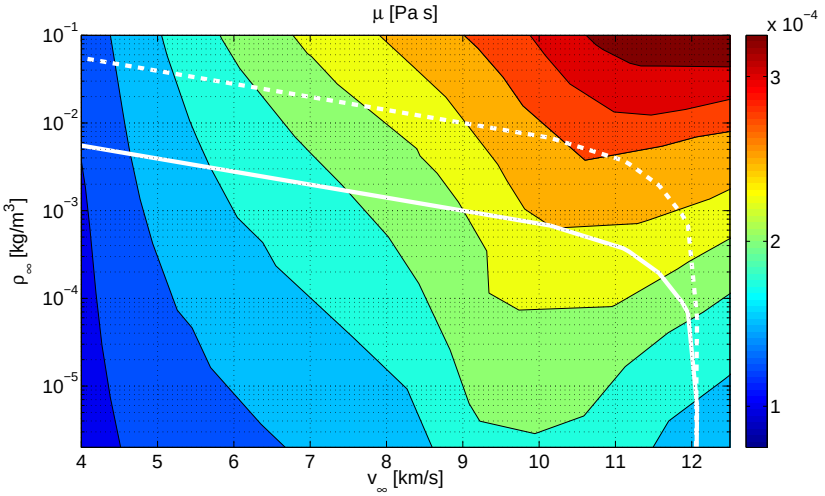

(c)

Figure 3.8: *Velocity-density map of the equilibrium mass fraction of dissociated nitrogen (a), temperature (b), and viscosity (c) obtained with CEA for air. Each level correspond a change of* $0.1\ \mathrm{kg/kg}$, $1000\ \mathrm{K}$ *and* $0.25 \cdot 10^{-4}\ \mathrm{Pas}$ *respectively in figure (a), (b) and (c).*

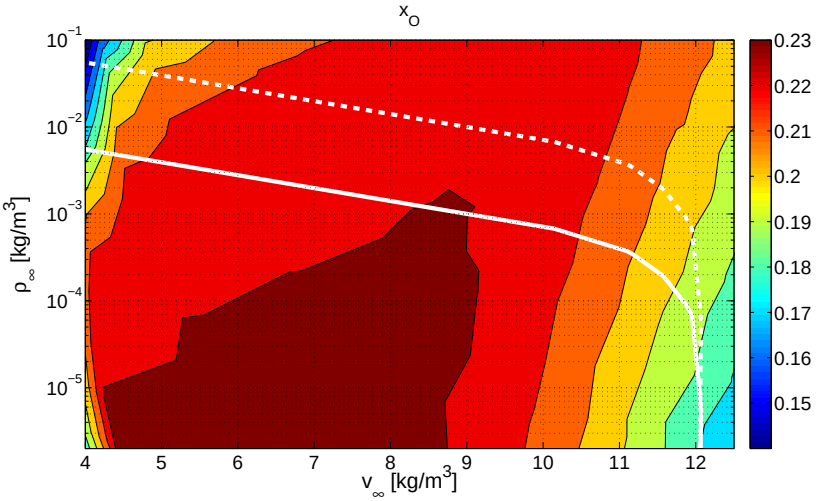

(a)

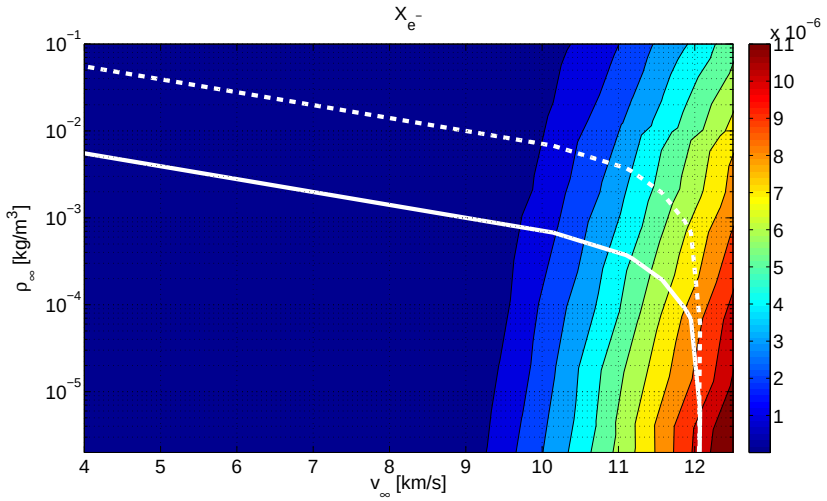

(b)

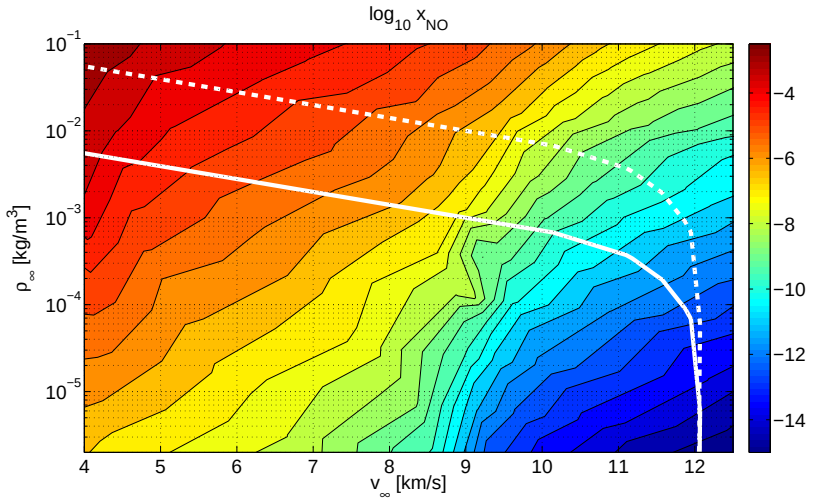

(c)

Figure 3.9: *Velocity-density map of the equilibrium mass fraction of dissociated oxygen (a), free electrons (b), and nitrogen oxide in logarithmic scale (c) obtained with CEA for air. Each level correspond a change of* 0.01 $\mathrm{kg/kg}$, $5 \cdot 10^{-6}$ $\mathrm{kg/kg}$ *and half an order of magnitude (factor* $x5$*) respectively in figure (a), (b) and (c).*

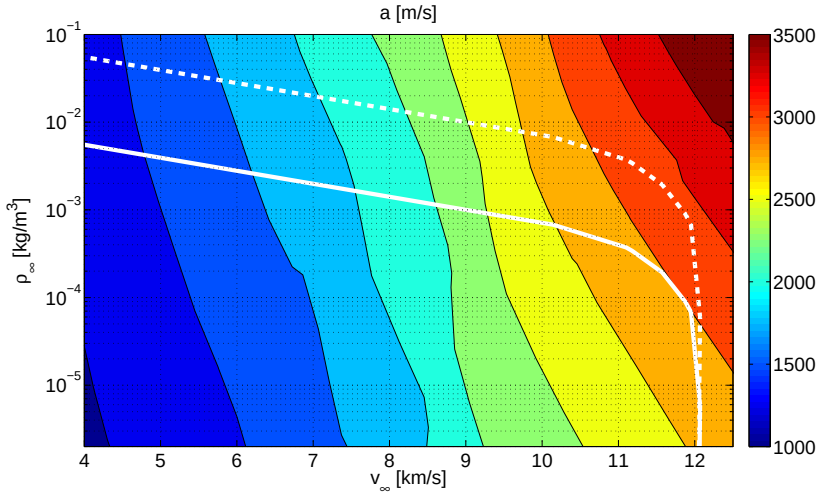

(a)

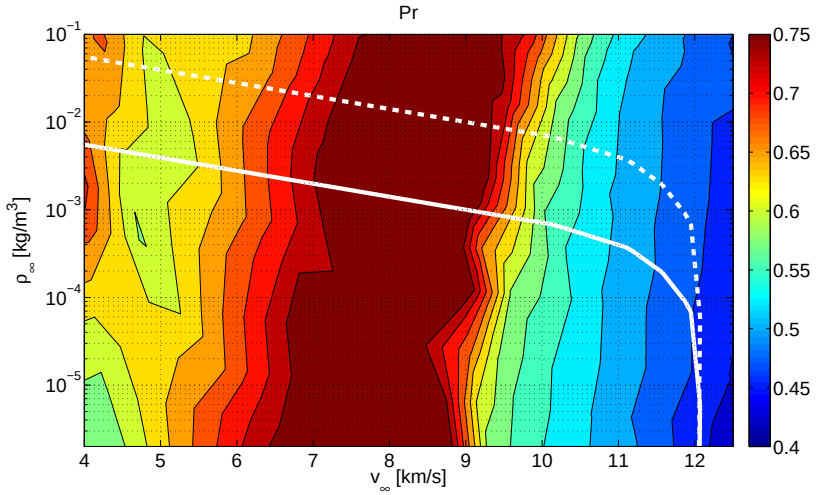

(b)

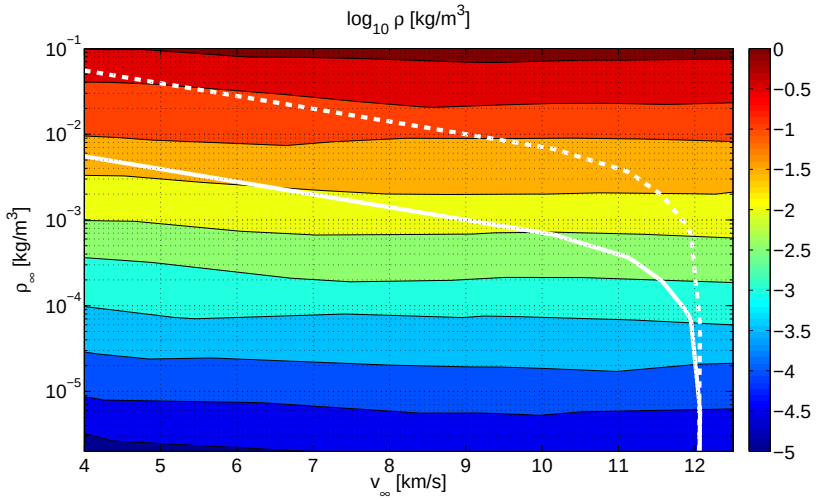

(c)

Figure 3.10: *Velocity-density map of the equilibrium sound velocity (a), Prandtl number (b), and density in logarithmic scale (c) obtained with CEA for air. Each level correspond a change of* $250\ \mathrm{m/s}$, 0.025 *and half an order of magnitude (factor* $x5$*) respectively in figure (a), (b) and (c).*

The dissociation mass fraction (figure 3.8 a) resembles that obtained for the Lighthill-Freeman case. The only difference is that past a certain threshold ionization becomes the dominant binary reaction instead of dissociation. In that instance, the scaled more is actually *more* dissociation but *less* ionized. Indeed, in figure 3.9 (b) the concentration of free electrons is smaller for the scaled flow. A similar same conclusion can be drawn from the concentration of atomic oxygen (figure 3.9 a), although it is relatively more affected by the concentration of nitrogen oxide, being present in smaller quantities than atomic nitrogen.

The case of nitrogen oxide is more complicated (figure 3.9 c). It is present in four reactions, one dissociation and three neutral exchanges:

$$\begin{aligned} NO + M &\underset{k_b}{\overset{k_f}{\rightleftharpoons}} N + O + M \\ O_2 + N &\underset{k_b}{\overset{k_f}{\rightleftharpoons}} NO + O \\ N_2 + O &\underset{k_b}{\overset{k_f}{\rightleftharpoons}} NO + N \\ N_2 + O_2 &\underset{k_b}{\overset{k_f}{\rightleftharpoons}} 2NO \end{aligned} \tag{3.14}$$

While the neutral exchanges are binary in both directions, the dissociation is ternary in the direction of the creation of NO. This results in large discrepancies between the original and scaled flow. In the Hayabusa example presented here, the concentration of NO is 5 to 10 times larger in the scaled flow.

The contour plot for the temperature (figure 3.8 b) exhibits a partially similar behavior to what was observed for the Lighthill-Freeman model: the temperature is larger over scaled flows. However, towards the large free-stream velocity the clean vertical isolines have been replaced by a gradient in temperature, due to the absorption of heat through the process of ionization. That change in temperature and mixture composition also impacts the viscosity (figure 3.8 c): there is a gradient in viscosity along the density axis towards large the large free-stream velocities.

Finally, the sound speed (figure 3.9 a) and Prandtl number (figure 3.8 b) are only mildly affected by changes in free-stream density. Conversely, the equilibrium density (figure 3.8 c) is a very weak function of the free-stream velocity.

For the sake of comparison, the points that were used for the study of the nonequilibrium flow in section 3.1.1 (white dots) and the trajectory of Hayabusa were depicted in figure 3.11. The three free-stream velocities correspond to the three chemistry regimes that were identified for air: dominated by dissociation, peak in concentration of dissociated species, and dominated by ionization.

3.1.3 Discussion and conclusion

First, binary scaling yields excellent results in the nonequilibrium layer. The main concern was the recombination reaction rate, that is larger for scaled flows. However, while there are visible changes in the nonequilibrium layer thickness, they are due to the *combined action of the recombination reaction (which tends to shrink it) and the different scaling of the free-stream and equilibrium densities (which*

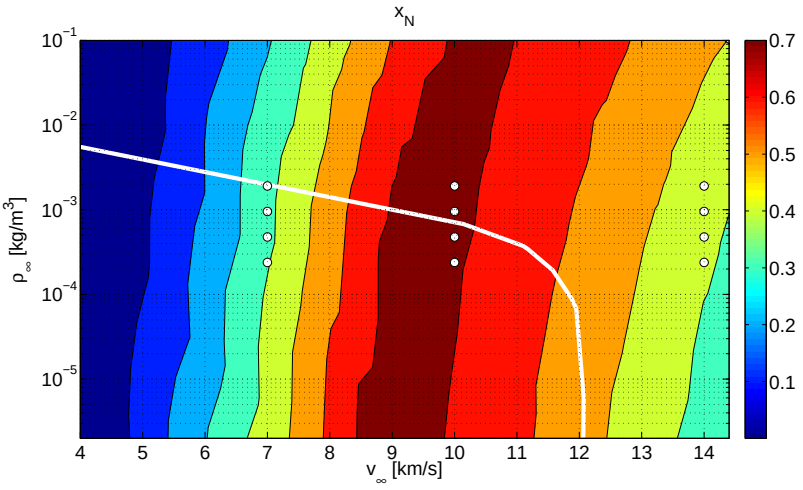

Figure 3.11: *Reproduction of figure 3.8, with the points that were used for the study of the nonequilibrium flow in section 3.1.1 (white dots) and the trajectory of Hayabusa. The three free-stream velocities correspond to the three chemistry regimes that were identified for air: dominated by dissociation, peak in concentration of dissociated species, and dominated by ionization.*

tends to inflate it). In the particular case chosen for the numerical simulation, both compensate each other for a range of free-stream velocities around $10\ \mathrm{km/s}$.

Second, regarding the equilibrium chemistry, a general rule is: *the scaled flow is always hotter and exhibits a smaller concentration in products of the dominant binary reaction (dissociation or ionization).* As a corollary, the scaled flow is also more concentrated in products of ternary reactions (i.e. such as NO in the case of air).

These changes in temperature and mixture composition induce further changes in other flow properties:

- The viscosity of the scaled flow is larger, and the difference is even larger for large free-stream velocities, viscosity being sensible to the degree of ionization of the flow.*The Reynolds number (Π_1) is thus slightly smaller in the laboratory* than in flight.

- The speed of sound being a strong function of temperature, it is also larger for the scaled flow. *The Mach number (Π_2) is thus also smaller in the laboratory* than in flight. Incidentally, since the specific heat ratio (Π_3) does almost not vary, the Knudsen number is less affected through the mutual compensation of the Mach and Reynolds numbers.

- The Prandtl number (Π_4) tends to be slightly larger for the scaled flow.

It should be reinstated that binary scaling is originally *only meant* for the nonequilibrium layer. This is why authors such as Gibson and Marrone [60] concluded that the limit of its applicability is only determined by the fraction of nonequilibrium in the shock layer. We have indeed found, both theoretically and through numerical simulations, that binary scaling performs very well in these conditions. These results were already known.

It is no surprise either that binary scaling does not perform as well under equilibrium conditions. Nevertheless, through careful examination, we were able to identify the changes incurred. Not only does this confer greater confidence to the experimentalist, but it also allows to target specific flow regimes for different applications.

Let us consider the example of a researcher studying the "blunt body paradox" [158] using data from the Apollo mission or to make prediction regarding the Crew Exploration Vehicle (CEV). Using figures 3.8 (c) and 3.10 (a), he will easily determine that he should focus on points of the trajectory characterized by a free-stream velocity lower than $\sim 9{-}10\,\mathrm{km/s}$ so as to avoid too large discrepancies in viscosity and compressibility between the experiment and flight.

A practical example of binary scaling applied to flows involving complex chemistry is given in appendix B. It is based on a study of Titan aerocapture by Morgan et al. [127].

3.2 Choice of reference density

The next issue, that has already been partially discussed in the previous section, is the choice of the reference density. Indeed, binary scaling requires to duplicate the product ρL, but which density and which dimension are we exactly referring to? For the sake of simplicity, one uses the free-stream density ρ_∞ and the nose radius R. As shown in figure 3.6, that approach is appropriate for the length scale in the region immediately downstream of the shock, i.e. the nonequilibrium layer where we seek to duplicate equation 2.56. Moving away downstream of the shock, however, the scaling becomes less and less appropriate. Let us thus investigate what are the mechanism driving the changes in density downstream of the shock, and how these are influenced by binary scaling.

3.2.1 Relation between shock standoff and density ratio

An important feature of hypersonic blunt-body flows is that the shock standoff distance Δ is inversely proportional to the average density on the stagnation streamline. This can be demonstrated by a very simple argument: let us apply the continuity to a small control volume adjacent to the stagnation line as shown in figure 3.12. For a two-dimensional flow, the rate at which mass enters the volume is $v_\infty \rho_\infty b$ where b is a length in the direction normal to the flow. For a small value of b, the rate at which mass leaves the volume if $v_b \overline{\rho} \Delta$, where $\overline{\rho}$ is the average density in the shock layer. Simple trigonometry gives $v_b \simeq v_\infty \cos\theta$ and $b = (R + \Delta)\cos\theta$. Therefore:

$$\frac{\Delta}{R} \simeq \frac{1}{\overline{\rho}/\rho_\infty - 1} \simeq \frac{\rho_\infty}{\overline{\rho}} \tag{3.15}$$

where we assumed that the density ratio across the shock was much larger than unity. Numerous authors have demonstrated, both numerically and experimentally, that the shock standoff distance is indeed a function of the density ratio across the shock, although the proportionality factor is not unitary [5, 12, 14, 75, 81, 86, 87, 110, 132, 201, 207, 212].

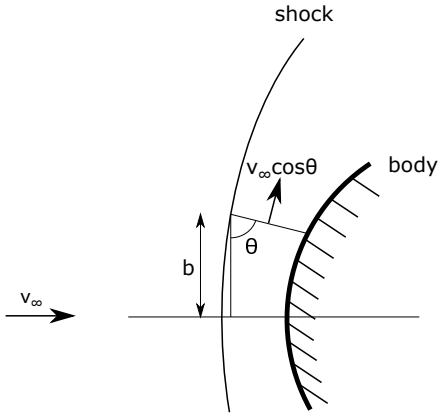

Figure 3.12: *Shematic representation of the control volume used to demonstrate the relation between shock standoff and shock layer density.*

The density ratio across the shock is a measure of the compressibility of the flow through the Mach number. Both are indeed related to one another through the normal shock equation:

$$\frac{\rho_{\text{fr}}}{\rho_\infty} = \frac{(\gamma+1)\,\mathrm{M}_\infty^2}{(\gamma-1)\,\mathrm{M}_\infty^2+2} \tag{3.16}$$

where the subscript fr stands for a frozen flow. Ambrosio and Wortman proposed one of the early correlations for the shock standoff distance as a function of the free-stream parameters [5], thereby assuming a frozen density $\overline{\rho} \simeq \rho_{\text{fr}}$. For cylinder-wedges, they obtained:

$$\frac{\Delta}{R} = 0.386 \exp\left(\frac{4.67}{\mathrm{M}_\infty^2}\right) \tag{3.17}$$

Although that correlation is a useful first order approximation, it is only applicable for flow regimes that can be approximated with the perfect gas assumption. For other regimes, it misrepresents the complexity of the processes taking place in the shock layer. While the value of post-shock density obtained applying equation 3.16 only represents that obtained in frozen conditions, in reality the density distribution in the shock layer might be very different. Correlations such as these are thus prone to lead to erroneous results if they are used out of their comfort zone. The equation proposed by Ambrosio and Wortman, in particular, was developed for air flows with Mach numbers up to ~ 7.

One of the most comprehensive semi-empirical correlation for constant density inviscid shock layers was suggested by Inger [86], who accounted for the flow's vortical properties:

$$\frac{\Delta}{R} = \frac{1+\lambda}{K\sqrt{\frac{2\rho_\infty}{\rho_{\text{fr}}}\left(1-\frac{\rho_\infty}{\rho_{\text{fr}}}\right)}}\frac{\rho_\infty}{\rho_{\text{fr}}} \tag{3.18}$$

where K is a parameter that reflects the inviscid shock layer vorticity and λ is a longitudinal curvature parameter. The value for both those parameters are tabulated by Inger as a function of the frozen density ratio across the shock, based on Newtonian theory calculations found in [75].

3.2.2 Chemistry in the shock layer

Some of the developments made in this section are detailed in appendix C.

Hornung investigated both numerically and experimentally the effect that chemical reactions have on density in nitrogen flows, correlating the shock standoff to a dissociation rate parameter [81], identified as the binary Damköhler number used in the present work. Wen and Hornung later generalized these results extending them to complex mixtures and taking into account the effect of the free-stream kinetic energy [207], which corresponds to our scaling parameter h_∞.

They first obtain, for the stagnation line for an inviscid adiabatic flow, that the density evolves as:

$$\begin{aligned} d\rho &= \frac{1-\rho\partial h/\partial p}{\partial h/\partial \rho}dh - \frac{\partial \rho}{\partial h}\sum_{s=2}^{n}\frac{\partial h}{\partial x_s}dx_s \\ \frac{d\rho}{\rho} &= \underbrace{\frac{u^2}{a_{\text{fr}}^2}\frac{du}{u}}_{\textit{compressibility}} \underbrace{- \frac{1}{\rho}\frac{\partial \rho}{\partial h}\sum_{s=2}^{n}\frac{\partial h}{\partial x_s}dx_s}_{\textit{chemistry}} \end{aligned} \tag{3.19}$$

Two distinct effects have thus an influence on the distribution of density downstream of the shock: compressibility and the chemistry. In the stagnation region, the effect of compressibility is very small due to the high temperature (and thus large speed of sound) and relatively small flow velocity, leading to typical value for the frozen Mach number $\mathrm{M}_{\text{fr}} \leq 0.2$ [207].

Only the chemistry is therefore further investigated. It can be quantified with a dimensionless number that stands for the ratio between the energy absorption rate by chemistry with the input rate of free-stream kinetic energy [207]. For a perfect gas, it is expressed as:

$$\tilde{\Omega} = \left(\sum_{s=2}^{n}\frac{e_{a,s}}{c_p T}\frac{dx_s}{dt}\right)_{\text{fr}}\frac{R}{v_\infty} \tag{3.20}$$

One can also consider that form as an extension of the Damköhler number for flows that have a more complex chemistry than a simple Lighthill-Freeman dissociation model. Wen and Hornung then related that parameter to the dimensionless shock standoff distance by simplifying the density distribution in the shock layer in two sections: first, immediately downstream of the shock, a region in which the density increases linearly with the distance from its frozen value to the equilibrium value, followed by a region in which the density is at a constant equilibrium value, up to the surface of the body (the flow being inviscid).

They further presented the result of numerical simulations, for an inviscid flow with a two-temperatures model, and experiments performed in the T5 free-piston shock tunnel T5 at GALCIT. The results for carbon dioxide are shown respectively in figure 3.13 (a) and (b). Both were performed for spheres of various diameter [207].

Clearly, the agreement between experiments, simulations, and theoretical predictions is rather good, indicating not only that the dimensionless shock standoff does indeed correlate with the ad-

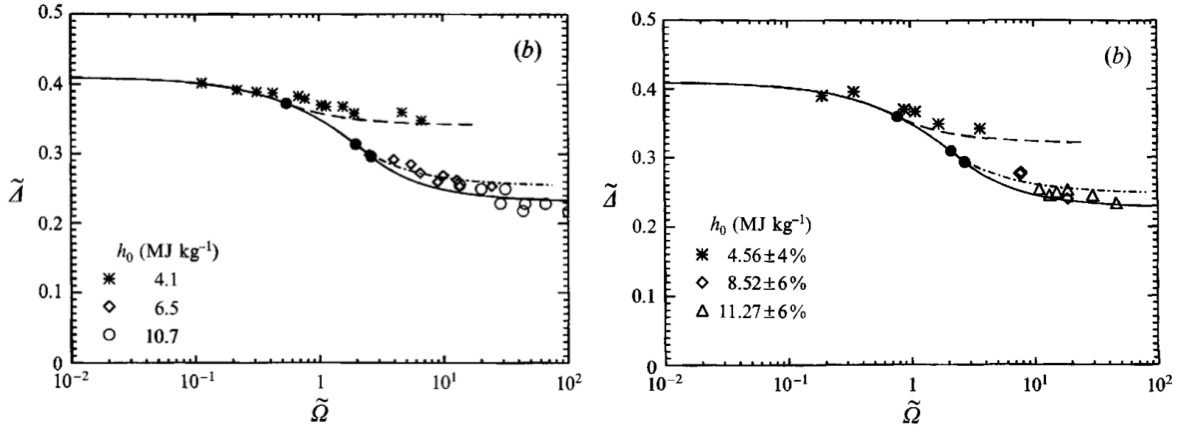

(a) (b)

Figure 3.13: *Numerical (a - on the left-hand side) and experimental (b - on the right-hand side) results reported by Wen and Hornung while measuring the shock standoff distance over spheres in carbon dioxide. The vertical axis is the standoff density product $\tilde{\Delta} = (\Delta/2R)(\rho_{fr}/\rho_\infty)$ and the horizontal axis is a the local binary Damköhler number immediately downstream of the shock Da_s, using the sphere radius as a typical length-scale. The full circles are the junction between equation C.19 and C.20. Images taken from [207].*

vancement of chemistry in the shock layer $\tilde{\Omega}$ and the kinetic energy of the flow $\tilde{K}$, but also that the model developed by Wen and Hornung is satisfying. They further draw two conclusions relevant for our study. First, in the case of carbon dioxide, the effect of $\tilde{\Omega}$ is more dramatic, because it has lower dissociation energies. Second, for a fixed $\tilde{\Omega}$ a higher enthalpy leads to a thicker nonequilibrium layer, and thus a small dimensionless shock standoff, until a certain enthalpy above which that effect is negligible (the flow being completely dissociated no matter what).

3.2.3 Viscid-inviscid interactions

The developments made in the previous subsection assumed an inviscid shock layer. However, in rarefied regime the boundary layer can become substantially large and have an impact on the rest of the flow. Inger points out that these viscid-inviscid interactions have a negligible influence on the shock standoff distance for Reynolds numbers larger than 300, but should be taken into account otherwise [86]. He defines the shock layer Reynolds number $\mathrm{Re}_{\mathrm{fr}}$ as:

$$\mathrm{Re}_{\mathrm{fr}} = \frac{\rho_\infty v_\infty R}{\mu_{\mathrm{fr}}} \tag{3.21}$$

Inger proposes a model for the continuum end of the rarefied flow spectrum, in which he splits the stagnation region in two layers: an outer inviscid layer of constant density ρ_{fr} from the shock to the edge of the boundary layer, and an inner viscid layer consisting of the whole boundary layer down to the body surface. The pressure is assumed constant throughout the shock layer. From that approach, he shows analytically that, assuming a frozen flow, the viscid shock standoff distance can be simplified to [86]:

$$\frac{\Delta - \Delta_{\mathrm{inv}}}{R} \simeq \sqrt{\frac{1}{\mathrm{Re}_{\mathrm{fr}}}}(1+\lambda)\, F[(1+2\lambda)(a+bg_w) + (K-1)(c+dg_w)] \tag{3.22}$$

where the subscript inv stands for the inviscid solution, F a function of the density ratio across the shock, and $g_w = T_w/T_0$ the ratio of the wall temperature and the total temperature, which is computed as:

$$T_0 = T_\infty \left[1 + 0.5(\gamma_\infty - 1)\,\mathrm{M}_\infty^2\right] \tag{3.23}$$

That relation accounts not only for the displacement thickness due to the presence of the boundary layer, but also for the contributions of the vorticity in the outer layer, the longitudinal curvature of the body, and the influence of the displacement on the inviscid flow speed. These contributions are consistent with the classification of low Reynolds number effects presented by Van Dyke [202].

3.2.4 Discussion and conclusion

The three driving mechanism having an influence on the distribution of density downstream of the shock are identified as: chemistry (Da_g), compressibility (M), and viscosity (Re). All three are governed by dimensionless numbers which are theoretically duplicated through binary scaling. Any density along the stagnation line could thus be chosen as a reference (ρ_∞, ρ_{fr}, ρ_{eq} or ρ_w). There are, however, some deviations from that theoretical frame that should be taken into account.

First, as we have concluded in section 3.1.3, in the equilibrium layer the scaled flow is always hotter and exhibits a smaller concentration in products of the dominant binary reaction. Referring back to equation 3.19, thus *the density gradient is shallower in the scaled flow*, for which less dissociation occurs. This explains the observations made in figure 3.6.

It also follows that *the dimensionless shock standoff tends to be larger for scaled flows*. Remember that the quantity that drives the dimensionless shock standoff is the average density downstream of the shock. A shallower density gradient yields a smaller average dimensionless density, and thus a larger dimensionless shock standoff (equation 3.15).

That side-effect of the binary scaling also provides a credible explanation for the effect related to the model size observed in figure C.1, and for which we dismissed the three-dimensional effects based on the work of Eichmann et al. [44]. The normal shock reaction rate parameter defined by Hornung (equation C.10) only accounts for the dissociation chemistry while, as demonstrated in section 3.1.2, the recombination reaction rate need to be considered in the equilibrium layer. The same Ω yields thus different equilibrium properties depending on the size of the model, resulting in larger shock standoff for smaller models. Nevertheless, this would not have happened with the reaction rate parameter later defined by Wen and Hornung (equation 3.20), for which each species is considered separately.

Second, as it was already discussed, those changes in temperature and chemistry also impact the Mach number - and hence the compressibility - in the equilibrium layer. Nevertheless, it is expected to have very little impact on the density distribution in the vicinity of the stagnation line.

Lastly, if the Reynolds number is low enough for the viscid-inviscid interactions to be taken into account, the temperature ratio g_w (or alternatively Π_5 as defined in equation 2.21) should also be taken into account. In other words, since the free-stream enthalpy is already one of our similarity parameters, the wall temperature should be duplicated as well.

3.3 Radiative coupling

Gases radiate a portion of their energy when they are brought up to sufficiently high temperatures, as it is typically the case for atmospheric entry. If so, radiation needs to be accounted for in two terms in the Navier-Stokes equation for the conservation of energy (2.17):

- First, in the heat flux vector, which is actually expressed as:

$$q_i = q_i^{cd} + q_i^d + q_i^r \tag{3.24}$$

  where the superscripts cd, d and r respectively the conductive, diffusive and radiative heating.

- Second, in the flow's energy (already expressed in equation 2.29). Indeed, radiation results both in energy losses, through emission in hot parts of the flowfield, and energy gain, through absorption in colder parts of the flowfield. As a result, the flow is not adiabatic.

3.3.1 Radiation gas dynamics

Prior to exploring the effect that binary scaling has on radiation gas dynamics, we will briefly introduce its theory. Let us consider the amount of radiative energy dE in the frequency interval $\nu, \nu + d\nu$ going across the surface area dA during a time dt in all directions formed by the solid angle $d\omega$ around a direction r perpendicular to that surface and going through a point P belonging to it. The specific radiative intensity I_ν is then, at P, the radiative energy transferred in the direction r per unit of frequency, per steradian (unit of solid angle), per unit of time:

$$I_\nu \equiv \lim_{d\nu, dA, d\omega, dt \to 0} \left(\frac{dE}{d\nu \cdot dA \cdot d\omega \cdot dt} \right) \tag{3.25}$$

The integrated intensity is simply obtained as:

$$I = \int_0^\infty I_\nu d\nu \tag{3.26}$$

The amount of energy E radiated over the whole spectrum through an area dA located in P in the interval of time dt is thus simply obtained as:

$$dE = I \cos\theta dA d\omega dt \tag{3.27}$$

The interval of time dt can be defined in term of an infinitesimal length dL such that $dt = dL/c$ where c is the speed of light. It follows that one can write:

$$dE = \frac{I}{c} dV d\omega \tag{3.28}$$

where $dV = \cos\theta dA dL$ is a control volume surrounding the surface dA. One can thus defined the radiation energy density per unit of volume E_V as:

$$E_V = \frac{1}{c} \int_0^{4\pi} I d\omega \tag{3.29}$$

For the sake of consistency with the rest of the report, we prefer to define the specific radiation energy:

$$e_r = \frac{1}{\rho c} \int_0^{4\pi} I d\omega \tag{3.30}$$

Moreover, an elementary solid angle defined by the range $\theta + d\theta$ and $\phi + d\phi$ expressed as:

$$d\omega = \sin\theta d\theta d\phi \tag{3.31}$$

We can thus finally write:

$$e_r = \frac{1}{\rho c} \int_{2\pi}^{0} \int_{\pi}^{0} I \sin\theta d\theta d\phi \tag{3.32}$$

which can be directly added to the definition of the flow's energy found in equation 2.29.

In turn, the radiative heat flux, i.e. the net flux of radiation across that surface per unit of time and per unit of area, is:

$$q^r = \int \frac{dE}{dA dt} = \int_0^{4\pi} I \cos\theta d\omega \tag{3.33}$$

which becomes, using the definition of a solid angle (equation 3.31):

$$q^r = \int_{2\pi}^{0} \int_{\pi}^{0} I \cos\theta \sin\theta d\theta d\phi \tag{3.34}$$

which can be directly added to the definition of the flow's energy found in equation 3.24.

Assuming radiation is steady[3], the specific radiative intensity in the direction i coming from a fluid element of length dy in the flowfield is equal to the difference between the energy emitted and that

[3]Temporal variation is neglected because the temporal evolution of the flowfield in considerably slower than the speed of light $v_\infty/c \sim O(10^{-5})$.

absorbed, and light scattering:

$$dI_\nu = \underbrace{\eta_\nu dy}_{\textit{emission}} - \underbrace{\kappa_\nu I_\nu dy}_{\textit{absorption}} - \underbrace{\sigma_{y,\nu} I_\nu + \frac{\sigma_{y,\nu}}{4\pi} \int I_\nu(\hat{y}_i)\, \phi(\hat{y}_i, \hat{y})\, d\Omega_i}_{\textit{scattering}} \tag{3.35}$$

where η is the emission coefficient, κ the absorption coefficient, and σ is the extinction coefficient. The scattering is composed of two terms: one for the specific radiative intensity scattered away from y and one for that scattered into y. However, scattering can be neglected if we assume that the medium is homogeneous and that there are no discontinuity in the distribution of density[4]. Re-arranging the terms, the rate of change of I_ν along the direction y can thus be expressed as:

$$\frac{dI_\nu}{dy} = \eta_\nu - \kappa_\nu I_\nu \tag{3.36}$$

At this stage, it is useful to introduce a flow property that will be used later on, the *optical thickness* τ_ν. Assuming an absorbing but non-emitting gas, equation 3.36 can be simplified to:

$$\frac{dI_\nu}{dy} = -\kappa_\nu I_\nu \tag{3.37}$$

which solution is:

$$I_{\nu,y+dy} = I_{\nu,y} e^{-\tau_\nu} \tag{3.38}$$

where we defined the optical thickness:

$$\tau_\nu \equiv \int_y^{y+dy} \kappa_\nu dy \tag{3.39}$$

Equation 3.36 can be further simplified. The radiative intensity through a blackbody is independent of the distance through it, as illustrated by Planck's law:

$$B_\nu = \frac{2h\nu^3}{c^2(e^{h\nu/k_B T} - 1)} \tag{3.40}$$

which, when applied to a blackbody equation 3.36, becomes:

$$\frac{dI_\nu}{dx} = 0 = \eta_\nu - \kappa_\nu B_\nu \tag{3.41}$$

And it follows:

$$\eta_\nu = \kappa_\nu B_\nu \tag{3.42}$$

[4]In the case of ablation of spalliation, each optical obstacle will scatter light at wavelengths which are of the same order as its size.

which is known as Kirchhoff's law. Since emitted radiation does not depend on absorbed radiation (except in the case of stimulated emission, see equation D.5), equation 3.42 is a general result valid whether or not the gas behaves like a blackbody, provided it is at local thermodynamic equilibrium (LTE). Equation 3.36 can then be expressed as:

$$\frac{dI_\nu}{dy} = \kappa_\nu (B_\nu - I_\nu) \tag{3.43}$$

This is the radiative-transfer equation. Or, in an alternative form using equation 3.42:

$$\frac{dI_\nu}{dy} = \eta_\nu \left(1 - \frac{I_\nu}{B_\nu}\right) \tag{3.44}$$

3.3.2 Discussion and conclusion

The emission coefficient η and absorption coefficient κ (and hence also the optical thickness τ) are not intrinsic properties of the mixture but rather depend in a linear fashion on its density through the number density (see appendix D and in particular equations D.6 and D.7). They can thus be replaced by their specific version (in terms of mass): κ_ρ, σ_ρ, and τ_ρ. Equation 3.36 can thus be written as:

$$dI_\nu = \rho \eta_{\rho,\nu} dy - \rho \kappa_{\rho,\nu} I_\nu dy \tag{3.45}$$

Hence, the radiative intensity scales as ρL (i.e. ρdy) and is thus preserved through binary scaling. From equation 3.39, the same reasoning holds for the optical thickness. Moreover, solid angles being dimensionless, it follows from equation 3.33 that the radiative heat flux is also preserved. These result are fundamental, as it implies that a specific point in the flow will radiate and receive the same intensity wether not matter what the scale of the flow is.

Following the same line of thought, from equation 3.27 the amount of energy radiated by a control volume scales as ρL^3 (i.e. IdA). In other words, it is proportional to the mass contained in that volume. However, the flux of mass into the shock layer scales as:

$$d\dot{m} = \rho_\infty v_\infty dA \tag{3.46}$$

As a result, the amount of heat radiated per unit of mass ingested in the shock layer scales as:

$$\frac{dE}{d\dot{m}} \propto \frac{\rho L^3}{\rho L^2} = L \tag{3.47}$$

Therefore, the heat radiated by a fluid element in the shock layer in the facility is smaller than that radiated by a scaled fluid element in flight. As a consequence, less heat is lost in the scaled flow and it is thus hotter and potentially more dissociated (or ionized).

The non-adiabaticity only poses a problem if the radiative heating is important enough to have an influence on the rest of the flowfield. Goulard presented a useful tool to estimate the extent of that coupling, based on an analytical solution of the incompressible shock layer in which radiation losses

are considered as a perturbation to the exact adiabatic solution [70]. He obtains an implicit solution for the temperature across the shock layer, and hence also for the total temperature losses:

$$\frac{dy}{y} = \frac{\rho_\infty v_\infty dh}{4\kappa_0 \Delta\sigma T^4} \tag{3.48}$$

where y is the distance along the stagnation line and σ is the Stefan-Boltzmann constant[5], and the subscript 0 refers to stagnation conditions. Re-arranging the terms, it can be written as:

$$\frac{dy}{y} = \frac{\rho_\infty v_\infty h_0}{4\kappa_0 \Delta\sigma T_0^4} \frac{T_0^4}{T^4} \frac{c_p dT}{h_0} \tag{3.49}$$

Goulard notes that the first fraction on the right-hand side of that equation is a dimensionless number that contains all the boundary conditions of the problem studied[6]. It can be interpreted as such: the numerator is the flux of total energy entering through the shock, and the denominator is the flux of energy radiated by the shock under adiabatic conditions [70]:

$$\Pi_9 = \Gamma = \frac{4\kappa_0 \Delta\sigma T_0^4}{\rho_\infty v_\infty h_0} \propto \frac{\text{energy radiated}}{\text{total energy}} \tag{3.50}$$

With the development of CFD, the adiabatic heat flux q^r_{ad} can now be estimated and the Goulard number is thus better known in the literature (see for example [142, 52, 106]) under the following form:

$$\Gamma = \frac{2q^r_{\text{ad}}}{\frac{1}{2}\rho_\infty v_\infty^3} \tag{3.51}$$

with the usual assumption $h_0 \simeq v_\infty^2/2$ (equation 3.12) has been made.

The Goulard number is thus obtained through proper similitude analysis rather than dimensional analysis, as it could be thought. Nevertheless, a certain number of assumptions were necessary: incompressible shock layer in the stagnation area, etc. The most stringent one is the hypothesis of a very small shock standoff distance ($\Delta/R \simeq 1/20$).

If Γ is small, which is the case for most ballistic and orbital entry problems, the total temperature can be considered constant along the stagnation line. If Γ is large, heat loss through radiation becomes important and the radiation term has to be included in the Navier-Stokes equation for the conservation of energy.

As a rule of thumb, the limit is considered to be around $\Gamma \simeq 0.01$. It corresponds to the peak heating of Stardust, often considered as a benchmark for the Goulard number [52]. Overall, radiation coupling implies that a significant portion of the flow's internal energy is leaking in the form of radiation. This occurs for the most part in the nonequilibrium region immediately downstream of the shock. Part of that radiation is thus reabsorbed further downstream of the shock, i.e. in the shock

[5]Interestingly, we have at this stage used all the fundamental constants of moderns physics. The Stefan-Boltzmann constant can be retrieved from the constants we had already used: $\sigma = 2\pi^5 k_b^4/15h^3c^2$.

[6]He actually recognized it, writing that *"its role in radiant dynamics has already been recognized in their application to the problems of stellar turbulence and radiant heat exchange."* [70]

layer, the boundary layer, or even possibly by the wall. However, radiation being isotropic, a certain fraction of it is lost to the free-stream. In other words, the total enthalpy in the shock layer is reduced. This further affect other macroscopic features of the flow, which will be discussed in section 4.2.

In equation 3.50, the stagnation temperature can be related to the stagnation enthalpy through $c_p T_0 \simeq h_0$. Therefore, one can express the Goulard number as:

$$\Gamma \simeq \frac{\sigma}{2} \frac{\kappa_{\rho,0}}{c_p^4} \frac{\rho_0 \Delta v_\infty^5}{\rho_\infty} \tag{3.52}$$

The first term on the right-hand side is a universal constant. The second term is a property of the gas and solely depends on its temperature (and mixture, in case of nonequilibrium). The numerator of the last term is conserved through binary scaling, since we demonstrated in section 3.2.4 that any density representative of the flow could be used as scaling parameter. The last term remaining is thus ρ_∞, which is consistent with what was observed in equation 3.47. It follows that, within a family of binary scaled flows, the Goulard number (i.e. the radiative coupling) will reduce with the characteristic length-scale. If the original flow is strongly coupled, the results obtained in laboratory will thus not be representative of flight.

3.4 Off-stagnation region

Lastly, let us briefly discuss how binary scaling affects the rest of the flow. In section 2.4.2, we obtained that the product ρv is constant across the shock. While this is true for a normal shock, away from the stagnation line the shock becomes increasingly oblique and weaker, eventually becoming a Mach wave at large distances from the body. This curvature deflects the post-shock velocity vector. The post-shock ρv product is then obtained as a function of the shock angle ζ and deflection angle ι as:

$$\rho v = \rho_\infty v_\infty \frac{\sin(\zeta)}{\sin(\iota)} \tag{3.53}$$

Numerous authors have demonstrated in their work that the shock shape is a function of the free-stream Mach number (see for example [14]. Assuming perfect gas, the deflection angle depends on the shock angle and free-stream Mach number through the following relation, referred to in the literature with a different nomenclature as the $\theta - \beta - \mathrm{M}$ equation:

$$\tan(\iota) = 2 \tan^{-1}(\zeta) \frac{\mathrm{M}_\infty^2 \sin^2(\zeta) - 1}{\mathrm{M}_\infty^2 \left(\gamma + \cos(2\zeta)\right) + 2} \tag{3.54}$$

In the limit of a very large free-stream Mach number, it becomes:

$$\tan(\iota) = 2 \frac{\sin(\zeta)\cos(\zeta)}{\left(\gamma + \cos(2\zeta)\right)} \tag{3.55}$$

From which we infer that $\zeta > \iota$. Therefore, $\rho v > \rho_\infty v_\infty$.

The density ratio is expressed as:

$$\frac{\rho}{\rho_\infty} = \frac{(\gamma+1)\,\mathrm{M}_\infty^2 \sin^2(\zeta)}{(\gamma-1)\,\mathrm{M}_\infty^2 \sin^2(\zeta)+2} \tag{3.56}$$

In the limit of a very large free-stream Mach number, it becomes:

$$\frac{\rho}{\rho_\infty} = \frac{\gamma+1}{\gamma-1} \tag{3.57}$$

which is the same expression as for a normal shock. The post-shock velocity gets thus smaller and smaller as the curvature of the shock increases. It is thus only the post-shock velocity that is affected by the curvature of the shock, gradually increasing as it gets away from the stagnation line until it reaches the value of the free-stream.

Because the free-stream Mach number is a similarity parameters within a family of binary scaled flows, the post-shock velocity is appropriately duplicated regardless of the curvature of the shock. However, the Mach number will gradually increase away from the stagnation line. From equation 3.19, the resulting compressibility effects will further influence the shock layer. The latter reads in the following form:

$$\frac{d\rho}{\rho} = \mathrm{M}_{\mathrm{fr}} \frac{du}{u} \tag{3.58}$$

which is, in itself, nondimensional and thus conserved through the application of binary scaling.

Based on these preliminary considerations, and given that all the similarity parameters are duplicated downstream of the shock (section 2.4.4), one can consider that the preceding developments can be extended beyond the stagnation point.

However, non-binary chemistry has is likely to degrade the proper duplication of the flow. Let us follow the flow along a streamline that crosses the shock in the vicinity of the stagnation line, i.e. where it is almost normal. It will first experience an increase in temperature and pressure similar to that of the flow along the stagnation line, and thus also similar thermochemistry. Further downstream, however, the flow cools down while the dissociation fraction remains important. Referring back to equation 3.2, both these elements play in favor of recombination, although the expansion of the flow has the opposite role (i.e. reduction in the number of collisions).

Chapter 4

Stagnation point heat fluxes under binary scaling conditions

"Although mechanical energy is indestructible, there is a universal tendency to its dissipation, which produces throughout the system a gradual augmentation and diffusion of heat, cessation of motion and exhaustion of the potential energy of the material Universe"
- Lord Kelvin, in *On the Age of the Sun's Heat* [189]

The harsh aeroheating environment to which entry probes are submitted might as well be compared to hell. Luckily, with the tool of engineering humanity is able to design them adequately so as to withstand those conditions, and deliver their payload to the ground. One of the major objective of this research is, after all and using Lord Kelvin's language, to quantify how much indestructible mechanical energy is dissipated into heat through the exhaustion of the potential energy of spacecraft exploring the Universe.

The stagnation point heat flux, in particular, is one of the main design guidelines for atmospheric entry probes. It is thus no surprise that an abundant literature describes tools and techniques to measure it, reports values of its experimental measurement, and proposes correlations to extrapolate from these measurements to flight.

As discussed in section 3.3, the heat fluxes in the flow - and hence also at the wall - are of different nature: conduction, diffusion, radiation. At the wall, equation 3.24 becomes thus:

$$q_w^t = q_w^{cd} + q_w^d + q_w^r \tag{4.1}$$

where q_w^t is the heat absorbed by the wall.

In this short chapter, we will explore how these different heat fluxes scale depending on their nature. As we will see, this is not a straightforward as one could imagine, as the total heat flux is composed of two distinctive parts that scale differently: convective on the one hand, which encompasses both conductive and diffusive, and radiative on the other. The current technique applied to

differentiate them will be briefly described, exposing some of its shortcomings. A new technique, enabled by binary scaling, will then be introduced.

This chapter serves as an theoretical basis for both chapter 5, where heat flux measurement is used to demonstrated the proper scaling of chemical diffusion, and chapter 8, where the method to perform flight extrapolation based on binary scaling is used.

4.1 Nature and scaling of the various heat fluxes

Numerous correlations can be found in literature to derive the stagnation point heat fluxes from the boundary conditions of the flow (geometric and free-stream parameters). Based on the analytical solution of the boundary layer of Lees [103] and Fay and Riddel [50], most of them are in the form of:

$$q_w \propto R^a \rho_\infty^b v_\infty^f \tag{4.2}$$

where the exponents a, b, and f depend on the type of heat flux considered and the mixture composition. For the convective heat flux, identified by the superscript c, it is usually expressed as:

$$q_w^c = K\sqrt{\frac{\rho_\infty}{R}} v_\infty^f \tag{4.3}$$

where K is a constant derived from the gas mixture. For air, Detra and Hidalgo [39] suggest to use $K = 5.16 \cdot 10^{-11}$ and $c = 3.15$, claiming the resulting accuracy is 10% for velocities up to $8\ \mathrm{km/s}$. Slightly different values can be found in literature, such as $K = 1.73 \cdot 10^{-10}$ and $c = 3$ for Sutton and Graves [181] which was later corrected into $K = 1.83 \cdot 10^{-10}$ by Tauber and Sutton [185, 184]. Let us mention that these correlations usually include a term for the enthalpy of the wall, with the free-stream velocity usually embedded in the free-stream enthalpy. The correlation of Zoby [214], for example, is expressed in its original form as:

$$q_w^c = K\sqrt{\frac{p_0}{2R}} \left(h_0 - h_w\right) \tag{4.4}$$

In equation 4.3, K and v_∞ are constant across flows from the same binary scaling family. Isolating the ρL which is also constant, one obtains that within a family of binary scaled flows the convective heat flux varies with the inverse of the characteristic length scale:

$$q_w^c = K\sqrt{\rho_\infty R}\frac{1}{R} v_\infty^f \propto \frac{1}{R} \tag{4.5}$$

Expressions for the radiative heat flux are usually more complex. A widely use correlation is based on the work of Tauber and Sutton [187], in which they propose as a general form:

$$q_w^r = K R^a \rho_\infty^b F(v_\infty) \tag{4.6}$$

where the values of the function F are tabulated and for air $a = f(\rho_\infty, v_\infty)$. Detra and Hidalgo provide a simpler correlation, expressed as:

$$q_w^r = 6.54 \cdot 10^{-27} R \rho_\infty^{1.6} v_\infty^{8.5} \tag{4.7}$$

Performing the same exercise as for equation 4.5, one obtains that the radiative heat flux scales as $q^r \propto 1/R^{0.6}$. One can already unfold one of the problems of binary scaling, since the convective and radiative heat fluxes do not scale in the same fashion. How could we then differentiate both? Let us investigate that question.

4.1.1 Convective heat flux

The conductive energy transport is defined as:

$$q_w^{cd} = -k \frac{\partial T}{\partial \widehat{y}} \tag{4.8}$$

where $\widehat{y}$ is the direction normal to the wall. In dimensionless form, it reads as:

$$q_w^{cd} = -\frac{k T_w}{L} \frac{\partial \overline{T}}{\partial \overline{y}} \tag{4.9}$$

From which it appears that the conductive heat flux scales proportionally to the inverse of the length-scale of the flow. It is thus larger in the scaled flow than in the original one.

The diffusive energy transport is defined as:

$$q_w^d = \rho \sum_{s=1}^{n} D_s h_{S,s} \frac{\partial x_s}{\partial \widehat{y}} \tag{4.10}$$

where $h_{S,s}$ is the species' sensible enthalpy (see equation 3.10). It should be noted that this formulation assumes a fully catalytic wall: all the dissociated species that reach the wall recombine there. The question of catalycity was already discussed in section 2.4.3. It results that, if the diffusive heat flux is important (i.e. if the flow is largely dissociated, diffusion important, and the surface reactive) the catalycity in the laboratory should at least be of the same order of magnitude as in flight.

Performing the same exercise as equation 4.8 reveals that the diffusive heat flux scales in the same fashion as the conductive heat flux, and thus also the convective heat flux as a whole.

Another angle of attack to that conclusion can be derived from boundary layer theory from reacting gases. Indeed, we have already presented the stagnation point heat flux relations obtained with Fay and Riddel theory [50] (equation 2.62) and Goulard [69] (equation 2.65). As we have demonstrated, for two binary scaled flows, the temperature, mixture composition, and velocity are approximately conserved in the vicinity of the stagnation line. The only variables in equations 2.62 or 2.65 that scale with the scale of the flow are the densities and velocity gradient. Under binary scaled conditions, one

can thus write for both of these relations:

$$q_w \propto \sqrt{\rho\beta} \tag{4.11}$$

For a sphere of radius R, a realistic formulation of the velocity gradient was suggested by Olivier from Newtonian theory [137]:

$$\beta_e = \frac{1}{R}\frac{\left(1+\overline{\Delta}\right)}{\overline{\Delta}}\frac{(p_e - p_{\text{fr}})}{\rho_\infty v_\infty}\frac{\rho_2}{\rho_e} \tag{4.12}$$

where the frozen conditions are those immediately downstream of the shock. The free-stream velocity v_∞ is one of the similarity parameters of binary scaling and is thus duplicated, as well as the nondimensional shock standoff distance $\overline{\Delta}$. The mixture and temperature being duplicated, the pressure difference scales in the same fashion as a density, and the dimensions of the ratio $(p_e - p_{\text{fr}})\,\rho_2/\rho_\infty\rho_e$ cancel thus out. Therefore, one can write that for hypersonic binary scaled flow $\beta_e \propto 1/R$, and equation 4.11 becomes:

$$q_w \propto \sqrt{\frac{\rho}{R}} = \frac{1}{R} \tag{4.13}$$

where we kept in mind that the product ρL is conserved through binary scaling. Other models for β_e, such as the expression proposed by Lees [103] or Truitt [195], lead to the same proportionality factor. Thus:

$$q^c_{w,\text{lab}} = \chi^{-1} q^c_w \tag{4.14}$$

where we have already defined the model scale as:

$$\chi = \frac{R_{\text{lab}}}{R} = \frac{\rho}{\rho_{\text{lab}}} < 1 \tag{4.15}$$

Equation 4.14 has been verified and used in numerous experimental campaigns (see for example [29, 30, 120]).

4.1.2 Radiative heat flux

At the wall, the radiative heat flux actually consists out of two parts: the incoming radiation from the shock layer, of which only a fraction will be absorbed depending on the material's absorbance α, and the outgoing radiation from the wall which is brought to a high temperature and depends on its emissivity ϵ:

$$q^r_w = \alpha q^r_{\text{in},w} - \epsilon\sigma T^4_w \tag{4.16}$$

where σT_w^4 is, from Plank's law, the irradiance of a black body at thermal equilibrium, and ϵ is the wall material's emissivity[1].

Furthermore, Kirchhoff's law developed for gases in section 3.3.1 (equation 3.42) can also be extended to solid to show that $\alpha_\nu = \epsilon_\nu$. Thus:

$$q_w^r = \epsilon \left(q_{\text{in},w}^r - \sigma T_w^4 \right) \tag{4.17}$$

The radiative heat flux incoming from the shock layer was obtained in equation 3.33. As discussed in section 3.3.2, it is preserved through scaling (i.e. it does not vary depending on the size of the flow):

$$q_{\text{in},w,\text{lab}}^r = q_{\text{in},w}^r \tag{4.18}$$

Moreover, emissivity is an intrinsic property of the material that depends on its temperature.

Unlike for the convective heat flux, the radiative heat flux depends not only on free-stream conditions but also on material properties. Nonetheless, another material can potentially be used for the model (i.e. in the laboratory) than for the original craft (i.e. in flight), provided that the function $\epsilon(\nu, T)$ is the wall temperature T_w is known for both.

4.1.3 Total heat flux

Finally, in the laboratory the heat flux in the material is usually only conductive. Therefore, it is also calculated using equation 4.8, where the thermal conductivity is that of the thermal protection material. One can thus write equation 4.1 as:

$$\underbrace{-k\frac{\partial T}{\partial \widehat{y}} + \rho \sum_{s=1}^{n} D_s h_{S,s} \frac{\partial x_s}{\partial \widehat{y}} + k_m \frac{\partial T_m}{\partial \widehat{y}}}_{\textit{convective heat flux, scales as } 1/R} + \underbrace{\epsilon_m \left(\int_{2\pi}^{0} \int_{\pi}^{0} I \cos\theta \sin\theta d\theta d\phi - \sigma T_w^4 \right)}_{\textit{radiative heat flux, is preserved}} = 0 \tag{4.19}$$

where the subscript m stands for the properties of the solid phase (i.e. the model), and all the terms are evaluated at the wall[2].

4.2 Radiative coupling

The causes of radiative coupling were discussed in section 3.3. However, its subsequent effect on the radiative heat flux and other macroscopic features of the flow was not commented.

The problem of radiative coupling is closely linked to that of ablation. Indeed, they both need to be addressed for high-enthalpy flows, when the surface heat fluxes are so important that ablating heat

[1] Outward radiation is beneficial as it will reduce the wall heat flux. Radiatively cooled TPS (also referred to as passively cooled) will even purposely use highly refractory materials such as reinforced carbon-carbon (RCC).

[2] Another way to look at the issue is to consider tha local heat-transfer coefficient through the Stanton number. The later is defined as: $\text{St} = q_w / \rho v \left(h_{aw} - h_w \right)$ where h_{aw} is the equilibrium enthalpy. It is preserved through binary scaling for the convective heat flux, since $q_w \propto 1/R$. For the radiative heat flux, however, within a family of binary scaled flows it scales linearly with the length-scale of the flow $\text{St} \propto R$.

shields need to be used. However, the later introduces ablation products (carboneous and hydrogenous species) in the flowfield, which further complicate the flowfield and radiation modeling.

Because engineers need solutions that will enable them to design actual spacecraft, the problem is often considered in literature as the coupling of these three fields at once: flow, radiation, ablation. Extensive research on the topic was conducted in the late sixties [6, 35, 70, 83, 209] and early seventies [42, 47, 49, 48, 55, 124, 128, 188]. These early efforts were motivated by a certain number of upcoming deep space exploration missions, including Apollo, Pioneer Venus Multiprobe (1978), and Galileo (launched in 1989). However, due to the complexity of the problem to be tackled, these studies relied on a certain number of simplifying assumptions (equilibrium viscous shock layer, etc.). Moreover, the only experimental data available came from the Fire II (1965) and Apollo 4 mission (1967).

More recent studies were enabled by advances in computational tools and more accurate experimental data, which led to a better understanding of the flow physics and more advanced modeling. That renewed interest was also motivated by the availability of flight data from the atmospheric entry of probes such as Stardust (2006) and Hayabusa (2010) for the Earth, Galileo (2003) for gas giants, and Huygens for Titan (2005). The number of publications on the topic that can be found in the literature since the last decade illustrates the renewed interest of the scientific community for these issues (see for example [67, 80, 52, 95, 118, 165, 174, 186, 210]).

The problem of radiation coupling is tackled in this section, and that of ablation coupling in section 4.3. General solutions on how to deal with these experimentally are given in section 4.4.2.

4.2.1 Non-adiabatic radiative heat flux

In section 3.3, we have discussed that for sufficiently high Goulard number, the heat lost to the freestream causes a significant reduction of the total enthalpy in the shock layer. There is thus a coupling between radiation and other macroscopic features of the flowfield. How can these be observed on the heat fluxes?

The most intuitive effect is a reduction in the stagnation point radiative flux compared to the adiabatic case, i.e. if the coupling is neglected. The dependance of the ratio between the actual radiative eating and what it would be if the flow was adiabatic q^r/q^r_{ad} and the Goulard number Γ has indeed been demonstrated numerically or used by various authors (see for example [42, 65, 80, 125, 136, 141, 155, 183, 188, 186, 210]). As depicted in figures 4.1 for different atmospheres, the function linking both (using the logarithm of Γ) can be expressed in the form of a sigmoïd: decreasing from a certain value slightly smaller than 1.0 for uncoupled flows down to another constant value for fully-coupled flows. An engineering relation usually found in literature is expressed as [188]:

$$\frac{q^r_w}{q^r_{w,\text{ad}}} = \frac{1}{1 + a\Gamma^{0.7}} \tag{4.20}$$

where the coefficient a is fitted depending on the type of atmosphere considered.

Based on numerical simulations, Tauber and Wakefield obtain $a = 3$ for $H_2 - He$ mixtures

[188] (figure 4.1 a). The band for air was obtained from calculations presented in [139]. Tauber and Wakefield further noted that the cooling is somewhat less pronounced for hydrogen-helium mixtures than for air, although the general trend is similar. The same relation was later used for air [155] and Venus [186], for which two justifications are put forward. First, there is no equivalent expression that can guarantee more precision. Second, the results thereby obtained are in close agreement with other numerical rebuilding, at least around the peak radiative heating [186]. They further note that this is no surprise, as at peak heating the emission is primarily due to atomic species and thus not as sensitive to the mixture composition [186].

Other efforts can be found literature. For example, Hollis et al. suggest to use the same $a = 3$ for Titan atmospheric entry [80], as do Palmer et al. for Mars entry due to the preponderance of CO [141]. Additional radiation coupling studies for Titan can be found in [136, 183]. Gnoffo demonstrates numerically that, for Mars entry, the relation of Tauber and Wakefield provides satisfactory results over the forebody but not over the afterbody due to non-local radiative cooling [65]. Wright et al. mention that a coefficient $a \simeq 3.45$ was shown to provide reasonable results for air, although they do not mention their source [210].

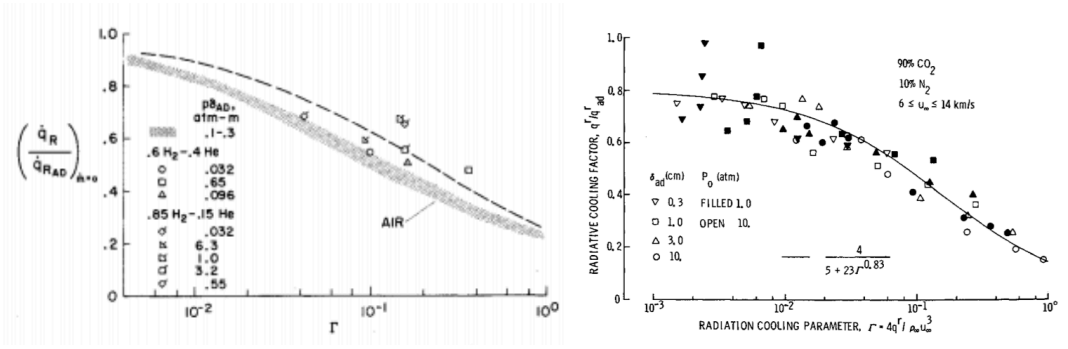

(a) (b)

Figure 4.1: *Calculated radiative cooling at stagnation point for Earth and gas giants (a) [188] and for Venus (b) [42] Notice that the deviation from the adiabatic case does indeed become non-negligible for* $\Gamma > 0.01$.

Another expression, slightly different from equation 4.20, was suggested by Edquist [42] for the venusian atmosphere (figure 4.1 b):

$$\frac{q_w^r}{q_{w,\text{ad}}^r} = \frac{4}{5 + 23 \cdot \Gamma^{0.83}} \tag{4.21}$$

For the adiabatic solution, Edquist first solved the inviscid flowfield with an inverse blunt body solution coupled with the method of characteristics so as to obtain the shock layer thickness and the thermodynamic variables [88]. This first step was done assuming a mixture of pure CO_2 in equilibrium, and the rest was done with the widely used $97 - 3\%\ CO_2 - N_2$ mixture. A boundary layer was then computed on top of that inviscid solution. Lastly, the radiative heat flux was obtained from an isothermal slab using the method of Nicolet [131].

The coupled solutions were obtained from Page and Woodward [140] for a $90 - 10\%\ CO_2 - N_2$ mixture. The gas is considered viscous, heat-conducting, emitting and absorbing, and in local

thermodynamic equilibrium. The radiation of the gas was modeled with a simple nongrey model consisting of six bands: one for the visible continuum, one for the infrared lines and CN violet, two for CO, a peak for the vacuum ultraviolet lines, and a last block for the vacuum ultraviolet continuum [140].

Mirskii suggests a slightly different relation of the form:

$$\frac{q_w^r}{q_{w,\text{ad}}^r} = \frac{a}{\Gamma^b} \tag{4.22}$$

where the coefficients are $a = 0.222$ and $b = 0.47$ for air and $a = 0.372$ and $b = 0.31$ for Mars [125]. Obviously, it only applies to coupled flows.

4.2.2 Other features

That reduction of the enthalpy in the shock layer results in a lower average temperature. In turn, this results larger density and thus a thinner shock standoff (equation 3.15). Let us also mention that the free-stream conditions upstream of the shock might be impacted by precursor photochemistry. In particular, photoionization and photodissociation may result in a significant thermal nonequilibrium and a non-negligible concentration of free electrons upstream.

The subsequent effect of radiative coupling on the convective heat flux is not as evident. Indeed, the conductive heat flux is driven by two competing effects: radiation absorption in the boundary layer and radiative cooling in the equilibrium layer temperature, both of which have different effects on the temperature gradient at the surface (4.8). Moreover, the smaller enthalpy will also induce a shift in the concentration of dissociated species, thus affecting the diffusive heat flux.

Nevertheless, an equivalent to figure 4.1 was developed for the convective heat flux, based on the results of numerical studies for air [6, 67, 95, 165, 174] and for Titan [210]. A least-square optimization was then performed on those datapoints to obtain an expression similar to that of Tauber presented in equation 4.20, where the exponent is also used as a variable. It resulted in the following expression:

$$\frac{q_w^c}{q_{w,\text{ad}}^c} = \frac{1}{1 + 0.98\Gamma^{0.73}} \tag{4.23}$$

The datapoints and their interpolation are presented in figure 4.2.

While the agreement is not perfect, it is nevertheless of the same order as what is obtained with other correlations for the radiative heat flux presented in figure 4.1. This implies that radiation coupling is likely to reduces the temperature gradient at the surface, and thus also the convective heating. Moreover, the exponent of Γ is almost the same to what is suggested by Tauber (equation 4.21) and Edquist (equation 4.20) while its coefficient (i.e. a in equation 4.21) is much smaller. Thus, the convective heat flux is less sensitive than the radiative heat flux to an increase in Γ.

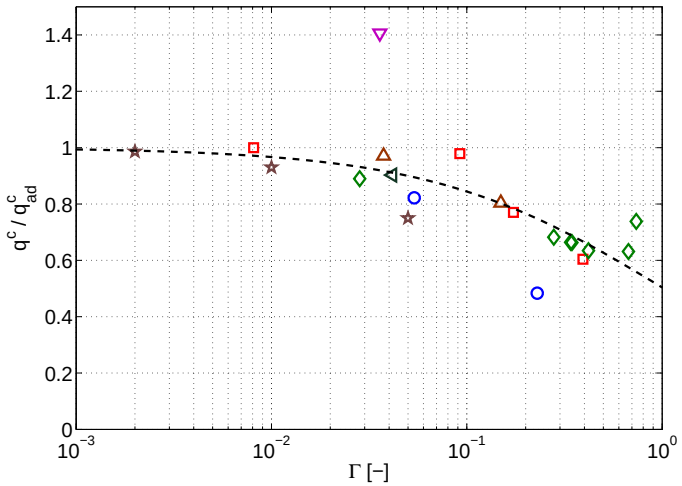

Figure 4.2: *Effect of the non-adiabaticity of the convective heat flux using numerical results from [70] (stars), [6] (circles), [67] (squares), [210] (diamonds), [95] (triangles pointing to the right), [165] (triangle pointing downwards), [174] (triangles pointing upwards). The dashed line correspond to the interpolation presented in equation 4.23.*

4.3 Ablation coupling

While ablation is out of the scope of the present study, we will briefly mention some of the effects it has on binary scaling.

The different types of thermal protection system (TPS) that have been used in the history of space-flight can be classified in two main categories: re-usable and ablative heat shields. At the velocities relevant for the application of binary scaling, and with the current technical know-how, ablation is often the preferred solution.

Two chemical processes are distinguished when an ablative material is exposed to heat. First, its outer surface chars, melts, and sublimes. The products of these reactions are gases such as O_2, N_2, O, N and OH. Second, the bulk of the material undergoes pyrolysis (anaerobic thermal decomposition), which creates gases such as CO, CH_4, H_2, etc. Most of the chemical reactions occurring are endothermic, and absorb thus an appreciable part of the heat transferred to the material. The gaseous products are blown away from the material's surface into the boundary layer, effectively lifting the shock layer. Furthermore, the carbon contained in the pyrolysis gases absorbs the radiation thus creating an optically opaque layer (i.e. an effect referred to as *blockage*).

The processes occurring in the material are governed both by a coupling between chemical reactions and transport of heat, mass, momentum, and chemical species.

Let us use a simple ideal model for the porous ablative material: an arrangement of non-overlapping cylinders (fibers) of radius R_f characterized by a macroscopic porosity ϵ. A third Damkhöler number can be defined, this time for the flow within that porous material:

$$\Pi_{10} = \mathrm{Da}_b = \frac{R_f k_w}{D_{\mathrm{ref}}\left(1-\epsilon_{\mathrm{ref}}\right)} \propto \frac{\text{chemistry}}{\text{mass diffusion}} \tag{4.24}$$

where the surface reaction k_w is as defined in equation 2.60 and the subscript ref refers to a reference value. This Damkhöler of the bulk is similar to that of the wall (equation 2.61), since both are heterogenous.

There are, however, two differences. First, the characteristic length-scale for Da_b is the radius of the fibers R_f, while it was a length-scale of the flow such as the boundary layer thickness δ or shock standoff Δ for Da_w. Second, there is a term to account for the porosity of the material. Since they are properties of the material, both the fiber radius and the porosity will be the same in flight as in the laboratory. Therefore, within a family of binary scaled flows Da_b will scale as the inverse of the length-scale of the flow $\mathrm{Da}_b \propto 1/L$.

What are the implications for the other macroscopic features of the flow? Based on the simplifying model we described earlier, Vignoles defines [204]:

$$\delta_a = \frac{3\sqrt{10}}{4} R_f \mathrm{Da}_b^{-1/2} \tag{4.25}$$

$$v_r = \frac{\sqrt{10}}{15} \frac{C}{1-\epsilon_{\text{ref}}} k_w \mathrm{Da}_b^{-1/2} \tag{4.26}$$

$$k_{\text{eff}} = \frac{1}{2\sqrt{10}} k_w \mathrm{Da}_b^{-1/2} \tag{4.27}$$

where δ_a is the ablation depth, v_r the recession velocity, C the condensation ratio (i.e. the ratio between the concentration of gas and that of solid) and k_{eff} the effective reactivity at the wall (i.e. a more appropriate definition for equation 2.61 for a porous wall). Under binary scaled conditions, all of these are proportional to the square root of the length-scale of the flow $\propto \sqrt{L}$.

The ablation depth being relatively thinner in the laboratory than in flight, one can thus also expect that the boundary layer would be poorer in the laboratory compared to flight, and thus that the blockage effect would not be as strong.

Moreover, we have mentioned earlier that under binary scaling conditions the different time-scales of the flow evolve as its length-scale (equation 2.52 and 2.61). In comparison, the time-scale for recession is thus proportional to $\propto L/\sqrt{L} = \sqrt{L}$, i.e. shorter. The recession velocity is thus not slowing down the flow establishment time.

Lastly, the effective reaction rate has an influence on the Damkhöler number of the wall. Referring back to definition in equation 2.61, we have:

$$\mathrm{Da}_w = \frac{L}{D_w} k_{\text{eff}} \psi_w \tag{4.28}$$

where $D_w \propto 1/\rho$. From equation 4.27 we know that within a family of binary scaled flow the effective reaction rate will depend on the length-scale of the flow $k_{\text{eff}} \propto \sqrt{L}$. Therefore, one obtains that

$\mathrm{Da}_w \propto \sqrt{L}$. In other words, the chemistry at the wall is shifted towards a more reaction-controlled balance and the diffusive heat flux is thus expected to be smaller.

4.4 Practical considerations for ground-to-flight extrapolation

Two different scalings come thus into play: one for the conductive or diffusive heat flux, as described by equation 4.14, and one for the radiative heat flux, as described by equation 4.18. Both need thus to be distinguished in order to extrapolate the measurement in the laboratory to flight. On top of these, for sufficiently high Goulard number the radiation coupling has also to be accounted for.

4.4.1 Separating heat fluxes

Let us first consider the adiabatic case. One option is to measure simultaneously the radiative and total heat fluxes, thus allowing to infer the convective heat flux. That technique has been successfully applied by numerous authors, notably including B. Capra in the frame of her Ph.D. dissertation [28, 29]. The most widely used technique is based on thin film gauges protected from the flow by an optical window. While it is today the most accurate and easily implemented technique, it presents some clear disadvantages:

- First, the measurement strongly depends on the thickness of the coating applied on the sensing element, which is difficult to control.
- Second, depending on the coating and the type of material used for the optical window, some wavelengths are inevitably blocked. If these wavelengths lie in the short range (e.g. VUV or UV), the radiative heat flux will be drastically different. The VUV radiation can also be blocked if there exist a cavity between the window and the sensing element.
- Third, calibration of the probes is both complex and time-consuming.
- Fourth, optical windows resist poorly to exposure to the flow. Even if they are only mildly damaged, they require a new calibration nonetheless as their optical properties are very likely to have changed through surface degradation (change in surface properties due to exposure to harsh environment, potential coating from oil vapor, impact of solid particles, etc.). If they are severely damaged, replacement will be necessary. Because the windows are glued, this might imply that a new model has to be used altogether.
- Lastly, two sensing elements (one for the total and one for the radiative heat flux) can not be accommodated at the stagnation point of an axisymmetric probe. This implies either to use a two-dimensional equivalent, or that both heat fluxes can not be measured simultaneously.

Binary scaling offers another option that transfer the complexity from instrumentation to test flow condition design. Indeed, using equations 4.14 and 4.18 one can write:

$$q^t_{w,\mathrm{lab}} = q^c_{w,\mathrm{lab}} + q^r_{w,\mathrm{lab}} = \chi^{-1} q^c_w + q^r_w \tag{4.29}$$

where the superscript t stands for the total heat flux, which is the actual measurement. We have thus one equation with two unknowns (the scale factor χ being known). This can be solved by performing another test, at another scale, thereby providing two equations with two unknowns. The main disadvantage of that technique is that it requires to design *at least* two test conditions. However, it presents two advantages:

- First, total heat flux measurement is much simpler than radiative heat flux measurement. It can be performed with thermocouples or thin film gauges, which are well-known and widely used instruments, even for transient measurement. Thermocouples in particular are much more resilient to exposure to the flow and can be reused for several tests without requiring additional calibration.

- Second, we will see in chapter 6 that the characterization of the free-stream is a complex task, and the result is often tarnished by large uncertainties. Using more than one points allows thus to benefit from a statistical average.

4.4.2 Dealing with radiation and ablation coupling

The Goulard number scales with the length-scale of the flow (equation 3.52), i.e. radiative coupling is thus weaker in the laboratory than in flight. This comes with all the consequences discussed in section 4.2: the shock layer in the laboratory flow is hotter[3], with a thicker shock standoff, larger wall heat fluxes, and the free-stream directly upstream of the shock is less impacted by precursor photochemistry.

Two strategies can be used to deal with it. On the one hand, the heat flux measured in the laboratory on a single probe can be considered as a conservative value for the one encountered in flight. The same heat flux can then be targeted during thermal protection material testing with a laser, in a plasma wind tunnel, or in an arcjet. In this case, the safety factor imposed on the measured heat flux can be relaxed (or even dismissed altogether) since the value measured in the laboratory can already be safely considered as a maximum.

On the other hand, for a more accurate estimation, the strategy outlined in section 4.4.1 can be used in conjunction with radiation coupling models. Equation 4.29 is then written as:

$$q^t_{w,\text{lab}} = q^c_{w,\text{lab}} + q^r_{w,\text{lab}} = \chi^{-1} \left(\frac{q^c_w}{q^c_{w,\text{ad}}} \right) q^c_{w,\text{ad}} + \left(\frac{q^r_w}{q^r_{w,\text{ad}}} \right) q^r_{w,\text{ad}} \tag{4.30}$$

where the non-adiabatic ratio for the convective heat flux is given in equation 4.23 and that for the radiative heat flux in equation 4.20. The values retrieved through the experiment are then that for an adiabatic flow, and the non-adiabatic effect can be quantified using these same non-adiabatic ratio. Again, only two measurements are required. Despite the uncertainties introduced through the estimation of the Goulard number and the use of non-adiabatic models, that method will be successfully applied in section 8.

[3] In addition to the increase in temperature due to the ternary reactions, as identified in section 3.1.3

Concerning ablation, while in the laboratory the absorbed heat flux is only conductive due to the materials used to manufacture the models (e.g. aluminum, stainless steel, etc.) and because of the short time-scales involved in high-enthalpy facilities, the situation is different in flight. Two processes can be identified when ablative heat shields are heated up. On the one hand, the surface exposed to the flow chars, melts and / or sublimes. All these chemical reactions absorb heat. On the other hand, the bulk of the material is pyrolyzed and thus expels gaseous products. Again, the process of pyrolysis absorbed heat. In addition, however, the gaseous products form a cooler boundary layer which absorbs some of the radiative heat flux (a phenomenon known as blockage) and lifts away the shock layer. There is thus a coupling between ablation and the flow, with the overall result of reducing the total heat flux at the wall.

Again, two strategies can be adopted. The first one is to consider the heat flux measured in the laboratory on a non-ablative model to be a conservative approximation of that obtained in flight, as suggested for radiation coupling.

The other option try to perform a duplication as close to reality as possible and use the same thermal protection material at the same temperature. Test time being too short in high-enthalpy facility to achieve a thermal response representative of that obtained in flight, a solution is to heat the model to the required temperature electrically prior to the test. Thereby, all the material properties (γ, k_m, ϵ_m, etc.) are reproduced as well as the surface temperature T_w. That technique, known as hot wall testing, as been pioneered by F. Zander [213, 211] and is still under development (see for example [4, 130]). Some key issues still need to be addressed: achieving the correct temperature profile (i.e. temperature gradient throughout the material rather than bulk heating), developing heating techniques for non-conductive materials, or duplicating Da_b (equation 4.24).

Part II

Experimental investigations

Chapter 5

Evolution of diffusive transport in binary scaled flows

"An experiment is a question which science poses to Nature,
and a measurement is the recording of Nature's answer."

- Max Planck, in *The Meaning and Limits of Exact Science* [152]

An important result of section 2.4.2, and more particularly equation 2.53, is that diffusion processes scale appropriately through binary scaling. The intuitive idea behind the models developed in section 2.4.2 can actually be laid out in simple term. Indeed, bearing in mind that the product ρL is constant between two binary scaled flows, the mass flux evolves in proportion to their length-scale:

$$\dot{m} \propto \rho v L^2 = (\rho L)\, L = L \tag{5.1}$$

where the velocity v is duplicated through the duplication of the enthalpy. The diffusive mass flux, in turn, does also scale in proportion to the length-scale of the flow:

$$\dot{m}_d \propto \left(\frac{\rho}{L}\right) L^2 D = (\rho L)\, L = L \tag{5.2}$$

where the ratio ρ/L stands for the concentration gradient, and the diffusion coefficient is proportional to the inverse of the density $D \propto 1/\rho$, and thus to the length-scale of the flow. Therefore, the ratio of both mass fluxes $\dot{m}_d/\dot{m}$ is conserved.

This important result allows the experimentalist who uses the binary scaling to investigate flows for which diffusive transport plays an important role rather than neglecting it, as it is usually done. Up to now, this has not been a problem since high-enthalpy facilities only allow for relatively small test sections (in the order of tens of centimeters) and short test times (in the order of micro- or milliseconds). For practical reasons, experimental campaigns have thus often been limited to the measurement of macroscopic flow features (e.g. stagnation point heat flux, shock standoff distance and shock shape,

or the radiation along the stagnation line) which are only mildly affected by diffusive transport.

With recent technical developments, however, there is a new wave of interest in the study of features that were traditionally considered to be impossible to resolve in high-enthalpy facilities. Such is for example the case of ablation-radiation coupling, which can now be studied despite the short test time associated with material response, thanks to electric pre-heating, a technique pioneered by F. Zander [213, 211]. This also implies that diffusion can not be neglected anymore.

As a consequence we can, as we did in section 4.1.1, conclude that the diffusive heat flux scales in the same fashion as the conductive heat flux, and thus also as the convective heat flux as a whole. This result is the angle of attack of the experimental campaign discussed in this chapter, in which these new hypotheses regarding the diffusive mass flux are verified experimentally.

The tests are performed in a subsonic plasma wind tunnel so as to focus in a region of the flow where diffusion plays a significant role; namely the boundary layer. The first section is therefore dedicated to a discussion regarding the scaling of the heat flux in a family of subsonic binary scaled flows. The experimental set-up is then described, and the results presented. The experimental results obtained from heat flux measurements verified very well the scaling law derived from the theoretical developments.

It is shown during a discussion of these results that other effects such as non-binary chemistry have a combined impact of $5 - 10\%$ on the measured heat flux. An important by-product of these developments is the validation of binary scaling applied in subsonic facilities, which opens a new range of potential applications.

5.1 Heat flux scaling in a subsonic flow

The radiative heat flux is usually neglected in plasma wind tunnels. The questions is thus if and how the convective heat flux will scale differently depending on wether the flow is subsonic or supersonic. The case for the convective heat flux under binary scaling condition was treated in section 4.1.1. The present experiment, however, is conducted in a subsonic flow.

In that instance, β can be approximated using potential flow theory and Bernoulli equation along the stagnation line:

$$\beta_e = \frac{3}{2}\frac{v_\infty}{R} \tag{5.3}$$

The free-stream velocity v_∞ is here that in the subsonic facility, which is thus not the same as the free-stream velocity encountered in flight. None of these terms are duplicated through binary scaling. Therefore, equation 4.11 becomes, in the subsonic case:

$$q_w \propto \sqrt{\frac{\rho v_\infty}{R}} \tag{5.4}$$

That expression is similar to equation 4.13 obtained in the hypersonic case. The presence of the free-stream velocity term in the subsonic case reflects the upstream influence of the body.

Let us remember that the product ρR is constant for binary scaled flows. Therefore, similarly to how equation 4.14 was developed in the hypersonic case, one can write for subsonic flows:

$$q_w\sqrt{\frac{R}{\rho v_\infty}} = q_{w,\text{ref}}\sqrt{\frac{R_\text{ref}}{\rho_\text{ref} v_{\infty,\text{ref}}}} \quad \Rightarrow \quad \frac{q_w}{q_{w,\text{ref}}} = \chi^{-1}\left(\frac{v_\infty}{v_{\infty,\text{ref}}}\right)^{0.5} \tag{5.5}$$

Three effects can cause the measure pitot pressure to depart from the total pressure: viscous effects (Barker), heat transfer to the probe, and the reference static pressure [114]. Assuming all three are negligible, the dynamic pressure p_dyn is preferred to the free-stream velocity, as it can be measured with a greater confidence. The previous equation is thus expressed as:

$$\frac{q_w}{q_{w,\text{ref}}} = \chi^{-0.75}\left(\frac{p_\text{dyn}}{p_\text{dyn,ref}}\right)^{0.25} \tag{5.6}$$

Equations 4.14 and 5.6 can actually be expressed in a more general form as:

$$q_{w,\text{ref}} = q_w\chi^{-0.5}\left(\frac{\beta_{e,\text{ref}}}{\beta_e}\right)^{0.5} \tag{5.7}$$

This allows comparison between two flows of the same binary scaling family, regardless of whether they are sub-, super-, or hypersonic. The velocity gradient β_e can be estimated with the most appropriate model or with CFD simulations.

5.2 Test set-up

Equation 5.6 was verified experimentally in a subsonic continuous facility, the Plasmatron, an Inductive Coupled Plasma (ICP) wind tunnel installed at the VKI. More information about the facility and its operation can be found in literature (see for example [17, 32]).

The adequacy of the scaling is judged by comparing the heat flux measured at the stagnation of two probes submitted to flows of the same free-stream enthalpy h_∞ but scaled density ρ_∞. The probes are two copper water-cooled half-spheres of different size. The small one has a radius of $30\ \text{mm}$ (referred to as the 'small' probe) and the large one $115\ \text{mm}$ ('large'). Both of them are equipped with copper calorimeters, $14\ \text{mm}$ diameter of sensing area A, placed in the centre of the front surface and thereby allowing cold wall heat flux measurement at the stagnation point. The heat flux is determined by the water mass flow, controlled by a calibrated calorimeter, and the temperature difference between the entering and exiting water:

$$q_w = \frac{\dot{m}c_p\left(T_\text{out} - T_\text{in}\right)}{A} \tag{5.8}$$

The uncertainty on the heat flux measurement for normal conditions of use, as applied within the present research, is between 7 and 12% [143].

Only the heat fluxes q_w and the static pressure p_{stat} were measured during the experimental campaign. This does not allow direct access to the control parameters, namely the enthalpy h_∞ and density ρ, and p_{dyn}, on which the scaling depends. The current practice for the Plasmatron is to measure the total pressure experimentally, from which the dynamic pressure is then inferred. The enthalpy and density are retrieved based on numerical rebuilding of the test flow. There exist an extensive database of flow conditions, that cover a vast portion of the operating range of the Plasmatron (see for example [143]). The quantities of interest were thus expressed in the form of polynomial interpolations on past experimental data, ensuring that the discrepancy between the measured and interpolated values remained below 10%. The control parameters were a reference heat flux and the static pressure, such that $f\left(h_\infty, \rho\right) = q_w, p_{\text{stat}}$, and the dynamic pressure was retrieved from those measured quantities $f\left(q_w, p_{\text{stat}}\right) = p_{\text{dyn}}$.

The small probe was chosen as a reference for the heat flux measurements. Its smaller radius implies a larger velocity gradient, and thus also a larger heat flux when submitted to the same flow conditions, allowing for a greater accuracy when targeting a certain heat flux.

A typical heat flux measurement presents itself as depicted in figure 5.1. The air mass flow was fixed at the start of each run. Once the static pressure was adjusted to the desired value, the small probe was injected and the generator power was adjusted until the measured heat flux reached the target value. The probe was left in the test section for an additional ~ 10 s to ensure that the flow is stabilized, after which the large probe is injected. Once the flow is in steady-state conditions, the probe is left in the test section for ~ 30 s, which consists the actual heat flux measurement.

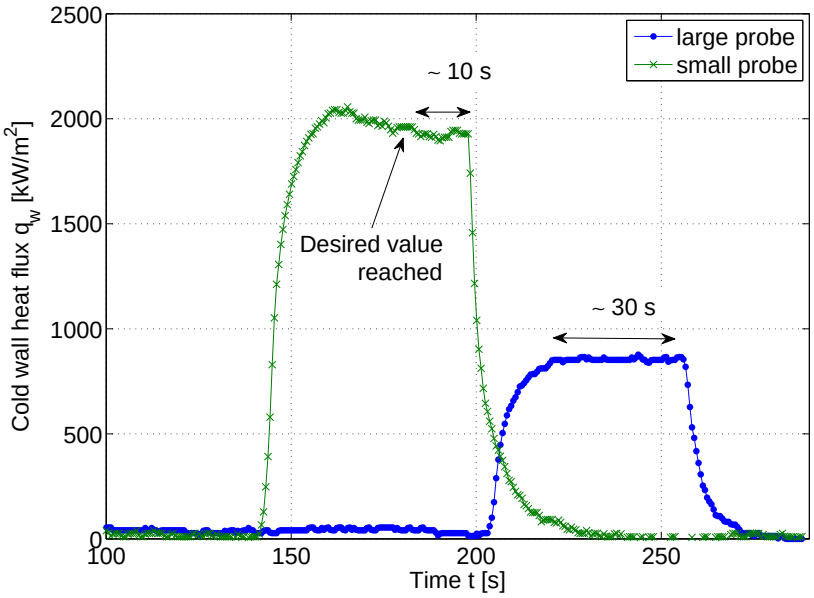

Figure 5.1: *Typical trace for a heat flux measurement.*

5.3 Experimental results

An overall representation of all the data points measured during the test campaign and what is predicted by the subsonic to subsonic binary stagnation point heat flux scaling developed in equation 5.6 is shown in figure 5.2. The raw experimental results are available in appendix H. The heat flux ratio was multiplied by the equilibrium pressure and temperature correction factors $\Pi_i G_{i,\text{ref}}/G_i$, that will be developed in section 5.4. It includes a term for the difference in dissociation mass fraction, a second one for the Prandtl number, and a last one for the viscosity, the total effect being smaller than 6% over all flow conditions that were tested. The overall agreement is good, although the scaled values are all smaller than the measured ones.

The uncertainty on the heat flux and dynamic pressure ratios were obtained as:

$$\frac{q_w}{q_{w,\text{ref}}} = \frac{\widehat{q}_w}{\widehat{q}_{w,\text{ref}}} \pm 0.2\frac{\widehat{q}_w}{\widehat{q}_{w,\text{ref}}} \tag{5.9}$$

$$\left(\frac{p_{\text{dyn}}}{p_{\text{dyn,ref}}}\right)^{0.25} = \left(\frac{\widehat{p}_{\text{dyn}}}{\widehat{p}_{\text{dyn,ref}}}\right)^{0.25} \pm 0.05\frac{\widehat{p}_{\text{dyn}}}{\widehat{p}_{\text{dyn,ref}}} \tag{5.10}$$

where the term on the left-hand side stands for the measured value, and the hatted terms stands for the actual value. According to what was outlined in the previous sub-section, a nominal value of 10% was used for the uncertainty on the measurement of dynamic pressure and heat flux.

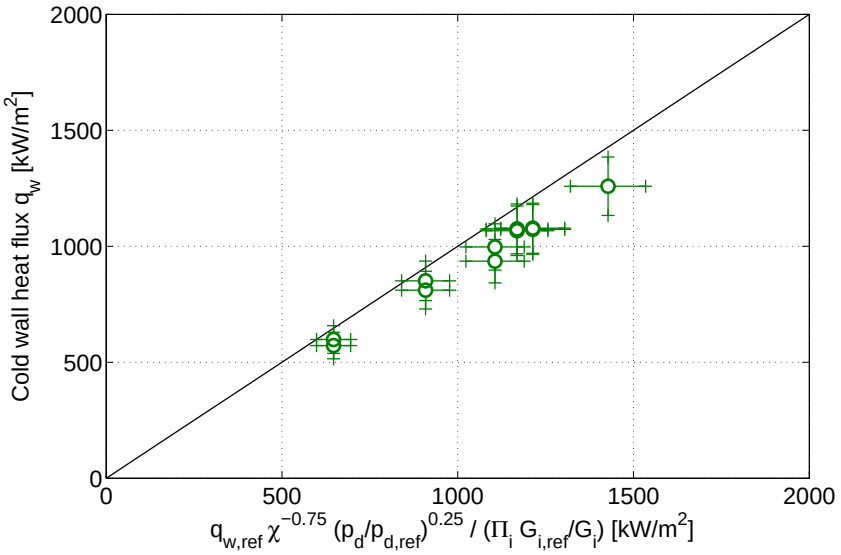

Figure 5.2: *Agreement between the heat flux measured at the stagnation point of the large probe and its predicted value based on the measurements obtained for the small probe and the scaling law developed in equation 5.6. The heat flux ratio was multiplied by the equilibrium pressure and temperature correction factors $\Pi_i G_{i,ref}/G_i$, although this results in changes no larger than 5%. The agreement between the experimental point and the theoretical relation is good.*

5.4 Discussion

In order to determine whether there was a change in agreement depending on the flow condition, the data points were plotted for a fixed reference density $\rho_{\text{ref}} = 4.00\ \text{g/m}^3$ while the enthalpy is changed (figure 5.3 a), and for a fixed enthalpy $h_\infty = 35\ \text{MJ/kg}$ while the reference density is changed (figure 5.3 b). The agreement quality was here expressed in terms of κ in order to be able to plot the result on a two dimensional figure. It is defined as:

$$\kappa = \chi^{-0.75} \frac{q_{w,\text{ref}}}{q_w} \left(\frac{p_{\text{dyn}}}{p_{\text{dyn,ref}}} \right)^{0.25} \tag{5.11}$$

A total of 7 data points were obtained in both cases, and they are all in good agreement for the ideal case of $\kappa = 1$ within the uncertainty. There is no visible correlation of the scaling quality with h_∞ or ρ_{ref}.

Although the overestimation of κ falls within the experimental uncertainty, it is interesting to explore the other possible sources of the change in density and improper duplication of temperature and composition, as identified in section 3.1.2. Three groups that could contribute to the error were identified in equation 2.62. The first group accounts for the diffusion of dissociated species to the wall. It is expressed as:

$$G_1 = \sum_{s=1}^{n} \left[1 + \left(Le_s^{0.52} - 1 \right) \frac{h_{d,s,e}}{h_e} \right] \tag{5.12}$$

where the subscript s stands for the dissociated species only. For this particular case $n = 2$ and the species are atomic oxygen and nitrogen. The Lewis number requires a definition of the diffusion coefficient, which is obtained using equation 2.46.

The second group accounts for the Prandtl number and is simply expressed as $G_2 = Pr^{-0.6}$ and the third group is linked to the viscosity $G_3 = \mu^5$. With the exception of the diffusion coefficient, all the flow parameters were obtained with CEA.

The effect of the correction brought by each of those terms is depicted in figure 5.4 (a) (and is included in figure 5.2). All of them result in an overestimation of the κ. The viscosity has the strongest effect, only comparable in magnitude with the Lewis number at high enthalpy. The total effect, however, remains smaller than 6% for the flow conditions considered here.

Another important source of error that was not accounted for is the incorrect duplication of ρ_∞. Targeting the correct heat flux and pressure is a complex operation, and result in small discrepancies between the desired and actual density. From equation 2.62, these are accounted for through the ratio $\sqrt{\rho_{\text{ref}}/\rho}$. It was depicted in figure 5.4 (b) . It has a similar magnitude as the total product of the groups depicted in figure 5.4 (a) , and also results in an overestimation of κ. Their combined effect is around $5 - 10\%$. That overall correction on Fay and Riddel was also added to figures 5.3. The agreement between the data points and that curve is excellent.

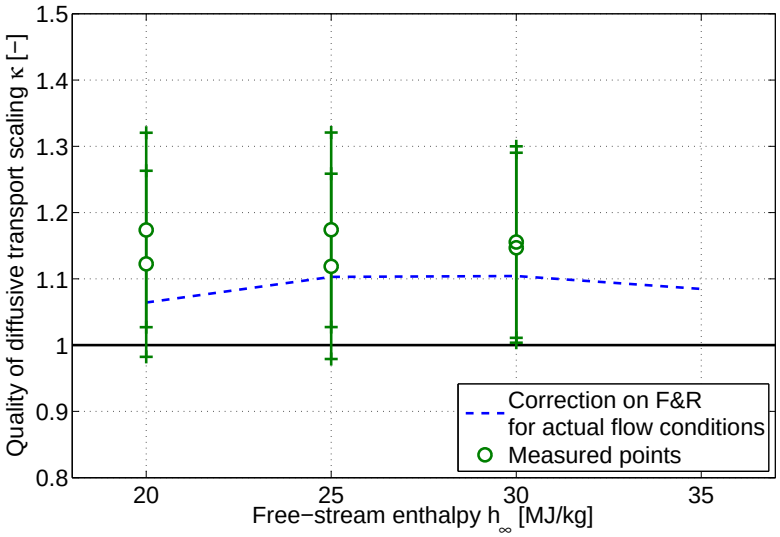

(a)

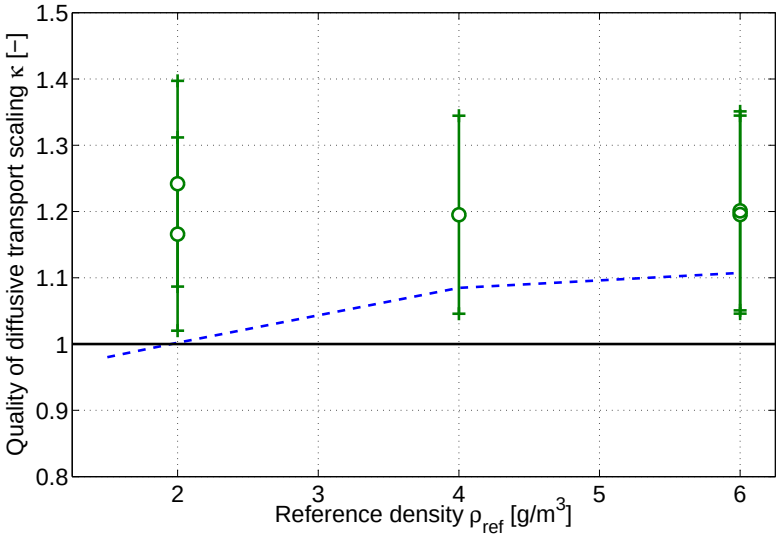

(b)

Figure 5.3: *Comparison between the ratio κ as measured in the facility (red circles) and what it should theoretically be when correcting for temperature and density (blue dashed curve, see figure 5.4 (b)). The results are depicted for a range of enthalpies and a reference free-stream density of* $4.00\ \mathrm{g/m^3}$ *(7 data points in (a), two measurements were obtained at* $30\ \mathrm{MJ/kg}$*), and for a range of reference density and a free-stream enthalpy of* $35\ \mathrm{MJ/kg}$ *(6 data points in (b), two measurements were obtained at* $6.00\ \mathrm{g/m^3}$*).*

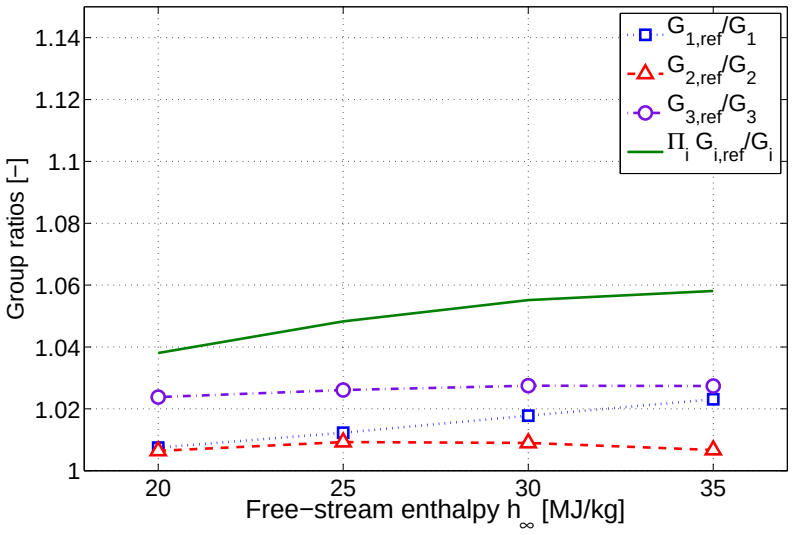

(a)

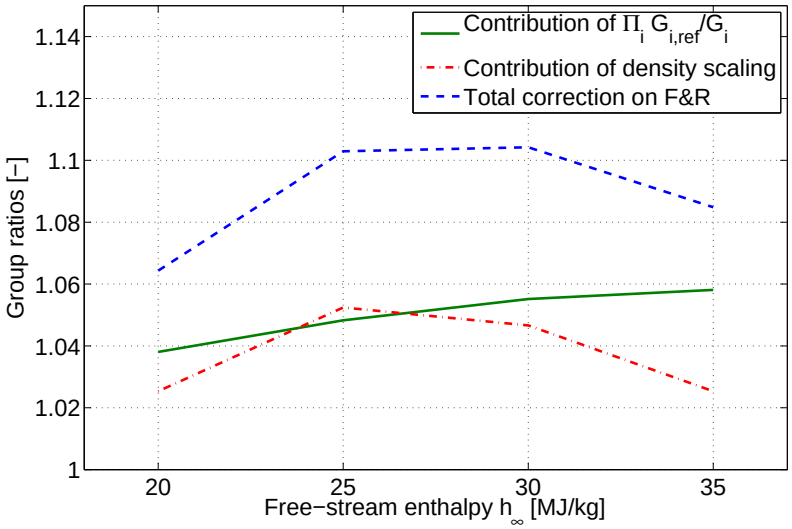

(b)

Figure 5.4: *Figure (a) depicts the ratios of the groups involved in Fay & Riddel's relation for the stagnation point heat flux (equation 2.62). All of them result in an overestimation of κ. The viscosity has the stronger effect, only comparable in magnitude with the Lewis number at high enthalpy. In figure (b), the total effect is put in perspective with the correction due to density. Both are of the same magnitude. Their combined effect result in an error slightly larger than* 10%.

5.5 Conclusion

The stagnation point heat flux scaling to apply between two binary scaled subsonic flows was developed in equation 5.6. The only additional flow parameters it requires compared to the hypersonic version is the dynamic pressure, which is usually easy to measure. If enough resources are available, the velocity gradient can also be directly estimated with CFD.

This scaling technique was validated during an experimental campaign and the agreement between theoretical scaling and measurements is good. Two possible sources of errors were identified. First, the difference of flow properties between two binary scaled flows (pressure, which is expected, but also temperature and mixture composition). Second, the discrepancy that can exist between the density ratio and geometrical ratio, due to the difficulty to control density in high enthalpy facilities, and resulting in an improper duplication of ρL. Both sources were quantified as having a similar effect, resulting in discrepancies in the order of 5% each. Once they were taken into account, the agreement between theory and measurements was excellent.

In addition to proving the proper scaling of diffusive transport, this also validates the application of binary scaling in subsonic high enthalpy facilities. The approach provides a new way to create partial similarity between flight and laboratory, thereby extending the range of application of such facilities. For example, a low pressure test flow could be replaced by a high pressure one more likely to fulfill the LTE requirement. Flight conditions for which the pressure is higher than the maximum operating pressure of a facility can still be obtained by increasing the model size.

Chapter 6

Design of test conditions for the X2 superorbital expansion tube

"Nightflight to Venus
Way out there in space
Nightflight to Venus
Our new fav'rite place"

- Boney M., in *Nightflight to Venus*

One of the major conclusion obtained in chapter 3, and more specifically in section 3.3, was that radiation coupling is a strong function of the length-scale of the flow. Given the complexity of radiatively coupled shock layers, it was decided to explore that effect experimentally rather than numerically. Moreover, an experimental campaign present four additional benefits:

1. Studying binary scaling in the environment where it is used, namely a laboratory. A similar study performed through numerical simulations would only be as good as the models used, and might thus lead to partially correct or even erroneous conclusions. Moreover, in this particular case we are interested in strongly coupled radiating flows, which are just at the limit of what can be done numerically.

2. Setting up a strategy to design multiple test conditions at different scales representative of a single flight condition. As it was already demonstrated for heat fluxes in section 4.4 and will be later confirmed for other features of the flow, this is central in order to perform accurate ground-to-flight extrapolation.

3. Creating a new set (i.e. database) of test conditions that can be later used by other researchers. In this particular case, we designed strongly coupled $CO_2 - N_2$ mixtures which can be (and have already been) reused by other researchers.

4. Obtaining information not only about binary scaling but also about the physics of a particular type of planetary entry, in this case Venus. As explained in appendix E, Venus is an interesting target for future planetary exploration missions for many reasons including exobiology and

climatology. Nevertheless, Venus atmospheric entry is complex and does not benefit from an important heritage in terms of scientific research.

The wind tunnel in which the test campaign will take place and the test condition design process are first explained, going through the numerical and experimental steps required to obtain an accurate picture of the flow conditions the closest to the target ones. The final flow conditions are then analyzed.

The strategy is then applied to the present binary scaling study. The target flow is defined as one representative for Venus atmospheric entry. It presents the advantage of being at very high enthalpy in a mixture having a low dissociation energy. The possibility of using the facility as an non-reflected shock tube is also briefly discussed in appendix G.

The models used for the experimental campaign are then described. These are three cylinders with an appropriate scale factor. Their respective radii have been chosen so as to ensure a constant density length product ρL for all three conditions.

6.1 The X2 super-orbital expansion tube

One of the major facilities at the Centre for Hypersonics at the University of Queensland is the X2 super-orbital expansion tube. An idealized schematic and time-distance diagram of its operations is shown in figure 6.1. The theoretical grounds on which expansion tubes are built were laid by Trimpi [194]. However, for a more up to date understanding of expansion tubes and for a specific presentation of the X2 facility, the reader is invited to refer to [62].

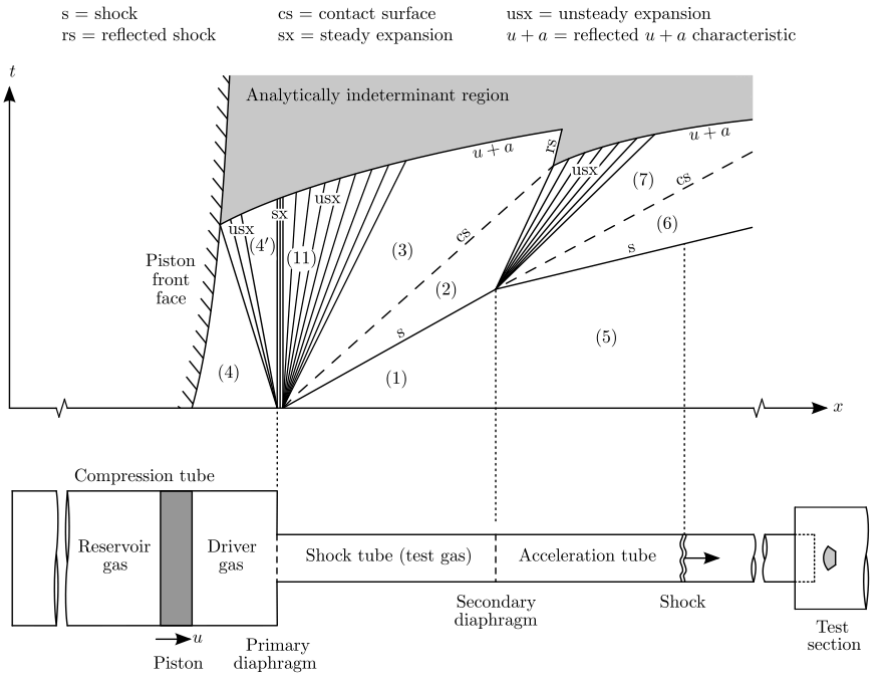

Figure 6.1: *Schematic operations of expansion tubes. Diagram extracted from [62].*

6.1.1 Idealized analytical approach

In this section, we consider perform an idealized analytical analysis of the expansion tube operations. The major hypothesis that enable such as simplified approach are: the flow is calorically perfect and inviscid, the diaphragm rupture is instantaneous, and the diaphragms are massless.

Schematically, the facility consists out of five main parts, going downstream: a reservoir, a piston, a compression tube, a shock tube, an acceleration tube, and a test section. Initially, the piston is maintained in place at the upstream end of the compression tube with a pump creating a vacuum in a cavity on its upstream face. A primary diaphragm, usually a thick sheet of steel, separate the compression tube from the shock tube. A secondary diaphragm, a thin sheet of aluminum or mylar, separates the shock tube from the acceleration tube. The reservoir is filled with high pressure air. The compression tube (between the piston and the primary diaphragm) is filled at low pressure with a light gas such as helium. The shock tube is filled with the test gas at the desired pressure. The acceleration tube is pumped down, usually at a pressure lower than that of the test gas in the shock tube. Finally, the model is placed in the test section.

The operation starts with the release of the piston, performed by connecting directly the cavity to the reservoir. The difference of pressure between the reservoir and the compression tube causes the piston to accelerate, thereby compressing the driver gas. Eventually, the driver gas pressure becomes larger than the reservoir pressure, causing the piston to decelerate. Nevertheless, the piston's kinetic energy is sufficient to bring the driver gas to a pressure considerably larger than the initial reservoir gas pressure. The free-piston driver method has been pioneered by Stalker [175, 176].

Once a certain pre-determined driver gas pressure is attained, the primary diaphragm ruptures, causing a great pressure difference between the driver gas and the test gas resting in the shock tube. This generates a normal shock wave that travels into the shock tube, and an unsteady expansion in the approximately stagnant driver gas, causing it to rush into the area change. The area change being large, one can consider as a first approximation that the stagnation properties of the driver gas remain unchanged through its expansion [126]. Therefore:

$$T_4 \simeq T_{4'} \simeq T^0_{4'} \tag{6.1}$$

The expanded driver gas $4'$ is then steadily expanded as it goes through the area change to the shock tube (region 11 in figure 6.1). Ideally, this is an isentropic processes and the Mach relation applies:

$$\frac{T^0_{11}}{T_{11}} = 1 + \frac{\gamma_{11} - 1}{2}\mathrm{M}^2_{11} \tag{6.2}$$

The flow across the throat being sonic $\mathrm{M}_{11} = 1$ and the stagnation properties being constant across the expansion begin $T^0_{11} = T^0_{4'}$. Assuming perfect gas $\gamma_4 = \gamma_{11}$ and using the approximation stated in

equation 6.1, the former equation becomes:

$$T_{11} = \frac{2T_4}{\gamma_4 + 1} \tag{6.3}$$

And therefore:

$$a_{11} = \sqrt{\gamma_{11} R_{11} T_{11}} = \sqrt{2\frac{\gamma_4 R_4 T_4}{\gamma_4 + 1}} = a_4 \sqrt{\frac{2}{\gamma_4 + 1}} \tag{6.4}$$

where the temperature of the driver gas upon rupture, T_4, can be obtained from the driver's initial fill pressure and the compression ratio at rupture. Similarly, using isentropic Mach relations for the pressure ratio from 4 to 11:

$$p_{11} = p_4 \left(\frac{T_{11}}{T_4} \right)^{\frac{\gamma_4}{\gamma_4 - 1}} = p_4 \left(\frac{2}{\gamma_4 + 1} \right)^{\frac{\gamma_4}{\gamma_4 - 1}} \tag{6.5}$$

The driver gas then enters the shock tube, which is at considerably lower pressure. Therefore, it goes through a strong unsteady expansion and becomes region 3, which obeys the relation:

$$v_3 + \frac{2a_3}{\gamma_3 - 1} = v_{11} + \frac{2a_{11}}{\gamma_{11} - 1} \tag{6.6}$$

Assuming once again perfect gas $\gamma_3 = \gamma_{11} = \gamma_4$, and noting that $v_{11} = a_{11}$:

$$v_3 = \frac{a_{11}(\gamma_4 + 1) - 2a_3}{\gamma_4 - 1} \tag{6.7}$$

As for the temperature ratio:

$$T_3 = T_{11} \left(\frac{p_3}{p_{11}} \right)^{\frac{\gamma_3 - 1}{\gamma_3}} \tag{6.8}$$

Substituting equation 6.3 and 6.5, and noting that the pressure is constant across a contact surface $p_2 = p_3$:

$$T_3 = T_4 \left(\frac{p_2}{p_4} \right)^{\frac{\gamma_4 - 1}{\gamma_4}} \tag{6.9}$$

And therefore:

$$a_3 = \sqrt{\gamma_3 R_3 T_3} = \sqrt{\gamma_4 R_4 T_4} \left(\frac{p_2}{p_4} \right)^{\frac{\gamma_4 - 1}{2\gamma_4}} = a_4 \left(\frac{p_2}{p_4} \right)^{\frac{\gamma_4 - 1}{2\gamma_4}} \tag{6.10}$$

Substituting 6.4 and 6.10 into equation 6.11, it becomes:

$$v_3 = \frac{a_4}{\gamma_4 - 1} \left(\sqrt{\gamma_4 + 1} - 2 \left(\frac{p_2}{p_4} \right)^{\frac{\gamma_4 - 1}{2\gamma_4}} \right) \tag{6.11}$$

The flow velocity is also constant across the contact surface $v_2 = v_3$. The normal shock wave that travels downstream the shock tube accelerates the test gas from rest, state 1, to state 2. Therefore, using the moving normal shock relations:

$$v_2 = \frac{a_1}{\gamma_1}\left(\frac{p_2}{p_1} - 1\right)\sqrt{\frac{2\gamma_1}{(\gamma_1+1)\,p_2/p_1 + \gamma_1 - 1}} \tag{6.12}$$

And equaling equation 6.11 to 6.12:

$$\frac{a_4}{\gamma_4 - 1}\left(\sqrt{\gamma_4+1} - 2\left(\frac{p_2}{p_4}\right)^{\frac{\gamma_4-1}{2\gamma_4}}\right) = \frac{a_1}{\gamma_1}\left(\frac{p_2}{p_1} - 1\right)\sqrt{\frac{2\gamma_1}{(\gamma_1+1)\,p_2/p_1 + \gamma_1 - 1}} \tag{6.13}$$

in which the only unknown is p_2. Equation 6.13 can thus be solved numerically for p_2 and v_2 is then obtained using equation 6.12. Finally, the temperature to which the test gas is brought is computed using the normal shock relation:

$$T_2 = T_1 \frac{p_2}{p_1}\left(\frac{\dfrac{\gamma_1+1}{\gamma_1-1} + \dfrac{p_2}{p_1}}{1 + \dfrac{\gamma_1+1}{\gamma_1-1}\dfrac{p_2}{p_1}}\right) \tag{6.14}$$

Once the primary shock reaches the secondary diaphragm, it causes it to rupture. Therefore, the same process that took place in the shock tube repeats itself in the acceleration tube. However, we are not interested by the gas at rest being processed by a shock (state 6) but by the test gas experiencing an unsteady expansion (state 7).

Following the same developments we made for the shock tube, all the properties of state 6 can be computed. Since pressure and velocity remain constant across the contact surface, one can write: $p_7 = p_6$ and $v_7 = v_6$. The temperature can then be retrieved using equation 6.9 where the subscripts 3 and 4 are respectively 7 and 2. The test gas is eventually processed through a Mach 10 nozzle before reaching the test section, in order to increase the size of the core flow.

6.1.2 Unsteady expansion

The real advantage of expansion tubes is the unsteady expansion through which the test gas goes when leaving the shock tube to arrive in the acceleration tube. Indeed, Trimpi [194] noted that unsteady expansion induced a gain in total enthalpy.

For the steady expansion, he shows that:

$$dv = -\left(\frac{dh_s}{v}\right) \tag{6.15}$$

$$dh_0 = 0 \tag{6.16}$$

where h_s and h_0 are respectively the sensible and total enthalpy. These equations rule the transfer of sensible energy (heat from the test gas processed by the primary shock) in kinetic energy. A given reduction in static enthalpy dh_s induces thus a velocity increment dv in proportion to the velocity v. Thus, the velocity increment is reduced as the velocity increases. Moreover, there is no change in total enthalpy.

The situation is quite different in the case of an unsteady expansion, for which he derives:

$$dv = -\left(\frac{dh_s}{a}\right) \tag{6.17}$$

$$dh_0 = -(\mathrm{M} - 1)\, dh_s \tag{6.18}$$

The flow being supersonic, the velocity increment is larger than in the steady case since it depends on the speed of sound. Moreover, the gain in total enthalpy is proportional to the Mach number. Enthalpy increments are thus not only achievable, but they will also increase proportionally to the Mach number. This process is referred to as *enthalpy multiplication*.

6.2 Venus entry and scaling campaign

6.2.1 Objective and constraints

Investigating binary scaling requires to design flows with different free-stream density ρ_∞ and with constant free-stream enthalpy h_∞. Thereby, if the dimensions of the test model are scaled so as to keep the product $\rho_\infty L$ constant, the flows should be similar from the binary scaling point of view.

An ideal gas analytical solution of the flow processes along the tube, such as presented in section 6.1.1, reveals that the test gas properties depend on the pressure ratios across its different sections [194]. By scaling the pressure in the different sections of the tube by a factor equal to the burst ratio (see table 6.1), one can therefore retrieve the same free-stream enthalpy but a scaled pressure. In the driver, however, it is not the fill pressure that needs to be scaled but rather the burst pressure of the primary diaphragm. This is achieved by using steel plates of different thicknesses: $t = 1.2$ mm, $t = 2.0$ mm and $t = 2.5$ mm. The reservoir and driver fill conditions corresponding to each of these plates were developed by D. Gildfind during the commissioning of the new piston [62].

Additionally, best practice for the operation of the X2 expansion tube requires that the fill pressure in the shock tube p_{st} should not be lower than ~ 2 kPa to ensure the test gas slug is not too rarefied, and that of the acceleration tube p_{at} should not be lower than ~ 1 Pa otherwise the time required to pump it down becomes unreasonably long. Generally, low fill pressures cause the facility to be more sensitive to leaks, reducing the repeatability and quality of the mixture of the test gas[1]

[1] As an illustration, the shock tube fill pressure for condition with a thin primary diaphragm (thickness $t = 1.2$ mm), that will be presented in the next section, is 1800 Pa. At that pressure, and starting with a volumetric concentration of 97.00% CO_2 and 3.00% N_2, a leak rate of 1 Pa would lead after 25 minutes to a mixture of 95.76% CO_2, 4.00% N_2,

The design process started with the condition obtained with the thinest diaphragm, with a thickness of $t = 1.2$ mm, and thus also the lowest fill pressures. Based on these recommendations, the fill pressures used were $p_{\text{st}} = 2$ kPa and $p_{\text{at}} = 2$ Pa. These were then scaled for the other conditions according to the burst pressure ratio for the other plate thicknesses[2].

The second item to decided upon is which gas mixture is used. As illustrated by the title of some of the Ph.D. dissertation of students in the Centre for Hypersonics, one major research objective of the X2 facility is the duplication of high enthalpy flows in atmospheres corresponding to the Earth [28, 154], Mars [20, 154, 43], Titan [28, 20, 89], and even gas giants [78]. No research, however, as been done to study Venus atmospheric entry.

A detailed review of Venus atmospheric entry is available in appendix E. Although Venus' atmospheric composition is similar to that of Mars, the entry flow conditions are very different, as explained in section E.2.1. In addition to being a new topic of investigations for X2, Venus is a particularly interesting target to study the effect of radiation coupling on the binary scaling methodology.

From table E.2, the Pioneer Venus probes were the smallest of all the Venus atmospheric probes and are therefore the less constraining regarding ρL scaling. Moreover, accurate trajectory information is available, at least for the North and the Day probes [167], and several numerical rebuilding of the flight were performed, in particular the extensive study of Park and Ahn [149]. The trajectory of the Day probes have the shallowest angle of entry, $-25.4\,^{\circ}$. The flow conditions it encountered is therefore the easiest to reproduce and it is thus used as an objective function.

All the numerical simulations and experiments are based on a 97.00% CO_2, 3.00% N_2 volumetric concentration for the test gas. This ratio is consistent with the actual composition of Venus atmosphere (see section E.1.2). Moreover, it also corresponds to the simulations conducted by Park [149], potentially allowing for later comparison. Assuming perfect gas the volume occupied by one mole of gas is constant, regardless the nature of the gas. The volumetric concentration is thus equal to the molar concentration $V_s = c_s$. The corresponding mass concentration is obtained as:

$$x_s = \frac{M_{m,s}}{M_{m,\text{tot}}} c_s \tag{6.19}$$

and is equal to 98.07% CO_2, 1.93% N_2.

6.2.2 Fill conditions and free-stream characteristics

The final operating conditions that were obtained after numerical and experimental investigations are detailed in table 6.1. Two sets were designed; set A for moderate enthalpy and set B for high enthalpy. Set B does not include the 1.2 mm diaphragm as it would have resulted in a too rarefied flow. Table 6.2 summarizes the main experimental measurement and corresponding binary scaling parameters.

and 0.24% of other components, mainly O_2. Such a leak rate and rest time are not uncommon, and yet they lead to a substantial variation in the mixture.

[2]Different configurations were tried, including a secondary driver set-up and a rarefied tube set-up. The most interesting and straightforward results, however, were obtained with the classical expansion tube set-up, without secondary driver. A brief discussion on the opportunity of using the facility as a non-reflected shock tube is included in appendix G.

As explained in the procedure, the two quantities that were directly measured during the tests are the cone total pressure and the velocity of the shock at the end of the acceleration tube. From these, the flow enthalpy h_∞ and density ρ_∞ are deduced using numerical rebuilding through Pitot, assuming the flow is in equilibrium. Those data points are also depicted in figure 6.2.

The other quantities of interest are obtained with CEA, and are tabulated in table 6.3. The mass composition of high altitude Venus atmosphere was added as a reference. The mixture is considerably more dissociated in the laboratory flow, due to the higher temperature. Furthermore, the concentration of N_2 seems less affected than that of all the species resulting from CO_2 dissociation. This is simply explained because the $N \equiv N$ bound is the strongest, with an energy of $945\ \mathrm{kJ/mol}$. By comparison, the $C = O$ bond in CO_2 has an energy of $799\ \mathrm{kJ/mol}$, the $C = O$ bond in CO has an energy of $730\ \mathrm{kJ/mol}$, and the $O = O$ bond in O_2 has an energy of $502\ \mathrm{kJ/mol}$.

The characteristic nondimensional number for the flow are tabulated in table 6.4. The flow's Mach number is around 10 for all cases, which is the nominal design value of the nozzle. As for the Goulard number, although it is a worst case estimation for an optically thin gas, it is largely above 0.01 in all cases and the flow is thus expected to be strongly radiatively coupled. As expected from what was concluded in section 3.3.2 (equation 3.52), the Goulard number decreases as the length-scale of the flow is reduced.

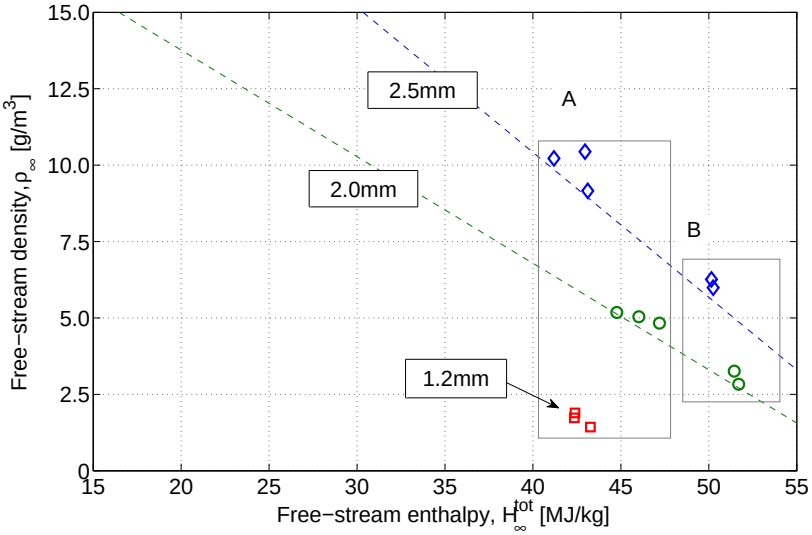

Figure 6.2: *Data points obtained during the experimental campaign; ρ_∞ vs. h_∞. The two rectangles correspond to the two sets of flow conditions. The dashed lines correspond to the flow conditions that can theoretically be achieved when varying the acceleration tube pressure while keeping the shock tube pressure at a constant value.*

In table 6.2, the sigma value on cone pressure p_{cone} and flow velocity v_{shock} only accounts for the repeatability, i.e. the dispersion from shot to shot on the value that was measured. The noise is considerably smaller than those values and was thus neglected. The dispersion is of the same magnitude as the uncertainty resulting from the measurement chain (see in appendix section F.2) and is therefore considered acceptable. Similarly, the sigma on the enthalpy h_∞ and density ρ_∞ only accounts for the repeatability from shot to shot. In this case, however, the numerical rebuilding makes

t [mm]	$p_{reservoir}$ [MPa]	p_{driver} [kPa]	p_{burst} [MPa]	$p_{burst}/p_{burst,ref}$ [%]	Set A p_{st} [kPa]	Set A p_{at} [Pa]	Set B p_{st} [kPa]	Set B p_{at} [Pa]
1.2	4.95	110.3	15.5	43.4	1.8	2	–	–
2.0	6.85	92.8	27.9	78.2	3.6	40	3.6	15
2.5	6.10	77.2	35.7	100.0	4.6	100	4.6	39

Table 6.1: *Change of operating conditions depending on primary diaphragm thickness. The driver is filled with light gas (*$100\%\ He$*), the shock tube with the test gas (*$97\%\ CO_2$ *and* $3\%\ N_2$*), and the rest of the tube with air. The diaphragm separating the shock tube from the acceleration tube is a single sheet of aluminum foil. The reservoir, driver, and burst pressures were taken from [62].*

Set	t [mm]	N [#]	p_{cone} [kPa]	v_{shock} [km/s]	h_∞ [MJ/kg]	v_e [km/s]	ρ_∞ [g/m^3]	χ [%]
A	1.2	3	10.63 ± 1.40	9.03 ± 0.05	42.67 ± 0.51	9.24 ± 0.06	1.68 ± 0.23	16.9 ± 2.6
	2.0	3	35.13 ± 0.43	9.29 ± 0.14	45.99 ± 1.21	9.59 ± 0.13	5.02 ± 0.18	50.5 ± 3.9
	2.5	3	65.89 ± 4.24	8.79 ± 0.16	42.42 ± 1.07	9.21 ± 0.12	9.94 ± 0.68	100 ± 9.7
B	2.0	2	23.49 ± 2.42	9.90 ± 0.03	51.57 ± 0.18	10.16 ± 0.02	3.04 ± 0.30	49.7 ± 5.13
	2.5	2	49.64 ± 1.28	9.87 ± 0.01	50.20 ± 0.07	9.71 ± 0.01	6.13 ± 0.19	100 ± 4.4

Table 6.2: *Measurements obtained during the Pitot survey for the operating conditions specified in tables 6.1. The first section stands for the measurements performed directly during the test campaign, with* N *standing for the number of shots performed. The second section stands for the transposition of those measurements into the working variables for binary scaling, the free-stream enthalpy and pressure, from which the flight equivalent velocity and scale factor are deduced.*

Set	t [mm]	T [K]	p [Pa]	v [km/s]	x_{N_2}	x_{NO}	x_{O_2}	x_O	x_{CO_2}	x_{CO}
					[g/kg]					
Venus		~ 200	–	–	19.3	0.0	0.0	0.0	980.7	0.0
A	1.2	2384	914	9.06	18.3	2.1	113.8	13.1	628.6	224.1
	2.0	2746	3578	9.59	17.2	4.5	167.2	47.2	384.2	379.7
	2.5	2957	8116	9.21	16.5	6.0	175.7	73.9	285.2	442.6
B	2.0	2654	2064	10.01	17.5	3.9	162.1	41.1	416.05	359.37
	2.5	2852	4729	10.02	16.8	5.3	174.1	65.0	315.3	423.5

Table 6.3: *Characteristics of the free-stream assuming equilibrium flow, based on the average enthalpy and density defined in table 6.2. The mass composition of high altitude Venus atmosphere was added as a reference. The concentration of* N_2 *is similar, while* CO_2 *is considerably more dissociated in the laboratory, due to the higher temperature.*

Set	t [mm]	Re [/m]	M [−]	Kn [m]
A	1.2	$1.9 \cdot 10^5$	11.8	$8.1 \cdot 10^{-5}$
	2.0	$5.3 \cdot 10^5$	10.6	$2.6 \cdot 10^{-5}$
	2.5	$9.5 \cdot 10^5$	9.5	$1.3 \cdot 10^{-5}$
B	2.0	$3.5 \cdot 10^5$	11.6	$4.4 \cdot 10^{-5}$
	2.5	$6.5 \cdot 10^5$	10.7	$2.2 \cdot 10^{-5}$

Table 6.4: *Main nondimensional numbers describing the flow, assuming the equilibrium conditions defined in table 6.3. All flow conditions are clearly characterized by a strong radiative coupling. The Goulard number is computed for a point* $1.5\,\mathrm{mm}$ *downstream of a normal shock in equivalent free-stream conditions, an estimation obtained with Poshax. As a reminder, the generally accepted limit for a continuum flow is Kn* < 0.01*. For example, this would impose for* $t = 1.2\mathrm{mm}$ *in set A a constraint on the length scale of the flow* $L > 8.1\mathrm{mm}$*.*

it impossible to quantify the impact of the uncertainty of the measurement chain, and it was thus not taken into account. The dispersion on the flight equivalent velocity Δv_e and on the density ratio were computed as:

$$\Delta v_e = \frac{\partial v_e}{\partial h}\Delta h = \sqrt{\frac{1}{2h}}\Delta h \tag{6.20}$$

$$\Delta\chi = \sqrt{\left(\frac{\partial\chi}{\partial\rho}\Delta\rho\right)^2 + \left(\frac{\partial\chi}{\partial\rho_{\text{ref}}}\Delta\rho_{\text{ref}}\right)^2} = \sqrt{\left(\frac{\Delta\rho}{\rho_{\text{ref}}}\right)^2 + \left(\frac{\rho}{\rho_{\text{ref}}^2}\Delta\rho_{\text{ref}}\right)^2} \tag{6.21}$$

6.2.3 Test flow quality assessment

An assessment of the quality of the test flow can be done inspecting the pressure traces and the high-speed video. The two criteria required from the test flow are a test time long enough to perform measurements, and repeatability. The signal recorded by the pressure transducer in the middle of the Pitot rake for the different shots are all plotted in figure 6.3, and stills from the high-speed video are shown in figure 6.4.

Four regions can be identified from both those figures: A is for the flow at rest, B is the pressure rise due to the acceleration tube gas, C is the actual test flow, and D the passage of the driver gas. The test flow is identified as the region between 40 and 70 µs after the photodiode records the shock arrival, 2 ms after the start of the recording time. There is thus 30 µs of usable test flow, which is a typical value for the transient measurements performed in the X2 expansion tube. The four regions start and finish at the same time for all three operating conditions, confirming the flow velocity is similar in all cases.

In figure 6.4 very little change in brightness is visible between the stills taken at 2.050 and 2.060 ms, while the flow is clearly brighter during the passage of the driver gas at 2.120 ms. The passage of the driver gas also appears to be less uniform than that of the test gas. Moreover, the flow for the 2.0 mm case is dimmer than the 2.5 mm, due to the lower pressure flow. Those crude observations will be confirmed quantitatively when inspecting the brightness of the shock layer.

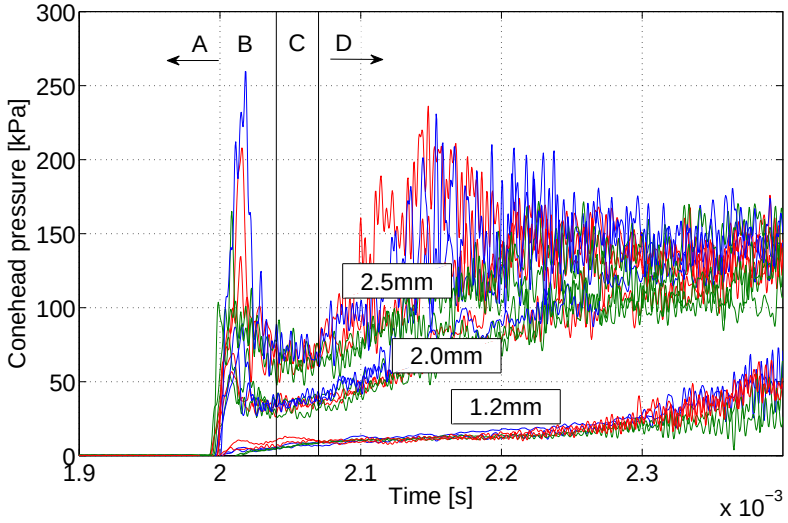

Figure 6.3: *Superposition of the pressure recorded during the different shots. Region A is for the flow at rest, B is the pressure rise due to the acceleration tube gas, C is the actual test time, and D the passage of the driver gas.*

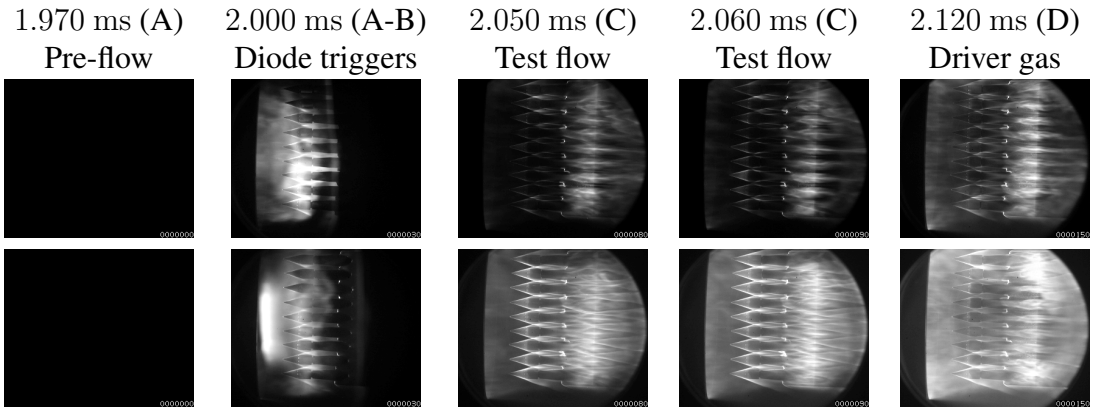

Figure 6.4: *Still of the high-speed video for different critical moments of the test flow, for the* 2.0 mm *(top) and* 2.5 mm *(bottom) cases of set A. The* 2.5 mm *being at higher pressure, it is considerably brighter.*

The pressure traces for the 1.2 mm case do not exhibit the pressure peak in region B as clearly as the others. A similar behavior was already observed for low pressures by C. Jacobs [89], and is due to the response time of the system. Indeed, there is a small cavity in the cone-head that protects the sensor. If the pressure is sufficiently large, the cavity is filled quickly enough to cause no impact on the response time. At lower pressure, however, the flow features are smoothed due to a longer response time.

6.2.4 Applicability to the study of binary scaling

The free-stream enthalpy is not exactly the same for the three test flows designed. We need therefore to determine whether they are sufficiently close so as not to be mistaken for the effect of the radiative coupling. The expected test flows were thus simulated with the Poshax without radiation coupling.

Only set A was considered at this stage, as set B will not be used for the rest of the study. The free-stream conditions are as specified in table 6.3, assuming equilibrium. A total of 15 species were included; CO_2, CO, CO^+, O_2, N_2, NO, CN, C_2, C, C^+, N, N^+, O, O^+, and e^-, with two temperatures. The Arrhenius reaction rates were taken from Ramjaun [156]. The energy exchange mechanisms were taken from Gnoffo [64] and Park [150].

The results are depicted in figure 6.5 (a) for temperature (vibrational T_v and electronic T_e), (b) for scaled density, and (c) for mass fraction of CO, C, and O. In each plot, the normal distance from the shock was scaled according to the relative density in table 6.3, and the density in figure 6.5 (b) was divided by the same scale factor. Despite small differences in free-stream enthalpy, all the scaled profiles match reasonably well. The equilibrium concentrations were included as symbols in figure 6.5 (c). Those were obtained with CEA. The flow appears to be frozen, indicating a small forward reaction rate constant.

6.3 Models constraints and description

The main subject of investigation being the stagnation line, it was decided to use cylindrical models of diameter D and length L, as illustrated in figure 6.6. Moreover, a two-dimensional geometry such as a cylinder will result in a thicker shock layer and a higher heat flux, as compared to a three-dimensional sphere in the same free-stream conditions. These will then be easier to measure. Their dimensions is based on three constraints presented hereafter, and the relative size between the cylinders is imposed by the density ratios as described in table 6.2.

The first constraint is imposed by the size of the core flow. For X2, it is traditionally considered to be around 100 mm in diameter. Therefore, using Pythagora's theorem, the ideal dimensions of the largest cylinder is bounded:

$$100^2 = L^2 + D^2 = 10D^2 \qquad \Longrightarrow \qquad R_l = D/2 < 15.81\text{mm} \tag{6.22}$$

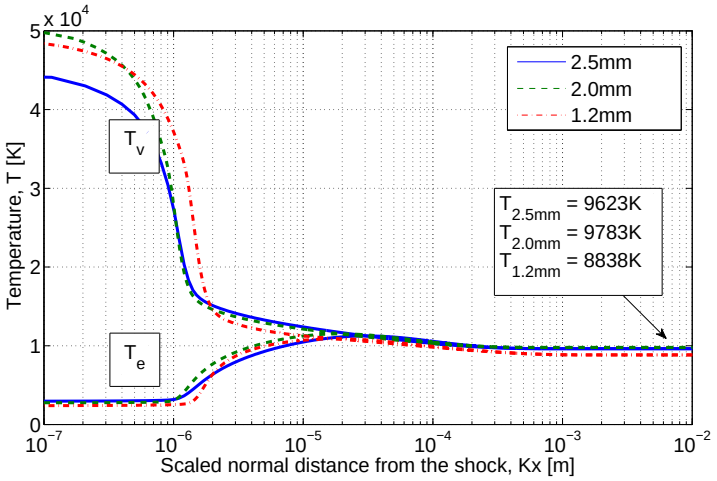

(a)

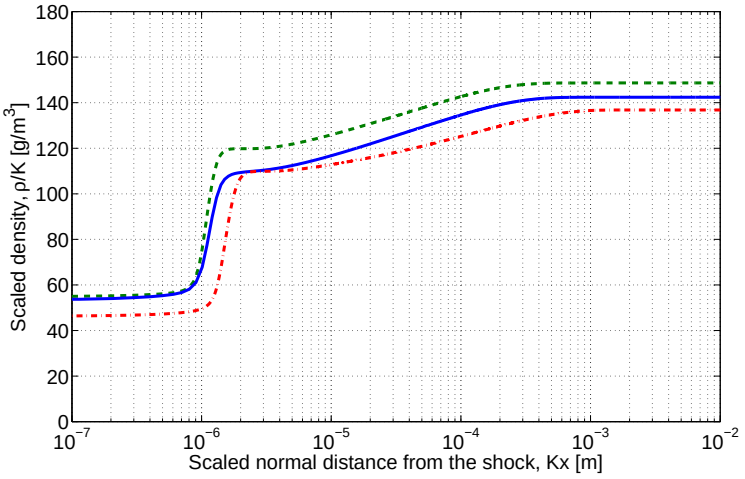

(b)

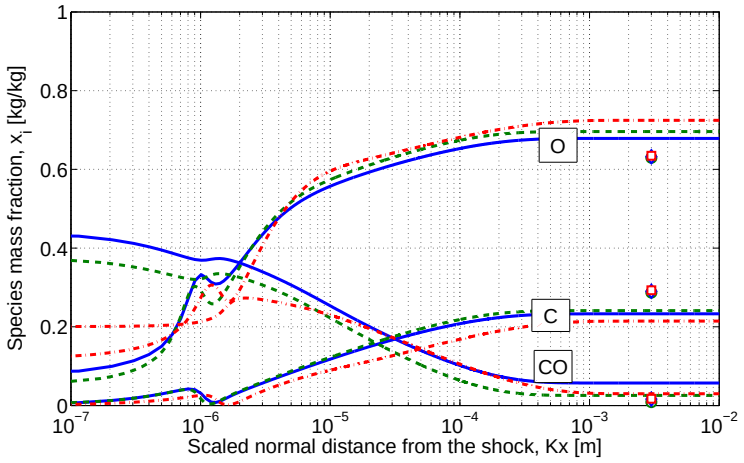

(c)

Figure 6.5: *Evolution of the temperature (a), scaled density (b), and concentration of O, C and CO (c) downstream of a normal shock in the test flow conditions as described in table 6.3. Those results were obtained with Poshax. The symbols in figure (c) correspond to the equilibrium concentrations. The scale factors* χ *are* 1.00 *for the* 2.5 mm *plate,* 0.505 *for the* 2.0 mm *plate, and* 0.169 *for the* 1.2 mm *plate.*

Second, regarding the instrumentation. Emission spectroscopy will be used to characterize the flow, and therefore the shock standoff needs to be large enough to be resolved. The shock standoff on the smallest cylinder has to be at least 0.5 mm thick otherwise it would not be possible to resolve it with the instrumentation available at the time of the experiment. A commonly used correlation for the shock standoff on cylinders is presented in appendix equation E.7. Simulations performed with Poshax for a one-dimensional normal shock and free-stream conditions as described in table 6.3 show that the expected density jump is $\rho_\infty/\rho_s \simeq 0.07$. For $\delta > 0.5$ mm, this implies $R_s > 3$ mm. Using the scale factor in table 6.2, the condition of the largest cylinder is $R_l > 17.75$ mm.

Our two first constraints are already impossible to meet simultaneously. They are thus somewhat relaxed, and the radius of the largest cylinder is fixed at $R_l = 17.50$ mm. This implies a scale factor $\chi = 17.1\%$ instead of 16.9%, which is well within the dispersion. Applying equation 6.22, one obtains $L = 95$ mm an aspect ratio of $L/D = 2.71$.

The instrumentation also imposes that the cylinder's aspect ratio L/D should not be too large so as to allow optics' alignment. Assuming that the maximum allowable misalignment over the entire line-of-sight in $0.1D$, and that the alignment can be made with an accuracy of $\alpha = 1\ ^\circ$, the largest possible aspect ratio is:

$$\tan\alpha = \frac{0.1D}{L} \qquad \Longrightarrow \qquad \frac{L}{D} < \frac{0.1}{\tan\alpha} = 5.73 \tag{6.23}$$

This limit was applied to determine the length of the smallest cylinder, rounding its length to $L_s = 35$ mm to accommodate the screw threads needed to fix the model to its base.

Lastly, regarding the three-dimensional effects associated to the use of cylinders. From previous studies on the three-dimensional effects on line-of-sight measurements of the flow cylinders [44], we obtain a second constraint on the aspect ratio $L/D > 3$. The smallest model is largely within that constraint, and the largest one will only cause minor three-dimensional deviations [44]. The resulting dimensions are tabulated in table 6.5.

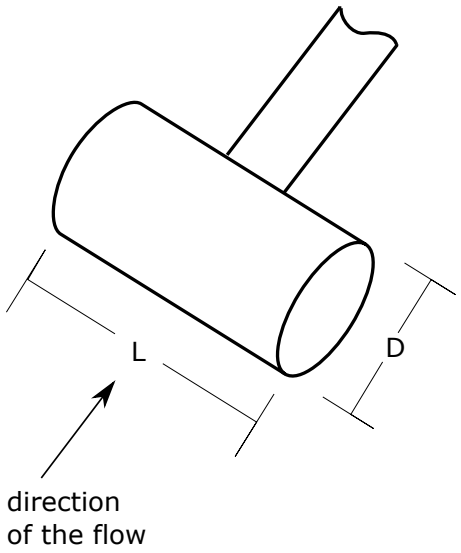

Figure 6.6: *Schematic of the cylindrical models used in the frame of this study.*

	Cylinders				
t	R	L	L/D	χ	$R\rho_\infty$
[mm]	[mm]	[mm]	[−]	[−]	[g/m^2]
1.2	17.50	95.0	2.71	17.1	0.0294
2.0	6.00	75.0	6.25	50.0	0.0301
2.5	3.00	35.0	5.83	100.0	0.0298

Table 6.5: *Dimensions for the three sets of models that were developed.*

Chapter 7

Shock standoff measurements

"The conclusion drawn from the different results [...] indicates that for the real gas regime an exact quantitative description of the shock stand- off distance is still missing and that for future work it is worth spending some effort on this topic."

- Herbert Olivier [137]

The shock standoff distance is both easy to measure and, as discussed in section 3.2, a good indicator of the vibrational and chemical state of the shock layer. As a consequence, there is plenty of data available in the literature, and as many empirical or semi-empirical correlations, for the evolution of shock standoff distance with respect to probe geometry and free-stream conditions [5, 12, 14, 75, 81, 86, 87, 110, 132, 201, 207, 212]. However, as noted by Zander et al. [212], most of that data was obtained in the low-speed hypersonic regime, i.e. up to $6\mathrm{km/s}$. There is very little publicly available experimental data in the high-speed hypersonic regime, where flow features such as finite-rate chemical kinetic effects and radiative coupling become significant.

In this chapter, we first present a preliminary estimation of the shock standoff distance based on some of the most widely used correlations, some of which have already been presented in section 3.2. We then describe the experimental technique used to quantify the dimensionless shock standoff. It is similar to what has been published by Zander et al. [212] with some small differences in the details of its implementation. The operating and free-stream conditions were described in section 6.2.2, and the models were detailed in section 6.3. Finally, we present and discuss the experimental results.

Theoretically, all the binary scaling parameters being duplicated, the dimensionless shock standoff is expected to remain the same for all three models. However, as predicted in the discussion of radiative coupling in section 3.3.2, it was found out that dimensionless shock standoff decreases as the length-scale of the flow increases. The chemical state of the shock layer, effects arising from using cylinders, viscid-inviscid interactions, and different dissociation states of the free-stream were all ruled out of the possible factors causing that decrease (although they can have some negligible contribution nonetheless). The main cause is therefore identified as the radiation coupling.

7.1 Preliminary estimation of the shock standoff distance

Predictions for the dimensionless shock standoff are presented in table 7.1. The correlations used were the first order approximation presented in equation 3.15, the experimental correlation based on Mach number proposed by Ambrosio and Wortman presented in equation 3.17 [5], the numerical correlation proposed by Hornung presented in equation E.7 [81], and the analytical correlation proposed by Inger presented in equation 3.18 together with its correction to account for the viscid boundary layer presented in equation [86]. The values tabulated in tables 6.2, 6.3, and 6.5 were used. All three correlations (Ambrosio and Wortman, Hornung, and Inger) are in relatively good agreement.

A few interesting conclusions can already be drawn at this stage. First, small differences can be observed from one scale to another. For Hornung and Inger, the most important contribution to those differences is the frozen density ratio across the shock. Indeed, the frozen density immediately downstream of the shock is a weak function of the free-stream enthalpy. The latter being slightly different from one condition to another, the frozen density does not scale exactly in the same fashion as the free-stream density. This can also be concluded from the crude estimations based on equation 3.15 tabulated in the second column of table 7.1.

Moreover, the second-order effects identified by Inger and represented in equation 3.18, namely the inviscid shock layer vorticity and curvature effects, are both a function of the density ratio across the shock in such a way that they accentuate the trend observed in the previous paragraph.

Second, taking the viscid shock layer into account would cause the dimensionless shock layer to increase slightly, and more so as the size of the model decreases. The shock layer Reynolds number as defined by Inger (equation 3.21) are $Re_s \simeq 870$, 830, and 770, respectively for the $R = 17.5$ mm, 6.0 mm, and 3.0 mm cases. Although those values are above the threshold proposed by Inger [86], his model was used to determine the viscid contribution to the shock standoff, using the average of the maximum temperature encountered during the test time is $T_w = 410$K, 710K, and 850K (see chapter 8).

For ideally binary scaled conditions, the extent of the viscous effect depends thus on $\Pi_3 = T_\infty/T_w$ (equation 2.21). The latter is nothing but another expression for the term g_w (equation 7.1) proposed by Inger to account for the effect of the wall temperature gradient on viscid-inviscid interactions [86].

R [mm]	$\rho_\infty/(\rho_s - \rho_\infty)$	Ambrosio [5]	Hornung [81]	Inger [86]	$(\Delta - \Delta_{inv})/R$ [86]
17.5	0.274	0.401	0.450	0.407	0.002
6.0	0.224	0.404	0.424	0.350	0.005
3.0	0.229	0.409	0.432	0.356	0.007

Table 7.1: *Expected dimensionless shock standoff distance Δ/R, R being the radius of the cylinder, based on different well-established correlations for a frozen inviscid shock layer.*

7.2 Test set-up and image processing

As demonstrated by Zander et al. [212], the significant radiation emitted by the shock layer allows to define its edges solely based on its luminosity. No specific set-up such as for example a Schlieren was thus necessary. The same Shimadzu HPV-1 camera used for the Pitot survey (section F.2) was used to visualize the flow over the model in this experiment. Each of the 102 images is saved as a 260×312 pixel greyscale bitmap

The HPV-1 was first set up to record into the test section from above, obtaining images along the polar axis of the cylinder, perpendicular to the flow direction, so as to verify that the entire cylinder is comprised within the test flow and that three-dimensional effects are negligible. After a few runs with each of the models, the HPV-1 was then installed on the side of the dump tank, looking laterally in the test section along the longitudinal axis of the cylinder. Those latter images were used to determine the shock standoff distance.

The processing of the images is done in several steps. These are illustrated in figure 7.1, obtained for the shot $x2s2706$, part of the $R = 17.5$ mm series, 60µs after diode triggering when steady time is reached. The methodology is similar to that applied by Zander et al. [212], with some variations in its exact implementation.

We first have the raw image, figure 7.1 (a), on which the streamwise direction is from left to right. The shock layer being very bright, the main features of the flow are clearly visible: the bow shock, the model, the boundary layer, etc. The reflection of the shock layer on the window at the other side of the test section can also be identified.

The raw image is processed with an averaging filter in order to get rid of undesirable high-frequency components of the signal such as thermal noise. For this particular image the features are very bright and the optical settings are properly adjusted, only minor differences can thus be seen between image (a) and image (b). For other cases, however, the filtering causes a significant improvement.

The resulting image is then analyzed using an edge detection function based on the Sobel method [173], already implemented in Matlab. The Sobel operators are smoothed derivatives in both spatial directions f_x and f_y, and the edges are then obtained as:

$$R = \sqrt{f_x^2 + f_y^2} \tag{7.1}$$

It is crude compared to other more sophisticated methods, but sufficient for the present application, and numerically inexpensive. Indeed, it can clearly be seen in figure (c) that the features of interest are correctly identified.

Four points that are on the edge of the cylinder are then identified manually. The only condition for the two first points is that they need to be in the shock layer. The third point also needs to be in the shock layer, but in the vicinity of the stagnation line. The fourth point needs to be in the vicinity of the stagnation line as well, but upstream of the shock (i.e. in the free-stream). These points are then used to create two masks.

- The first three points are used to define a disk that contains the model edge but not the shock. The slope of two curves passing through those points is then obtained as:

$$m_r = \frac{y_2 - y_1}{x_2 - x_1} \qquad\qquad m_R = \frac{y_3 - y_2}{x_3 - x_2} \tag{7.2}$$

  Based on which the centre of the disk (x_d, y_d) is obtained as:

$$\begin{aligned} x_d &= \frac{m_r m_t \left(y_3 - y_1\right) + m_r \left(x_2 + x_3\right) - m_t \left(x_1 + x_2\right)}{2\left(m_r - m_t\right)} \\ y_d &= -\frac{1}{m_r}\left[x_d - \frac{1}{2}\left(x_1 + x_2\right)\right] + \frac{1}{2}\left(y_1 + y_2\right) \end{aligned} \tag{7.3}$$

  This first mask obstructs everything except the model edge. When applied, the resulting image is as depicted in figure (e).

- The two last points, along the stagnation line on each side of the shock, are used to define a thin vertical band that only contains the shock. Following the work of Billig [14], the shock shape in the vicinity of the stagnation line can indeed be approximated with an arc of circle. It is thus primordial to capture a portion of the shock small enough for that approximation to be valid. When applied, the resulting image is as depicted in figure (e').

The coordinates of the points corresponding to the shock in figure (e) and the model in figure (e') are then stored in two vectors and fed to a circle interpolation function. The latter is based on the Modified Least Square method described by Umbach and Jones in [198]. They demonstrated that the interpolation of the centre of the circle (x_c, y_c) can be described as a set of partial derivatives of which the solution is:

$$x_c = \frac{DC - BE}{AC - B^2} \qquad\qquad y_c = \frac{AE - BD}{AC - B^2} \tag{7.4}$$

where the terms are defined as:

$$\begin{aligned} A &= n\sum_i x_i^2 - \left(\sum_i x_i\right)^2 \\ B &= n\sum_i x_i y_i - \left(\sum_i x_i\right)\left(\sum_i y_i\right) \\ C &= n\sum_i y_i^2 - \left(\sum_i x_i\right)^2 \\ D &= 0.5\left[n\sum_i x_i y_i^2 - \left(\sum_i x_i\right)\left(\sum_i y_i^2\right) + n\sum_i x_i^3 - \left(\sum_i x_i\right)\left(\sum_i x_i^2\right)\right] \\ E &= 0.5\left[n\sum_i x_i^2 y_i - \left(\sum_i x_i^2\right)\left(\sum_i y_i\right) + n\sum_i y_i^3 - \left(\sum_i y_i\right)\left(\sum_i y_i^2\right)\right] \end{aligned} \tag{7.5}$$

The radius R is then obtained as:

$$R = \frac{1}{n} \sum_i \sqrt{(x_i - x_c)^2 + (y_i - y_c)^2} \tag{7.6}$$

The two interpolated circles are depicted in figure (f). The advantage of the interpolation is to obtain a sub-pixel accuracy, using to the fullest the information contained in the frame.

The shock standoff distance is then simply defined as the shortest distance separating those two circles. The quantities thereby obtained are depicted in figure (g): the radius is the blue dashed line defined by two dots, and the shock standoff is the green continuous line defined by two stars.

The same steps are repeated for each image, except for the identification of the four points which is only performed once. Two typical measurements are shown in figure 7.2. These were obtained for two consecutive shots, $x2s2703$ and $x2s2704$, both part of the $R = 17.5$ mm series. The apparent discontinuity is due to the measurement being based on the location of the shock, which is a single pixel while the shock layer itself is only a few pixels wide. The beginning of the test $t = 0$ corresponds to the triggering of the photodiode, while the steady test time is considered to last from about 50μs to about 150μs. In those particular instances, the frame-rate was set on 0.5MHz, allowing to record up to 200μs.

7.3 Experimental results

For the sake of simplicity, the largest contribution to the overall uncertainty is assumed to arise from the shock standoff (i.e. rather than from the radius) and be smaller than the length of a pixel. One can thus write, for the dimensionless shock standoff:

$$\frac{\Delta}{R} = \frac{\widehat{\Delta}}{R} \pm \frac{L_{\text{pixel}}}{R} \pm \sigma_{\text{meas}} \frac{\Delta}{R} \tag{7.7}$$

where $\widehat{\Delta}$ stands for the mean of the measured shock standoff and L_{pixel} is the length of a pixel, and depends thus on the magnification factor. It is therefore constant within each set, and the corresponding values are tabulated in table 7.2. For most measurements, one can safely consider that $\epsilon_\Delta \ll \sigma_{\text{meas}}$ and thus ignore the latter. For a set of N measurements, the standard deviation over the whole set also has to be included. One can thus write:

$$\frac{\Delta}{R} = \frac{\widehat{\Delta}}{R} \pm \frac{1}{\sqrt{N}} \frac{L_{\text{pixel}}}{R} \pm \sigma_{\text{set}} \frac{\Delta}{R} \tag{7.8}$$

Because of the test set-up used, any misalignment of the model could lead to the shock standoff appearing smaller than it actually is. As mentioned in section 6.3, and more particularly through equation 6.23, the models were designed so as to ensure that, for an alignment accuracy of $1\ ^\circ$, the error on the shock standoff would be equal to 0.1Δ, which is largely negligible compared to the other sources of errors.

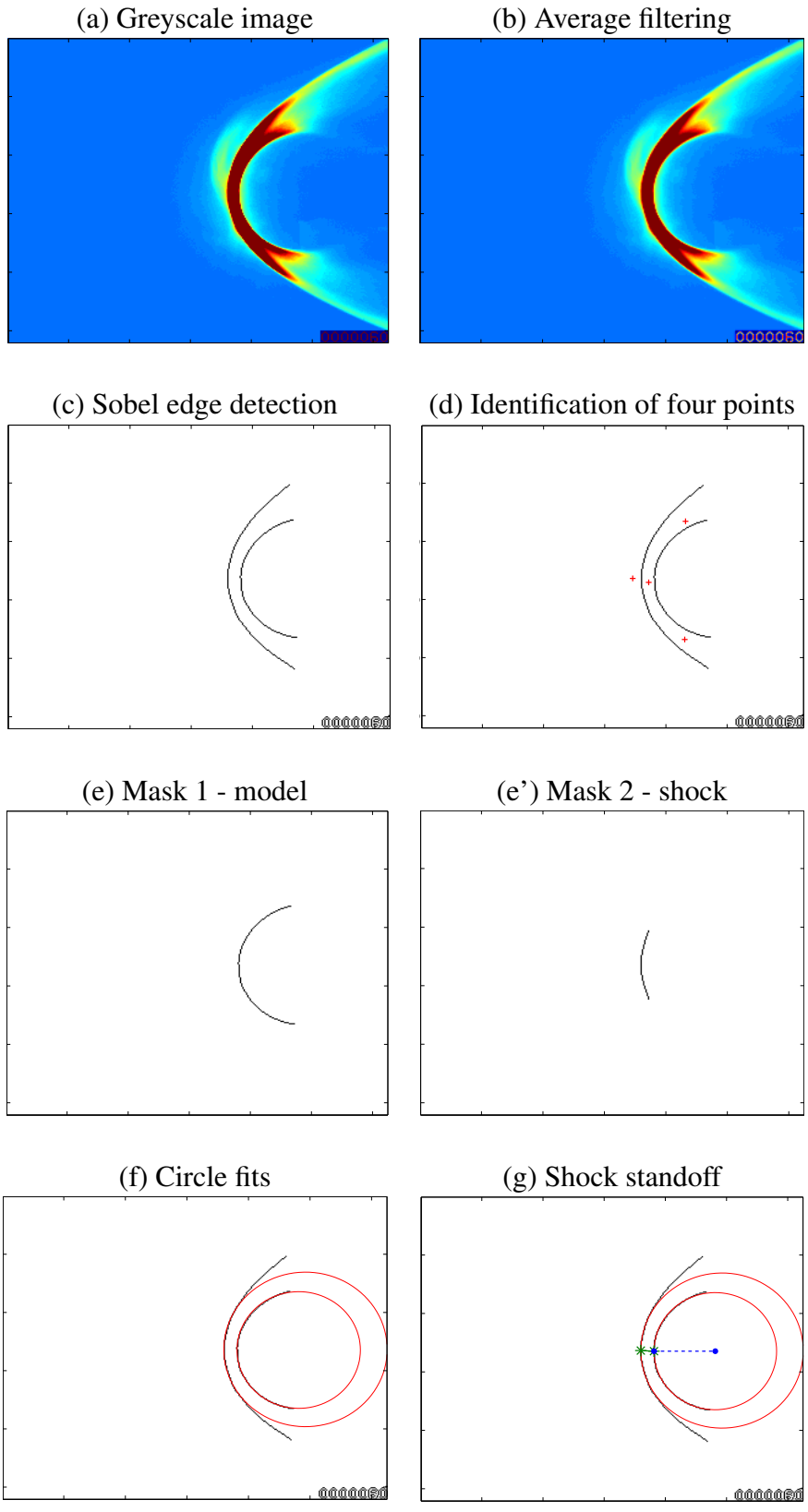

Figure 7.1: *Step-by-step detail of the method used to identify the geometric features of interest on any bitmap image, for the shot* $x2s2706$*, part of the* $R = 17.5$ mm *series,* 60 µs *after diode triggering. The raw image is first processed with an average filter. The edges are then detected with the Sobel method. Four points are then identified in order to create two separate images: one for the model, and one for the shock. The two images are then fed to a circle interpolation function.*

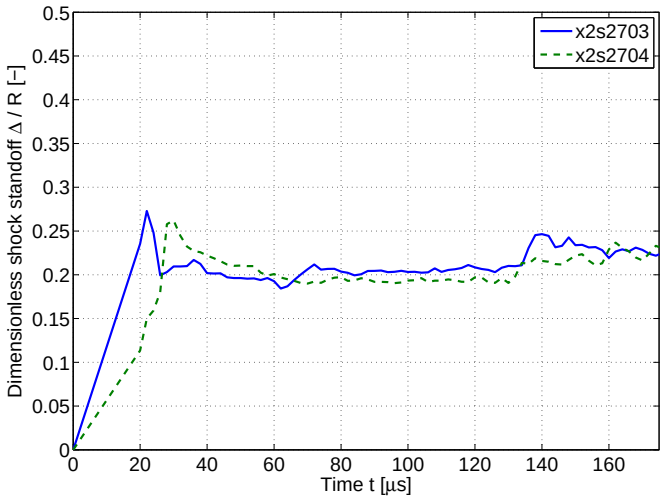

Figure 7.2: *Typical measurement of the nondimensional shock standoff distance obtained for two consecutive shots,* $x2s2703$ *and* $x2s2704$*, both part of the* $R = 17.5$ mm *series. The beginning of the test* $t = 0$ *corresponds to the triggering of the photodiode, while the steady test time is considered to last from* 50 µs *to* 130 µs*.*

The average value obtained for each condition, the corresponding number of shots performed, and the associated uncertainty are tabulated in table 7.2. The results are also depicted in figure 7.3 in terms of dimensionless shock standoff with respect to cylinder radius. Let us directly point out the large uncertainty for the smallest cylinder is simply due to the difficulty to resolve the shock layer which is only made of 7 pixels. The uncertainty margin is, in the two other cases, relatively small. Because cylinders are used, and not spheres, there could be a three-dimensional effect to be accounted for [207]. The results obtained applying the experimental correction factor of Eichmann et al. [44] were thus also tabulated, but the difference proves to be negligible.

R [mm]	N	L_{pixel}/R	Δ/R	$\sigma\Delta/R$	$2D$ [44]
17.5	11	0.010	0.209	0.009	0.211
6.0	6	0.028	0.279	0.023	0.279
3.0	7	0.057	0.401	0.061	0.401

Table 7.2: *Measured dimensionless shock standoff distance* Δ/R*.*

7.4 Discussion and conclusion

The experimental values are smaller or equal to those obtained with the correlations given in table 7.1, and there is a tendency for the nondimensional shock standoff distance to increase as the size of the model is reduced. As discussed previously, the same behavior was observed by Hornung [81]: in figure C.1, for a certain Damkhöler number, the dimensionless shock standoff is larger over the smaller models.

We established in section 3.2.1 that the dimensionless shock standoff depends on the ratio between the free-stream density and the average density in the shock layer (equation 3.15). The different

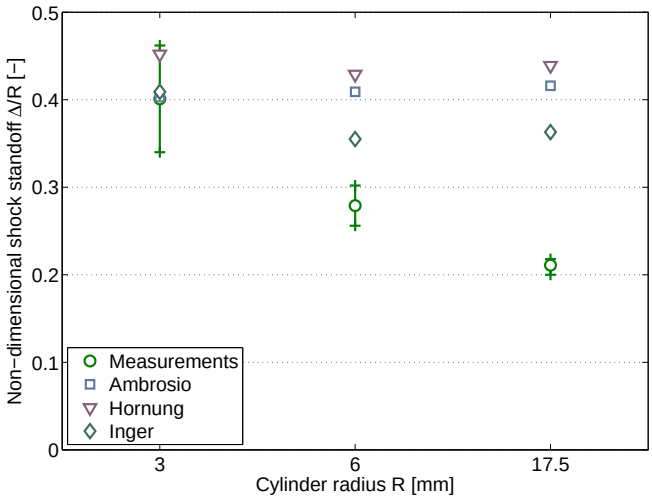

Figure 7.3: *Measurements obtained for the nondimensional shock standoff distance compared to well-established correlations.*

phenomena that have an influence on the post-shock density in the case of an adiabatic flow were explored in section 3.2. These apply to the present experiments as follows:

- The **three-dimensional effects** arising from using cylinders was pointed out as a possible cause by Wen and Hornung [207]. As illustrated in table 7.2, applying the experimental correction factor of Eichmann et al. [44] does indeed provide some correction, but it is too small to be relevant.

- There could also be a **chemical regime** from model to model within the boundary layer (see discussion in section 3.2.2). The Damkhöler number $\tilde{\Omega}$ as defined in equation 3.20 was thus evaluated for each case, using for the sake of simplicity $c_{p,s}T_s \simeq h_\infty$. The resulting values are $\tilde{\Omega} = 4.33 \cdot 10^7$, $2.68 \cdot 10^7$, and $4.27 \cdot 10^7$ respectively for the $R = 17.5$, $R = 6.0$ and $R = 3.0$ mm cases. The flow is thus, for all three cases, largely in equilibrium. This confirms the normal shock simulations presented in section 6.2.4.

- The **viscid-inviscid interactions** (see discussion in section 3.2.3) contribute to slightly inflate the shock layer, following a trend that concurs with what is observed experimentally. Nevertheless, as for the three-dimensional effects, that effect is probably too small to have any visible impact. It is important, however, to keep it in mind when applying the binary scaling. If the Reynolds number is lower than the limit defined by Inger [86], the wall temperature might become an important factor, especially when comparing the (supposedly) hot heat shield in flight with the relatively cooler model in the laboratory.

- We mentioned in section 3.2.2 that Inger did a parametric study on the effect of the **free-stream dissociation** fraction [87]. He noted that its effect was more important for large values of Ω, which is the case in the present study, and would cause the shock standoff to inflate. This is compatible with the measurements: the free-stream dissociation increases as the size of the model decreases (e.g. $x_{CO_2} = 63\%$ for $R = 17.5$ mm while $x_{CO_2} = 29\%$ for $R = 3.0$ mm).

Again, however, Inger points out that the effect of free-stream dissociation is negligible [87].

While the free-stream dissociation, three-dimensional effects and viscid-inviscid interactions can contribute to the trend observed, none of these adiabatic phenomenon is sufficient to explain it. Therefore, the main contributor is identified as being radiative cooling.

From equation 3.52 we know that the Goulard number (i.e. the radiative coupling) is weaker for scaled flows. This will be confirmed in table 8.2 where the actual values of the Goulard number of each flow are determined. A high Goulard number implies that the shock layer absorbs the radiative heat it generates and heats up. A higher temperature corresponds to a lower density all other flow parameters being equal, and ultimately a smaller dimensionless shock standoff. This concurs with the discussion in section 3.3.2.

These elements being known, it would be of great interest to build for the dimensionless shock standoff a correlation of the form $\Delta/\Delta_{\text{ad}} = f(\Gamma)$, as it already exists for the radiative heat flux (equation 4.20). However, there is, at this stage, almost no relevant numerical data available in the literature.

Chapter 8

Heat flux measurements

"A question that remains to be answered is as follows: for flows with significant radiation coupling, can we develop prediction methodologies with enough accuracy to reduce design margins? To achieve this goal, research and development are needed [...] (particularly for other planetary atmospheres) [...]. More important, experimental data are needed to validate these models."

- Peter Gnoffo [63]

The theoretical scaling of the different stagnation point heat fluxes were exposed in chapter 4 and the proper scaling of the diffusive heat flux was verified experimentally in chapter 5. If the flow is adiabatic, the relations derived in section 4.4.1 can thus be used in a simple fashion. If the flow is non-adiabatic, however, the situation is not as simple. In this chapter, we will verify some of the developments made in chapter 4, more specifically in sections 4.2 and 4.4.2, and apply them to a practical case.

We first present approximations of the heat fluxes as well as the expected reduction due to non-adiabatic effects. This first step allows us to justify and introduce the use of thin-film theory. The test set-up is then described: the thermocouple, the thermophysical properties of the junction, which is the sensing element, and the post-processing strategy. The experimental results are then presented and discussed.

8.1 Preliminary estimation of the heat fluxes

8.1.1 Correlations for adiabatic flows

As explained in section 4.1, two natures of heat fluxes need to be identified: the convective q^c, and the radiative q^r[1]. Numerous correlations are available in the literature describing them in terms of boundary conditions of the flow such as free-stream properties (pressure or density, enthalpy), gas

[1]The subscript w will not be used in the rest of this chapter as it is implicitly implied that all the heat fluxes dealt with concern the wall.

composition, and probe nose radius.

The results obtained with some of the correlations presented in that section are tabulated in table 8.1. We assumed $h_w \ll h_0$, since the surface is at room temperature. The values downstream of the shock were computed using Poshax assuming an uncoupled flow with the equilibrium free-stream conditions tabulated in table 6.3. For the correlation of Zoby [214], the constant K is specified for different species and then obtained as:

$$K = \left(\sum_{i=1}^{n} \frac{x_i}{K_i} \right)^{-1} \tag{8.1}$$

and is equal to $K = 4.3515 \cdot 10^{-4}\ \mathrm{m^{1.5}sPa^{0.5}}$ for the mixture used in this test campaign.

The correlation of Tauber et al. for the radiative heat flux in Venus atmospheric entry presented in section E.4.5, equation E.6 was also tabulated. Let us note that the expression for the convective heat flux account for cylindrical models. From the approach of Lees (and Fay and Riddell) to the solution to the heat transfer in the laminar boundary layer, the stagnation point heat flux for an axisymmetrical flow is $\sqrt{2}$ larger than that for a two-dimensional one (see for example [36]). However, there is no simple factor to correct from axisymmetric to two-dimensional radiative heating. The actual radiative heat flux is expected to be larger due to the larger view factor and thicker shock standoff distance.

R [mm]	q^c [MW/m^2]			q^r [MW/m^2]		
	Detra [39] *Earth*	Zoby [214] *Venus*	Tauber [185] *Earth*	Detra [39] *Earth*	Tauber [187] *Mars*	Tauber [186] *Venus*
17.5	33.18	34.22	31.63	21.25	0.49	0.30
6.0	116.31	120.05	104.39	57.59	1.16	0.89
3.0	204.03	212.13	184.01	60.92	1.59	1.05

Table 8.1: *Values predicted by classical correlations for the stagnation point heat fluxes. It should be noted that only the convective heating predicted by Zoby and the radiative heating predicted by Tauber were meant for Venus atmospheric entry.*

8.1.2 Non-adiabatic effects

These test conditions were designed with the objective to cause significant radiation coupling. It is therefore of prime importance to properly estimate the Goulard number and, subsequently, the effect of the coupling of the heat fluxes. Let us repeat here the expression for the Goulard number, already presented in equation 3.51:

$$\Gamma = \frac{2q^r_{\mathrm{ad}}}{\frac{1}{2}\rho_\infty v_\infty^3} \tag{8.2}$$

The adiabatic heat flux was estimated using Poshax, in a similar fashion to the simulations detailed in section 6.2.4. The original development of the Goulard number are based upon an inviscid flow

[70], which justifies the use of an inviscid numerical solution. The distances at which the radiative heat flux are measured are based upon the correlation of Hornung [81] tabulated in table 7.1.

The effect of the coupling on the heat fluxes was then estimated using the developments made in section 4.2. Two propositions are retained for the radiative heat flux: either equation 4.20 with $a = 3$ [188], or equation 4.21. Although the later has been specifically developed for Venus atmosphere, the former remains the most popular and has been widely used for air, gas giants, Titan, Mars, and Venus. Equation 4.23 was used for the convective heat flux has, to the author's knowledge, no equivalent exists.

The results are tabulated in table 8.2 in the hypothesis of an optically thin and optically thick flow.

Optical thickness	R [mm]	Δ [mm]	q^r [MW/m^2]	Γ [−]	q^r/q^r_{ad} [188] [−]	q^r/q^r_{ad} [42] [−]	q^c/q^c_{ad} [−]
thin	17.5	7.91	39.43	0.119	0.597	0.448	0.828
	6.0	2.57	83.43	0.075	0.671	0.520	0.871
	3.0	1.32	105.67	0.054	0.719	0.567	0.895
thick	17.5	7.91	52.28	0.156	0.548	0.401	0.797
	6.0	2.57	114.43	0.103	0.620	0.471	0.842
	3.0	1.32	126.72	0.065	0.692	0.541	0.882

Table 8.2: *Effect of radiation coupling on the stagnation point heat fluxes in the hypothesis of an optically thin or optically thick flow. The effect of the coupling on the convective heat flux is obtained with equation 4.23.*

A striking point is that the computed radiative heat fluxes are much higher (approximately two orders of magnitude) than those obtained with the correlations presented in table 8.1. While there is a certain margin of uncertainty associated with the values obtained from Poshax, it is very likely that these correlations underestimate the actual value because they are used out of the region for which they were designed.

Regarding Mars entry, for example, Tauber and Sutton specify that their correlations is built upon CFD simulations for an inviscid non-adiabatic flow for velocities from 6 to 9 km/s, nose radii from 1 to 23 m, and free-stream densities from 0.1 to 1 g/m^3 [187]. The reported difference between the correlation and experimental measurements is the highest (i.e. $> 10\%$) for small nose radii (table 6.5), large velocities and large free-stream densities (table 6.2), all three of which are the case in the experimental campaign. The most sensitive point is obviously the nose radii, which is a thousands of order of magnitude smaller than that considered in the work of Tauber and Sutton.

Another interesting point is that the radiative heat flux actually increases with the size of the model, for the correlations as well as for the Poshax computations. This is likely to be a side effect of the non-binary chemistry, as presented in section 3.1. Within the same family of binary scaled flows, a shorter length-scale implies a hotter and less dissociated equilibrium flow, thus also affecting the optical thickness, as well as changes in the thickness of the nonequilibrium layer, which is the region responsible for most of the radiation. From figure 6.5 (a), it appears that the large difference between the $R = 17.5$ mm case than for the two other ones can mostly be attributed to the large difference

in equilibrium temperature (~ 1000 K). On top of that, the uncertainty on the free-stream conditions and on the adiabatic shock standoff may also have contributions.

8.2 Transient heat flux measurements

Assuming the heat flux is measured using instrumentation compatible with the thin-film theory, the temperature increase to be expected can be approximated as:

$$\Delta T \simeq \frac{q\sqrt{\Delta t}}{\sqrt{\rho c k}} \tag{8.3}$$

where $\sqrt{\rho c k}$ is the gauge's thermal product, with c its specific heat, and Δt the total test time. For the sake of simplicity, we assume $\sqrt{\rho c k} \simeq 1 \cdot 10^4$ kg/m^2/K/s$^{1/2}$ and $\Delta t \simeq 70$ µs. This leads, to $\Delta T \simeq 180$ K for $q = 200$ MW/m^2. The large heat flux to measure over such a short test time only allows for transient heat transfer measurement. In that case, the instrumentation is based on the semi-infinite principle formalized by Schultz and Jones [163].

That principle relies on two geometrical constraints:

- First, the sensing element must be a conductive (metallic) slab thin enough (i.e. low thermal inertia) to consider that the temperature history is not affected by heat losses throughout the duration of the test time;

- Second, the sensing element must be mounted on substrate material large (and especially long) enough for the gauge to be considered one dimensional. The resulting instrument is schematically represented in figure 8.1.

With those two hypothesis, the heat transfer through the sensing element can be considered as a one-dimensional problem, expressed as:

$$\frac{\partial^2 T}{\partial y^2} = \frac{1}{\alpha}\frac{\partial T}{\partial t} \tag{8.4}$$

with the following boundary and initial conditions:

$$k\left(\frac{\partial T}{\partial y}\right)_{y=0} = q\left(t\right) \qquad T\left(+\infty, t\right) = T_i \qquad T\left(y, 0\right) = T_i \tag{8.5}$$

where α is the material's thermal diffusivity, T_i the initial temperature, and the surface is located at $y = 0$ with positive x in the streamwise direction. The solution for the surface temperature as a function of heat flux and time is expressed as [163]:

$$T_{y=0}\left(t\right) = \frac{1}{\sqrt{\pi}\sqrt{\rho c k}} \int_0^t \frac{q\left(\tau\right)}{\sqrt{t-\tau}} d\tau \tag{8.6}$$

which is the expression from which the approximate equation 8.3 was derived. Inversely, the heat flux

can be retrieved from the temperature as [163]:

$$q\left(t\right)=\frac{\sqrt{\rho ck}}{\sqrt{\pi}}\int_{0}^{t}\frac{\frac{dT(\tau)}{d\tau}}{\sqrt{t-\tau}}d\tau \tag{8.7}$$

The differential of the temperature and the presence of noise on the signal, however, might create some difficulties when solving that integral. It is thus replaced by a more convenient form [163]:

$$q\left(t\right)=\frac{\sqrt{\rho ck}}{\sqrt{\pi}}\left[\frac{T\left(t\right)}{\sqrt{t}}+\int_{0}^{t}\frac{T\left(t\right)-T\left(\tau\right)}{\left(t-\tau\right)^{3/2}}d\tau\right] \tag{8.8}$$

where T is not the absolute temperature but the temperature difference with respect to an initial time $T\left(\tau=0\right)=0$.

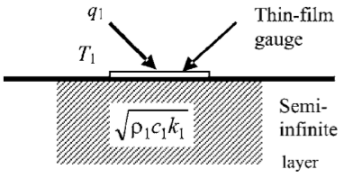

Figure 8.1: *Schematic representation of a thin-film gauge. Illustration from [135].*

For large heating rates, Schultz and Jones recommend to use a sensing elements with a high thermal product so as to limit the surface temperature. They further suggest to use a metallic substrate instead of an insulating one, as the thermal stress might cause the surface of the gauge to erode.

8.3 Test set-up

8.3.1 Instrumentation

The heat gauges used in the frame of this campaign were fast-response type-E thermocouples that were manufactured in-house following the design of Lourel et al. [112]. The junction of type-E thermocouples is chromel and constantan. Chromel is an alloy of chromium ($9-9.5\%$) and nickel ($89-90\%$) with traces of silicon, iron, manganese, carbon, cobalt, and niobium. Constantan is an allow of copper ($55-57\%$) and nickel ($43-45\%$) with traces of iron and manganese. Both materials are corrosion resistant and can withstand temperatures up to $\sim$ 1350 K. Furthermore, they have similar thermal properties, which reduces the variation and uncertainty in the thermal product of the sensing element. [26]

In the design of Lourel et al. [112], the two thermoelements are coaxial, as represented in figure 8.2. The inner element is tapered in order to form an interference fit with the outer one. The insulating material between them is minimized, thus reducing the amount of bridging material needed to make

the actual junction, and thereby achieve the required low thermal mass for the sensing element. The outer annulus is made out of chromel and has the following dimension: $2.00\ \mathrm{mm}$ outer diameter with a inner hole of $0.88\ \mathrm{mm}$ in diameter, for a length of $3.00\ \mathrm{mm}$. The inner element is made out of constantan and has the following dimension: $0.55\ \mathrm{mm}$ diameter at the thin end and $0.80\ \mathrm{mm}$ at the thick end, resulting in a $11.26\,\mathrm{deg}$ taper angle. The insulting material is epoxy resin. The thermocouples are wired to a shielded low-microphonic BELDEN 9452 co-axial cable. On the surface, the junction is simply obtained by creating by hand a local plastic deformation with abrasive paper. [112] This method has proved to be more suited for measurements in the microsecond time-scale than scalpel scratches, although it increases gauge to gauge variability [24].

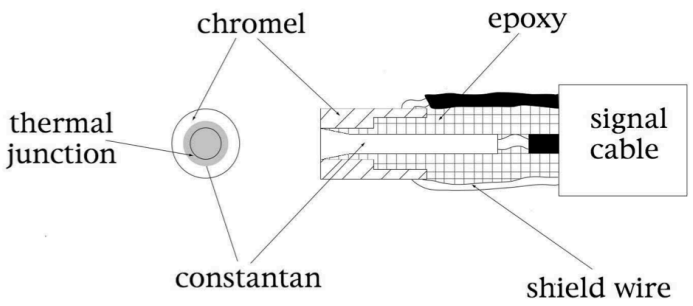

Figure 8.2: *Schematic representation of the type-E thermocouple developed by Lourel et al. for expansion tube testing. Illustration from [112].*

The favorable material characteristics and the design of Lourel et al. give these gauges an adapted response-time, typically less than $1\ \mu\mathrm{s}$, while the signal achieved is devoid of EMF interferences. They have been successfully used during previous test campaign for stagnation point heat flux measurement, with repeated use despite the harsh aerothermal environment (see for example [120, 29, 30]).

8.3.2 Junction thermophysical properties

Two properties of the thermocouple will determine its response to temperature change: its sensitivity a in terms of $\mu\mathrm{V/K}$, and its thermal product. For what concerns its sensitivity, calibration of thermocouples at high temperatures being a complicated operation, it was decided to use the polynomial response curved referenced in the NIST database [1]. The same approach was used in other experimental campaign while measuring heat flux in hypersonic carbon dioxide flows, see for example [169]. The values for each coefficient a_n are tabulated in table 8.3. The reported error for the temperature range from $0\,\mathrm{deg}$ to $1000\,\mathrm{deg}$ is $\pm 0.02\,\mathrm{deg}$ [1]. McIntyre et al., while measuring heat fluxes with the same instrumentation in the same facility, considered a contribution of $\pm 1.7\%$ for standard EMF-temperature correlations in the uncertainty of the heat flux calculated [120].

Lourel et al. performed a calibration for the thermocouples they designed for temperatures up to $\sim 350\ \mathrm{K}$ and obtained a linear sensitivity of $a = 1.6 \cdot 10^{-2}\mathrm{K}/\mu\mathrm{V}$ [112]. Capra later performed two calibrations following the same method and obtained a value within 4% of what was reported by

Lourel et al. [28]. As depicted in figure 8.3, both results are sufficiently close to what is referenced in the NIST database in the temperature range where they performed their calibration to assume that the design of Lourel et al. does not incur any unforeseen deviation.

V^n	a_n
V^0	0.0
V^1	$1.7057035 \cdot 10^{-2}$
V^2	$-2.3301759 \cdot 10^{-7}$
V^3	$6.5435585 \cdot 10^{-12}$
V^4	$-7.3562749 \cdot 10^{-17}$
V^5	$-1.7896001 \cdot 10^{-21}$
V^6	$8.4036165 \cdot 10^{-26}$
V^7	$-1.3735879 \cdot 10^{-30}$
V^8	$1.0629823 \cdot 10^{-35}$
V^9	$-3.2447087 \cdot 10^{-41}$

Table 8.3: *Polynomial fit of the response for type-E thermocouples according to the NIST database [1] in terms of* $\mathrm{K}/\mu\mathrm{V}$.

The thermal product of the junction, however, depends on the particular design of the thermocouples. As the thermal junction is created by hand with abrasive paper, one needs to determine the relative amounts of chromel, constantan, and epoxy it contains, and each of them contributes to the final value. Due to the tapered design of the thermocouple, however, the contribution of epoxy is expected to be negligible. Lourel et al. performed a finite element analysis from which they obtained for the thermal junction a value that is 99.63% that of chromel, indicating that the contributions of the two other materials are negligible.

The thermophysical properties of chromel can be found in two references. Sundqvist measured experimentally the thermal conductivity and thermal diffusivity α [179]. The latter can also be used to infer the thermal product, as it can also be expressed as $\sqrt{\rho c k} = \sqrt{k^2/\alpha}$. Touloukian et al. review different sources which provide experimental data for the thermal conductivity and specific heat [192, 191]. These are used in conjunction with the density of chromel, $8730\ \mathrm{kg}/\mathrm{m}^3$ [115], to infer its thermal product. As depicted in figure 8.4 both sets of data are not for the same temperature range but have a significant overlap. The slight disagreement that can be observed between both sources over that temperature overlap can be attributed to experimental uncertainties.

Buttsworth [24] performed shock tube experiments with type-K thermocouples of a similar design, from which he reports a shot-to-shot variability of $\pm 9.2\%$ on the thermal product, although the associated uncertainty is only $\pm 3.3\%$. He identifies, as a possible explanation, impacts of diaphragm fragments which might have an influence on the junction structure. Furthermore, he notes a larger variability (but shorter response-time) when the junction is created with abrasive paper rather than with scalpel scratches. A possible explanation is the difficulty to quantify the number of junctions on each substrate, making it difficult to estimate the weighting to apply for each material.

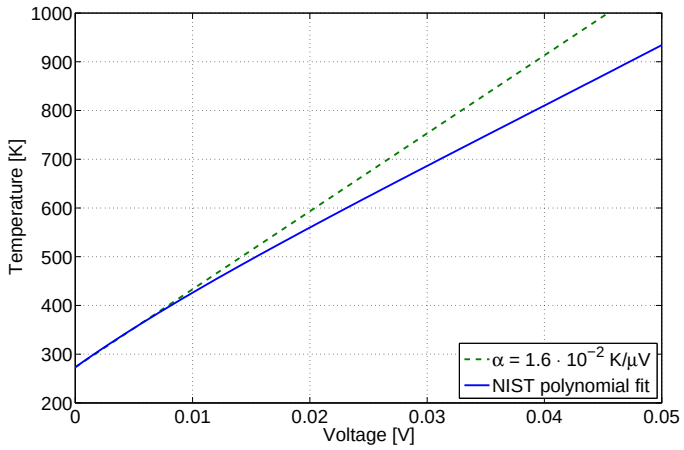

Figure 8.3: *Sensitivity of type-E thermocouples according to the calibration of Lourel et al. [112] compared to the polynomial fit of the NIST database [1]. The linear relation adopted by Lourel et al. appears to be a reasonable assumption for temperatures below* ~ 450 K *but not higher.*

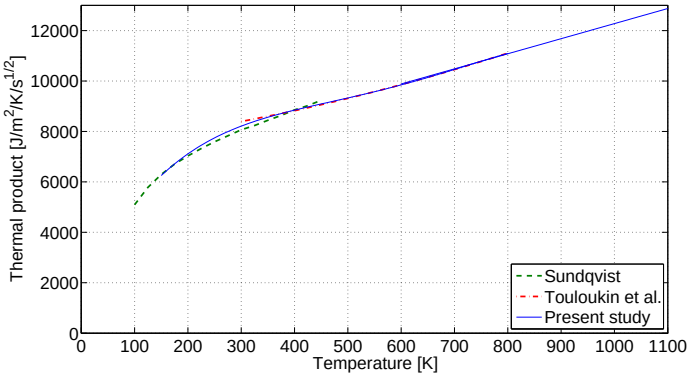

Figure 8.4: *Changes in thermal product with temperature for chromel (*90% *nickel* 10% *chromium according to the experimental data from Sundqvist [179] and Touloukian et al. [192, 191]. The values finally used for the post-processing of this experimental campaign are interpolated from both those datasets.*

Kovàcs and Mesler [101] note that when the junction is formed by a thin bridge over the insulation, the measured temperature signal overshoots the anticipated surface temperature history based on a single value for the thermal product, i.e. the thermal product is actually smaller than expected. They claim that the junction is, in that case, to some extent isolated from the bulk material and can thus not transmit heat as fast as if they were completely in contact with it [101]. Buttsworth points out the proximity of the insulation layer to the junction as a more likely explanation, especially for the high frequency components of the response [24]. Furthermore, he reports differences in response time (although it remains smaller or equal to 1 µs) were also noted depending on which type grit of abrasive paper was used [24]. That effect is assumed to be encompassed in the uncertainty of the thermal product.

Table 8.4: *Polynomial fit for the evolution of the thermal product with temperature, based on experimental values found in [179, 192, 191], in terms of* $\mathrm{J/m^2/K^2/s^{1/2}}$.

	$T < 600$ K	$T > 600$ K
T^n	a_n	a_n
T^0	$1.608 \cdot 10^3$	$6.294 \cdot 10^3$
T^1	$4.456 \cdot 10^1$	$5.984 \cdot 10^0$
T^2	$-1.086 \cdot 10^{-1}$	
T^3	$1.274 \cdot 10^{-4}$	
T^4	$-5.349 \cdot 10^{-8}$	

8.3.3 Signal post-processing

The post-processing is performed in two steps. The raw voltage measurement is first converted in temperature. An impulse response filter is then created, depending on the evolution of the thermal product with respect to time and the sampling frequency, and applied to the temperature measurements.

The conversion from voltage to temperature is simply obtained as:

$$T = \sum_{n=0}^{9} a_n \left(\frac{V}{K}\right)^n \tag{8.9}$$

where K is the amplification factor, in this case 100x, the values for each coefficient a_n are tabulated in table 8.3, and V is the voltage in µV.

Oldfield in [135] notes that the response of a thin-film gauge is a linear time invariant system for which the initial readings are steady. Therefore, that system (equation 8.8) can be characterized by an impulse response $h\,(t)$ and described by the following convolution integral:

$$q\,(t) = h\,(t) \star T\,(t) = \int_{-\infty}^{+\infty} h\,(\tau)\, T\,(t-\tau)\, d\tau \tag{8.10}$$

where $\star$ is the convolution symbol. Since that integral can be difficult to evaluate, and because there can exist singularities at the origin, the continuous-time domain form is replaced by its discrete-time

domain one:

$$q[n] = h[n] \star T[n] = \sum_{k=-\infty}^{+\infty} h[k]\, T[n-k] = \sum_{k=-\infty}^{+\infty} h[n-k]\, T[k] \tag{8.11}$$

where the continuous signal has been sampled at a sampling period T_s:

$$T[n] = T(nT_s) \tag{8.12}$$

for $n = -\infty, \cdots, -1, 0, 1, \cdots, +\infty$. The filter is created by deconvoluting a signal and its known response. For example, a parabolic temperature profile with respect to time indicates a step heat flux. The discrete convolution is, in the frame of this project, carried out using a fast Fourier transform implemented in Matlab. More detailed explanations can be found in [135].

A typical measurement is depicted in figure 8.5 for two consecutive shots of the $R = 3.0$ mm case. The passage of the test gas over the model can be identified by a parabolic increase in temperature, and a plateau on the heat flux trace. The recording time was typically around 100 µs for the model with $R = 3.0$ mm and $R = 6.0$ mm cases, and 200 µs for the model with $R = 17.5$ mm. A small peak in temperature (more pronounced for the heat flux) can be observed prior to the test time. The same kind of typical trace was observed for heat flux measurements in an expansion tube by Sharma et al., who postulated its origin to be a perturbed response of the thermocouple due to the sharp temperature difference in the interface separating the relatively hot accelerator gas from the colder test gas [169].

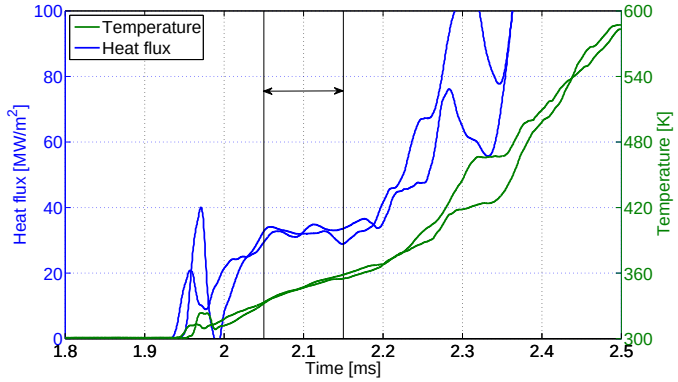

Figure 8.5: *Temperature and corresponding heat flux traces for two consecutive shots of the* $R = 3.0$ mm *case. The averaging period for the heat flux measurement is comprised within the two black solid lines, and lasts for* 100 µs.

8.3.4 Limiting assumptions

The thermocouples used for this experimental campaign differ from the idealized thin-film gauge presented in figure 8.1 in two main aspects: the substrate is not infinite, and the surface is not flat but curved. Buttsworth and Jones [25] show that, even for large heat fluxes, both these effects can be

neglected with a 1% tolerance in the accuracy if:

$$\frac{\alpha \Delta t}{R^2} \ll 4 \cdot 10^{-2} \tag{8.13}$$

The thermal diffusivity of chromel encountered during those test was bound by $\alpha \leq 10 \cdot 10^{-6}\ \mathrm{m}^2/\mathrm{s}$. The largest recording test time was 200 µs, with 50 µs of delay prior to measurement, thus an exposure to high heat flux of $\Delta t \simeq 250$ µs in total. The smallest radius was $3\ \mathrm{mm}$. A worst-case scenario for the group in equation is therefore $\alpha \Delta t / R^2 \simeq 2.8 \cdot 10^{-4}$. The hypothesis of infinite substrate and flat surface are thus verified.

8.4 Experimental results

The uncertainty on the heat flux measured consists thus of a contribution for the sensitivity $\pm 1.7\%$ [120] and another for the thermal product $\pm 9.2\%$ [24], resulting in an uncertainty of 10.9%. The uncertainty on a single measurement also needs to include the standard deviation of the measurement over the recording time $\sigma_{\text{meas}} q$. For each single measurement, one can thus write:

$$q = \widehat{q} \pm 0.109 \widehat{q} \pm \sigma_{\text{meas}} q \tag{8.14}$$

where $\widehat{q}$ stands for the mean of the measured heat flux. For most measurements, one can safely consider that $\widehat{q} \gg 10 \sigma_{\text{meas}}$ and thus ignore the latter. For a set of N measurements, the standard deviation over the whole set also has to be included. One can thus write:

$$q = \widehat{q} \pm \frac{0.109}{\sqrt{N}} \widehat{q} \pm \sigma_{\text{set}} q \tag{8.15}$$

Other strategies than the one presented here were followed during previous research campaign using the same instrumentation in the same facility. McIntyre et al. [120] also used a temperature-dependent thermal product. However, instead of considering chromel alone, as it is done for the present study, they considered the average of the two thermoelements. Since each of the thermal products remains within $\pm 7\%$ of the average, they then considered an uncertainty of $\pm 7\%$ on the heat flux calculated [120]. Capra and Morgan [29, 30], considered a fixed value for the thermal product, equal to 99.63% that of chromel based on numerical simulations of Lourel et al. [112], with a 7% uncertainty on the heat flux based on the work of McIntyre et al. [120].

The average value obtained for each condition, the corresponding number of shots performed, and the associated uncertainty are tabulated in table 8.5. It should be noted that the uncertainty is relatively high, evolving from $\sim 35\%$ for the model with $R = 17.5\ \mathrm{mm}$ case down to $\sim 15\%$ for the model with $R = 3.0\ \mathrm{mm}$. This simply translates the fact that a larger heat flux is easier to measure and that - for this test campaign - the uncertainty of the standard deviation on the free-stream conditions increases with the free-stream density (see table 6.2).

The heat fluxes can be rescaled in order to account for the variation in free-stream properties from shot to shot. Indeed, the generalized empirical correlations in equation 4.3 (and the corresponding analysis in section 4.1) show that:

$$q^c \propto h_\infty^{1.5} \sqrt{\rho_{\infty,\text{ref}}} \tag{8.16}$$

Assuming the radiative heat flux is small and will behave approximately in the same fashion, at least locally, we can express a modified total heat flux $q^{t\prime}$ as:

$$q^{t\prime} = q^t \frac{\left(v_{e,\text{ref}}^2/2\right)^{1.5}}{h_\infty^{1.5}} \frac{\sqrt{\rho_{\infty,\text{ref}}}}{\sqrt{\rho_\infty}} \tag{8.17}$$

where we defined the reference equivalent velocity $v_{e,\text{ref}} = 9.3\ \text{km/s}$ (see table 6.2) and the reference density so that its product with the cylinder radius is equal to $(\rho R)_{\text{ref}} = 30\ \text{kg/m}^2$.

		Non-modified		Modified	
R	N	q^t	σq^t	$q^{t\prime}$	$\sigma q^{t\prime}$
[mm]	[#]	[MW/m^2]	[MW/m^2]	[MW/m^2]	[MW/m^2]
17.5	14	41.29	14.05	42.37	17.42
6.0	10	182.90	33.59	164.26	34.45
3.0	14	254.36	41.94	238.37	40.95

Table 8.5: *Measurement q^t and modified measurement $q^{t\prime}$ of the stagnation point heat fluxes.*

8.5 Discussion

Let us now investigate how, based on the measurements tabulated in table 8.5 and the predictions emerging from various correlations presented in table 8.1, we can use the theoretical developments of chapter 4 to infer the various heat fluxes as accurately as possible

In order to insist on the novelty of the inclusion of radiative coupling, we will first go through the traditional approach of binary scaling, for which it is not taken into account. We will then show how the inclusion of non-adiabatic effects can drastically improve the agreement between the post-processed measurements and the theoretical values.

Our goal, in this exercise, is to retrieve the quantities that are common to the family of binary scaled flows which we are investigating. That is the product of the adiabatic (i.e. uncoupled) convective heat flux with a length scale of the flow $q_{\text{ad}}^c R$ and, to a lesser extent, the adiabatic radiative heat flux q_{ad}^r. The later is only partially true since, as demonstrated in section 8.1.2, it is actually altered by the changes in equilibrium properties of the shock layer identified in section 3.1.3.

8.5.1 Traditional approach

Negligible radiative heat flux

In the traditional approach of binary scaling, the experimentalist would either measure the total heat flux and the radiative heat flux separately, as described in section 4.4.1, or make simplifying assumptions. In this case, a possible approach would be to refer to the values tabulated in table 8.1 for the radiative heat flux to assume that the radiative heat flux is negligible compared to the convective one.

Before going any further, let us point out that, as we already mentioned earlier, these values were obtained with correlations that are used out of their envelope of confidence. A simple CFD simulation as the one we performed for a normal shock with Poshax demonstrates that the radiative heat flux is actually of the same order of magnitude as the convective one. Nevertheless, the assumption of a negligible radiative heat flux could appear as a sound first-order approximation.

In that case, we simply obtain $q^c_{\text{ad}}R$ as the average of the measurements that were performed:

$$q^r_{\text{ad}} \ll q^c_{\text{ad}} \qquad\qquad q^c_{\text{ad}} \simeq q^t_{\text{ad}} \tag{8.18}$$

$$q^c_{\text{ad}}R = \frac{1}{3}\sum_{n=1}^{3} q^c_{\text{ad},n}R_n \tag{8.19}$$

The results are tabulated in table 8.6 and the values based on the modified measurements are depicted in figure 8.6 (a) against experimental data for the total heat flux and correlations for the adiabatic convective heat flux (i.e. in this case assumed to be equal to the total heat flux).

The results from our binary scaled model fall just within the error margin of the experimental data. The values derived from the correlations also fall at the edge of the error margin, but not especially in agreement with the results of our model. Overall, one could be tempted to attribute these differences to experimental uncertainties (i.e. mainly on free-stream conditions). Moreover, unless other practical limitations prevent it, it is likely that during an actual experimental campaign a model as large as possible would be used. In the present case, it would thus be the $17.5\ \text{mm}$ radius cylinder, for which both the binary scaled model and the correlations fall within the uncertainty of the experimental data.

Measurement	$q^c_{\text{ad}}R$ $[\text{kW/m}]$	q^r_{ad} $[\text{MW/m}^2]$
modified	814.05	$\ll$
non-modified	861.02	$\ll$

Table 8.6: *Estimation of the heat flux quantities common to the family of binary scaled flows investigated in this test campaign in the hypothesis of an adiabatic flow with negligible radiative heat flux.*

Numerical estimation of the adiabatic radiative heat flux

Another option would be to account for the radiative heat flux. If the radiative heat flux is not measured experimentally, because of one or the other of the disadvantages mentioned in section 4.4.1, the only remaining option is to estimate it with CFD. One can imagine that, because of the complexity and low TRL of radiatively coupled CFD models, an uncoupled simulation is preferred, such as for example the estimations presented in table 8.2.

In that case, we obtain $q^c_{\text{ad}}R$:

$$q^c_{\text{ad}}R = \frac{1}{3}\sum_{n=1}^{3}\left(q^t_{\text{ad},n} - q^r_{\text{ad},n}\right)R_n \tag{8.20}$$

The results are tabulated in table 8.7 and the values based on the modified measurements for an optically thick flow are depicted in figure 8.6 (b) against experimental data for the total heat flux and correlations for the adiabatic convective heat flux.

The agreement between the various methods is obviously very poor, with the value of $q^c_{\text{ad}}R$ being approximately half of what was obtained when neglecting the radiative heat flux. Without the proper tools to account for the effect of the coupling on the radiative heat flux or to measure it directly, it is overestimated and the convective heat flux is thus underestimated. This approach is conservative for the radiative heat flux but not for the convective one. Because the former has been estimated through CFD, the experiment is useless.

Optical thickness	Measurement	$q^c_{\text{ad}}R$ [kW/m]	$q^r_{\text{ad},1.2}$ [MW/m^2]	$q^r_{\text{ad},2.0}$ [MW/m^2]	$q^r_{\text{ad},2.5}$ [MW/m^2]
thin	modified	441.54	39.43	83.43	105.67
	non-modified	521.44	39.43	83.43	105.67
thick	modified	316.96	52.28	114.43	126.72
	non-modified	396.87	52.28	114.43	126.72

Table 8.7: *Estimation of the heat flux quantities common to the family of binary scaled flows investigated in this test campaign in the hypothesis of an adiabatic flow with an estimation of the radiative heat flux based on CFD.*

8.5.2 Non-adiabatic gas phase and non-ideal binary scaling

In the previous section we have determined that, *if the radiative heat flux cannot be measured or evaluated with radiatively coupled CFD simulations*, it can simply be neglected. The convective heat flux that is then obtained is therefore a conservative estimate. However, that preliminary result could be refined.

From the developments done in the first part of this document, we know that a change of length scale in a family of binary scaled flows will affect the stagnation point heat fluxes in two ways. First, through non-binary chemistry as discussed in section 3.1. Its effect on the radiative heat flux has already been pointed out when presenting the adiabatic CFD estimation in table 8.2.

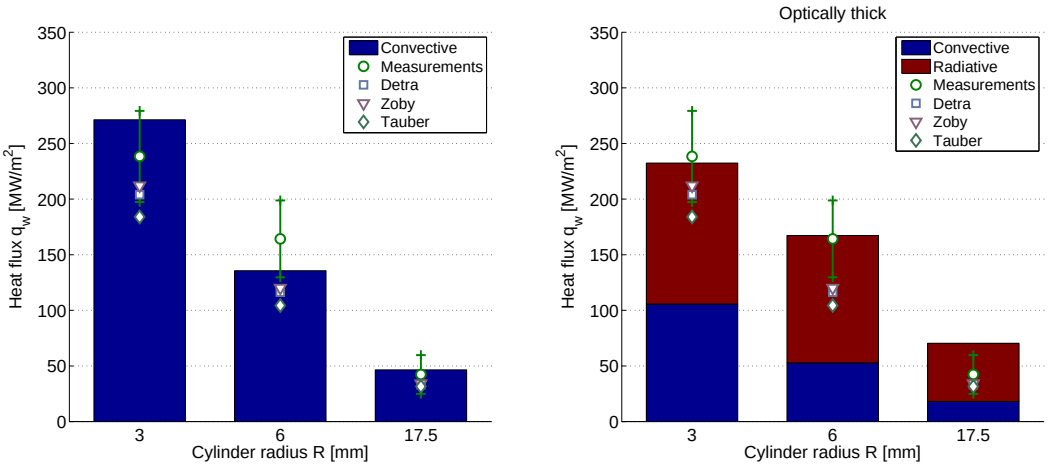

(a) (b)

Figure 8.6: *Visual comparison of the $q^c_{ad}R$ and q^r_{ad} fits, experimental measurements of the total heat flux, and correlations for the adiabatic convective heat flux. Both figures were obtained with the traditional approach of ground-to-flight extrapolation, i.e. not accounting for the radiative coupling. Figure (a) is built upon the assumption of a negligible radiative heat flux, and figure (b) using the adiabatic radiative heat flux values obtained with Poshax for an optically thick flow.*

We will assume that the effect of non-binary chemistry on the convective heat flux is negligible. Indeed, as a first order approximation one can link the radiative heat flux to the fourth power of the temperature using Stefan-Boltzmann's law $q^r_{\text{ad}} \propto \sigma T^4$ while, from equation 4.8, the conductive heat flux is only directly proportional to the temperature $q^{\text{cd}}_{\text{ad}} \propto T$.

Second, through the radiative coupling as discussed in section 3.3 and more specifically for heat fluxes in section 4.2. It should be noted that the developments made in these sections only concerns the comparison between an uncoupled flow and it coupled counterpart (e.g. adiabatic and non-adiabatic). They are therefore valid on their own, independently from considerations regarding the non-binary chemistry.

In this section, we will determine how these can be taken into account. First only considering the non-adiabaticity of the gas phase, i.e. considering a constant radiative heat flux. Second, taking into consideration the effect of non-binary chemistry on the radiative heat flux.

Ideal binary scaling

Equation 4.30 is then solved simultaneously for all three datapoints. That system of linear equation can be represented in the matricial form $Ax = B$ as:

$$\begin{bmatrix} q^c_{1.2}/q^c_{\text{ad},1.2}R_{1.2} & q^r_{1.2}/q^r_{\text{ad},1.2} \\ q^c_{2.0}/q^c_{\text{ad},2.0}R_{2.0} & q^r_{2.0}/q^r_{\text{ad},2.0} \\ q^c_{2.5}/q^c_{\text{ad},2.5}R_{2.5} & q^r_{2.5}/q^r_{\text{ad},2.5} \end{bmatrix} \begin{bmatrix} q^c_{\text{ad}}R \\ q^r_{\text{ad}} \end{bmatrix} = \begin{bmatrix} q^t_{1.2} \\ q^t_{2.0} \\ q^t_{2.5} \end{bmatrix} \tag{8.21}$$

where the non-adiabatic ratios q^c/q^c_{ad} and q^r/q^r_{ad} were tabulated in table 8.2[2]. The total heat fluxes q^t on the right-hand correspond to the experimental measurements tabulated in table 8.5. The only unknowns are thus the product $q^c_{\text{ad}}R$ and q^r_{ad}, which are both constant across all binary scaled flows.

Because the system is overdetermined[3], the solution to that system computed in Matlab as $x = A\backslash B$ will yield a least-square solution.

Eight sets of solutions were obtained, using different models for the optical thickness, re-scaling of measurements, and non-adiabatic radiative heat flux. The results are tabulated in table 8.8. Each set is also depicted in figures 8.7.

The agreement between the adiabatic convective heat flux and the values predicted by the correlations is relatively good, as is the agreement between the coupled total heat flux and the experimental measurements. The best results are achieved with the modified measurements (i.e. accounting for slight free-stream differences) rather than the original one. For what concerns the convective heat flux, changing the coupling model and the optical thickness will incur a change of 2% at most. For the radiative heat flux, however, an optically thick flow with Edquist's coupling model yields a value almost twice as large as an optically thin flow with Tauber and Wakefield's coupling model. All these values remain nevertheless in the same order of magnitude as what was obtained with CFD (table 8.2) and surprisingly close to the correlation of Detra but much larger than these of Tauber (table 8.1).

The overall result is thus better than what had been achieved in section 8.5.1. First, the convective heat flux is estimated with greater accuracy. In the most conservative case (optically thick with Tauber and Wakefield) it appears to be $\sim 10\%$ smaller than what was previously obtained. Second, the radiative heat flux could be evaluated in terms of order of magnitude and bounded to maximum ~ 75 $\mathrm{MW/m^2}$.

The least satisfying result is obtained for the middle-size cylinder, $R = 6.0$ mm. A likely explanation is that the similarity parameters for this condition are the further from the two others, both in terms of free-stream enthalpy (table6.2) and density-length product (table 6.5). It is thus also the one that yields the largest error when applying equation 8.17.

Non-ideal binary scaling

It is possible to be even more accurate taking into account the effect of non-binary chemistry on the radiative heat flux. Instead of relying on a least-square solution for the adiabatic radiative heat flux, the later is thus directly estimated with CFD. Equation 8.21 is thus simplified down to:

$$\begin{bmatrix} q^c_{1.2}/q^c_{\text{ad},1.2}R_{1.2} \\ q^c_{2.0}/q^c_{\text{ad},2.0}R_{2.0} \\ q^c_{2.5}/q^c_{\text{ad},2.5}R_{2.5} \end{bmatrix} \left[q^c_{\text{ad}}R\right] = \begin{bmatrix} q^t_{1.2} - \left(q^r_{1.2}/q^r_{\text{ad},1.2}\right) q^r_{\text{ad},1.2} \\ q^t_{2.0} - \left(q^r_{2.0}/q^r_{\text{ad},2.0}\right) q^r_{\text{ad},2.0} \\ q^t_{2.5} - \left(q^r_{2.5}/q^r_{\text{ad},2.5}\right) q^r_{\text{ad},2.5} \end{bmatrix} \tag{8.22}$$

[2]The attentive reader will note that we are indirectly taking the effect of non-binary chemistry into account, since the CFD estimations of the radiative heat flux were used to determine the Goulard number.

[3]There are three equations for two unknowns. Alternatively, the matrix A has three rows for only two columns.

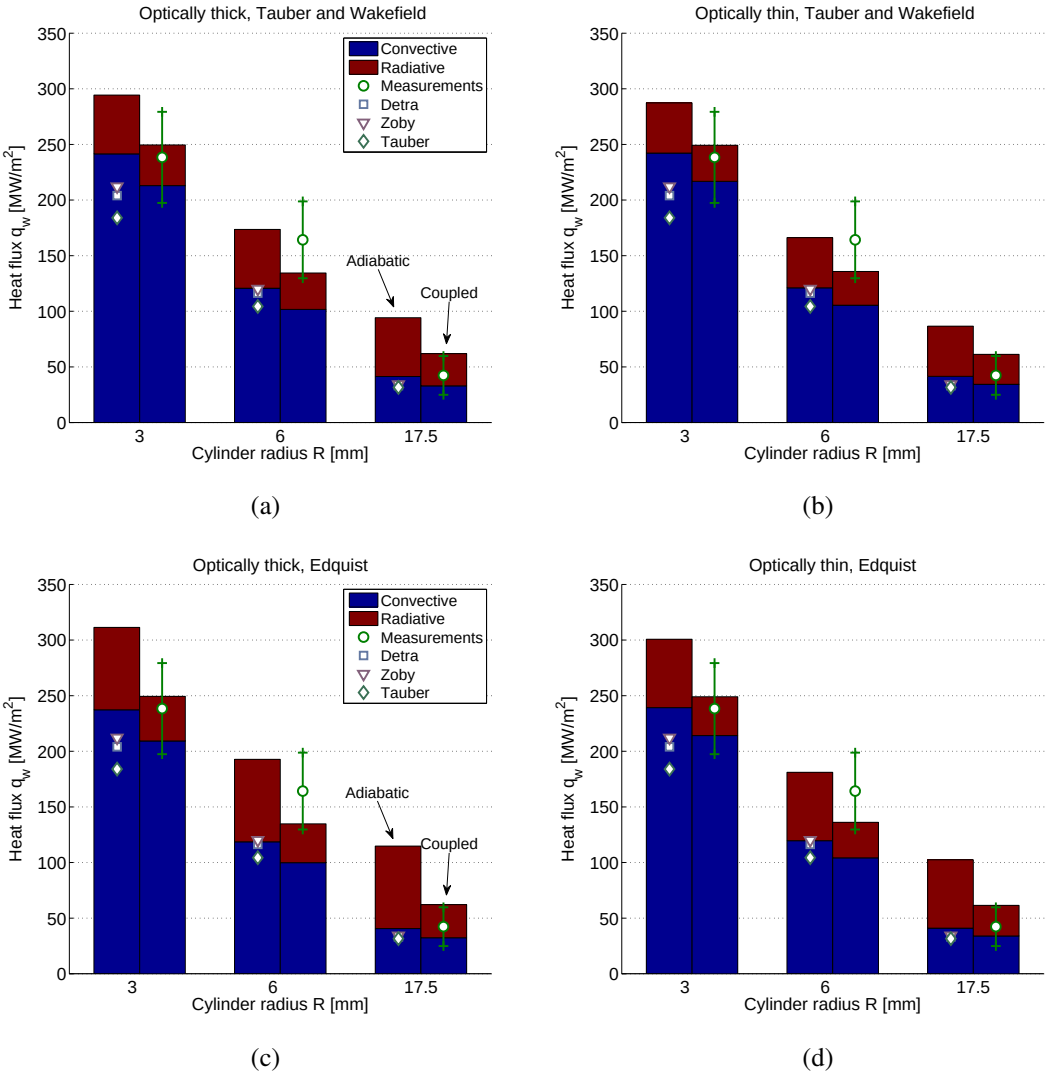

Figure 8.7: *Visual comparison of the $q^c_{ad}R$ and q^r_{ad} fits, experimental measurements of the total heat flux, and correlations for the adiabatic convective heat flux. The radiative coupling is accounted assuming a* ***constant heat flux*** *for an optically thin (a, c) and an optically thick (b, d) flow, and the model of Tauber and Wakefield (a, b) and that of Edquist (c, d) for the effect of the coupling on the radiative heat flux.*

Coupling model	Optical thickness	Measurement	$q^c_{\text{ad}}R$ $[\text{kW/m}]$	q^r_{ad} $[\text{MW/m}^2]$
Tauber and Wakefield [188]	thin	modified	726.67	45.12
		non-modified	783.78	48.09
	thick	modified	724.42	52.87
		non-modified	781.50	56.33
Edquist [42]	thin	modified	717.73	61.51
		non-modified	773.69	65.80
	thick	modified	711.85	74.10
		non-modified	767.61	79.17

Table 8.8: *Estimation of the heat flux quantities common to the family of binary scaled flows investigated in this test campaign, accounting for the radiative coupling but not for the effect of the non-binary chemistry.*

where the values for q^r_{ad} are retrieved from table 8.2. We are thus left with three equations for one unknown.

As for the previous post-processing method, eight sets are obtained. They are all tabulated in table 8.9 and the results obtained with the modified measurements are depicted in figures 8.8.

The agreement between the adiabatic convective heat flux and the values predicted by the correlations is excellent, as is the agreement between the coupled total heat flux and the experimental measurements. Again, the best results are achieved with the modified measurements (i.e. accounting for slight free-stream differences) rather than the original one. The coupled total heat flux falls in all cases within the error margin of the experimental data. The best agreement with the correlation for the adiabatic convective heat flux is obtained for an optically thin gas with Edquist's coupling model. It is also the most conservative one in terms of convective heat flux. The most conservation solution for the radiative heat flux is obtained with Tauber and Wakefield's model for an optically thick flow.

Another step in accuracy has thus been achieved. The convective heat flux is a further $\sim 12\%$ smaller than with the constant radiative heat flux, and thus a total of $\sim 21\%$ smaller than what had been obtained with the traditional approach. The results obtained for the radiative heat flux are irrelevant since it is part of the boundary conditions of the problem we posed rather than its solution.

8.6 Conclusion

In this chapter, we have applied to a practical experimental case the theoretical development of chapters 4 and 3 regarding the evolution of the stagnation point heat flux with changes of length-scale in a family of binary scaled flows. As expected, it appears that both non-binary chemistry *and* radiation coupling affect the wall heat fluxes. The former causes the radiative heat flux to decrease as the length-scale of the flow increases. The latter has the decreasing effect but both for the radiative and the convective heat flux. Overall, ground-to-flight extrapolation based on laboratory measurement will overestimate the heat flux.

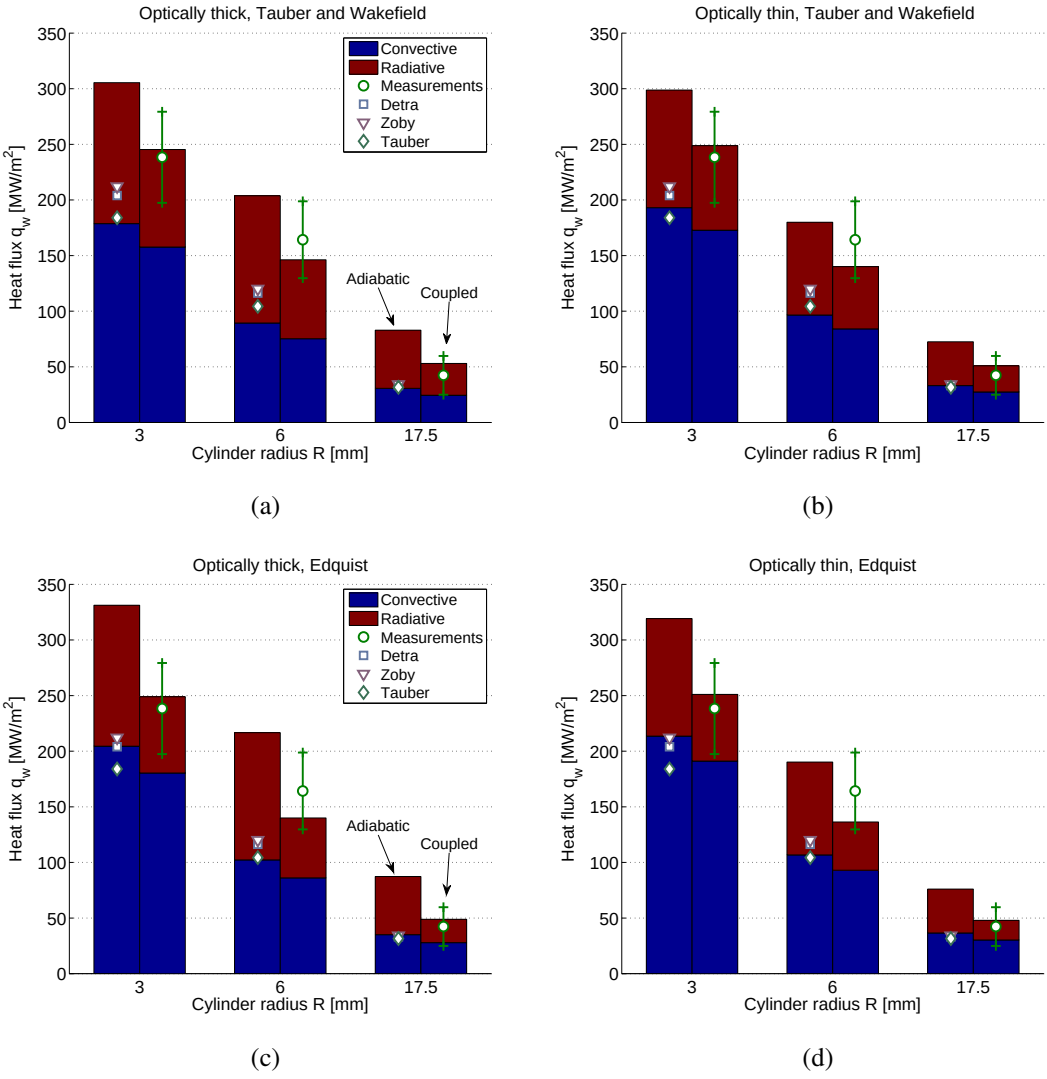

Figure 8.8: *Visual comparison of the $q^c_{ad}R$ and q^r_{ad} fits, experimental measurements of the total heat flux, and correlations for the adiabatic convective heat flux. The radiative coupling is accounted using the* ***adiabatic radiative heat flux values obtained with Poshax*** *for an optically thin (a, c) and an optically thick (b, d) flow, and the model of Tauber and Wakefield (a, b) and that of Edquist (c, d) for the effect of the coupling on the radiative heat flux.*

Coupling model	Optical thickness	Measurement	$q^c_{\text{ad}}R$ [kW/m]	$q^r_{1.2}$ [MW/m^2]	$q^r_{2.0}$ [MW/m^2]	$q^r_{2.5}$ [MW/m^2]
Tauber and Wakefield [188]	thin	modified	579.24	23.54	55.98	75.98
		non-modified	645.35	23.54	55.98	75.98
	thick	modified	536.21	28.65	70.95	87.69
		non-modified	603.38	28.65	70.95	87.69
Edquist [42]	thin	modified	640.66	17.66	43.38	59.91
		non-modified	706.77	17.66	43.38	59.91
	thick	modified	613.55	20.96	53.90	68.56
		non-modified	680.71	20.96	53.90	68.56

Table 8.9: *Estimation of the heat flux quantities common to the family of binary scaled flows investigated in this test campaign, accounting for the radiative coupling and the effect of the non-binary chemistry.*

Based on this observation, we proposed a new methodology to scale the stagnation point heat fluxes of binary scaled flows, and thus to perform more accurate ground-to-flight extrapolation. The method consists in the following steps:

1. An experiment is performed in a high-enthalpy facility for a flow that belongs to the same binary scaling family as the flow under investigation. During that experiment, the total stagnation point heat flux q^t_{lab} is measured.

2. The adiabatic (uncoupled) radiative heat flux is computed with CFD simulations both for the laboratory flow $q^r_{\text{ad,lab}}$ and the flow of interest $q^r_{\text{ad,flight}}$.

3. The Goulard number Γ of each flow is determined (equation 3.51), as well as the corresponding non-adiabatic ratios using the most appropriate models (e.g. equation 4.20 for the radiative heat flux and equation 4.1 for the convective heat flux).

4. The adiabatic convective heat flux in flight is then retrieved as:

$$q^c_{\text{ad,flight}} = \left(\frac{q^c_{\text{ad}}}{q^c}\right)_{\text{lab}} \frac{R_{\text{flight}}}{R_{\text{lab}}} \left(q^t_{\text{lab}} - \left(\frac{q^r}{q^r_{\text{ad}}}\right)_{\text{lab}} q^r_{\text{ad,lab}}\right)_{\text{lab}} \tag{8.23}$$

5. At this stage an estimation is available for both the adiabatic radiative and convective heat fluxes in flight, the former based on CFD and the later based on experimental measurements. The coupled counterparts are then simply obtained based on the non-adiabatic ratios derived at step 3.

That methodology was successfully validated when applying it to three different flows of the same binary scaling family, as illustrated in figures 8.8. The coupled total heat fluxes fall within the uncertainty margins of the experiments, and the adiabatic convective heat fluxes correspond to what is obtained with some of the well-established correlations.

Let us insist on the fact that the reason we performed these experiments over three flows of the same binary scaling family is to validate that new methodology. One experiment is sufficient for future applications, although numerous flows can help increasing the level of confidence in the results

by cross-validating them. This is in our interest, both as scientists in order to come closer to the truth and as engineers to perform more accurate ground-to-flight extrapolation for the atmospheric entry flows under investigation.

This work fills a gap. Indeed, in the event of a flow with significant radiative coupling, there is no accurate method to determine the heat fluxes in flight with a reasonable degree of accuracy. Indeed, CFD simulations of radiatively coupled flows are complex and require important computational resources. Moreover, the codes that allow to perform these simulations remain limited to the research domain and are characterized by a low TRL.

Experiments, on the other hand, only allow for a conservative estimation of the heat fluxes. If the total heat flux is measured alone, a conservative estimation can be provided for the convective heat flux but nothing can be concluded about the radiative one.

The approach proposed here is a mix of experiments, CFD, and an informed use of engineering correlations. Compared to an exclusively numerical or exclusively experimental strategy, it presents the following advantages:

- First and foremost, it allows to determine the different heat fluxes with a greater accuracy. This is extremely important from a design point of view. Let us for example consider the practical case of the experimental campaign conducted here: what is the effect of a $\sim 20\%$ more accurate determination of the convective heat flux? Laub and Venkatapathy observed a correlation in the design of ablative TPS between its mass fraction μ_{TPS} (i.e. the fraction of the entry probe mass devote to TPS) and the total heat load Q^t [102]:

  $$\mu_{\text{TPS}} = 0.091 \left(Q^t\right)^{0.51575} \tag{8.24}$$

  Assuming the correction on the convective heat flux directly translates into the total heat load, this corresponds thus to a reduction of 11% of the TPS mass fraction. For a craft of the type of the Pioneer Venus probes with a mass of $\sim 200\ \text{kg}$, this corresponds to an additional $\sim 30\ \text{kg}$ made available for experiments, batteries, or whatever is needed for the sake of the mission.

- A physical-based approach of the phenomenon driving the evolution of the heat fluxes are actually accounted for, within the limitation of the different models used, rather than ignored or embedded in large safety factors and uncertainty margins. Therefore, not only are the results more accurate, but they can also be looked at with greater confidence.

- Lastly, from the perspective of the experimentalist the work is greatly simplified. Indeed, the only measurement needed is the total heat flux, which is relatively simple to obtain (and in any case simpler than measuring the radiative heat flux), conjointly with two CFD simulations. Past results can also be reinterpreted in the light of these new developments.

Chapter 9

Stagnation line radiation

"But in the heavens we discover by their light, and by their light alone, stars so distant from each other that no material thing can ever have passed from one to another; and yet this light, which is to us the sole evidence of the existence of these distant worlds, tells us also that each of them is built up of molecules of the same kinds as those which we find on earth. "

- James Clerck Maxwell [117]

Throughout chapters 7 and 8, experimental evidence has been presented to demonstrate that the three binary scaled flows designed in chapter 6 are indeed radiatively coupled to various degrees. The effects of this different degree of coupling confirm that they do indeed correspond to the theoretical developments made in the first part of this thesis. The purpose of this chapter is to provide a third set of argument to back up these theoretical developments. After the shock standoff and the heat flux, it is now the spectral radiance along the stagnation line that is examined.

We first present the test set-up, including optical hardware and software post-processing procedures. The spectral radiation along the stagnation line is then examined for two regions of the spectrum: a portion of the near-infrared, and part of the C_2 Swan system. As expected, it appears that radiation (i.e. temperature) is higher as the length-scale of the flow decreases, with stronger atomic lines and less molecular features.

9.1 Test set-up

9.1.1 Optical hardware

This chapter is dedicated to the measurements performed using emission spectroscopy. Two types of measurements were done: first with spectral resolution and spatial resolution along the stagnation line, second for a single frequency (or frequency band) with two-dimensional spatial resolution. In

both cases, the camera used was a Princeton Instruments PI-MAX image-intensified charge-coupled device (ICCD) with a SB slow gate generation II image intensifier. Spectral resolution was obtained by coupling the ICCD camera to an Acton Research Spectra Pro 2300i spectrometer, a Czerny-Turner spectrometer with a pair of collimating mirrors having a $300\mathrm{mm}$ focal length[1].

The ICCD array has a resolution of 1024 pixels in the horizontal axis, used either as wavelength or spatial cross-stream dimension, and 256 pixels in the vertical axis, used in both cases as spatial streamwise dimension. Each pixel is a square with an approximately 26 μm-long side. The number of photons detected by each element of the array (i.e. pixel) is represented by a 16-bit integer, resulting thus in a value from 0 to 65535.

The windows mounted on each side of the test section were made out of UV-grade synthetic fused silica. Any additional optical elements required were chosen depending on the wavelength range observed: aluminum-coated or silver-coated mirrors respectively for the shorter or longer wavelengths. A periscope was used to rotate the image by an angle of $90\ ^\circ$ so that the horizontal streamwise direction would be aligned with the vertical spectrometer slit, and to adjust the height of the light-beam.

Two different optical arrangements were used for the spectrally resolved images: with a magnification factor for the models with radii $R = 6.0$ mm and $R = 3.0$ mm, and without magnification for the model with a radius of $R = 17.5\mathrm{mm}$. These are based on the simple requirement that the shock layer needs to be resolved, and thus be spread over as many pixels as possible.

In both cases, flat turning mirrors were used to direct the light beam while a concave mirror with a focal length of $f = 500$ mm was used to refocus the image of the shock layer onto the entrance slit of the spectrometer. All mirrors were positioned so as to keep the reflection angle below $5\ ^\circ$ in order to limit astigmatism as much as possible. The flow was focused onto the spectrometer slit. Taking geometrical constraints into account, the dimensions that were finally settled on are detailed in table 9.1. It should be noted that, for the largest model, the image of the shock layer on the ICCD array (275 pixels) appears larger than the array itself (256 pixels). However, the estimations for the shock standoff distance were based on the correlation of Inger listed in table 7.1. It does not account for the radiative coupling which causes the shock standoff to deflate, as observed in section 7.3.

The limiting aperture of the concave mirror was adapted depending on the test condition, so as to control its focal ratio (also called f-number). The latter is the ratio between the mirror's focal length and the diameter of the mirror's entrance pupil D_a (i.e. the mirror itself or the limiting aperture), $f_N = f/D_a$. Its value will affect the value of the circle of confusion c_c. The depth of field is the range over which the flow will be accurately resolved. In this case, we require it to be no shorter than the cylinder's length. The circle of confusion is the size of a spot as seen through the optical system.

The depth of field and circle of confusion are linked to one another through the following relation:

[1] Different parameters can be acted upon on the spectrometer itself: the centre wavelength, grating groove density, slit width, exposure, and gain. Spectral resolution is mostly controlled by the entrance slit and grating groove density. A large entrance slit result in a stronger signal but also in a loss of resolution. As for the diffraction grating, denser grooves will result in more spectral resolution but also in a smaller imaged spectral range. Only two different ones where used in the frame of this work: 150 lines/mm and 600 lines/mm.

$$c_c = M D_a \frac{D_f/2}{a + D_f/2} \tag{9.1}$$

Two apertures were used: $D_a = 19.5$ mm, and $D_a = 10$ mm in diameter, resulting in focal ratios of 26, and 50. The mirror without an iris has a diameter of $D_a = 50.8$ mm, and thus a focal ratio of $f_N = 9.84$. The size of the circle of confusion obtained for a point at the edge of the cylinders are listed in table 9.1 for the three cases: 1 without aperture ($D_a = 50$ mm, the diameter of the mirror), 2 for $D_a = 19.5$ mm and 3 for $D_a = 10$ mm. Clearly, the introduction of an aperture improves the spatial resolution of the spectrometer[2]. Nevertheless, the circle of confusion seems relatively important as compared to the shock standoff. However, it should be reminded that these numbers were obtained for the edges of the model and are thus extreme values.

In an ideal world the circle of confusion should be smaller than the size of a pixel on the ICCD array. Practically, however, this would require an excessively small aperture and significantly reduce the amount of light collected[3].

R [mm]	D_f [mm]	f [mm]	M [x]	Δ [mm]	Δ [pixels]	$c_{c,1}$ [pixels]	$c_{c,2}$ [pixels]	$c_{c,3}$ [pixels]
17.5	95	500	1.00	7.16	275	88	34	17
6.0	75	500	2.21	2.13	180	212	81	41
3.0	35	500	2.21	1.09	92	101	39	20

Table 9.1: *Main characteristics of the optical arrangements. The depth-of-field is simply considered as equal to the cylinders' length. The estimations for the shock standoff distance were based on the correlation of Inger listed in table 7.1. The three cases correspond to:* 1 *without aperture (*$D_a = 50$ mm*, the diameter of the mirror),* 2 *for* $D_a = 19.5$ mm *and* 3 *for* $D_a = 10$ mm

Lastly, filters were used to prevent the second order source caused by diffraction of the spectrometer's holographic grating[4].

[2] Using an aperture also has the advantage of further reducing astigmatism.

[3] Indeed, the solid angle of the aperture ω is obtained as:

$$\omega = \pi \left(\frac{D_a}{2a} \right)^2 \tag{9.2}$$

The amount of light collected decreases thus as the square of the limiting aperture.

[4] Indeed, a plane wave incident to a grating of groove spacing d at an angle θ_i will diffract with an angle θ_m according to the relation:

$$d\,(\sin\theta_i + \sin\theta_m) = m\lambda \tag{9.3}$$

where m is an integer and λ the wavelength. As a result, light of wavelength λ diffracted at the order $m = 1$ will coincide (in terms of angle of diffraction) with light of wavelength $\lambda/2$ diffracted at the order $m = 2$.

9.1.2 Image post-processing

The raw image that is recorded $S_{\text{meas}}(x, y)$ may be expressed as:

$$S_{\text{meas}}(x, y) = S_{\text{raw}}(x, y) + B_{\text{raw}}(x, y) + N_{\text{raw}}(x, y) \tag{9.4}$$

where S is the signal, i.e. the image of the slit spread over a range of wavelengths, B the background noise mostly due to the thermal noise of the CCD array, and finally N the shot noise. The subscript raw is to remind that these values are obtained in *"counts"*, and arbitrary unit that still need to be converted in spectral irradiance.

The shot noise N is for the most part high frequency and originates from two sources: cosmic rays and hot pixels. The former have typically a very high energy sufficient to saturate a pixel and even cause an overflow into its neighbors. They are random and transient. The latter are actually a malfunction of the CCD array due to pixels having a rate of charge leakage higher than the average. Since they are recurring, they can be identified and remove during the post-processing. Two filters are applied to remove most of that noise:

1. A 2-D adaptive noise-removal filter based on the Wiener method [108], implemented as a Matlab function under the name wiener2. It estimates the value of each pixel based on the statistical value in its local neighborhood. In this case, the filtering was found to perform better using neighborhoods of size 3 by 5 pixels respectively in the wavelength and spatial dimensions. Only three pixels are used in the wavelength dimension because atomic transition lines and molecular band structures are inherently high frequency features that can rise sharply.

2. A smoothing filter based on the Savitzky-Golay method, implemented as Matlab function under the name sgolayfilt. For the same reason mentioned above regarding high frequency spectral features, that filter operates only in the spatial direction. In this case, the filtering was found to perform better when using vectors of 30 pixels and a second order polynomial.

The background noise B is accounted for by measuring it prior to the shot. The resulting background image consists in the average of the accumulation of a series of images, each of them being taken with the same parameters (e.g. exposure, slit width, etc.) as the image of the shot. Averaging a series of images allows to smooth out the shot noise N inherent to each of them. However, as a series of images is taken the camera heats up and could thus artificially inflate the background image. This was minimized by limiting the accumulation to 50 images.

The calibration image, needed to convert from counts to spectral radiance, is affected by all the elements of the optical system: solid angle bound by the aperture, reflectivity of the different mirrors, transmissivity of air, transmissivity of the filter (if any), and response of the spectrometer, which itself depends on different elements such as the internal mirrors, grating efficiency, response of the camera, etc. In order to account for all of these at once, a calibration source is placed at the location of the model's centerline during the tests. The calibration source is a Labsphere CSTM-LR-2Z-4

whose spectral radiance is a known quantity. The response of each pixel, measured in number of counts, can thus be compared with the radiance of the lamp at the corresponding frequency, and a two-dimensional calibration image is obtained for each set of optical parameters that were used.

Lastly, the measured spectral radiance was divided by the length of the cylinder (i.e. the length of cross-stream integration). Indeed, we have seen in section 3.3.2, and more particularly in equation 3.45, that the radiative intensity is preserved through the binary scaling. Assuming the flow is optically thin[5], the spectral radiance per unit of length provides thus an appropriate point of comparison between the different flow conditions.

Experimental uncertainties associated with spectral radiance are complex to quantify. It has been shown in previous studies, such as [170, 211] that the shot-to-shot variation of the spectral radiance is in the order of $10 - 20\%$. The error on the measurement itself has been estimated to be 8% for a similar test set-up [105]. This leads to a total relative error of $\pm 22\%$ for the spectral radiance. The same study has shown that the broadening is well represented with a Voigt profile with a full width at half-maximum (FWHM) of $1.2\ \mathrm{nm}$, the Gaussian and Lorentzian contributions being respectively 1.1 and $0.3\ \mathrm{nm}$ [105]. While these numbers cannot be readily applied to the present case, they give at least an order of magnitude of what is to be expected.

9.2 Experimental results and discussion

Two regions were more specifically inspected. First, the near-infrared (IR) from $750\ \mathrm{nm}$ to $860\ \mathrm{nm}$, which is supposed to be densely populated in atomic signatures of carbon and oxygen. Second, the blue to green part of the visible spectrum, which is the location of part of the C_2 Swan system.

Prior to presenting the results, it is worth noting that the shock layers for the flows around the small and medium model are only respectively $\sim 1\ \mathrm{mm}$ and $\sim 2\ \mathrm{mm}$ thick (referring to table 9.1). Resolving them with a fair level of longitudinal resolution (streamwise) is thus a technical challenge. Given the poor resulting accuracy, no conclusions will be withdrawn regarding the different regions of the shock layer (i.e. extent of the non-equilibrium region, etc.).

9.2.1 Near-infrared from $750\ \mathrm{nm}$ to $860\ \mathrm{nm}$

The near-IR region is populated with atomic signatures of oxygen, notably with the bright triplet at $777\ \mathrm{nm}$. Atomic oxygen is produced through the dissociation of CO_2, CO, NO, and O_2, all of which are ternary in the backward direction. It is also involved in a series of neutral exchanges that are binary in both direction and thus insensitive to the length-scale of the flow. Recalling the developments presented in section 3.1, we can conclude for this specific case that a shorter characteristic length-scale should correspond to a higher concentration in O.

[5]Referring back to equation 3.39, if $\tau_\nu = 0$ then the irradiance remains constant despite of the integration length.

Moreover, given that the governing reactions are dissociative, all things being equal a higher temperature will lead to a higher concentration in O. In section 3.3, we have identified that within a family of binary scaled flows the radiative coupling is weaker for flows with a smaller characteristic length-scale. Therefore, the shock-layer of these flows contains more energy, which tends to increase their temperature. Radiation coupling will thus have the same effect as that of binary chemistry identified in the previous paragraph: a shorter characteristic length-scale should also correspond to a higher concentration in O.

Overall, the signature of O should thus be the strongest for the smaller model, due to both a higher concentration and a higher temperature. Although we would not be able to differentiate the relative contributions of the radiative coupling and the non-binary chemistry, at least we will be able to conclude that these observations are due to side effects of the binary scaling.

This is indeed what is observed in figure 9.1, where the spectral radiance maps are depicted for each of the different models. The vertical scale is the streamwise distance, with the dashed lines indicating the model edge (top) and the shock edge (bottom) and the arrow indicating the direction of the flow. The horizontal scale is the wavelength. The vertical scale and spectral radiance intensity have been adapted to increase the visibility of the different figures.

Two observations can be done. First, the level of radiance in the shock layer is, as expected, the highest for the smallest model (figure 9.1 c), almost twice as important as for the largest model (figure 9.1 a). Second, while the same lines are identified in all three flows, they are clearly more pronounced for the smallest model (figure 9.1 c), indicating a larger concentration in dissociated species and / or a higher temperature.

9.2.2 C_2 Swan system in the visible green

The second region that was investigated is the visible green from $530\ \mathrm{nm}$ to $570\ \mathrm{nm}$. There lies the $(A-X)\,\Delta v=+1$ part of the C_2 Swan system. While the C_2 Swan bands are generally a relatively unimportant contributor, they can be considered as a good indicator for the quality of the scaling. Indeed, production of C_2 is obtained through neutral exchange between either CO or CN with an atom of carbon C. The main reaction in which C_2 is involved is then its dissociation in atomic C, which is ternary in the backward direction. A variation of characteristic length-scale should have the opposite effect to what was concluded for atomic oxygen: to a shorter length-scale corresponds a lower concentration in C_2.

Overall, the signature of C_2 is thus the most likely to appear in the shock layer of the largest model. The brightness of that signature, however, depends not only on the molecule's concentration but also on its temperature. It is thus only the presence of absence of the C_2 Swan bands that will allow to conclude on the effect of binary scaling.

As expected, one can see in figure 9.2 that the spectral signature of C_2 is the strongest for the largest model (figure a) while it is barely visible for the smallest one (figure c). The spectral signature of the latter is rather populated with atomic lines, including what appears to be ionized carbon at $564\ \mathrm{nm}$.

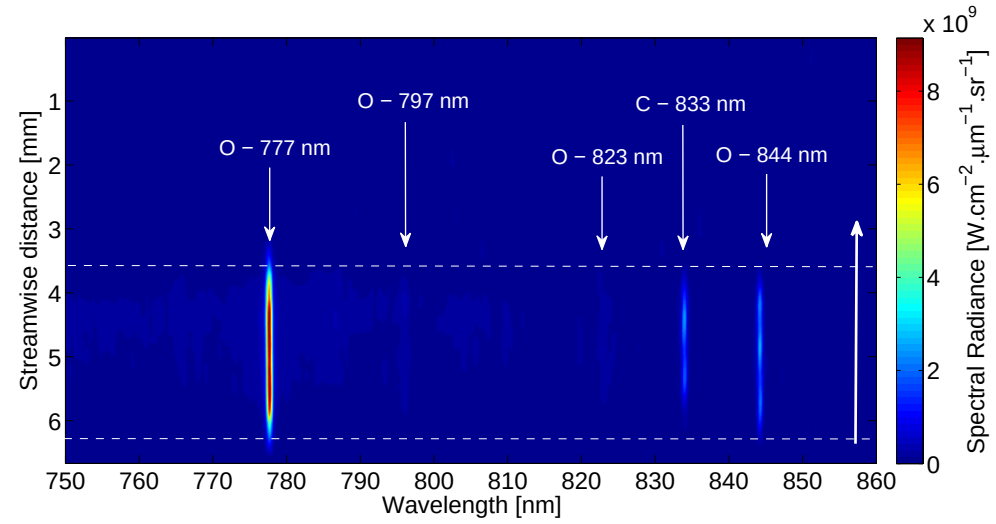

(a)

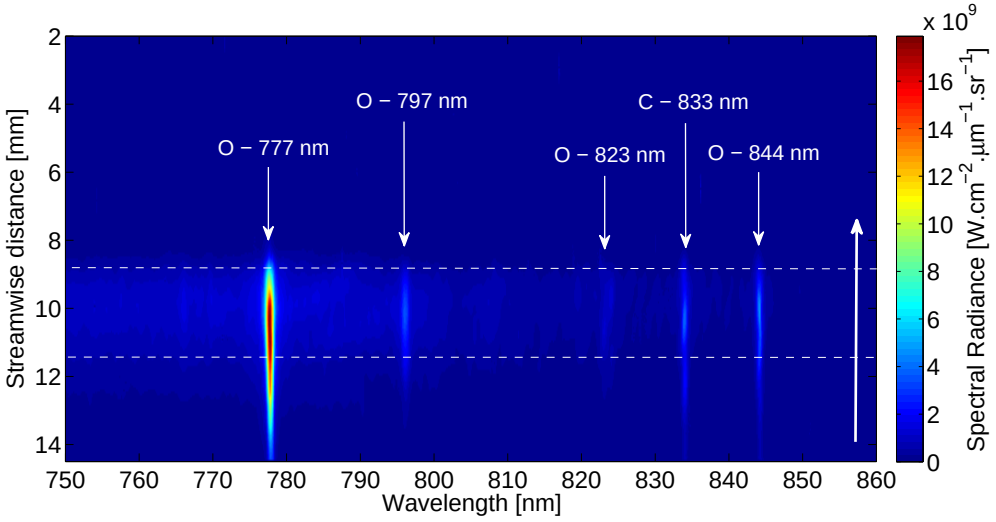

(b)

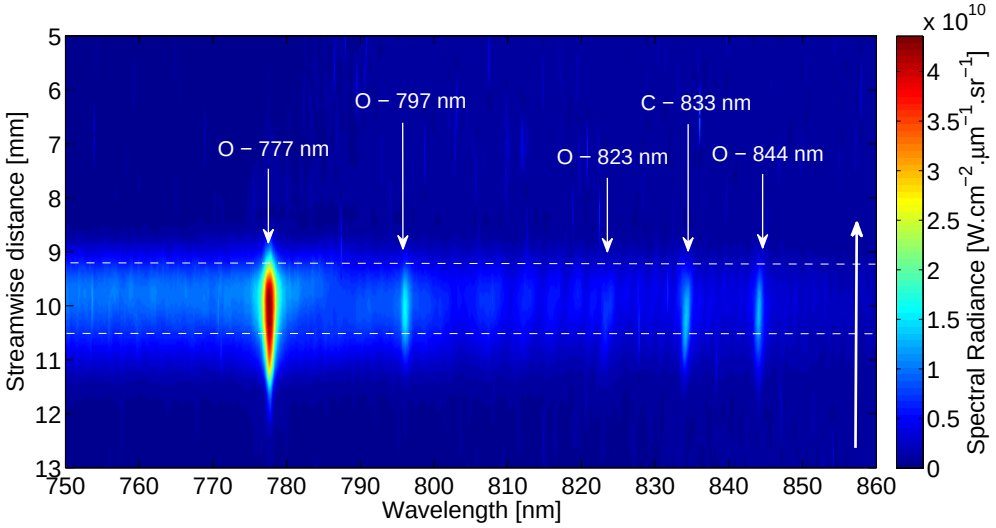

(c)

Figure 9.1: *Distribution of the spectral radiance along the stagnation line for the large (a, shot $x2s2707$), medium (b, shot $x2s2712$) and small (c, shot $x2s2728$) models. The vertical scale is the streamwise distance, with the dashed lines indicating the model edge (top) and the shock edge (bottom) and the arrow indicating the direction of the flow. The horizontal scale is the wavelength. The vertical scale and spectral radiance intensity have been adapted to increase the visibility of the different figures.*

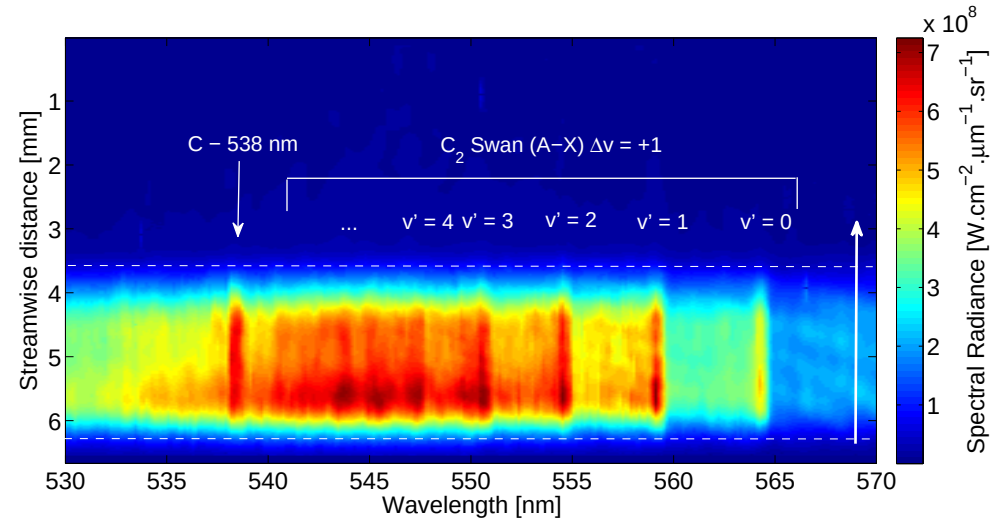

(a)

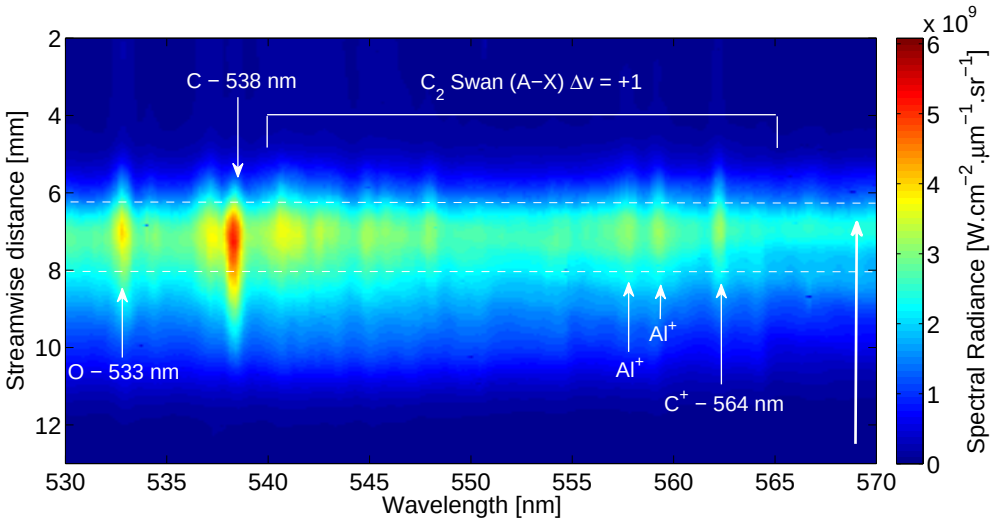

(b)

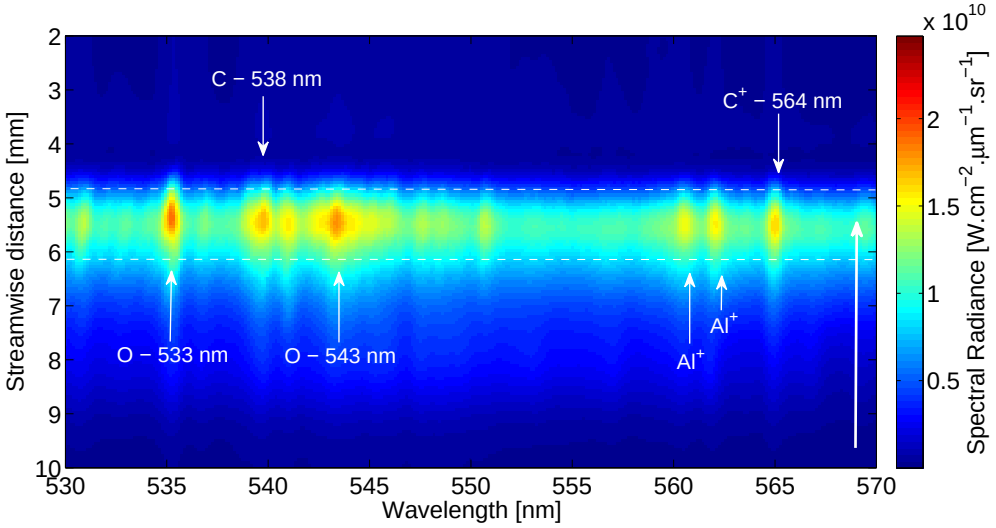

(c)

Figure 9.2: *Distribution of the spectral radiance along the stagnation line for the large (a, shot $x2s2708$), medium (b, shot $x2s2717$) and small (c, shot $x2s2723$) models. The vertical scale is the streamwise distance, with the dashed lines indicating the model edge (top) and the shock edge (bottom) and the arrow indicating the direction of the flow. The horizontal scale is the wavelength. The vertical scale and spectral radiance intensity have been adapted to increase the visibility of the different figures.*

9.3 Conclusion

Despite the technical challenge associated with the thin shock layers to resolve, a set of conclusions could be drawn based on the qualitative inspection of the results obtained. More specifically, the evolution of the shock layer spectral radiance with respect to the characteristic length scale of the flow corresponds to what was expected from the theoretical developments performed in the first part of this thesis: the signature of atomic species - and in particular O - is the strongest for the smaller model while the signature of molecular features - in this case C_2 - is the strongest for the larger model. This confirms that a shorter length-scale leads to a more dissociated mixture and a higher temperature in the shock layer. It is not possible, however, to determine to relative contribution of radiative coupling and non-binary chemistry.

Part III

Overall discussion and conclusion

Chapter 10

Conclusion

"Understanding precedes and succeeds knowledge. Preliminary understanding, which is at the basis of all knowledge, and true understanding, which transcends it, have this in common: they make knowledge meaningful."

- Hanna Arendt, in *Understanding and Politics* [8]

Throughout this document, we have contributed to the discussion on the validity and applications of similitude analysis to hypersonic flows, focusing more particularly on the binary scaling law.

Binary scaling is a useful and widely used tool to perform ground-to-flight extrapolation of high-enthalpy flows. In its simplest expression, it is based on the assumption that the shock layer forming in front of bodies in hypersonic flows is dominated by binary (dissociation) reactions. If so, the chemical processes will take place over lengths that evolve in proportion to the length-scale of that flow, under the conditions that the nature of the gas, the free-stream enthalpy h_∞ and the product of the free-stream density and a characteristic length of the flow $\rho_\infty L$ area duplicated.

More formally, the requirement to duplicate the nature of the gas, h_∞ and $\rho_\infty L$ are introduced with the intention to obtain the same Damkhöler number for the gas-phase Da_g. As a matter of fact, these requirements are actually also sufficient to duplicate the Péclet number Pe and Damkhöler number for the wall Da_w, as well as the similarity parameters that govern the other flow features of interest: Re, M, γ, and Pr.

Throughout our journey, we have identified the limits of that method and - *most importantly* - we have understood what were the roots of these limits. We started, in the introduction, with a contextualization of this research in the wider role of experimental hypersonics. We then divided the bulk of our work in two main parts: the first one was dedicated to theoretical and numerical developments, the second one to experimental verification.

In chapter 2, the opening chapter of the first part, we replaced binary scaling in the wider framework of similitude laws used in super- and hypersonic fluid dynamics. Two of the main limits of

binary scaling were then identified in chapter 3 as being non-binary chemistry effects and radiation coupling. Lastly, chapter 4 was devoted to the scaling of heat fluxes.

We then started the second part, in chapter 5, with an experiment to validate an hypothesis made in chapter 4; that the diffusive heat flux scales in the same fashion as the conductive heat flux. The four following chapters were then to another experiment allowing us to identify the effect of radiation coupling within a family of binary scaled flows: in chapter 6 we designed the test flow conditions and confirmed that they would suit our needs, in chapter 7 we post-processed and interpreted the shock standoff distance, in chapter 8 the stagnation point heat fluxes, and in chapter 9 the stagnation line radiation.

10.1 Discussion

Let us verify that all these steps allowed us to answer the four research questions asked in the introduction.

Which testing methodology can we apply for high-enthalpy ground-to-flight extrapolation?

Two methodologies were identified:

- The binary scaling, the state-of-the-art of which is reviewed in section 2.4.1.
- The LHTS, briefly explained in section 2.5.

Do all the flow features scale appropriately within a family of binary scaled flows?

No, they do not:

- Binary scaling is built on the assumption of an adiabatic[1] flow governed by binary reactions. These drastically narrow down the envelope of flows for which it can be used. The flow features that do not scale appropriately (and are relevant for practical cases) are thus chemistry and radiation.
- On the other hand, we were able to demonstrate that diffusive transport and the chemistry at the wall do scale appropriately. These had not been addressed in the past.

[1]Let us remind the reader that the term *adiabatic* in this work refers to the gas-phase and not the wall. An adiabatic gas-phase is one for which radiation coupling is negligible.

If not, what macroscopic differences will these discrepancies cause?

Two main side-effects were identified:

- The main consequence of non-binary chemistry is that, within a family of binary scaled flows, a reduction of the length-scale will cause the equilibrium layer to be hotter and less dissociated, further impacting other flow properties such as a reduction in viscosity and Mach number, or a larger Prandtl number.

- If it is strong enough, radiation will cause a substantial amount of energy to leak out of the shock layer to the free-stream. The strength of that coupling, however, will increase as the length-scale of the flow increases, impacting other flow properties such as its chemical composition or temperature. The resulting effect on macroscopic features of the flow are for example a reduction of the wall heat flux (both convective and radiative) or of the shock standoff distance.

These side effects were identified with experimental measurements on the shock standoff (chapter 7), the stagnation point heat flux (chapter 8), and the stagnation line radiance (chapter 9).

Can we provide tools to account for these differences when performing ground-to-flight extrapolation?

Yes, two methods are suggested:

- The effect of non-binary chemistry can easily be assessed using very simple numerical tools such as the CEA database. With these, it is possible to draw velocity-density maps (i.e. similar to velocity-altitude maps) allowing to identify clearly what free-stream conditions will affect the least the flow variables of interest, as it is for example done in figures 3.8 and 3.9 in chapter 3.

- The intensity of the radiative coupling can be estimated through the Goulard number (equation 3.51). A new method, based on a mix of experiments, CFD, and informed use of engineering correlations is proposed to extrapolate the stagnation heat flux to flight for cases for which the radiative coupling is non-negligible (section 8.6). Compared to what is done at the moment, that methodology yields results that are more accurate, can be looked upon with greater confidence (smaller uncertainty margins), and are simpler to obtain.

10.2 Recommendations for future work

Out of the many recommendations and leads for future work, four particularly stand out.

First, more efforts should be dedicated to the **consolidation of correlations for the effect of radiation coupling on macroscopic flow features** such as the radiative heat flux (figures 4.1), convective heat flux (figure 4.2), shock standoff distance, etc. These can be constructed either numerically, as it is already the case, and validated or complemented experimentally. Experimental campaign would simply compare the non-adiabatic flow obtained in the wind tunnel with an adiabatic numerical simulation.

With that regard, new experiments are not specifically needed as there already exist a substantial database of tests already conducted for air, Mars, Venus, Titan, and gas giants. The only thing needed is thus to perform one additional adiabatic numerical simulation for each of these experiments and determine how radiation coupling has affected the variables of interest. Similarly, any future test can be added to that database at the only cost of an adiabatic numerical simulation. Let us note, however, that if it is the heat fluxes that are under investigation then the radiative and convective heat fluxes have to be separated one way or another.

Consolidating these engineering correlations would not only benefit the post-processing methodology presented in this thesis, but also allow for a better grip of radiation coupling itself. Furthermore, state-of-the-art radiatively coupled simulations costly and complicated. It is therefore useful to have access to a quick and easy tool to estimate how flow coupling affects the variables that will determine the spacecraft's design.

Second, a validation of the ground-to-flight methodology developed throughout this work **comparing flight data and laboratory results** (i.e. rather than using only a controlled laboratory environment). There is a fair amount of literature compiling flight data of atmospheric entry probes (e.g. STS-1 to 5, Fire II, Galileo, Hayabusa, etc.) which could be used to select a test case to perform in an expansion tube. Such a validation, however, would only be relevant if the radiation coupling is significant. Useful quantitative data to compare include any of the flow features used in the present work, such as the shock standoff distance, the stagnation point heat flux, or the shock layer radiation.

Third, the **application of binary scaling in a subsonic flow** described in chapter 5 opens a wide range of possibilities. A few examples of potential applications were already cited, such as the replacement of a low pressure flow by a high pressure one more likely to fulfill the LTE requirement. However, with some imagination, many more applications can be found.

For example, TPM testing is usually performed simply aiming for a certain heat flux rather than using the LHTS. Under these conditions, an interesting property derived from binary scaling is that, for a flow of constant enthalpy, the stagnation point heat flux remains constant as long as the product of free-stream density and a characteristic length-scale of the flow ρL is constant. This allows thus to freely adjust the size of the material sample depending on the free-stream density envelope of the facility, or inversely to adjust the static pressure depending on the size of sample.

Another interesting application is to investigate the wall catalycity[2]. Indeed, the applicability of binary scaling in subsonic flows is based on the assumption that catalycity is an intrinsic property of

[2]This could actually be done both in subsonic and hypersonic facilities. Subsonic facilities, however, allow for greater freedom and resolution when investigating wall phenomena.

the material function of the wall temperature only. However, some results have proven that catalycity could also vary depending on flow conditions. If so, a clear deviation should be observed when producing figures such as figure 5.2. It is therefore highly advisable to repeat the experiment described in chapter 5 using a more accurate definition of the velocity gradient (i.e. CFD) and a more reliable determination of free-stream conditions (i.e. direct measurement rather than databases).

Lastly, there remains a substantial amount of work to be done regarding the **extension of binary scaling beyond the stagnation line**. This was just touched upon in section 3.4, but not expanded to a point where it can be practically used in the laboratory. The vicinity of the stagnation line can be obtained in a plasma wind tunnel with an appropriate use of the LHTS, or even binary scaling as it was demonstrated in this work. However, there are many other interesting features that require a broader picture of the flow and can thus only be studied in expansion tubes: turbulent transition, recombination in the expanded flow, afterbody radiation, etc.

From the modeling perspective, an interesting starting point could be to use the work of Barbante for the LHTS and apply to to binary scaling. In [11] he presents a formalization of the LHTS methodology applied to the duplication of the stagnation region, in the same fashion as what we did here for the binary scaling. In [10], he extends the previous work the boundary layer downstream of the stagnation point. The same could be done in our case, applying the analysis we did for the Navier-Stokes equations in 2.4 to the boundary layer equations. The shock mapping technique developed by Gibson and Marrone [60] might also prove to be a useful angle of attack.

The quality of these models could be assessed with flat plate experiments. These, however, should allow for sufficiently long test times so as to allow for a boundary layer to develop over a significant distance.

This list is obviously far from being exhaustive. We will leave it up to the reader's creativity and ingenuity to connect one or the other part of this thesis with his own personal research, and thereby hopefully progress in an interesting direction. Thus is the relentless march of science.

References

[1] Nist its-90 thermocouple database, nist standard reference database 60, version 2.0. NIST Monograph 175, National Institute of Standards and Technology (NIST), 1995.

[2] H.-K. Ahn, C. Park, and K. Sawada. Dynamics of pyrolysis gas in charring materials ablation. In *36th AIAA Aerospace Sciences Meeting and Exhibit*, pages AIAA–98–0165. AIAA, 1998.

[3] H.-K. Ahn, C. Park, and K. Sawada. Response of heatshield material at stagnation point of pioneer-venus probes. *Journal of Thermophysics and Heat Transfer*, 16(3):432–439, July - September 2002.

[4] C. R. Alba et al. Investigation of surface radiation in earth re-entry flows with graphite ablation. In *6th Ablation Workshop*, Urbana-Champaign, Illinois, April 2014.

[5] A. Ambrosio and A. Wortman. Stagnation-point shock-detachment distance for flow around spheres and cylinders in air. *Journal of the Aerospace Sciences*, 29(7):875, March 1962.

[6] J. D. Anderson. Nongray radiative transfer effects on the radiating stagnation region shock layer and stagnation point heat transfer. Aerodynamics Research Report 281 NOLTR 67-104, U.S. Naval Ordnance Laboratory White Oak MD, July 1967.

[7] J. D. Anderson. *Hypersonic and High-Temperature Gas Dynamics Second Edition*, chapter Viscous Flow: Basic Aspects, Boundary Layer Results, and Aerodynamic Heating, pages 268–272. Number 6. AIAA, 2006.

[8] H. Ardent. Understanding and politics. *Partisan Review*, 20(4):377–392, July - August 1953.

[9] A. J. Ball et al. *Planetary Landers and Entry Probes*. Cambridge University Press, Cambridge, UK, 2007.

[10] P. F. Barbante. Heat flux duplication between ground facility and hypersonic flight. *Journal of Thermophysics and Heat Transfer*, 23(4):684–692, October-December 2009.

[11] P. F. Barbante and O. Chazot. Flight extrapolation of plasma wind tunnel stagnation region flowfield. *Journal of Thermophysics and Heat Transfer*, 20(3):493–499, July - September 2006.

[12] N. Belouaggadia et al. Shock detachment distance on blunt bodies in nonequilibrium flow. *AIAA Journal*, 45(6):1424–1429, June 2007.

[13] J. Bertrand. Sur l'homogeneite des formules en physique. *Comptes Rendus*, 86(15):916–920, 1878.

[14] F. S. Billig. Shock-wave shapes around spherical- and cylindrical-nosed bodies. *Journal of Spacecraft and Rockets*, 4(6):822–823, June 1967.

[15] G. Birkhoff. *Hydrodynamics: a Study in Logic, Fact, and Similitude*, chapter Modeling and Dimensional Analysis, pages 109–110. Dover Publications, Inc., 1955.

[16] D. Bose et al. Modelling and experimental validation of cn radiation behind a strong shock wave. In *43rd AIAA Aerospace Sciences Meeting and Exhibit*, number AIAA-2005-0768, Reno, Nevada, 2005. AIAA.

[17] B. Bottin et al. The vki plasmatron characteristics and performance. In RTO, editor, *Measurement Techniques for High Enthalpy and Plasma Flows NATO-RTO-EN 8*, pages 6–1, 6–26. VKI, March 2000.

[18] G. E. P Box and N. R. Draper. *Empirical Model-Building and Response Surfaces*, page 424. John Wiley and Sons, Inc., 1987.

[19] Natural Environments Branch. Venus global reference atmospheric model (venus-gram). Technical report, NASA Marshall Space Flight Center, 2005.

[20] A. M. Brandis. *Experimental Study and Modelling of Non-equilibrium Radiation During Titan and Martian Entry*. PhD thesis, School of Mechanical and Mining Engineering, The University of Queensland, St. Lucia, QLD, Australia, 2009.

[21] P. W. Bridgman. *Dimensional Analysis, 2nd Edition*, pages 13–14. New Haven : Yale University Press, 1931.

[22] E. Buchen and D. DePasquale. Nano / microsatellite market assessment. Technical report, SpaceWorks Enterprises, 2014.

[23] E. Buckingham. On physically similar systems, illustrations of the use of dimensional equations. *Physical Review*, 4(4):345–376, October 1914.

[24] D. R. Buttsworth. Assessment of effective thermal product of surface junction thermocouples on millisecond and microsend time-scales. *Experimental Thermal and Fluid Science*, 25(6):409–420, December 2001.

[25] D. R. Buttsworth and T. V. Jones. Radial conduction effects in transient heat transfer experiments. *The Aeronautical Journal*, 101(1005):209–212, May 1997.

[26] F. R. Caldwell. Thermocouple materials. Monograph 40, The National Bureau of Standards, Washington, March 1962.

[27] M. Capitelli et al. Collision integrals of high-temperature air species. *Journal of Thermophysics and Heat Transfer*, 14(2):259–268, April - June 2000.

[28] B. R. Capra. *Aerothemodynamic Simulation of Subscale Models of the FIRE II and Titan Explorer Vehicles in Expansion Tubes*. PhD thesis, School of Mechanical and Mining Engineering, The University of Queensland, St. Lucia, QLD, Australia, 2006.

[29] B. R. Capra and R. G. Morgan. Radiative and total heat transfer measurements to a titan explorer model. *Journal of Spacecraft and Rockets*, 49(1):12–23, January - February 2012.

[30] B. R. Capra and R. G. Morgan. Total heat transfer measurements on a flight investigation of reentry environment model. *Journal of Spacecraft and Rockets*, 50(3):494–503, May 2013.

[31] Y. A. Cengel and M. A. Boles. *Thermodynamics: an Engineering Approach*, chapter Appendix 1: Property Tables and Charts (SI UNITS). McGraw-Hill Education, 2001.

[32] O. Chazot. Experimental studies on hypersonic stagnation point chemical environment. In RTO, editor, *Experiment, Modeling and Simulation of Gas-Surface Interactions for Reactive Flows in Hypersonic Flights RTO-EN-AVT-142*, pages 13–1, 13–32. VKI, 2007.

[33] O. Chazot, F. Panerai, and M. Marotta. Ground testing for gsi database, what do we determine? In *7th European Aerothermodynamics Symposium*, number 55, Brugge, Belgium, May 2011. ESA.

[34] H. K. Cheng. Similitude of hypersonic real-gas flows over slender bodies with blunted noses. *Journal of Aerospace Sciences*, 26(9):575–585, September 1959.

[35] J. H. Chin. Radiation transport for stagnation flows including effects of lines and ablation layer. *AIAA Journal*, 7(7):1310–1318, July 1969.

[36] L. F. Crabtree et al. Estimation of heat transfer to flat plates, cones and blunt bodies. Aeronautical Research Council Reports and Memoranda 3637, Ministry of Technology, 1970.

[37] B. A. Cruden. Absolute radiation measurement during planetary entry in the nasa ames electric arc shock tube facility. In *27th International Symposium on Rarefied Gas Dynamics*, May 2011.

[38] B. A. Cruden, D. Prabhu, and R. Martinez. Absolute radiation measurement in venus and mars entry conditions. *Journal of Spacecraft and Rockets*, 49(6):1069–1079, November - December 2012.

[39] R. W. Detra and H. Hidalgo. Generalized heat transfer formulas and graphs for nose cone re-entry into the atmosphere. *American Rocket Society Journal*, 31(3):318–321, January 1961.

[40] S. Dutta et al. Mission sizing and trade studies for low ballistic coefficient entry systems to venus. In *Aerospace Conference IEEE*, pages 1–14, 2012.

[41] R. A. East, R. J. Stalker, and J. P. Baird. Measurement of heat transfer to a flat plate in a dissociated high-enthalpy laminar air flow. *Journal of Fluid Mechanics*, 97(4):673–699, 1980.

[42] C. T. Edquist. Correlation of radiative heating calculations for venus entry. *Journal of Spacecraft and Rockets*, 11(6):440–442, June 1974.

[43] T. N. Eichmann. *Radiation Measurements in a Simulated Mars Atmosphere*. PhD thesis, School of Mechanical and Mining Engineering, The University of Queensland, St. Lucia, QLD, Australia, 2012.

[44] T. N. Eichmann et al. Three-dimensional effects on line-of-sight visualization measurements of supersonic and hypersonic flow over cylinders. *Shock Waves*, 16(4-5):299–307, February 2007.

[45] A. Einstein. *Ideas and Opinion, 3rd Edition*. Broadway Books, June 1995.

[46] D. Ellington. Binary scaling limits for hypersonic flight. *AIAA Journal*, 5(9):1705–1706, September 1967.

[47] C. D. Engel, C. F. Farmer, and R. W. Pike. Ablation and radiation coupled viscous hypersonic shock layers. *AIAA Journal*, 11(8):1174–1181, August 1973.

[48] R. A. Falanga and W. B. Olstad. An approximate inviscid radiating flowfield analysis for sphere-cone venusian entry vehicles. In *AIAA/ASME 1974 Thermophysics and Heat Transfer Conference*, 1974.

[49] R. A. Falanga and E. M. Sullivan. An inverse-method solution for radiating, nonadiabatic, equilibrium inviscid flow over a blunt body. Technical note D-5907, NASA Langley Research Center, 1970.

[50] J. A. Fay and F. R. Riddell. Theory of stagnation point heat transfer in dissociated air. *Journal of Aeronautical Sciences*, 25(2):73–85, 1958.

[51] B. Fegley et al. *Venus II: Geology, Geophysics, Atmosphere, and Solar Wind Environment*, chapter Geochemistry of Surface-Atmosphere Interactions on Venus, pages 591–636. University of Arizona Press, 1997.

[52] A. M. Feldick, M. F. Modest, and D. A. Levin. Closely coupled flowfield-radiation interactions during hypersonic reentry. *Journal of Thermophysics and Heat Transfer*, 25(4):481–492, October - December 2011.

[53] R. O. Fimmel, L. Colin, and E. Brugess. Pioneer venus. Technical Report NASA SP-461, NASA Scientific and Technical Information Branch, 1983.

[54] N. C. Freeman. Non-equilibrium flow of an ideal dissociating gas. *Journal of Fluid Mechanics*, 4(4):407–425, January 1958.

[55] L. B. Garrett, G. L. Smith, and J. N. Perkins. An implicit finite-difference solution to the viscous shock layer, including the effects of radiation and strong blowing. Technical report R-388, NASA Langley Research Center, 1972.

[56] C. Gebhardt and C. Bergin. Nasa awards crs2 contracts to spacex, orbital atk, and sierra nevada. *Nasa Spaceflight*, January 2016.

[57] W. E. Gibson. Dissociation scaling for nonequilibrium blunt-nose flows. *American Rocket Society Journal*, 32(2):285, February 1962.

[58] W. E. Gibson and P. V. Marrone. A correspondence between normal schok and blunt-body flows. *Physics of Fluids*, 5:1949–1956, December 1962.

[59] W. E. Gibson and P. V. Marrone. Non-equilibrium scaling criterion for inviscid hypersonic airflows. Technical Report QM-1626-A-8, Cornell Aeronautical Laboratory, November 1962.

[60] W. E. Gibson and P. V. Marrone. A similitude for nonequilibrium phenomena in hypersonic flight. In W. C. Nelson, editor, *AGARD Meeting on High Temperature Aspects of Hypersonic Fluid Dynamics*, pages 105–131, Rhodes-Saint-Genese, Belgium, March 1962.

[61] W. E. Gibson and A. Sowyrda. An analysis of inviscid non-equilibrium flows. Technical Report AF-1560-A-2, Cornell Aeronautical Laboratory, June 1962.

[62] D. Gildfind. *Development of High Total Pressure Scramjet Flow Conditions using the X2 Expansion Tube*. PhD thesis, School of Mechanical and Mining Engineering, The University of Queensland, St. Lucia, QLD, Australia, 2012.

[63] P. A. Gnoffo et al. Computational aerothermodynamic design issues for hypersonic vehicles. *Journal of Spacecraft and Rockets*, 36(1):21–43, January - February 1999.

[64] P. A. Gnoffo, R. N. Gupta, and J. L. Shinn. Conservation equations and physical models for hypersonic air flows in thermal and chemical nonequilibrium. Technical Report Technical Paper 2867, NASA, 1989.

[65] P. A. Gnoffo, C. O. Johnston, and B. Kleb. Challenges to computational aerothermodynamic simulation and validation for planetary entry vehicle analysis. Technical report, NASA Langley Research Center, 2010.

[66] R. J. Gollan. *The Computational Modelling of High-Temperature Gas Effects with Application to Hypersonic Flows*. PhD thesis, School of Mechanical and Mining Engineering, University of Queensland, Australia, St. Lucia, QLD, Australia, 2008.

[67] R. J. Gollan et al. Numerical modelling of radiating superorbital flows. *The ANZIAM Journal*, 45(E):C248–C268, 2004.

[68] R. J. Gollan et al. A simulation technique for radiating shock tube flows. In K. Hannermann and F. Seiler, editors, *26th International Symposium on Shock Waves*, volume 1, pages 465–470. Springer Berlin Heidelberg, 2009.

[69] R. Goulard. On catalytic recombination rates in hypersonic stagnation heat transfer. *Jet Propulsion*, 28(11):737, 1958.

[70] R. Goulard. The coupling of radiation and convection in detached shock layers. *Journal of Quantitative Spectroscopy and Radiative Transfer*, 1:249–257, 1961.

[71] C. M. Guldberg and P. Waage. Concerning chemical affinity. *Erdmann's Journal für Practische Chemie*, 127:69–114, 1879.

[72] J. G. Hall, A. Q. Eschenroeder, and P. V. Marrone. Inviscid hypersonic airflows with coupled chemical reactions. In *IAS 30th Annual Meeting, New York*, volume 29, pages 1038–1051, September 1962.

[73] J.G. Hall, A. A. Eschenroeder, and P. V. Marrone. Blunt-nose inviscid airflows with coupled nonequilibrium processes. *Journal of the Aerospace Sciences*, 29(9):1038–1051, September 1962.

[74] W. D. Hayes and R. F. Probstein. Viscous hypersonic similitude. *Journal of the Aerospace Sciences*, 26:815–824, 1959.

[75] W. D. Hayes and R. F. Probstein. *Hypersonic Flow Theory*. Academic Press, New York London, 1966.

[76] S. J. Henderson and J. A. Menart. Equilibrium properties of high-temperature air for a number of pressures. *Journal of Thermophysics and Heat Transfer*, 22(4):718–726, October - December 2008.

[77] C. Henry. Europe to study semi-reusable launcher for small satellites. *Satellite Today*, December 2015.

[78] C. E. Higgins. *Aerothermodynamics of the Gas Giants*. PhD thesis, School of Mechanical and Mining Engineering, University of Queensland, Australia, St. Lucia, QLD, Australia, 2004.

[79] E. H. Hirschel and C. Weiland. *Selected Aerothermodynamic Design problems of Hypersonic Flight Vehicles*, volume 229. Progress in Astronautics and Aeronautics, AIAA, 2009.

[80] B. R. Hollis et al. Prediction of the aerothermodynamic environment of the huygens probe. In *38th AIAA Thermophysics Conference*, number AIAA 2005-4816, Toronto, Canada, June 2005. AIAA.

[81] H. G. Hornung. Non-equilibrium dissociating flow over spheres and circular cylinders. *Journal of Fluid Mechanics*, 53(1):149–176, May 1972.

[82] H. G. Hornung. 28th lanchester memorial lecture - experimental real-gas hypersonics. *Aeronautical Journal*, 92(920):379–389, December 1988.

[83] H. Hoshizaki and L. E. Lasher. Convective and radiative heat transfer to an ablating body. *AIAA Journal*, 6(8):1441–1449, 1968.

[84] W. T. Huntress Jr., V. I. Moroz, and I. L. Shevalev. Lunar and planetary robotic exploration missions in the 20th century. *Space Science Reviews*, 107(3-4):541–649, 2003.

[85] G. R. Inger. Similitude of hypersonic flows over slender bodies in non-equilibrium dissociated gases. *AIAA Journal*, 1(1):46–53, January 1963.

[86] G. R. Inger. Low-reynolds-number effects on hypersonic blunt-body shock standoff. *Journal of Thermophysics and Heat Transfer*, 18(1):108–113, 2004.

[87] G. R. Inger, C. Higgins, and R. G. Morgan. Shock standoff on hypersonic blunt bodies in nonequilibrium gas flows. *Journal of Thermophysics and Heat Transfer*, 16(2):245–250, April-June 2002.

[88] M. Inouye, J. V. Rakich, and H. Lomax. A description of numerical methods and computer programs for two-dimensional and axisymmetric supersonic flow over blunt-nosed and flared bodies. TN D-2970, NASA, August 1965.

[89] C. Jacobs. *Radiation in Low Density Hypervelocity Flows*. PhD thesis, University of Queensland and Ecole Centrale Paris, St. Lucia, QLD, Australia, 2011.

[90] P. A. Jacobs. Quasi-one-dimensional modelling of a free-piston shock tunnel. *AIAA Journal*, 32(1):137–145, 1994.

[91] P. A. Jacobs. Shock tunnel modelling with l1d. Technical Report Research Report 13/98, The University of Queensland, 1998.

[92] P. A. Jacobs et al. The compressible-flow cfd project, 2012.

[93] P. A. Jacobs and R. J. Gollan. The eilmer3 code: User guide and example book. Technical report, School of Mechanical and Mining Engineering, the University of Queensland, 2013.

[94] C. James et al. Designing and simulationg high enthalpy expansion tube conditions. In *2013 Asia-Pacific International Symposium on Aerospace Technology*, November 2013.

[95] C. O. Johnston, P. A. Gnoffo, and K. Sutton. Influence of ablation on radiative heating for earth entry. *Journal of Spacecraft and Rockets*, 46(3):481–491, May - June 2009.

[96] D. Kliche, C. Mundt, and E. H. Hirschel. The hypersonic mach number independence principle in the case of viscous flow. *Shock Waves*, 21(4):307–314, August 2011.

[97] I. Klotz. U.s. space tourism set for takeoff by 2014, faa says. *Reuters*, March 2012.

[98] A. F. Kolesnikov. Conditions of simulation of stagnation point heat transfer from a high enthalpy flow. *Fluid Mechanics, Plenum*, 28(1):131, 1993.

[99] A. F. Kolesnikov. Extrapolation from high enthalpy tests to flight based on the concept of local heat transfer simulation. In *Measurement Techniques for High Enthalpy and Plasma Flows NATO-RTO-EN-8*, number 8B, Rhodes-Saint-Genese, Belgium, October 1999. VKI.

[100] A.F. Kolesnikov. The aerothermodynamic simulation in sub- and supersonic high-enthalpy jets: Experiments and theory. In *2nd European Symposium on Aerothermodynamics for Space Vehicles*, number ESA SP-367, page 583, ESTEC, Noordwijk, The Netherlands, November 1994.

[101] A. Kovàcs and R. B. Mesler. Making and testing small surface thermocouples for fast response. *Review of Scientific Instrumentation*, 35(4):485–488, April 1964.

[102] B. Laub and E. Venkatapathy. Thermal protection technology and facility needs for demanding future planetary missions. In *International Workshop on Planetary Probe Atmospheric Entry and Descent Trajectory Analysis and Science*, 2003.

[103] L. Lees. Hypersonic flow. In *Proceeding of the 5th International Aeronautical Conference, IAS-RAeS*, pages 241–276, Los Angeles, 1955.

[104] A. Lemal and other. Effect of heavy-particle impact excitation processes on post shock nonequilibrium air radiation. In *8th European Symposium on Aerothermodynamics for Space Vehicles*. European Space Agency, March 2015.

[105] S. Lewis, R. G. Morgan, T. J. McIntyre, C. R. Alba, and R. B. Greendyke. Expansion tunnel experiments of earth reentry flow with surface ablation. *Journal of Spacecraft and Rockets*, 2016.

[106] P. Leyland et al. Radiation-ablation coupling for capsule reentry heating via simulation and expansion tube investigations. In *5th European Conference for Aeronautics and Space Sciences*. ESA, 2013.

[107] M. J. Lighthill. Dynamics of a dissociating gas. part i. equilibrium flow. *Journal of Fluid Mechanics*, 2(1):1–32, 1957.

[108] J. S. Lim and A. V. Oppenheim. Enhancement and bandwidth compression of noisy speech. *Proceedings of the IEEE*, 67(12):1586–1604, December 1979.

[109] S. Limay and S. Smrekar. Pathways for venus exploration. Technical report, Venus Exploration Analysis Group, 2009.

[110] R. K. Lobb. *The High Temperature Aspect of Hypersonic Flow*, chapter Experimental Measurement of Shock Detachment Distance on Spheres Fired in Air at Hypervelocities, pages 519–527. Pergamon Press Oxford London New York Paris, 1964.

[111] A. J. Lofthouse, I. D. Boyd, and M. J. Wright. Effects of continuum breakdown on hypersonic aerothermodynamics. *Physics of Fluids*, 19(2):027105–027101, 2007.

[112] I. Lourel, R. G. Morgan, and D. R. Buttsworth. Fast response coaxial type-e thermocouple gauges for the measurement of heat flux in expansion tubes. Departemental Report 2001/05, School of Mechanical and Mining Engineering, The Univerisity of Queensland, 2001.

[113] F. K. Lu and D. E. Marren. *Advances Hypersonic Test Facilities, Progress in Astronautics and Aeronautics*, chapter Principles of Hypersonic Test Facility Development, pages 17–25. AIAA, New York, 2002.

[114] T. Magin. Cooled pitot probe in air plasma jet. what do we measure? In *Aerothermodynamics and Fluid Mechanics Seminar*. The University of Texas at Austin, 2012.

[115] MatWeb Material Property Data. *Hoskins Manufacturing Chromel Thermocouple Wire*, 2015.

[116] J. R. Maus. Aerodynamic and aerothermal facilities ii short-duration, high-enthalpy facilities. In von Karman Institute, editor, *Methodology of Hypersonic testing*, 1993.

[117] J. C. Maxwell. The theory of molecules. *The Popular Science Monthly*, 4(17):276–290, 1873.

[118] F. Mazoué and L. Marraffa. Flow-field/radiation coupling analysis for huygens probe entry into titan atmosphere. In *38th AIAA Thermophysics Conference*, number AIAA 2005-5392, Toronto, Canada, 2005. AIAA.

[119] D. McBride and G. Gordan. Computer program for calculations of complex chemical equilibrium and applications ii, users manual and program description. Technical report, NASA Lewis Research Centre, 1996.

[120] T. J. McIntyre et al. Experimental expansion tube study of the flow over a toroidal ballute. *Journal of Spacecraft and Rockets*, 41(5):716–725, 2004.

[121] A. D. McRonald and J. E. Randolph. Hypersonic maneuvering for augmenting planetary gravity assist. *Journal of Spacecraft and Rockets*, 29(2):216–222, 1992.

[122] A.A. Michelson. *Light Waves and Their Uses*, pages 23–25. The University of Chicago Press, 1903.

[123] H. Mirels. Shock tube test time limitation due to turbulent-wall boundary layer. *AIAA Journal*, 2(1):84–93, Janurary 1963.

[124] V. N. Mirskii. Radiative heat transfer at the leading edge of a body during intense evaporation. *Journal of Fluid Dynamics*, 10(2):363–365, March 1975.

[125] V. N. Mirskii. Radiative heating of bodies entering the atmosphere of venus. *Fluid Dynamics*, 27(4):556–559, 1992.

[126] R. G. Morgan. *Handbook of Shock Waves, Volume 1*, chapter 4.2 Free Piston-Driven Reflected Shock Tunnels, pages 587–601. Academic Press, 2001.

[127] R. G. Morgan et al. Radiation measurements in nonreflected shock tunnels. In *25th AIAA Aerodynamic Measurement Technology and Ground Testing Conference*, June 2006.

[128] J. N. Moss. Radiative viscous-shock-layer solutions with coupled mass ablation. *AIAA Journal*, 14(9):1311–1317, 1976.

[129] J. N. Moss et al. A study of the aerothermal environment for the pioneer venus multiprobe mission. In *AIAA 12th Thermophysics Conference*, 1977.

[130] A.J. Neely, A. Dasgupta, and R. Choudhury. A new method for prescribing non-uniform wall temperatures on wind tunnel models. In *19th Australasian Fluid Mechanics Conference*, Melbourne, Australia, December 2014.

[131] C. T. Nicolet. User's manual for the generalized radiation transfer code (rad/equil). Rept. UM-69-9, Aerotherm. Corp., Mountain View, California, October 1969.

[132] S. Nonaka et al. Measurement of shock standoff distance for sphere in ballistic range. *Journal of Thermophysics and Heat Transfer*, 14(2):225–229, 2000.

[133] G.T. Nothwang. Pioneer venus spacecraft design and operation. *IEEET Transactions on Geoscience and Remost Sensing*, 18(1):5–10, 1980.

[134] E. Obermeier and A. Schaber. A simple formula for multicomponent gaseous diffusion coefficients derived from mean free path theory. *International Journal of Heat and Mass Transfer*, 20(12):1301–1306, December 1977.

[135] M. L. Oldfield. Impulse response processing of transient heat transfer gauge signals. *Journal of Turbomachinery*, 130(2), December 2006.

[136] J. Olejniczak et al. An analysis of the radiative heating environment for aerocapture at titan. In *39th AIAA/ASMA/SAE/ASEE Joint Propulsion Conference and Exhibit*, Huntsville, Alabama, 2003.

[137] H. Olivier. Influence of the velocity gradient on the stagnation point heating in hypersonic flow. *Shock Waves*, 5(4):205–216, December 1995.

[138] K. Oswatitsch. *Contributions to the Development of Gasdynamics*, chapter Laws of Similarity and Equivalence. Vieweg, 1980.

[139] W. A. Page et al. *AIAA Progress in Astronautics and Aeronautics: Thermal Design Principles of Spacecraft and Entry Bodies*, volume 21, chapter Radiative Transport in Inviscid Nonadiabatic Stagnation-Region Shock Layers, pages 75–114. Academic Press, New York, 1969.

[140] W. A. Page and H. T. Woodward. Radiative and convective heating during venus entry. *AIAA Journal*, 10(10):1379–1381, 1972.

[141] G. E. Palmer et al. Coupled fluids-radiation analysis of a high-mass mars entry vehicle. Paper 3495, AIAA, 2011.

[142] G. E. Palmer, T. White, and A. Pace. Direct coupling of the neqair radiation and dplr cfd codes. In *10th AIAA/ASMA Joint Thermophysics and Heat Transfer Conference*, number 5051. AIAA, June-July 2010.

[143] F. Panerai. *Aerothermochemistry Characterization of Thermal Protection Systems*. PhD thesis, von Karman Institute and Universita Degli Studi di Perugia, 2012.

[144] C. Park. Calculation of nonequilibrium radiation in the flight regimes of aeroassisted orbital transfer vehicles. In H. F. Nelson, editor, *Progress in Astronautics and Aeronautics*, volume 96, pages 395–418, 1985.

[145] C. Park. Radiation enhancement by nonequilibrium in earth's atmosphere. *Journal of Spacecraft and Rockets*, 22(1):27–36, January - February 1985.

[146] C. Park. Assessment of two-temperature kinetic model for ionizing air. *Journal of Thermophysics and Heat Transfer*, 3(3):233–244, 1989.

[147] C. Park. *Nonequilibrium Hypersonic Aerothermodynamics*, chapter Review of Experimental Results, pages 255–328. John Wiley and Sons, 1990.

[148] C. Park. Review of chemical-kinetic problems of future nasa missions, i: Earth entries. *Journal of Thermophysics and Heat Transfer*, 7(3):385–398, 1993.

[149] C. Park and H.-K. Ahn. Stagnation-point heat transfer rates for pioneer-venus probes. *Journal of Thermophysics and Heat Transfer*, 13(1):33–41, 1999.

[150] C. Park, J. Howe, R. Jaffe, and G. Candler. Review of chemical-kinetic problems of future nasa missions, ii: Mars entries. *Journal of Thermophysics and Heat Transfer*, 8(1):9–22, 1994.

[151] W. C. Pitts and R. M. Wakefield. Performance of entry heat shields on pioneer venus probe. *Journal of Geophysical Research*, 85(A13):8333–8337, December 1980.

[152] M. Planck. The meaning and limits of exact science. *Science*, 110(2857):325, September 1949.

[153] K. R. Popper. *The Open Universe: An Argument for Indeterminism*. Routledge, 1988.

[154] D. Potter. *Modelling of Radiating Shock Layers for Atmospheric Entry at Earth and Mars*. PhD thesis, School of Mechanical and Mining Engineering, University of Queensland, Australia, St. Lucia, QLD, Australia, 2011.

[155] D. Prabhu et al. Preliminary estimates of radiative heating for the cev heatshield. CAP TN/EG-CEV-06-8, NASA, January 2006.

[156] D. Ramjaun. Tc2: Definition of shock tunnel test cases for gas radiation prediction in a planetary atmosphere. In *Proceedings of the International Workshop on Radiation of High Temperature Gases in Atmospheric Entry*, number ESA SP-533, Lison, Portugal, October 2003.

[157] J.W. Strutt (Lord Rayleigh). The principle of similitude. *Nature*, 95:66–68, 1915.

[158] E. Reshotko and A. Turnin. *Laminar-Turbulent Transition*, chapter The Blunt Body Paradox - A Case for Transient Growth, pages 403–408. Springer Berlin Heidelberg, 2000.

[159] P. H. Rose and J. O. Stankevics. Stagnation point heat-transfer measurements in partially ionized air. *AIAA Journal*, 1(12):2752–2763, December 1963.

[160] P. H. Rose and W. I. Stark. Stagnation point heat-transfer measurements in dissociated air. *Journal of the Aerospace Sciences*, 25(2):86–97, 1958.

[161] D. E. Rosner. *Transport Processes in Chemically Reacting Flow Systems*, chapter Similitude Analysis with Application to Chemically Reactive Systems. Number 7. Dover Publications, Inc., 2000.

[162] M. Rundle. Oxford-made skylon 'super-plane' gains bae and uk backing. *Wired.co.uk*, November 2015.

[163] D. L. Schultz and T. V. Jones. Heat transfer measurements in shot-duration hypersonic facilities. Technical Report 165, AGARDograph, Department of Engineering Science, University of Oxfort, UK, 1973.

[164] D. Schulze-Makuch et al. A sulfur-based survival strategy for putative phototrophic life in the venusian atmosphere. *Astrobiology*, 4:11–18, 2004.

[165] J. B. Scoggins et al. Coupled flow, radiation, and ablation simulations of atmospheric entry vehicles using the hybrid statistical narrow band model. In *45th AIAA Thermophysics Conference*, page 3112. AIAA, 2015.

[166] C. Segal. *The Scramjet Engine, Processes and Characteristics*, chapter Scaling Factors, pages 198–201. Cambridge University Press, 2009.

[167] A. Seiff and D. B. Kirk. Structure of the venus mesosphere and lower thermosphere from measurements during entry of the pioneer venus probes. *Icarus*, 49:49–70, 1981.

[168] A. Sengupta and L. Hall. Challenges of a venus entry mission. In *2011 IEEE Aerospace Conference*, 2011.

[169] M. Sharma et al. Experimental and numerical investigations of hypervelocity carbon dioxide flow over blunt bodies. *Journal of Thermophysics and Heat Transfer*, 24(4):673–683, October - December 2010.

[170] U. Sheikh. *Re-Entry Aerothermodynamics in the Vacuum Ultraviolet*. PhD thesis, School of Mechanical and Mining Engineering, The University of Queensland, St. Lucia, QLD, Australia, 2014.

[171] J. L. Shinn, J. N. Moss, and A. L. Simmonds. Viscous shock-layer laminar heating analysis for the shuttle windward-symmetry plane with surface finite catalytic recombination rates. In *AIAA/ASME Joint Fluids, Plasmas, Thermophysics and Heat Transfer Conference*, June 1982.

[172] M. Smart and M. Flanagan. Uq system set to launch australia into space. *UQ News*, December 2015.

[173] I. Sobel and G. Feldman. A 3x3 isotropic gradient operator for image processing. In *Stanford Artificial Intelligence Project*, 1968.

[174] L. Soucasse et al. Flow-radiation coupling for atmospheric entries using a hybrid statistical narrow band model. *Journal of Geophysical Research*, 2015.

[175] R. J. Stalker. The free-piston shock tube. *Aeronautical Quarterly*, 17:351–370, 1966.

[176] R. J. Stalker. A study of the free-piston shock tunnel. *AIAA Journal*, 5:2160–2165, 1967.

[177] R. J. Stalker. Hypervelocity aerodynamics with chemical nonequilibrium. *Annual Review of Fluid Mechanics*, 21:37–60, 1989.

[178] D. A. Stewart, D. B. Leiser, M. Smith, and P. Kolodziej. Thermal response of integral multi-component composite thermal protection systems. *Journal of Spacecraft and Rockets*, 23(4):420–427, July - August 1986.

[179] B. Sundvist. Thermal diffusivity and thermal conductivity of chromel, alumel, and constantan in the range 100-450k. *Journal of Applied Physics*, 2(72):539–545, 1992.

[180] K. Sutton. Heating analysis for the pioneer venus multiprobe mission. Technical report, NASA, July 1974.

[181] K. Sutton and Jr. R. Graves. A general stagnation-point convective heating equation for arbitrary gas mixtures. Technical Report R-376, NASA, 1971.

[182] M. Takahashi and K. Sawada. Simulation of entry flight flowfield over four probe vehicles in pioneer-venus mission. In *40th AIAA Aerospace Sciences Meeting and Exhibit*, January 2002.

[183] N. Takashima and other. Preliminary aerothermodynamics of titan aerocapture aeroshell. In *39th AIAA/ASMA/SAE/ASEE Joint Propulsion Conference and Exhibit*, Huntsville, Alabama, 2003.

[184] M. E. Tauber. A review of high-speed, convective, heat-transfer computation methods. TP 2914, NASA, 1989.

[185] M. E. Tauber, G. P. Menees, and H. G. Adelman. Aerothermodynamics of transatmospheric vehicles. *Journal of Aircraft*, 24(9):594–602, 1987.

[186] M. E. Tauber, G. E. Palmer, and D. Prabhu. Stagnation point radiative heating relations for venus entry. Technical report, ERC Corp., 2010.

[187] M. E. Tauber and K. Sutton. Stagnation-point radiative heating relations for earth and mars entries. *Journal of Spacecraft*, 28(1):40–41, January - February 1991.

[188] M. E. Tauber and R. M. Wakefield. Heating environment and protection during jupiter entry. *Journal of Spacecraft and Rockets*, 8(6):630–636, June 1971.

[189] W. Thomson. On the age of the sun's heat. *Macmillan's Magazine*, 5:388–393, 1862.

[190] A. P. Thorne. *Spectrophysics*. Chapman and Hall, 1974.

[191] Y. S. Touloukian and E. H. Buyco. *Thermophysical Properties of Matter - The TPRC Data Series*, volume 4. Specific Heat - Metallic Elements and Alloys. Thermophysical and Electronic Properties Information Analysis Center Lafayette In, 1971.

[192] Y. S. Touloukian et al. *Thermophysical Properties of Matter - The TPRC Data Series*, volume 1. Thermal Conductivity - Metallic Elements and Alloys. Thermophysical and Electronic Properties Information Analysis Center Lafayette In, 1970.

[193] L. L. Trimmer and E. L. Clark. Stagnation-point velocity gradients for spherical segments in hypersonic flow. *AIAA Journal*, 7(10):2040–2041, October 1969.

[194] R. L. Trimpi. A preliminary theoretical study of the expansion tube, a new device for producing high-enthalpy short-duration hypersonic gas flows. Technical Report R-133, NASA, 1962.

[195] R. Truitt. *Fundamentals of Aerodynamic Heating*, pages 169–179. The Ronald Press Company, New York, 1960.

[196] H. Tsien. Similarity laws for hypersonic flows. *Journal of Mathematics and Physics*, 25:247–251, 1946.

[197] M. Ueda et al. Trajectory of hayabusa reentry determined from multisite tv observations. *Publications of the Astronomical Society of Japan*, 63:947–953, October 2011.

[198] D. Umbach and K. N. Jones. A few methods for fitting circles to data. *IEEE Transactions on Instrumentation and Measurement*, 52(6):1881–1885, December 2003.

[199] Pulsonnetti M. V. and R. J. Stalker. A study of scramjet scaling. In *International Space Plane and Hypersonic Systems and Technology Conference*, number 96-4533. AIAA, 1996.

[200] M. van den Berg and P. Falkner. Study overview of the venus entry probe. Technical report, European Space Agency, Planetary Exploration Studies Section & Science Payload and Advanced Concepts Office, 2007.

[201] M. D. Van Dyke. The supersonic blunt-body problem review and extension. *Journal of Aeronautical Sciences*, 25:485–495, 1958.

[202] M. D. Van Dyke. *Hypersonic Flow Research*, chapter Second Order Compressible Boundary Layer Theory with Application to Blunt Bodies in Hypersonic Flow, pages 37–76. Academic Press, 1962.

[203] A. Vaschy. Sur les lois de similitude en physique. *Annales Télégraphiques*, 19:25–28, January - February 1892.

[204] G. L. Vignoles. Reactive processes in high temperature porous materials. In O. Chazot and F. Panerai, editors, *Lecture Series on Porous Media Interaction with High Temperature and High Speed Flows*, number 5 in STO-AVT-VKI Lecture Series 2014/15 - AVT 261. von Karman Institute for Fluid Dynamics, 2015.

[205] W.G. Vincenti and C.H. Kruger. *Introduction to Physical Gas Dynamics*. Wiley, New York, 1965.

[206] R. M. Wakefield and W. C. Pitts. Analysis of the heat-shield experiment on the pioneer-venus entry probes. In *AIAA 15th Thermophysics Conference*, 1980.

[207] C. Y. Wen and H. G. Hornung. Non-equilibrium dissociating flow over spheres. *Journal of Fluid Mechanics*, 299:389–405, 1995.

[208] C. Wilke. Diffusional properties of multicomponent gases. *Chemical Engineering Progress*, 46(5):95–104, 1950.

[209] K. H. Wilson and H. Hoshizaki. Effect of ablation product absorption and line transitions on shock layer radiative transport. Technical Report CR-1264, NASA, 1969.

[210] M. J. Wright, D. Bose, and J. Olejniczak. Impact of flowfield-radiation coupling on aeroheating for titan aerocapture. *Journal of Thermophysics and Heat Transfer*, 19(1):17–27, January-march 2005.

[211] F. Zander. *Hot Wall Testing in Hypersonic Impulse Facilities*. PhD thesis, School of Mechanical and Mining Engineering, The University of Queensland, St. Lucia, QLD, Australia, 2013.

[212] F. Zander, R. J. Gollan, P. A. Jacobs, and R. G. Morgan. Hypervelocity shock standoff on spheres in air. *Shock Waves*, 24:171–178, 2014.

[213] F. Zander, R. G. Morgan, U. A. Sheikh, D. R. Buttsworth, and P. R. Teakle. Hot wall reentry testing in hypersonic impulse facilities. *AIAA Journal*, 51(2):476–484, 2013.

[214] V. Zoby. Empirical stagnation-point heat-transfer relation in several gas mixtures at high enthalpy levels. Technical report, NASA Langley Research Center, October 1968.

Part IV

Appendices

Appendix A

Cheaper, safer, larger: a new age for hypersonics

"We shall one day travel to the moon, the planets, and the stars, with the same facility, rapidity, and certainty as we now make the voyage from Liverpool to New York! Distance is but a relative expression, and must end by being reduced to zero."

- Jules Vernes, in *From the Earth to the Moon* (1865)

Since the early ages[1], funding for hypersonic research has been going up and down in accordance with government priorities. The growth and decline of the scientific community has been dictated by a few large-scale projects. In the US, these were embodied by famous examples such as the Apollo missions, the Space Shuttle, or the series of X-vehicles and the National Aero-Space Plane (NASP) in the eighties. Europe too had important successes such as the Hermes spaceplane, the Atmospheric Reentry Demonstrator (ARD) or more recently the Intermediate Experimental Vehicle (IXV). On top of these, there is on both sides of the Atlantic a long list of paper projects that were stopped at various stages of their development.

Despite this unsteadiness, illustrated in figure A.1, substantial progress has been done over the past century. We are now able to send humans in space (up to the Moon) and bring them back safely, both in lifting bodies and ballistic vehicles. We have landed probes on Venus, Mars, Titan, and plunged into the atmosphere of Jupiter. We have even brought back samples of asteroids and solar wind. It may seem from this brief overview that there is no real need to further invest time and effort in hypersonic research. Emerging trends of the space industry, however, might require a new wave of developments.

Firstly, evolutions in the design of launchers are being introduced, with most notably **reusable elements** (figure A.2). Two important players in that arena are Space-X (Falcon 9) and Blue Origin

[1]The term *hypersonic* was supposedly coined by the Chinese scientist Hsue-shen Tsien in a paper published in 1946 using the following definition: *"Hypersonic flows are flowfields where the fluid velocity is much larger than the velocity of propagation of small disturbances, the velocity of sound."*[196].

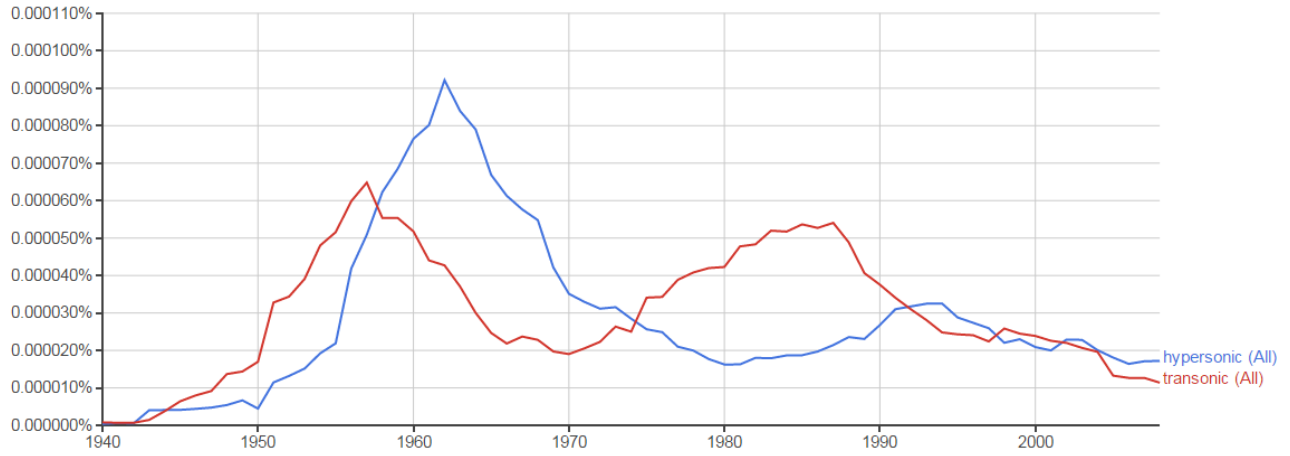

Figure A.1: *The popularity of hypersonics over time can be roughly represented with this graph provided by Google's Ngram application. In this case, we searched for the occurrence of the terms "hypersonic" and "transonic" in all the English books available on the Google Books database, depending on their year of publication (i.e. number of books contained the word divided by total number of books). Clearly, the Apollo era was the true golden age for hypersonic research. The small resurgence in the late eighties and nineties could be explained by the National Aero-Space Plane (NASP). (Source: Google)*

(New Shepard). There are, however, many more projects such as for example Adeline, a concept by Airbus Defense & Space, or Altair, a project by a European consortium led by Onera that recently received a €4 million grant from the European Commission [77]. Some interesting developments are also taking place in Australia with the Austral Launch Vehicle (ALV) concept [172]. While these reusable elements are retrieved at relatively moderate speed (e.g. ~ 2 km/s or Mach 6 for the Falcon 9 booster), they remain in the realm of hypersonic flows nonetheless.

There is also a certain resurgence of **air-breathing launchers**, with for example Reaction Engines Ltd. moving forward with its Skylon airbreathing rocket vehicle. Last year, the defense company BAE System bought a 20% stake in the company for €29 million, and the UK government confirmed it would allocate €85 million in grant funding to the project [162]. The purpose of these moves is to support the transition from a successful research phase into development and testing of the engine.

Secondly, a second generation of **cargo vehicles**, both manned and unmanned, is being developed to travel back and forth between the Earth and Low Earth Orbit (LEO). In the US, after a few years of quietness the follow-ups of the Space Shuttle are starting to make progress. In January NASA awarded the second share of its Commercial Resupply Services contract to Space-X (Dragon), Orbital ATK (Cygnus), and Sierra Nevada (Dream Chaser) for a total of $14 billion industry. Another contract for manned spaceflight had been awarded to Space-X (Dragon) and Boeing (CST-100) for a total of $6.8 billion in September 2014 [56].

In the wake of these achievements is the development of **space tourism**. All these vehicles will enable the take-up of orbital tourism, currently the domain of the sole Bigelow Aerospace and its space hotel. While there is no market yet, the company does own two inflatable modules in orbit around the Earth and is spending a considerable amount of resources in research and development[2]. Companies involved in suborbital tourism have not yet delivered up to the expectations of the public.

[2]Its revenues were estimated at $40 million in 2010

Even Virgin Galactic, considered by many as the leading contender in the race, is suffering from a massive delay after major technical incidents and safety concerns. However, the reality of suborbital tourism might be just around the corner. Once space tourism (sub-orbital and orbital) takes up, it has been predicted by some to represent a $\$1$ billion over the first decade [97].

The main lesson to be learned from these two trends is that private companies are being involved. The scientific community might have a fair knowledge of Earth entry, but the actors of the private sector want to do it at a higher frequency, they want it to be safer, and, most importantly, *they want to reduce their costs*. This implies that additional research needs to be done so as to obtain more accurate predictive tools and more performing materials. It is thus very likely that a fair fraction of all the budgets mentioned above will be dedicated to research and development in atmospheric entry.

Thirdly, the reduction in the typical size of satellites over the past few years led to an increase in the number of space missions. The number of satellites launched in 2013 was 3.3 times higher than in 2012. This growth was mainly driven by nano- and microsatellites (i.e. the $1 \cdots 50$ kg mass range) which increased from 36 to 92 launches [22]. These numbers are expected to grow even further in the coming years with the reduction of launch costs, due to aforementioned trends and the emergence of microlaunchers, as well as the development of small satellite constellations for Earth observation and telecommunication purposes.

The evident problem posed by that increased activity is the **multiplication of space debris**, which not only concerns spacecraft but also rocket upper stages. As illustrated in figure A.3, it is not unusual to read in the news about a rocket casing found nearby a village in remote regions of the world . The current regulations state that the orbital lifetime of objects passing through LEO shall be shorter than 25 years after the end of operation. To comply with that best practice rule, space systems manufacturers will need to implement new solutions. One specific challenge that needs to be tackled is to ensure that the entire craft burns up upon re-entry and is therefore not a threat for populations. These uncontrolled re-entries of unusual shapes and exotic materials are relatively new for the scientific community.

Lastly, while Earth orbit will increasingly become the realm of commercial companies, space agencies will step up towards new objectives. The current US space program foresees a manned mission to Mars around 2035, with incremental deep space missions in order to perfect the technologies required to protect astronauts from health hazards. On the old continent, the new director general of the European Space Agency (ESA) has clearly stated his ambitions for human spaceflight after the International Space Station (ISS): a village on the Moon.

These deep space missions will require to master **super-orbital entry to a whole new level**. Current capabilities for that type of mission are limited to relatively small spacecraft compared to what a typical manned mission would require. Moreover, the reliability of Entry, Descent and Landing (EDL) systems needs to be drastically improved. The short documentary describing the EDL of the Mars Science Laboratory (MSL) was entitled *"7 Minutes of Terror"* in reference to the large

(a) (b)

Figure A.2: *These two pictures represent very well the diversity of the efforts conducted in the frame of reusable launchers. On the right-hand side a picture of the first stage of Space-X' Falcon 9 rocket heading back to a floating platform during the first (failed) attempt to retrieve it. At the other end of this bold attempt are more modest projects. On the left-hand side, for example, a mock-up of rocket booster flies with a wing deployed during a test conducted in the frame of the ALV. (Source: NASA and Heliaq)*

(a) (b)

Figure A.3: *This fairing of Ariane V found nearby a fishermens village in Brazils Amazon region (a) and titanium motor casing of Delta 2 third stage slammed down in Saudi Arabia (b) illustrate the potential threat posed by the uncontrolled re-entry of rocket upper stages. (Source: AFP and NASA)*

uncertainties associated with that phase of the mission. It goes without saying that such a title would be unacceptable if the craft was to carry astronauts.

There is thus hope that a new age of hypersonics will come in the next decade, with research and development efforts aiming to develop cheaper and safer vehicles, master the re-entry of space debris, and perfect our knowledge or super-orbital entry. This will be both privately and publicly funded, as private entities are becoming increasingly involved in the space sector.

Appendix B

Complex chemistry example: Titan aerocapture

B.1 Simulations description and results

Let us confront our findings to a practical example that can be found in literature: the study of Titan hardshell aerocapture by Morgan et al. [127]. They performed numerical simulations in order to determine what changes could be observed between the peak heating conditions in flight and the corresponding flow obtained in a wind tunnel for a scale factor of $1/100$. The atmosphere of Titan is particularly interesting in that the main contributor to radiation is CN, which is produced through a complex chain of reactions involving primarily binary reactions but also ternary reactions [16].

The simulations were performed using the LAURA code developed at NASA Langley, with a two-temperature thermal and chemistry model, and does not consider radiation. The simulation of the flight assumed a radiative equilibrium wall boundary condition while for the scaled model the wall temperature was fixed at $T_w = 300\ K$. Both considered a super-catalytic wall, i.e. the flow is forced to return to free-stream mass fractions [127].

The contour of CN concentration obtained in both cases and the concentration of CN, CH_4, and N and temperatures profiles along the stagnation line are respectively depicted in figures B.1 and B.2 (a) and (b).

In order to better understand the mechanisms leading to the production of CN, Morgan et al. assessed the relative importance of the reactions that will ultimately produce CN with a one-dimensional standing shock using a single temperature model [127]. These are, from the most to the least dominant:

$$\begin{aligned} C + N_2 &\rightleftharpoons CN + N \\ HCN + M &\rightleftharpoons CN + H + M \\ C_2 + N &\rightleftharpoons 2CN \\ CN + C &\rightleftharpoons C_2 + N \\ C + N + M &\rightleftharpoons CN + M \end{aligned} \tag{B.1}$$

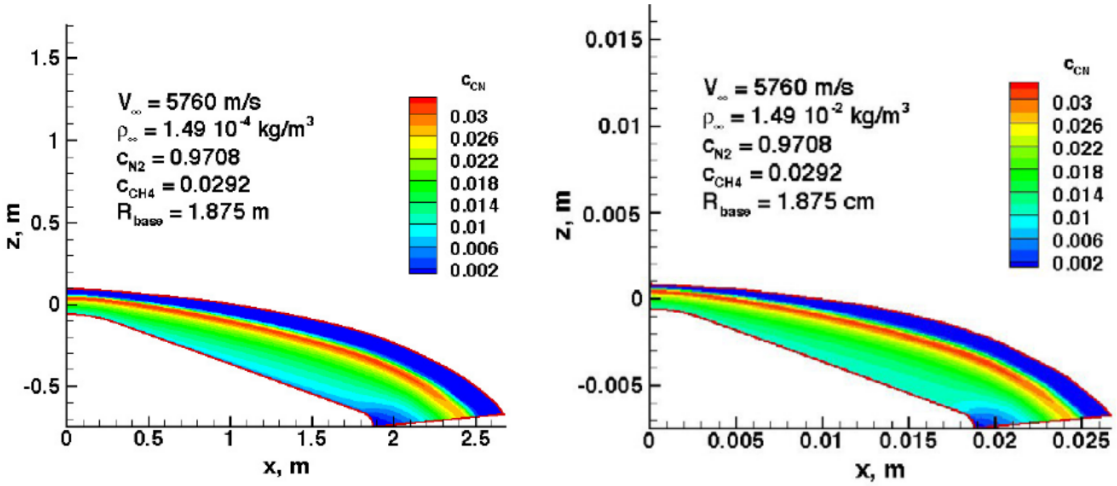

Figure B.1: *Contours of CN concentration for numerical simulation of flight (left-hand side) and $1:100$ scaled model (right-hand side) of Titan entry for flow conditions corresponding to peak radiative heating. Figure extracted from [127].*

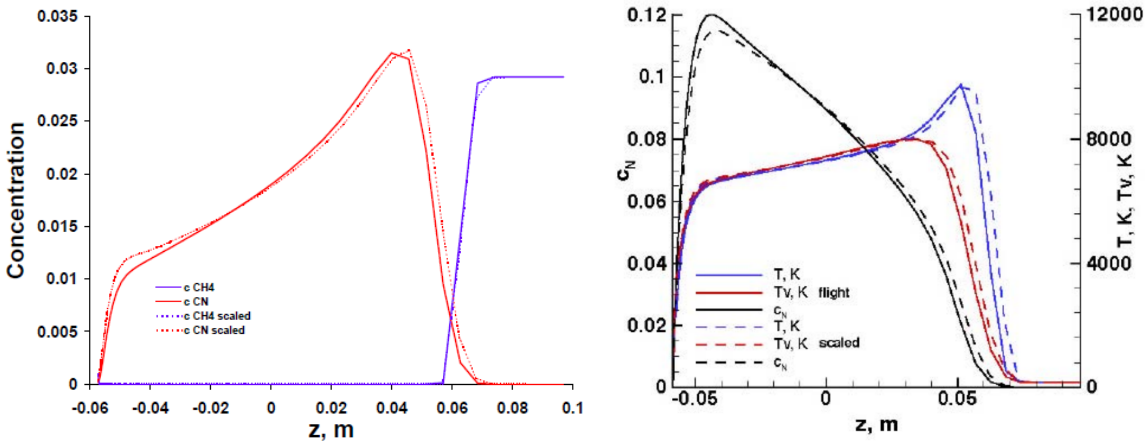

(a) (b)

Figure B.2: *Concentration of CN, CH_4 (a), N and temperatures (b) along the stagnation line for numerical simulation of flight (continuous) and $1:100$ scaled model (dashed) of Titan entry for flow conditions corresponding to peak radiative heating. Figures extracted from [127].*

The most dominant reaction is favored by a higher N_2 concentration. The second most dominant reaction is favored by a larger HCN concentration, which is itself produced through ternary reactions.

B.2 Confrontation with our own findings

The authors note that the two flows present very good similarity, especially in the nonequilibrium layer, the main source of radiation [127]. This can be attributed to the importance of binary chemistry in the production of the two species observed, i.e. CN and N.

Our first observation is that, from figure B.1, the shock standoff is slightly smaller for the laboratory flow. This goes against our conclusion made in section 3.2.4. However, we determined throughout section 3.2.1 that the two driving factors that could explain such a reduction were either a chemistry closer to equilibrium, or a colder average temperature in the shock standoff.

The latter, a colder flow is unlikely since, if anything, the shock layer appears to be hotter for the scaled flow (figure B.2 b). On the other hand, it does indeed appear that equilibrium is reached faster for the smaller-scale flow (figures B.2 a and b). This concurs with what we observed in equation 3.5; ternary reactions are taking place over a relatively shorter length-scale in the laboratory than in flight.

This counter-intuitive conclusion helps emphasize the importance of adjusting the conclusions made in chapter 3 when dealing with complex chemistries such as that encountered during titanic entry.

Our second observation is that, apart from the nonequilibrium region, the scaled flow is both hotter and less dissociated. This is immediately visible from the concentration of N (figure B.2 b) but also through that of CN (figure B.2 a). Indeed, as we saw in equations B.1, the concentration of the latter depends on a series of ternary reactions. It concurs to what we concluded in section 3.1.3. One should note that the wall conditions imposed for both simulations could also play a role.

B.3 Consequences for ground-to-flight extrapolation

Overall, if the scale 1 simulation was representative of the flight and the scale $1/100$ one was representative of an experiment conducted in a ground-based facility, the latter could be used to qualitatively represent the former. Nonetheless, it could not be used to quantify flow features such as the stagnation point heat flux. It is indeed clear from figures B.2 (a) and (b) that the temperature and species concentration gradients at the wall are not accurately reproduced.

Moreover, the results presented in this study are valid for what they are: numerical simulations, bounded by models. One can easily imagine that the discrepancies between the two actual flows would be even greater. As an example, the wall is likely to be colder in the laboratory than in flight, due to the shorter duration of the flow. If it is the case, it would remove more heat from the shock layer, causing the temperature to drop and / or the mixture to be less dissociated.

Appendix C

Impact of shock layer chemistry on density

C.1 Chemistry in the shock layer

Hornung investigated both numerically and experimentally the effect that chemical reactions have on density in nitrogen flows, correlating the shock standoff to a dissociation rate parameter [81], identified as the binary Damköhler number used in the present work. Wen and Hornung later generalized these results extending them to complex mixtures and taking into account the effect of the free-stream kinetic energy [207], which corresponds to our scaling parameter h_∞.

They first identify the effect of dissociation on the post-shock density as follows: let us consider the stagnation line for an inviscid adiabatic flow. Under those conditions, the momentum (equation 2.6) and energy (equation 2.17) balance equations read respectively as:

$$dp + \rho v dv = 0 \qquad\qquad dh + v dv = 0 \tag{C.1}$$

Therefore, one can write:

$$dp = \rho dh \tag{C.2}$$

which indicates that the only allowed entropy change is associated with chemical reactions. Indeed, when the number of particles in the closed thermodynamic system is variable, the specific internal energy u is expressed as:

$$du = Tds - pd\left(\frac{1}{\rho}\right) + \sum_i e_{a,s} dx_s \tag{C.3}$$

where s is the specific entropy. Expressing the specific internal energy in term of the specific enthalpy gives:

$$du = dh - pd\left(\frac{1}{\rho}\right) + \frac{1}{\rho} dp \tag{C.4}$$

which allows to write equation C.3 in terms of the specific enthalpy:

$$dh = Tds + \frac{1}{\rho}dp + \sum_i e_{a,s}dx_s \tag{C.5}$$

Using equation C.2, it simply becomes:

$$Tds = -\sum_s e_{a,s}dx_s \tag{C.6}$$

We have thus that the equation of state of the enthalpy must be of the form $h = h(p, \rho, x_s)$, and we can thus write:

$$\begin{aligned} dh &= \frac{\partial h}{\partial \rho}d\rho + \frac{\partial h}{\partial p}dp + \sum_{s=2}^{n}\frac{\partial h}{\partial x_s}dx_s \\ &= \frac{\partial h}{\partial \rho}d\rho + \rho\frac{\partial h}{\partial p}dh + \sum_{s=2}^{n}\frac{\partial h}{\partial x_s}dx_s \end{aligned} \tag{C.7}$$

where the mass fraction of the first constituent x_1 was chosen as dependent variable for the sake of simplicity. Solving for $d\rho$, one obtains:

$$\begin{aligned} d\rho &= \frac{1-\rho\partial h/\partial p}{\partial h/\partial \rho}dh - \frac{\partial \rho}{\partial h}\sum_{s=2}^{n}\frac{\partial h}{\partial x_s}dx_s \\ \frac{d\rho}{\rho} &= \underbrace{\frac{u^2}{a_{\text{fr}}^2}\frac{du}{u}}_{\textit{compressibility}} \underbrace{- \frac{1}{\rho}\frac{\partial \rho}{\partial h}\sum_{s=2}^{n}\frac{\partial h}{\partial x_s}dx_s}_{\textit{chemistry}} \end{aligned} \tag{C.8}$$

where we used the frozen speed of sound a_{fr} defined with the second order terms as:

$$a_{\text{fr}}^2 = \frac{-\partial h/\partial p}{\partial h/\partial p - 1/\rho} \tag{C.9}$$

Two distinct effects have thus an influence on the distribution of density downstream of the shock: compressibility and the chemistry. In the stagnation region, the effect of compressibility is very small due to the high temperature (and thus large speed of sound) and relatively small flow velocity, leading to typical value for the frozen Mach number $\text{M}_{\text{fr}} \leq 0.2$ [207]. Only the chemistry is therefore further investigated.

C.2 Hornung [81]

To account for the effect of chemistry, Hornung only considers the binary reactions and introduces a normal shock reaction rate parameter Ω [81]:

$$\Omega = \left(\frac{\partial \alpha}{\partial t}\right)_{\text{fr}}\frac{R}{v_\infty} \tag{C.10}$$

which is equivalent to the local binary Damköhler number Da defined in equation 2.52 taken immediately downstream of the shock, i.e. where the assumption of a flow governed by dissociation reactions is the most accurate.

Hornung shows then numerically, over a wide range of parameters (for inviscid pure nitrogen), that the binary Damköhler number Da (as defined in equation C.10) correlates with the standoff density product defined as:

$$\tilde{\Delta} = \frac{\Delta}{2R}\frac{\rho_{\text{fr}}}{\rho_\infty} \tag{C.11}$$

Indeed, as depicted in figure C.1, where the interpolation of the numerical results is the dashed line, it seems to evolve from one constant value in frozen regime, to another smaller value in equilibrium regime, with a smooth transition (sigmoid-type) between both. From figure C.1, one can also see that equation E.7, which is the form under which Hornung's correlation is often encountered in the literature, is the solution obtained numerically for a frozen flow:

$$\frac{\Delta}{R} = 2.32\frac{\rho_\infty}{\rho_{\text{fr}}} \tag{C.12}$$

He further presents the results of a series of tests he performed in the free-piston driven shock tunnel T3 a series of experiments on cylinders of various sizes in different flows, also using nitrogen as a test gas [81]. Although the same general trend can be observed, there is a substantial difference between his experimental results and numerical prediction. First, the results follow a steeper slope than the theoretical one, and lie well to the right of it. Second, there seem to be an effect connected to the model size: for a constant Da the standoff density product is systematically higher for smaller cylinders. A possible explanation for that unforeseen effect is the three-dimensional effect that arise when using cylinder [207]. However, using the experimental correlation of Eichmann et al. [44] to characterize the ratio between the three- and ideal two-dimensional shock standoff, it appears that the three-dimensional effects incur a change smaller than 99.999% only for the two smallest cylinder. Their scale factor being $L/D = 3.0$ and 1.5, the resulting ratio is 99.350% and 91.950% respectively, which is not sufficient to explain the experimental discrepancy observed by Hornung.

C.3 Wen and Hornung [207]

In a later paper, Wen and Hornung define Ω in a slightly different fashion [207]. Indeed, the dissociation rate can be expressed as:

$$\left(\frac{\partial\alpha}{\partial t}\right)_{\text{fr}} = \left(\frac{1}{\rho}\frac{d\rho}{dt}\right)_{\text{fr}} \tag{C.13}$$

in which case equation C.10 becomes:

$$\tilde{\Omega} = \left(\frac{1}{\rho}\frac{d\rho}{dt}\right)_{\text{fr}}\frac{R}{v_\infty} \tag{C.14}$$

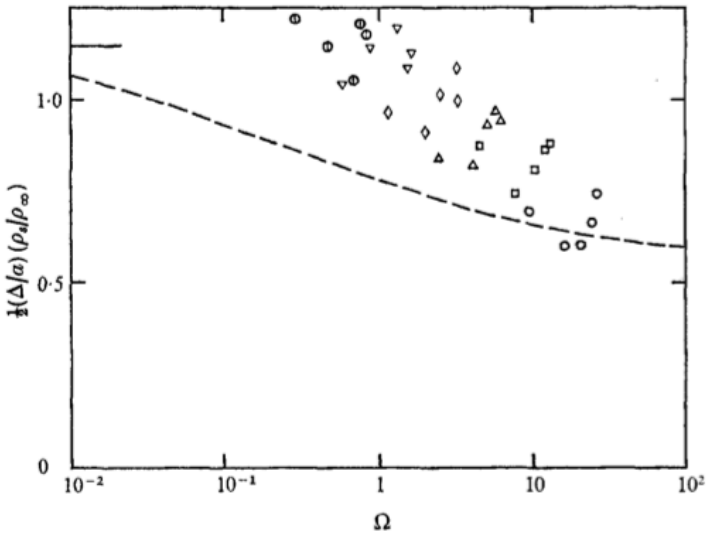

Figure C.1: *Numerical (dashed line) and experimental (symbols) results reported by Hornung while measuring the shock standoff distance over cylinders in nitrogen. The vertical axis is the standoff density product* $(\Delta/2R)(\rho_{fr}/\rho_\infty)$ *and the horizontal axis is a the local binary Damköhler number immediately downstream of the shock* Da_s*, using the cylinder radius as a typical length-scale. Different cylinder radius were used:* 4in *(empty circle),* 2in *(square),* 1in *(triangle on its base),* 0.5in *(diamond),* 0.25in *(triangle on its summit),* 0.125in *(dotted circle). Image taken from [81].*

and using the definition for the density gradient obtained in equation C.8, where the effect of compressibility is neglected, one obtains:

$$\tilde{\Omega} = \left(\frac{\partial \rho}{\partial h} \sum_{s=2}^{n} \frac{\partial h}{\partial x_s} \frac{dx_s}{dt} \right)_{\text{fr}} \frac{R}{\rho_{\text{fr}} v_\infty} \tag{C.15}$$

They further show that, assuming the mixture behaves like a perfect gas, one can write:

$$\tilde{\Omega} = \left(\sum_{s=2}^{n} \frac{e_{a,s}}{c_p T} \frac{dx_s}{dt} \right)_{\text{fr}} \frac{R}{v_\infty} \tag{C.16}$$

where we also used equation 3.10 (or equation 2.63) to express the partial derivative of enthalpy with respect to mixture composition. Wen and Hornung interpret that dimensionless number $\tilde{\Omega}$ as the ratio between the energy absorption rate by chemistry with the input rate of free-stream kinetic energy [207].

One can also consider that form as an extension of the Damköhler number for flows that have a more complex chemistry than a simple Lighthill-Freeman dissociation model. Indeed, in equation 2.52 we considered the ratio between two characteristic time-scales: one for convection, here $\tau = R/v_\infty$ and the other for chemistry, here:

$$\tau = \frac{1}{\left(\sum_{s=2}^{n} \frac{e_{a,s}}{c_p T} \frac{dx_s}{dt} \right)_{\text{fr}}} \tag{C.17}$$

In addition, equation C.16 includes a dimensionless number to characterize the dissociation potential:

$$\tilde{D}_s = \frac{e_{a,s}}{c_p T} \tag{C.18}$$

That parameter $\tilde{D}$ is equivalent to the Arrhénius parameter defined in equation 2.55. As already mentioned, it is implicitly conserved through the application of the binary scaling: the total enthalpy has to be duplicated, which conserves $c_p T$, and the same gas mixture has to be used, which conserves $e_{a,s}$.

Wen and Hornung then relate that parameter to the dimensionless shock standoff distance by simplifying the density distribution in the shock layer in two sections: first, immediately downstream of the shock, a region in which the density increases linearly with the distance from its frozen value to the equilibrium value, followed by a region in which the density is at a constant equilibrium value, up to the surface of the body (the flow being inviscid). From that model, they obtain two solutions. If the density does not reach its equilibrium value, then equation 3.15 becomes [207]:

$$\frac{\Delta}{2R}\frac{\rho_{\text{fr}}}{\rho_\infty} = \frac{1}{\tilde{\Omega}}\left(-1 + \sqrt{1 + 4L\tilde{\Omega}}\right) \tag{C.19}$$

where L is a geometrical factor that corresponds to the proportionality factor between the dimensionless shock standoff and the density ratio, in the case of a non-reacting flow (i.e. $\tilde{\Omega} = 0$). Its reported value is $L = 1.16$ for cylinders [81] and $L = 0.41$ for spheres [207]. If the density does reach its equilibrium value ρ_{eq} before reaching the surface of the body, then equation 3.15 becomes [207]:

$$\frac{\Delta}{2R}\frac{\rho_{\text{fr}}}{\rho_\infty} = \frac{\rho_{\text{fr}}}{\rho_{\text{eq}}}\left[L + \frac{1}{4\tilde{\Omega}}\left(\frac{\rho_{\text{eq}}}{\rho_{\text{fr}}} - 1\right)^2\right] \tag{C.20}$$

where the equilibrium density ρ_{eq} can be linked to a dimensionless kinetic energy $\tilde{K}$ of the form:

$$\tilde{K} = \frac{v_\infty^2}{2e_a} \tag{C.21}$$

However, $\tilde{K}$ is already included in $\tilde{\Omega}$ through the term that we identified as the dimensionless dissociation potential $\tilde{D}$.

They further present the result of numerical simulations, for an inviscid flow with a two-temperatures model, and experiments performed in the T5 free-piston shock tunnel T5 at GALCIT. The results for carbon dioxide are shown respectively in figure C.2 (a) and (b). Both were performed for spheres of various diameter [207].

Clearly, the agreement between experiments, simulations, and theoretical predictions is rather good, indicating not only that the dimensionless shock standoff does indeed correlate with the advancement of chemistry in the shock layer $\tilde{\Omega}$ and the kinetic energy of the flow $\tilde{K}$, but also that the model developed by Wen and Hornung is satisfying. They further draw two conclusions relevant for our study. First, in the case of carbon dioxide, the effect of $\tilde{\Omega}$ is more dramatic, because it has lower

dissociation energies. Second, for a fixed $\tilde{\Omega}$ a higher enthalpy leads to a thicker nonequilibrium layer, and thus a small dimensionless shock standoff, until a certain enthalpy above which that effect is negligible (the flow being completely dissociated no matter what).

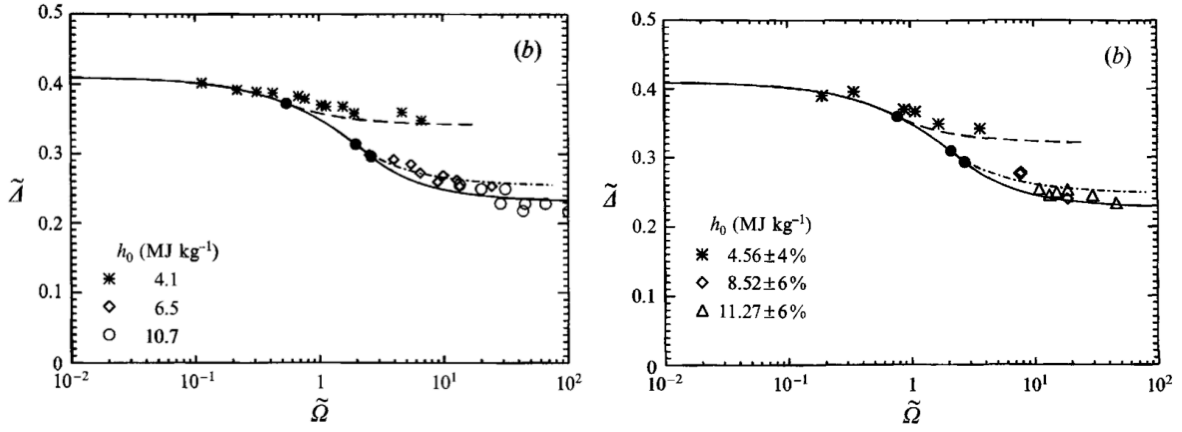

(a) (b)

Figure C.2: *Numerical (a - on the left-hand side) and experimental (b - on the right-hand side) results reported by Wen and Hornung while measuring the shock standoff distance over spheres in carbon dioxide. The vertical axis is the standoff density product $\tilde{\Delta} = (\Delta/2R)(\rho_{fr}/\rho_{\infty})$ and the horizontal axis is a the local binary Damköhler number immediately downstream of the shock Da_s, using the sphere radius as a typical length-scale. The full circles are the junction between equation C.19 and C.20. Images taken from [207].*

C.4 Inger et al. [87]

Inger et al. had a similar approach, but proposed a more developed model for the density distribution across the shock layer with a new analytical theory based on the use of a compressibility coordinate transformation layer for inviscid shock layers [87]. While the development of their theory is out of the scope of the present study, it is nevertheless interesting to examine the results of a parametric study they conducted:

- The evolution of dimensionless shock standoff distance with respect to the Damköhler number Ω follows a similar trend as what is predicted by the model of Hornung [81], although Inger et al. obtain a smaller value for the frozen limit.

- The dimensionless kinetic energy $\tilde{K}$ has a similar effect to what was observed by Wen and Hornung [207]: a higher $\tilde{K}$ will flatten the relationship between dimensionless shock standoff and Damköhler number, until $\tilde{K} \simeq 1$ above which its influence is negligible. That result is indeed what would be expected: a higher free-stream enthalpy would cause more dissociation, until the entire flow is dissociated.

- A larger frozen molecular vibrational excitation (larger γ_{fr}) results in a smaller nonequilibrium shock standoff distance. Again, this is compatible with what is intuitively expected: some of the free stream's kinetic energy is used to excite the internal energy modes instead of causing dissociation.

- The free-stream dissociation fraction α_∞ has a limited effect for much of the nonequilibrium region (up to $\Omega \leq 10$). For larger values, free-stream dissociation will cause the shock standoff to inflate slightly.

Although they only accounted for spheres in nitrogen or hydrogen, the measurements are taken on the stagnation line and these trends are thus expected to be to some degree universal.

Appendix D

Elements of statistical thermodynamics

Determining the value of the emission and absorption coefficients requires a deeper dive in statistical thermodynamics. Recall equation 2.29 where we have briefly explored the different energy modes. For a molecule, there are the *translational*, *rotational*, *vibrational* and *electronic* energy. For atoms, this is restricted to translational and electronic. According to quantum physics, atoms and molecules are allowed to take only a certain number of discrete values, called levels, in each of these modes. A particular *energy level* can correspond to different *energy states*. The number of states leading to a particular level is called its statistical weight of degeneracy g.

At equilibrium and temperature sufficiently larger than 5 K, the ratio of population between two energy levels is given by Boltzmann's relation:

$$\frac{n_u}{n_l} = \frac{g_u}{g_l} e^{-E_{ul}/k_B T} \tag{D.1}$$

where g is the degeneracy or statistical weight of a certain energy level. Be n the total number density of a certain species, n_0 the population of the ground state, n_1 the population of the first excited level and so forth, one can thus write:

$$n = \sum_{i=0}^{\infty} n_i = \frac{n_0}{g_0} \sum_{s=0}^{\infty} g_s e^{-E_s/k_B T} = \frac{n_0}{g_0} Q(T) \tag{D.2}$$

where we introduced the partition function $Q(T)$. The number density of any level n_s can thereby be obtained as:

$$n_s = \frac{n}{Q(T)} g_s e^{-E_s/k_B T} \tag{D.3}$$

The energy difference between those two states e_{ul} is discrete and corresponds to the energy of the photon emitted or absorbed. It can thus be related to its frequency ν or wavenumber σ:

$$E_{ul} = E_u - E_l = h\nu_{ul} = hc\sigma_{ul} \tag{D.4}$$

where h is Planck's constant and the subscripts u and l refer to the upper (or excited) and lower states. The wavenumber will be used instead of the frequency in the rest of this section, as it is the unit

preferably used in spectrophysics.

Change of state can occur through tree family of mechanisms: bound-bound, bound-free and free-free transitions. The case for bound-free and free-free transitions is slightly different and will thus be treated at a later stage. Three bound-bound transition mechanisms can be identified. For a certain species Y:

$$\begin{aligned} \text{Spontaneous emision: } & Y_u \rightarrow Y_l + hc\sigma_{ul} \\ \text{Stimulated emision: } & Y_u + hc\sigma_{ul} \rightarrow Y_l + 2hc\sigma_{ul} \\ \text{Absorption: } & Y_l + hc\sigma_{ul} \rightarrow Y_u \end{aligned} \tag{D.5}$$

Photons having no mass, these are all unitary. From equation 3.6, and assuming the density and distribution of photons remains constant these mechanisms are taking place over a relatively longer length-scale in the laboratory than in flight.

The emission coefficient of the medium is the sum of the emission coefficient associated to each transition, derived by multiplying the emission intensity with a line shape function ϕ_σ:

$$\eta_\sigma = \sum_{ul} \frac{n_u A_{ul} hc\sigma_{ul}}{4\pi} \phi_\sigma \tag{D.6}$$

where n_u the number density of the upper state and A_{ul} is Einstein's spontaneous transition probability. The factor $1/4\pi$ is used to express the intensity in a single direction. Similarly, for the absorption coefficient:

$$\kappa_\sigma = \sum_{ul} \frac{\left(n_l B_{lu} - n_u B_{ul}\right) hc\sigma_{ul}}{4\pi} \phi_\sigma \tag{D.7}$$

where B_{lu} and B_{ul} are respectively Einstein's absorption and stimulated emission probability. This relation is preferred to equation 3.42 as it includes stimulated emission and is not constrained by the LTE hypothesis.

The three Einstein coefficients are linked through the Einstein-Milne relations:

$$A_{ul} = 8\pi hc\sigma_{ul}^3 B_{ul} \qquad\qquad g_u B_{ul} = g_l B_{lu} \tag{D.8}$$

All three of them can thus be determined if only one of them is known.

The Einstein coefficients, the energy levels of each states, and their degeneracy are intrinsic properties of the radiating species. As such, they can be calculated from their wave function. However, the associated development are vastly out of the scope of this document. The reader interested in those developments can find further information in any good spectrophysics textbooks such as [190].

Let us finally examine our last unknown: the line-shape function. The developments made so far assume an ideal monochromatic line for each transition. Transitions are actually associated with line profiles spread over a range of wavenumbers. This is due to three different processes:

- *Natural broadening.* Heisenberg's uncertainty principle requires that the uncertainty on the energy of a particle ΔE times the duration during which that particle is observed Δt must be larger or equal to $h/2\pi$. Therefore, the shorter the particle's lifetime is, the larger the uncertainty on its energy will be. The associated profile is shaped like a Lorentzian distribution. Its overall contribution however, is in most cases negligible compared to Doppler broadening.

- *Doppler broadening.* The particles that compose the gas have a certain thermal motions; some of them travel towards the detector while some others travel away from it. This results in a wavenumber shift distributed among the particles according to their thermal velocity distribution. The associated profile is thereby shaped like a Gaussian distribution.

- *Pressure broadening.* While interacting with other particle, spectral lines are broadened and even shifted. This effect is more important as pressure increases. The associated profile is shaped like a Lorentzian distribution.

The resulting line shape is therefore a convolution of a Gaussian and a Lorentzian distribution, assuming Doppler and pressure broadening are independent mechanism. The result of such a convolution is called a Voigt function. Evaluating that function is extremely complicated, due to the amount of processes involved, and an analytical solution does not exist. The line shape function is therefore usually a least-square fit approximation of a Voigt function, based on experimental data.

Bound-free transition mechanisms are expressed in their general form as:

$$YZ_k + hc\sigma \rightarrow Y_i + Z_j \tag{D.9}$$

The expression for energy conservation is therefore different from equation D.4 as there are two different products. Three different energy levels are thus involved, in addition to kinetic energy:

$$hc\sigma = \frac{1}{2}\mu_{Y,Z}\Delta v_{Y,Z} + E_i^Y + E_j^Z - E_k^{YZ} \tag{D.10}$$

where $\Delta v_{Y,Z}$ is the relative velocity of the products and $\mu_{Y,Z}$ their reduced mass:

$$\mu_{Y,Z} = \frac{m_Y m_Z}{m_Y + m_Z} \tag{D.11}$$

Three bound-free transition mechanisms can be identified:

$$\begin{aligned} \text{Photoionization: } & Y + hc\sigma \rightleftharpoons Y^+ + e^- \\ \text{Photodissociation: } & Y_2 + hc\sigma \rightleftharpoons Y + Y \\ \text{Photodetachment: } & Y^- + hc\sigma \rightleftharpoons Y + e^- \end{aligned} \tag{D.12}$$

As for bound-bound transitions, expressions are developed for the emission and absorption coefficients. They are, however, more complex to obtain and therefore out of the scope of this document. Nevertheless, it is interesting to note that level-to-level cross sections are used instead of Einstein's coefficients. Furthermore, accurate knowledge of the velocity distributions are also required as collisional processes are involved.

Free-free transition, or Bremsstrahlung transition, is due to free electrons slowing down after collisions with other species. The loss of kinetic energy results in the emission of a photon of equivalent energy.

Appendix E

Venus atmospheric entry

"With other men, perhaps, such things would not have been inducements; but as for me, I am tormented with an everlasting itch for things remote. I love to sail forbidden seas, and land on barbarous coasts."

- Herman Melville, in *Moby Dick* (1851)

The main experimental campaign conducted in the frame of this work concerns Venus atmospheric entry. It is therefore legitimate to dedicate an appendix to a brief survey of the current knowledge of our sister planet, the rationales to explore it further, and the endeavors already performed regarding the plumbing of its atmosphere.

The relationship between mankind and the planet Venus is briefly overviewed in this appendix; from the first observations with the naked eye to the present day. Although it is not a popular space exploration target, the Earth's sister planet has had its time of glory. The Soviet Union, in particular, had a very dense agenda with their successive Venera and Vega programs. The scientific community's current knowledge of Venus is then shortly summarized, insisting on the many points that remain unsolved: was Venus habitable? What is its inner structure? Why did the Earth and Venus end up with such different fates although they are so similar? Numerous questions are still to be answered.

The section section goes through all the past atmospheric probes and landers, explaining their differences and specificities. Three design families have flown through the atmosphere of Venus: two generations of Venera probes, and the Pioneer Venus probes.

The studies performed on Venus atmospheric entry are then synthesized. Only one flight experiment was flown, onboard the Pioneer Venus probes. The numerical studies subsequently performed aim at reproducing the results of that experiment, and the attempts to develop correlations for the aeroheating figures are based on those numerical studies. Lastly, the results of some experimental studies are presented, and in particular data obtained in the EAST shock tube.

E.1 A brief overview of Venus and mankind

E.1.1 Historical perspective

Being the second brightest object in the night sky, Venus was known to mankind long before the developments of astronomy. The first wanderers who took the time to look up at the stars were probably intrigued by this luminous point that did not seem to follow the same path as its companions. Venus' trajectory is indeed surprising; constantly in the vicinity of the Sun, sometimes rising a few hours before and sometimes setting a few hours later, a feature that was most certainly useful for navigation. Venus has therefore also been know as the *morning* or *evening star*, or even the poetical *shepherd star* in French. The early cultures believed that those were two distinctive celestial objects: Phosphorus and Hesperus according to the Greeks, Lucifer and Vesper according to the Romans. The Venus tablet of Ammisaduqa, originating from the Babylonians in the 16^{th} century BC, is the first document referring to the two as a single object. They named it Ishtar, after their goddess of love. It was only in the 6^{th} century BC that the Romans came to the same conclusion, and named it Venus, after their own deity. Venus is present in many myths and stories from different cultures all around the world. It is, for example, at the centre of a major ceremony of the aboriginal people Yolngu. They too had understood it was a single object, that they called Banumbirr, bound to the Sun by some kind of rope (figure E.1).

Centuries later, Venus constituted a major tool for the advances of astronomy. While observing it with his telescope during the beginning of the 17^{th} century, Galileo Galilei discovered that the planet had phases (figure E.2). The Italian scientist had the insight to interpret it as one more evidence to support heliocentrism. Transits of Venus were also historically of great importance as they allowed to measure the solar system. After their observation of the transit of 1639, Horrocks and Crabtree estimated the distance from the Sun to Earth equal to 97 millions of km. Although the actual figure is 150 millions of km, their estimate was roughly ten times larger than what was previously thought and provided an idea of the magnitude of the size of the solar system. James Cook's first expeditions was set up not only to look for the Terra Australis Incognita, the future Australia, but also to observe the 1769 transit from Tahiti. More recently, the 2012 Venus transit provided a great opportunity to tune the techniques used to search for exoplanets. The next one, however, will only take place in 2117.

Modern-day astronomical observations seemed to prove that Venus and the Earth were relatively similar. Some of their main characteristics, summarized in the upper part of table E.1, clearly show how much the two planets seem to look alike. Venus, however, remained a mystery to astronomers as its surface is hiding beneath a thick layer of clouds impenetrable to telescopes. Unsurprisingly, our sister planet was subject of the wildest dreams: perhaps its climate was similar to the equatorial regions of our own, potentially even harboring life?

The advent of new observation tools would settle the question. Two independent observation campaigns of Venus were conducted with radiotelescopes during the year 1956, both suggesting a $600\ \mathrm{K}$ temperature. The source of that signal could be the surface, which was in better agreement with radar observations, or the ionosphere. Exploring the planet's surface and answering that question

Figure E.1: *Banumbirr the Morning Star, aboriginal art by Jack Wunuwun (1983). Credits: "Aboriginal Art" by Wally Caruna.*

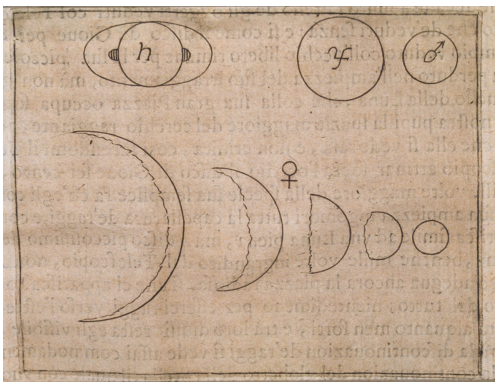

Figure E.2: *One of the historical engravings in Galileo's Saggiatore: Saturn, Jupiter, Mars, and Venus, with its phases, as he observed them through his telescope (1623). Credits: Instituto e Museo di Storia della Scienza, Firenze, Italy.*

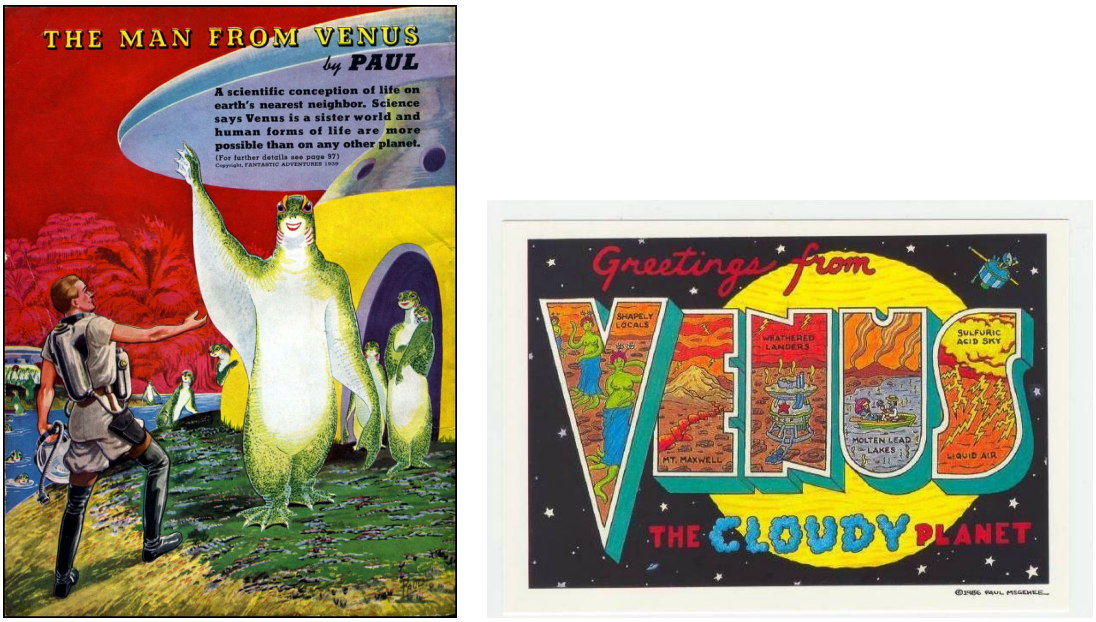

(a) (b)

Figure E.3: *Only half a century separates these two pop representations of Venus, and yet they are drastically different: the illustration on the right, from 1939, claims that "human forms of life are more possible than on any other planet" while the more realistic postcard on the left, from 1986, advertises a "sulfuric acid sky". This perfectly illustrates our change of perception of our so-called sister planet before and after the Venera missions: once a hospitable planet potentially harboring life, it is now considered as what most resembles hell in the solar system. Credits: Fantastic Adventures, July 1939 and Paul McGehee*

became therefore the main rationale for the first missions sent to Venus [84].

In February 1961, a few months only after the failure of their first Mars probes, the USSR launched two spacecraft to Venus. Although the first one remained in Earth orbit due to a failure of the launcher, the second one, then called Venera 1, became the first man-manned object to be placed on an interplanetary trajectory. Unfortunately, communication was lost a few days later. Nevertheless, many successes and historical firsts followed. One of prime importance was the first picture from an alien world ever taken, reproduced in figure E.4. Since then, the USSR missed only three launch windows, totalizing 29 launch attempts, until 1984 when their Venus exploration program was closed. Most of those probes were atmospheric sounders or landers and are described in section E.2.2.

Figure E.4: *Pictures of Venus' surfaces taken by Venera 9 (top) and 10 (bottom). Those historic documents are the very first pictures from an alien world. Credits: NASA, National Space Science Data Centre.*

Despite the Soviet efforts, the US would be the first to have a successful mission; Mariner 2, launched in August 1962. The probe measured Venus' radio emissions and confirmed the hypothesis of an extremely hot surface, very different from that of the Earth (see table E.1). The perspective on Venus changed, as illustrated in figure E.3, and the US space exploration program was thus redirected to Mars. Up to now the US have made only 10 launch attempts to Venus, many of them being flybys as Venus is a privileged target for gravity boost in interplanetary trajectories. Messenger was, in 2007, the last US-based observation of Venus.

Venus Express, the European orbiter launched in November 2005, is the last spacecraft to have explorer the planet. After 8 years of investigations, the perigee of the spacecraft was gradually lowered from $\sim 200\ \mathrm{km}$ down to $130\ \mathrm{km}$ to study aerobreaking. That phase lasted from the 18^{th} of June to the 11^{th} of July 2014, and the orbiter behaved exceptionally well. The mission terminated on the 16^{th} of December 2014, as the spacecraft was out of fuel and could thus not maintain its attitude.

E.1.2 Venus as a planet

As depicted in the second part of table E.1, scientists finally learned from robotic exploration that Venus' surface is actually very different from that of the Earth. Venus' atmosphere is the thickest of all the terrestrial planets, with a surface pressure of $9.2\ \mathrm{MPa}$, and is primarily composed of CO_2,

similarly to that of Mars. This results in a strong greenhouse effect and an average surface temperature of 735 K, hotter than Mercury's.

Physical property			Venus	Earth	Mars
Mass	m	[kg]	$4.87 \cdot 10^{24}$	$5.97 \cdot 10^{24}$	$6.42 \cdot 10^{23}$
Equatorial radius	R	[km]	$6,051$	$6,378$	$3,396$
Mean density	ρ	[kg/m^3]	$5,243$	$5,515$	$3,933$
Surface gravity	g	[m/s^2]	8.87	9.81	3.71
Solar irradiance	I	[W/m^2]	$2,613.9$	$1,367.6$	589.2
Major atmospheric components	ϕ	[m^3/m^3]	96.5% CO_2, 3.5% N_2	78.8% N_2, 20.9% O_2	97.3% CO_2, 2.7% N_2
Surface temperature	T	[K]	737	288	210
Surface pressure	p	[kPa]	9200	101.32	0.63

Table E.1: *Major outer and surface characteristics of Venus, Earth, and Mars. It is no wonder that Venus was called the sister planet of the Earth. Its surface parameters, however, do not make it a very appealing candidate for astrobiology.*

Orbit and rotation

Venus is the second planet of the solar system, lying at an average distance of about 0.72 AU from the Sun. As it is in the inner solar system, Venus presents phases when observed from the Earth. Its orbit is the most circular of all the planets, with an eccentricity smaller than 0.01. A Venusian year lasts 224.7 Earth days. Surprisingly, Venus has a retrograde rotation, meaning it rotates clockwise when viewed from above the North pole. Furthermore, that rotation is extremely slow; 6.5 km/h at the equator as compared to $1,670$ km/h for the Earth. This causes the sidereal Venusian day to lasts 243.0 Earth days, longer than a Venusian year. The solar Venusian day, however is significantly smaller: 116.7 Earth days. The reason for this retrograde rotation is still unknown.

Venus has no natural satellites. The asteroid 2002 VE68 is currently in quasi-orbital relationship with the planet. The asteroids 2001 CK32 and 2012 XE133 are also temporary co-orbitals.

Geology

The planet's surface is relatively young, 500 million to 1 billion years, and smooth; three quarter being covered by plains with occasional large basins. This is due to the planet's intense volcanic activity, relatively recent and still residual. So far, $1,700$ volcanoes have been identified, and many more are believed to be discovered. Two large elevated areas could be considered as the equivalent of Venusians continents. *Ishtar Terra*, in the polar region of the northern hemisphere, is roughly the size of Australia. It is home to the planet's highest point, *Skadi Mons*, part of the *Maxwell Montes*. The second one, *Aphrodite Terra*, is three times as large but considerably less elevated. It spreads along the equator, mainly in the southern hemisphere. It is home to the planet's highest volcano, *Maat Mons*.

Thus far, no seismic experiments have been conducted on Venus and little information is therefore available about its internal structure. As its size and density are similar to that of Earth, it is believe to

have the same structure: core, mantle and crust. Unlike the Earth, however, there is no plate tectonic on Venus.

Climate

Venus and the Earth's climates are believed to have been very similar in the early times. An anomalous presence of deuterium has indeed been detected on Venus, which is consistent with a primordial ocean. However, Venus being closer to the Sun it received slightly more energy. Strictly considering the difference in irradiance, the planet should be only ~ 35 K hotter.

It is believed that while the Earth's oceans transformed the atmospheric carbon dioxide into limestone, that small temperature difference was sufficient to cause Venus' oceans to boil away. The greenhouse effect caused the temperature to rise to such extremes that the soil released most of the gases it contained, reinforcing the greenhouse effect and increasing further the surface pressure. Since Venus posses no intrinsic magnetic field, its upper atmosphere interacts thus directly with the solar wind. The water vapor and other atmospheric compounds were thus ionized and transformed into a plasma wake swept away in outer space.

Indeed, measurements performed by Venus Express in the plasma wake showed it mainly consists of hydrogen, oxygen and helium ions. The $2:1$ ratio of hydrogen to oxygen ions tends to prove they originate from water molecules, probably from the planet's primordial oceans and then photodissociated in the atmosphere. This would explain the relatively low amount of water vapor in the planet's atmosphere today.

More data is needed to confirm that scenario, and to gain a better idea of the time-scales involved. Nevertheless, departing from almost the same initial conditions the Earth and Venus ended up with very different climates.

Atmosphere

Venus' atmosphere is mainly composed out of CO_2; 97% at the surface up to an altitude of 100 km, then decreasing to slightly less than 80%. The rest is primarily N_2, with traces of SO_2 (150 ppm at the surface), Ar (70 ppm), H_2O (20 ppm), CO (17 ppm), He (12 ppm), and Ne (7 ppm). This leads to a perfect gas constant of:

$$R_{\text{Venus}} = 0.97 \cdot R_{CO_2} + 0.03 \cdot R_{N_2} = 8.3230\text{J/molK} \tag{E.1}$$

It is divided in four section. The troposphere extends from the surface up to an altitude of 65 km. At the surface, the conditions are the harsh one already stated earlier and the CO_2 is in fact not gaseous anymore but a supercritical fluid, which has a very high heat transfer coefficient. Together with the thickness of the troposphere, this layer of supercritical fluid results in a temperature buffer between the night side and the day side, despite the planet's retrograde rotation. In the tropopause, the boundary layer between the troposphere and the mesosphere, the pressure and temperature reach levels similar to that of the Earth. The wind velocity increases from less than 2 m/s at the surface up to 100 m/s at the mesopause, almost purely in the longitudinal direction. The mesosphere starts at

$65\ \mathrm{km}$ and ends around $120\ \mathrm{km}$. It is characterized by two parts of distinct constant temperature: the lower, up to $73\ \mathrm{km}$, is at $\sim 230\ \mathrm{K}$, and the upper is at $\sim 165\ \mathrm{K}$. The thermosphere starts around $120\ \mathrm{km}$ and ends at $220 - 350\ \mathrm{km}$, where the exosphere starts. On the day side, its temperature is around $300 - 400\ \mathrm{K}$, and on the night side down to $100\ \mathrm{K}$.

The planet is completely covered with thick clouds, from about 40 up to $70\ \mathrm{km}$ and sometimes even $80\ \mathrm{km}$, with haze below and above up to $90\ \mathrm{km}$. They reflect around 75% of the sunlight, although their opacity is variable, so that the solar energy received at the surface is less than that on the Earth, despite Venus being much closer. They are composed of SO_2 and H_2SO_4. Although there is sulphuric rain, it evaporates before reaching the surface.

The Venus Global Reference Atmospheric Model (Venus-GRAM 2005) [19] is publicly available and widely used by the scientific and engineering community, including as a design tool for future entry missions. It has been developed by the Marshall Space Flight Centres Natural Environments Branch as an updated version of the Committee on Space Research (COSPAR) Venus International Reference Atmosphere (VIRA). It provides information of density, temperature, pressure, winds, and selected atmospheric constituents for any given time and geographic location at an altitude up to $1000\ \mathrm{km}$. It even allows for the generation of random perturbations. The model has been validated against data from Pioneer, Venera and Vega Venus entry probes and landers.

E.1.3 Venus today

Rationales

The modern rationales for Venus exploration are quite different. The Venus Exploration Analysis Group (VEXAG), established by NASA in 2005, has led many think tanks on the rationales and strategies for Venus exploration. Their 2009 report summarized the scientific community's view [109]. As stated in their document, there is *"an overarching goal - understanding Venus and the implications for the formation of habitable worlds - supported by a set of three scientific goals:*

- *Origin and evolution: How did Venus originate and evolve, and what are the implications for the characteristic lifetime and conditions of habitable environments on Venus and similar extrasolar systems?*
- *Venus as a terrestrial planet: what are the processes that have shaped and still shape the planet?*
- *Climate change and the future of Earth: what does Venus tell us about the fate of Earth's environment?"*

Besides the strict exploration for the sake of science, there is thus a demand for a better understanding of the Venusian climate. As explained in section E.1.2, Venus is believed to have had the same initial conditions as the Earth but its runaway greenhouse effect caused it to find a very different equilibrium climate. Gaining a better understanding of what happened to Venus' climate will help scientists understand global climate mechanisms on Earth, as well as the threat of the greenhouse effect.

Interestingly, current knowledge of Venus does not exclude for the planet to have been habitable sometime in the distant past, possibly long enough for life to develop. Again, to confirm that seductive idea more has to be discovered about the planet's geological and climatological history. Nevertheless, some astrobiologists have been thinking about how life could have adapted itself to the harsh Venusian environment [164]. It is known, indeed, that certain bacteria live and reproduce themselves within clouds on Earth, an unexpected environment for life to develop. Could the clouds of Venus be considered as an habitat? At around $50\ \mathrm{km}$ altitude, in the tropopause, the pressure and temperature are closer to that of Earth and water vapor is present, although in the form of concentrated sulphuric acid. The hypothetical life form would also have had to adapt to the high ultraviolet (UV) radiation level.

Future missions

Despite its relative loss of attractiveness, some exploration missions are still heading for Venus. The next mission to explore Venus is the Japanese spacecraft Akatsuki, launched in May 2010, missed its first orbital insertion but performed a successful second maneuver in December 2015. The ESA-JAXA probe Bepi-Colombo is planned to perform two flybys of Venus on its way to Mercury as it uses its gravitational assistance in September 2019 and May 2020. Unfortunately, the science package will be protected during the journey and the spacecraft will not be able to make any measurements of Venus.

Three mission are under development by major space agencies. First, the Venus Orbiter Mission, supervised by the Indian Space Research Organisation (ISRO), should be launched between 2017 and 2020. Little information is available about the mission objectives and exact timeline.

Second, Venera-D, supervised by Roscomos, the Russian Federal Space Agency, in collaboration with NASA's Planetary Science Division should be launched around 2024. It is a very ambitious project, including an orbiter and an air-ground segment. The air-ground segment would consist out of a lander, which upon re-entry would release two balloons, in the fashion of the Vega probes. The second balloon, in turn, would release up to four microprobes. It was supposed to be Roscosmos' second exploration mission of the solar system, after Phobos-Grunt. Originally, the launch of Venera-D was planned for 2017, with an even more ambitious mission, Venera-Glob, to be launched some years later. The failure of Phobos-Grunt, however, delayed Venera-D of several years and Venera-Glob indefinitely. Because of the political situation, even Venera-D has a very uncertain future.

Lastly, out of the five concepts proposed for the next launch opportunity in the Discovery Program of NASA, two are dedicated to Venus (the other three being for asteroïds). One of them, the Deep Atmosphere Venus Investigation of Noble gases, Chemistry, and Imaging (DAVINCI), is an atmospheric probe that would perform an hourlong[1] descent through the atmosphere.

Several other studies have been conducted, but not realized. A fairly comprehensive list is available in [200]. Unsurprisingly, many of them involve balloons (aerobots), atmospheric probes, and landers. Venus' thick atmosphere makes it a particularly interesting target for airborne exploration.

[1] 63 minutes, to be precise.

As for flybys, some advanced concepts propose to make even more efficient use of Venus' gravity assist for interplanetary spacecraft by penetrating its atmosphere, a technique referred to as aerogravity assist [121]. Enabling those future missions and maneuvers will require deeper understanding of Venus' atmospheric entry, a field in which there remain much to do.

Although Venus has lost its attractiveness, it has thus had its time of glory. During its golden age, in the mid 60s, NASA even seriously considered a manned flyby of the planet using Apollo hardware. Unfortunately, the budget of the Apollo Applications Program, which was supposed to support the mission, were cut and focus was set on the Skylab program. The URSS also had its own plans for a manned Venus flyby, although less advanced. However, some new rationales have been highlighted for its exploration and one of the many preliminary studies for a future mission could be concretized.

E.2 Venus atmospheric entry probes

E.2.1 Specific challenges

Atmospheric entry is a maneuver that only concerns the Earth, Mars, Venus, Titan, and the gas giants. Each of these is characterized by a different free-stream density, entry velocity, and atmospheric composition. While the frame of the problem is thus the same, the boundary conditions are very different. From table E.1, it is clear that Venus and Mars have a very similar atmospheric composition and one could thus question why Mars and Venus entry are not studied jointly. The thicker atmosphere of Venus should not pose a problem as the deceleration phase takes place at very high altitude. However, Venus is considerably more massive than Mars, resulting in a larger escape velocity: respectively $10.36\ \mathrm{km/s}$ and $5.03\ \mathrm{km/s}$.

The resulting effect for ballistic entry is illustrated in figure E.5, where the trajectories of two typical cases are put in comparison: the Pioneer Venus Day probe and the Mars Science Laboratory. At the same static pressure the flight velocity of Venus probes is almost twice as important as that of Mars probes. The energetics of the shock are thus considerably more important, leading to a higher rate of dissociation and ionization. Similarly, for the same flight velocity the free-stream static pressure encountered by the Venus probe is ten times as important as that encountered by the Mars probe. The kinetic energy intake is thus also more important, as well as the collisional rate, resulting in a shorter nonequilibrium layer.

Design rules developed for Mars entry can thus not be applied to Venus in a straightforward manner. Nevertheless, it is interesting to dig in the important amount of knowledge that has been gathered over the years for Mars entry, in order to observe the evolution of different flow quantities with larger entry velocities.

Sengupta and Hall describe the Venusian entry environment as being *"characterized by a* $11 - 12$ $\mathrm{km/s}$ *entry velocity,* $100 - 200\ gs$*, peak heat flux of* $> 30\ \mathrm{MW/m^2}$*, sulphuric acid cloud layer, high altitude winds, and [harsh] surface ambient temperature and pressure"*. They further identify the challenges of a Venus entry mission as being: *"heat shield technologies, acid resistant parachutes,*

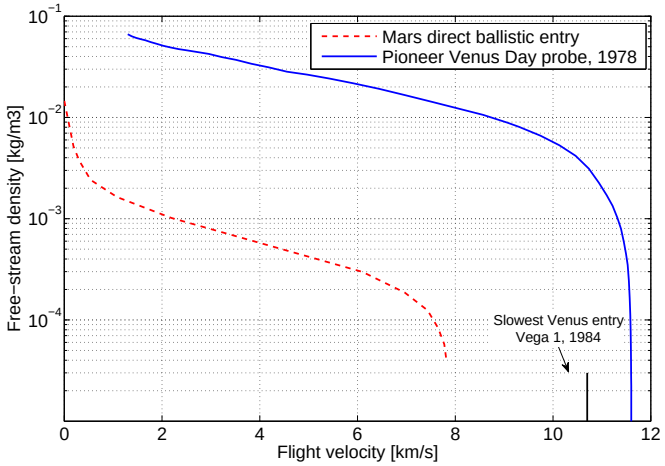

Figure E.5: *Comparison of the Mars Science Laboratory expected trajectory with the Pioneer Venus Day probe trajectory.*

pressure vessel to house the instrumentation, landing attenuation system, high temperature wiring and terminal descent dynamics through the Venus atmosphere" [168]. While entry and descent are complex maneuvers, landing is on the contrary rather simple from a mechanical perspective; the surface conditions are so extreme that CO_2 is not a gas anymore but a supercritical fluid[2] [51] which damps the landing shock.

Table E.2 summarizes the key parameters of the 17 probes which have entered Venus' atmosphere and transmitted data during at least part of their descent. All the probes performed a direct entry from their interplanetary trajectory, and had therefore a velocity higher than the planet's escape velocity.

With the exception of the Pioneer Venus mission, none of the probe were instrumented to record temperature or heat fluxes during the aeroheating phase of entry. The peak deceleration and peak heat flux figures are thus derived from trajectory rebuilding using engineering estimates and not from actual flight data. This leads to significantly underestimated values, at least for the heat fluxes. As an example, the flight validated rebuilding of the Pioneer Venus aeroheating by Ahn and Park [149] indicates a peak heat flux of 15.53 and 12.13 $\mathrm{MW/m^2}$ respectively for the North and Day probes while Dutta et al. [40] obtain 10.6 and 7.8 $\mathrm{MW/m^2}$ with trajectory rebuilding. The same conclusion is reached for the Sounder probe in section E.4.

E.2.2 Venera and Vega

Venera is the name of the series of Soviet spacecraft that were launched to explore Venus, except for the last two which were called Vega although their design was similar. Many advances in the field of planetary exploration were made during the program: Venera 3 became the first man-made device to enter the atmosphere of another planet in 1966, although it did not transmit any data. Venera 4 achieve that prowess in 1967. Venera 7 was in 1970 the first to make a soft landing on another planet. Venera 9 was in 1975 the first to take pictures of an alien world and send them back to Earth (figure

[2]The critical point of CO_2 lies at $T = 304.25$ K and $p = 7390$ kPa.

Table E.2: *Main parameters of all Venus atmospheric probes and their trajectories. Compiled from [9] and [40].*

Probe name	Year launched	Nation	Shape	Nose radius R [m]	Mass [a] m [kg]	Ballistic coefficient β [kg/m^2]	Entry velocity [b] v_{entry} [km/s]	Entry angle γ_{entry} [deg]	Peak deceleration [c] a [m/s^2]	Peak heating [d e] q_w [MW/m^2]
Venera 4	1967	USSR	Sphere	0.50	383	519	10.70	-78	450	9.66
Venera 5	1969	USSR	Sphere	0.50	405	549	11.20	-62 to -65	450	13.5
Venera 6	1969	USSR	Sphere	0.50	405	549	11.20	-62 to -65	450	13.5
Venera 7	1970	USSR	Sphere	0.50	500	677	11.20	-60 to -70	452	17
Venera 8	1972	USSR	Sphere	0.50	495	670	11.60	-77	500	30
Venera 9	1975	USSR	Sphere	1.20	1,500	367	10.70	-20.5	150	2.04
Venera 10	1975	USSR	Sphere	1.20	1,500	367	10.70	-22.5	170	3.37
Pioneer Sounder	1978	USA	45 deg sphere-cone	0.36	316	188	11.54	-32.4	280	40
Pioneer North	1978	USA	45 deg sphere-cone	0.19	94	190	11.54	-68.7	458	15.53
Pioneer Night	1978	USA	45 deg sphere-cone	0.19	94	190	11.54	-41.5	350	12.89
Pioneer Day	1978	USA	45 deg sphere-cone	0.19	94	190	11.54	-25.4	223	12.13
Venera 11	1978	USSR	Sphere	1.20	1,600	376	11.20	-18 to -21	167	4.35
Venera 12	1978	USSR	Sphere	1.20	1,600	379	11.20	-18 to -21	167	4.35
Venera 13	1981	USSR	Sphere	1.20	1,650	387	11.20	-18 to -21	167	4.35
Venera 14	1981	USSR	Sphere	1.20	?	?	11.20	-18 to -21	167	4.35
Vega 1	1984	USSR	Sphere	1.20	1,750	412	10.70	-18.2	130	3.06
Vega 2	1984	USSR	Sphere	1.20	1,750	412	10.80	-19.1	139	3.29

[a] Venera 9-13 and Vega 1-2 estimated by author with the ballistic coefficient's definition.
[b] At an altitude of 200 km.
[c] Except for Pioneer mission which come from [133], the trajectories were simulated in [40] for given entry conditions.
[d] At the stagnation point.
[e] Except for Pioneer mission which come from [149], the trajectories were simulated in [40] for given entry conditions under the cold wall assumption.

E.4). All the probes' thermal protection systems (TPS) were roughly based on the same idea: a large spherical heat shield would protect the payload during the aeroheating phase.

Two different design strategies were used. The first probes had a diameter of $1\ \mathrm{m}$. The sphere's cap was removed after the aeroheating phase and a parachute deployed. There was thus no separate lander and the probe was supposed to land with its heat shield. Little information is available on the heat shield itself. It was most probably made out of ablative material, such as phenolic epoxy resin.

Soviet scientists thought Venera 4 had successfully landed on the planet and measured a surface pressure of $25\ \mathrm{atm}$. However, a year later it appeared from data of the US mission Mariner 5 that the surface pressure was in fact more in the range of $75 - 100\ \mathrm{atm}$. Venera 4 did not land but simply stopped transmitting data while still flying through the atmosphere; it was not design for such high pressure. It was too late for Venera 5 and 6, which were sent as atmospheric probes rather than surface experiments. Venera 7 and 8 had the same outer design as the previous probe but were massively overbuilt to survive the harsh surface conditions and make a soft landing, reducing the scientific payload to the strict minimum. Venera 8 landed on the day side of the planet and, although it was not equipped with a camera, measured the illumination to be sufficient to make pictures.

From Venera 9 onwards the probe's design would be different, larger and more massive, as their goal was clearly to explore the surface. The outer spherical heat shield's diameter was thus increased to $2.4\ \mathrm{m}$. The landing procedure for Venera 9 and 10 was the following: after the aeroheating phase, at an altitude of around $65\ \mathrm{km}$, a parachute was deployed for aerobreaking and, soon after, a second parachute removed the upper half of the sphere. When the probe, still attached to the lower half of the sphere, reached a velocity of $150\ \mathrm{m/s}$, another aerobreaking parachute was deployed and data transmission started. There is thus no trajectory or temperature information for higher altitudes. The second parachute was jettisoned, and at an altitude of $62\ \mathrm{km}$ three final aerobreaking parachutes were deployed, while the lower half of the sphere was separated from the lander. Around an altitude of $50\ \mathrm{km}$, those were cut off and the lander finished its trajectory in free fall. The landing procedures for the following probes were roughly the same, with some minor differences

The lander presented itself as a sphere protecting all the sensitive material from the pressure and heat, sandwiched between a crushable ring to ensure a soft landing on the bottom, and a large aerobrake disk on the top. The trajectory strategy was also changed; the first probes had very steep entry angles leading to high peak deceleration and heat fluxes, while the later ones were considerably shallower.

E.2.3 Pioneer Venus Multiprobe

Pioneer Venus was a US mission that consisted of two components, launched separately in 1978: the Orbiter and the Multiprobe. The Multiprobe was a bus carrying four atmospheric probes, a large one and three smaller ones (figure E.6). The primary goal of these probes was an in-depth study of Venus' atmosphere. The Large probe, or Sounder, entered the Venusian atmosphere on the night side near

the equator. At an altitude of ~ 50 km, the aeroshell separated from the probe and a parachute was released.

The small probes were meant to study the variation of the atmospheric parameters depending on the location (figure E.8). As they were smaller, their science package was less comprehensive and they were not equipped with a parachute. The North and Night probe both entered the night side, at about $60\,\mathrm{deg}$ north latitude and close to the equator respectively, and the Day probe the day side. Although none of the probes were designed to reach the surface, the Day probe continued to send a radio signal for some 70 minutes after the impact.

The four probes were geometrically similar: blunt sphere-cones, with a half-cone angle of $45\,\mathrm{deg}$. The heat shield was made out of carbon-phenolic, which was at the time the only robust and properly characterized ablating material able to withstand the high heating rates the probes would be experience [102]. They were instrumented with two thermocouple each, $3 - 4$ mm below the surface, one near the stagnation point and the other close to the frustum edge. All the thermocouples data were properly transmitted. The accelerometer data was only retrieved for the North and Day probes. Trajectory data is also available for the Night probe. However, its accuracy is lower as the data transmission rate was lower than expected. These are therefore the only probes for which a velocity-altitude map can be drawn based on actual measurements (figure E.9).

E.3 Experimental studies

E.3.1 Flight experiment

The only in-flight aerothermodynamics experiment conducted on any of the Venusian spacecrafts is the *heat shield experiment* on the Pioneer Venus probes. The rationale for that experiment was to learn how well the heat shields actually performed and add to the knowledge base for future design, and to determine with a great accuracy the ablation rate. Indeed, another experiment on-board concerned the atmospheric structure and required to know the probes' mass within 1%. That second experiment provided accurate tables for altitude, velocity, flight angle, density, pressure and temperature as a function of flight time, all compiled by Seiff and Kirk in [167]. The Pioneer Venus flights are therefore extremely well documented, and consist a useful base for the study of Venus atmospheric entry.

The experimental setup of the heat shield experiment is depicted in figure E.7. Each heat shield was instrumented with two chromel-alumel thermocouples; one at the stagnation point buried 4.10 ± 0.05 mm below the surface, and one closer to the flank 3.00 ± 0.05 mm below the surface. Because of the important temperature gradient normal to the surface, the junctions were flattened to a thickness of 0.02 mm [151].

Figure E.6: *The Pioneer Venus Multiprobe spacecraft being inspected by Charles Hall, then project manager of the mission, at Hughes Aircraft Co. in December 1976. Credits: NASA Ames Research Centre.*

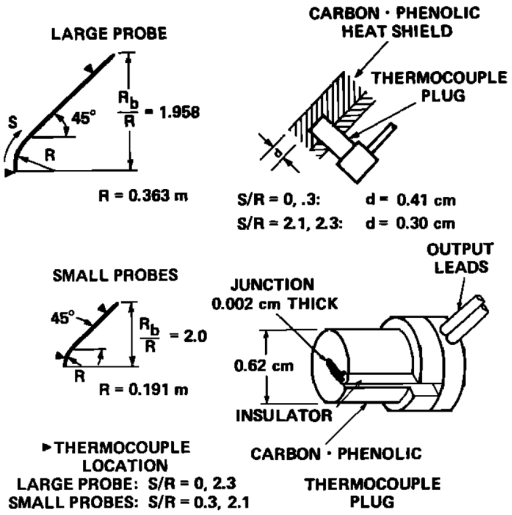

Figure E.7: *Detailed view of the Pioneer Venus heat shield experiment set-up and geometrical characteristics of the heat shields. Figure extracted from [151].*

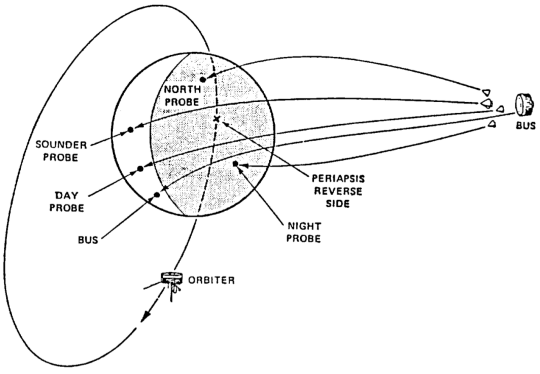

Figure E.8: *Pioneer Venus Orbited in position while the Bus has released the four probes that all land at their respective location. Figure extracted from [53].*

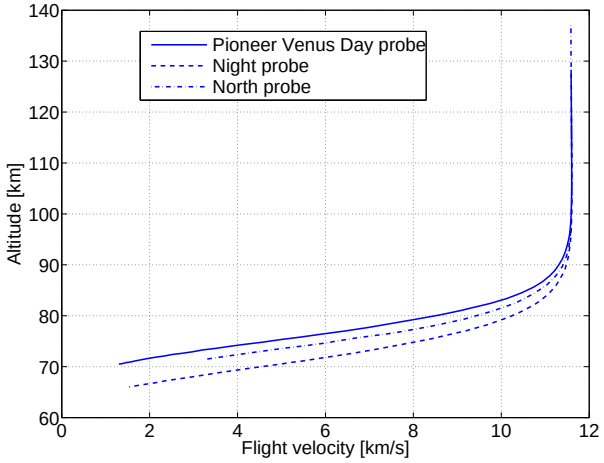

Figure E.9: *Velocity-altitude map for the Pioneer Venus probe based on [167].*

E.3.2 Shock tube campaing at EAST

One of the only experimental campaign that included flow conditions relevant for Venus entry was performed at the Electric Arc Shock Tube (EAST) located at the NASA Ames Research Centre. Schematically, the operation of a shock tube is to generate a shock wave by means of an explosion (blast-driven) or the rupture of a diaphragm caused by a build-up of pressure (compressed-gas driven).

In the case of EAST, the high energy source is the discharge of a capacitor, able to store up to 1.2 MJ, in the driver section, which is filled with a light gas such a helium. The dissipation of a large amount of energy in a short time causes a sudden rise of temperature and pressure in the driver, resulting in the diaphragm separating it from the shock tube to burst. A shock wave propagates through the shock tube, filled with the test gas, down to the test section. That facility is a non-reflected shock tube, therefore it does not have enough test time to establish a flowfield around a model, but rather allows for the observation of the normal shock traveling through the test chamber.

The facility's instrumentation allows for mapping of the spectroscopic signature of the shock over a wide range of wavelengths covering simultaneously Vacuum Ultraviolet (VUV, 120-500 nm), UV - visible 'blue' (200-600 nm), visible 'red' - Near Infrared (NIR, 480-900 nm) and IR (800-$5,500$ nm). The measurements are done through two horizontal slots windows. The ability to cover the VUV region is of particular interest to investigate the large radiance from low lying states of N and O atoms in air, and the CO 4$^{\text{th}}$ positive radiation in CO_2 [38].

Cruden and his team performed a series of tests with conditions relevant for Mars and Venus entry, with a 96% CO_2, 4% N_2 and 96.5% CO_2 3.5% N_2 volumetric ratio. Simulations were performed with CEA [119] for various flow conditions. They showed that post-shock equilibrium mole fraction, density and pressure does not vary by more than a few percent whether Mars or Venus mixture is used, all other parameters being kept constant [38]. Therefore, they could directly compare the results obtained for Mars and Venus cases and observe trends with pressure and velocity variations.

The equilibrium flow was assumed to be the region of steady radiance downstream of the nonequilibrium overshoot. That assumption was partly confirmed by temperature measurements. Several spectral features were observed in the equilibrium region, and can be classified according to the shock velocity. Attention should be paid to the fact that static pressure was also changed while varying shock velocity. However, the comparison remains interesting.

For velocities lower than 10 km/s:

- The range between 120 to 300 nm dominates the whole spectrum. It is mainly due to the CO 4$^{\text{th}}$ positive system, which peaks around 160 nm and a contribution from NO in longer wavelengths.
- The second major feature is the CN violet transition, with major bands at 359, 388 422 and 461 nm.
- At longer wavelengths, the C_2 Swan system is identified through its major bands $[0,0]$, $[0,1]$ and $[2,5]$ respectively at 517, 564, 619, and 670 nm. The $[1,0]$ and $[2,0]$ bands are also observed at

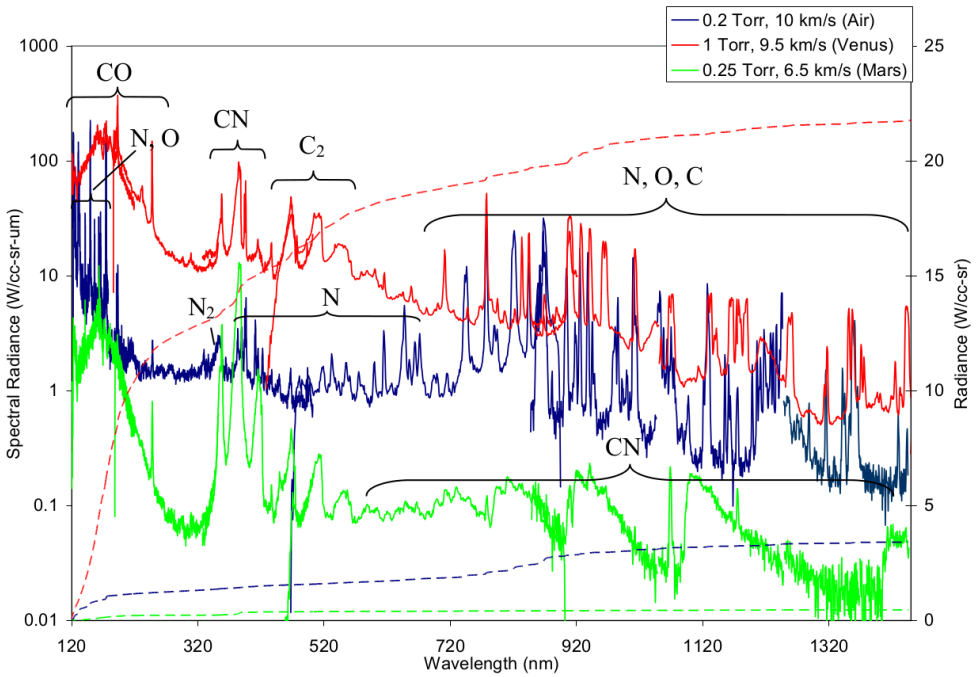

Figure E.10: *Spectral radiance and total radiance obtained for different entry conditions in the EAST facility. As it can be seen, the Venus and Mars entry spectra present similar features, although the magnitude of radiation is considerably more important for Venus than for Mars. Figure extracted from [37].*

respectively 474 and 438 nm, overlapping the CN violet system. The C_2 Swan system is at first weaker than the CN violet system, but it grows in magnitude at velocity and pressure increase.

- The CN red system is visible from 700 nm on, extending to the NIR region. At 8.5 km/s, numerous atomic lines from O, C and N appear in the long wavelength region, on top of the CN red system.

As velocity increases, the energy of the shock becomes sufficient to cause strong dissociation of the gas. That behaviour is made apparent by the following observations:

- Atomic signatures become increasingly important, with resonant states appearing in the region from 120 to 300 nm.
- The background continuum radiation grows in magnitude, especially for short wavelengths and decreasing towards longer wavelengths.
- The features of the CO 4^{th} positive system, the CN violet and red systems, and the C_2 Swan system almost entirely disappear.
- The relative contribution of the different spectral regions to the total radiation changes:
  - The region from 125 to 330 nm is an important contributor: from 57% at 6.8 km/s up to 66% at 11.5 km/s, first due to the CO 4^{th} positive system progressively replaced by the strong background radiation.
  - The contribution of the CN violet region between 330 and 480 nm decreases as velocity increases: from 29% down to 6%.

- The C_2 Swan system region, around 480 to 700 nm remains a small contributor throughout the entire velocity range, around $4 - 8\%$, although at higher velocity there is no trace of C_2.
- Finally, the region above 700 nm contributes at low velocity for less than 9% but then increases to 12%, first due to the CN red system progressively replaced by atomic features.

Cruden and his team then provide line fits for the integrated radiance as a function of pressure and velocity for ten separate wavelength range [38]. The general form assumes radiation to be an activated process, with the activation energy scaling as the incoming flow's kinetic energy:

$$I = A_1 p^n e^{\left(-E_1/v^2\right)} + A_2 p^n e^{\left(-E_2/v^2\right)} \tag{E.2}$$

where the second term only becomes significant for velocities in excess of 10 km/s to capture the change from molecular to atomic radiation.

Finally, the spectrometric data was compared with spectra generated by the Nonequilibrium Air Radiation (NEQAIR) code for the equilibrium temperature and densities obtained with CEA. Broadening and radiative transport were accounted for over the path length of the shock tube. Qualitatively, NEQAIR is in relative good agreement with the experimental data. The main differences are, for velocities relevant to Venus entry:

- From 130 to 150 nm, the spectral lines are well matched although their relative intensities is not always correct;
- From 400 to 900 nm, the agreement is very good but the 795 nm from O is missing in NEQAIR;
- From 900 to $1,200$ nm, the agreement is mixed. However, the IR camera used was operating near its saturation limit.

Quantitatively, NEQAIR underestimates the radiance by 77 to 164%, both for Mars and Venus conditions. This has already been noted for previous comparisons between EAST experimental data and NEQAIR. It was found out that the difference could be corrected by an average of 30% by applying an additional background radiation following a $1/\lambda^2$-type dependence, as described by the Kramers-Unsold formula. However, this leads to electron densities several orders of magnitude higher than what is predicted by equilibrium conditions.

E.4 Numerical studies

E.4.1 Pre-flight of Pioneer Venus

In the 1970s, while the Pioneer Venus probes were being designed, aeroheating models were needed in order to size their TPS. Several numerical analyses were conducted, complemented by extensive laboratory testing for material response, in particular ablation. However, the tools and techniques

of those days were not nearly as advanced as what is available today, and knowledge about Venus' atmosphere was relatively limited. The mission designers were aware of those limitations and applied a liberal margin of safety in the heat shield thickness. Some of them can be consulted chronologically in [140, 48, 180, 129].

Let us point out the comprehensive study performed by Edquist's [42] and already presented in section 4.2.1. He performed computations for 23 cases, changing both entry (velocity and angle) and geometric (ballistic coefficient, shape, nose radius) parameters. The analyses were made for the correct 97% CO_2 and 3% N_2 volumetric ratio. He applied the correction factor for radiative cooling presented in equation 4.21 but no correction factor was applied for ablation, as the blockage effect of pyrolysis gases was assumed to be small for the entry velocities considered. The work of Park and Ahn later proved that assumption to be false [149].

Based on these results, Edquist developed the following correlations to estimate the maximum heating rate and the integrated heating, identified with a capital Q, at the stagnation point and at a forebody point located radially at two third of the base radius. That second point is identified by the subscript $2/3$.

$$q_w^r = C \cdot R^a \cdot (\beta \sin \gamma_{\text{entry}})^b (\sin \theta)^c \cdot v_{\text{entry}}^d \tag{E.3}$$

$$Q_w^r = \frac{K \cdot R^a \cdot (\beta \sin \gamma_{\text{entry}})^b (\sin \theta)^c \cdot v_{\text{entry}}^e}{v_{\text{entry}} \cdot \sin \gamma_{\text{entry}}} \tag{E.4}$$

where θ is the cone angle and the subscript i stands for the initial conditions. The constants that do not depend on location are $a = 0.50$, $b = 1.25$ and $c = 4.75$. Those that do are $C_{\text{stag}} = 6.17 \cdot 10^{-26}$, $C_{2/3} = 3.04 \cdot 10^{-15}$, $d_{\text{stag}} = 23.1$, $d_{2/3} = 13.2$, $K_{\text{stag}} = 1.09 \cdot 10^{-18}$, $K_{2/3} = 1.06 \cdot 10^{-16}$, $e_{\text{stag}} = 17.2$, $e_{2/3} = 15.6$. The dependence on entry velocity is obviously the largest, although the velocity range considered is small and the correlations should therefore be considered with care if they are used outside the velocity range considered, that is from 11.16 to 11.40 $\mathrm{km/s}$, which does not include the Pioneer Venus probes.

E.4.2 Wakefield and Pitts

The post-flight rebuilding of the heat shield experiment data is rather complex, as the only information is two temperature points embedded within the heat shield, simulations that encompass several aspects of the problem (convective and radiative heat rates estimation and material response) are therefore needed in order to go from the known free-stream conditions to the thermocouple measurements, without any possibility to validate the intermediate results.

The first attempt was performed in 1980 by Wakefield and Pitts [151] and [206]. Their computations were made with the material code Charring Material Ablation (CMA) with convective and radiative heating computed using the methods described by Moss et al. in [129]. However, shortly

after the onset the temperatures climbed up to unrealistic values and caused the simulation to stop. It was also noticed while confronting the results obtained so far with the flight data that the computed temperature rise was happening too soon, and the temperature measured at the frustum was lower than that at the stagnation point while it was the opposite in flight.

E.4.3 Park and Ahn

It is only in 1999 that a second attempt was made, this time by Park and Ahn [149] from the Tohoku University. At that time, the Institute of Space and Aeronautical Sciences (ISAS) of Japan was planning Hayabusa, then referred to as MUSES-C, a mission that would bring asteroid samples back to the Earth. In that frame, they needed to perfect the models used to design super-orbital re-entry vehicles. Although Venus' atmosphere is completely different from that of the Earth, the flight velocities were roughly similar and both involved ablation. Pioneer Venus was therefore an interesting test case.

The models used by Park and Ahn vastly improved what had been done in previous work. Namely, they did take into account:

- Finite rate chemistry,
- An atmosphere consisting of a 97% CO_2 , 3% N_2 volumetric mixture rather than the $90 - 10\%$ as it was previously assumed,
- Line-by-line technique to describe the radiative heating rather than cruder step models,
- An improved version of the CMA ablation code, the Super CMA [2]. Although the previous version had been validated experimentally, it assumed steady-state pyrolysis gas flow; the pyrolysis gas production in the heat shield material is constant whereas the rate of advance of the pyrolysis zone and that of the receding surface are different. However, the entry angle of the Pioneer Venus probes being relatively steep, the heating pulse were sudden and steady-state can therefore not be assumed [149].

They considered 17 species, so as to take into account the pyrolysis-gas: CO_2, CO, C_2, C_3, N_2, NO, $NO+$, CN, C, $C+$, N, O, $O+$, H, CH, OH, and H_2O. Two other components, O_2 and H_2, were considered in early simulations but later removed as their concentrations were negligible. Furthermore, as previous work showed vibrational relaxation downstream the shock was fast, they only considered a one-temperature description.

New models lead to new results, and numerous surprises with respect to what was previously thought. It appeared that the flow was actually in nonequilibrium in the boundary layer for much of the flight trajectory, and not in equilibrium as it was previously assumed. They also discovered that the blockage from pyrolysis-gases absorbing radiation had been greatly underestimated. As a result, the heating rates were significantly lower than expected; the convective heating rate appeared to be approximately $2/3$ of what was obtained before, and the radiative heating rate about $1/2$. According to Park and Ahn, the difference is mainly due to the non-equilibrium boundary layer, and the treatment

and characteristics of the pyrolysis-gas [149]. The newly computed heating rates were then used to evaluate the material response, and validate that end result with the thermocouples data [3]. The temperature profile was in good agreement with flight data for the North and Day probes, for which both the entry angle and the trajectory are known, whereas the temperature profile of the Sounder and Night probes show higher temperatures and earlier onset [3]. Their rebuilding is the best information available so far regarding the aeroheating of the Pioneer Venus probes.

The evolution of the stagnation point heat fluxes as a function of probe altitude are depicted in figure E.11. Park and Ahn's results are stated as a function of flight time, which allows for matching them with the free-stream parameters compiled in Seiff and Kirk's tables [167]. The aeroheating onset is around an altitude of $110\ \mathrm{km}$, at which atmospheric density crosses the limit of $1 \cdot 10^{-5}\ \mathrm{kg/m^3}$ and starts rapidly increasing while the probes, until then free-falling in an almost perfect vacuum, have been accelerated up to $11.6\ \mathrm{km/s}$. The three flux profiles show first a radiative heat pulse, induced by the probe's high velocity, followed by a convective one, due to the rising free-stream density. The convective heat flux is roughly the same magnitude in the three cases but the radiative one is clearly largest for the North probe and the smallest for the Day probe. This is consistent with the probes entry angles: steepest for the North probe and shallowest for the Day probe, the North probe's velocity is thus higher at lower altitude. This also causes the radiative heat flux to last until lower altitudes for the North probe.

Although the Sounder probe was not part of Park and Ahn's research, one can easily get an idea of its heat fluxes profile. Its entry angle was a few degrees steeper than that of the Day probe, but still considerably smaller than the North and Night probes'. Qualitatively, the trajectory would thus be closer to that of the Day probe. From there on, for a quick estimate of the stagnation point heating, the only difference of the Sounder probe is it's larger nose diameter, roughly 1.90 times that of the small probes (figure E.7). The convective heating q_c^{stag} is known to behave as the inverse of the square of the nose radius R (equation 4.2). It should therefore be $\sim\ 0.73$ times smaller. The radiative heating q_r^{stag}, however, is linearly related to the nose radius R (equation 4.7). All other conditions assumed to be equal, it should be $\sim\ 1.90$ times larger. The aeroheating of the Sounder probe was thus most probably very large and mainly radiative. This fosters the conclusion on the poor quality of aeroheating estimates of trajectory rebuilding codes for Venus entry made regarding table E.2: the $6.90\ \mathrm{MW/m^2}$ foreseen by Dutta et al. [40] seems unrealistic.

E.4.4 Takahashi and Sawada

A similar study was later performed by Takahashi and Sawada [182], members of the same research group at Tohoku University as Park and Ahn. They extended the previous study to the frustum edge of the heat shield, on the location of the second thermocouple. Their computation used more advanced turbulent models and a two temperatures description. The CFD solution was loosely coupled with the Super CMA code for thermal response analysis of the ablative heat shield.

However, they made two questionable hypothesis that do not hold for the stagnation region. Firstly, they considered only 11 species, namely the same as Park and Ahn without nitrogen and

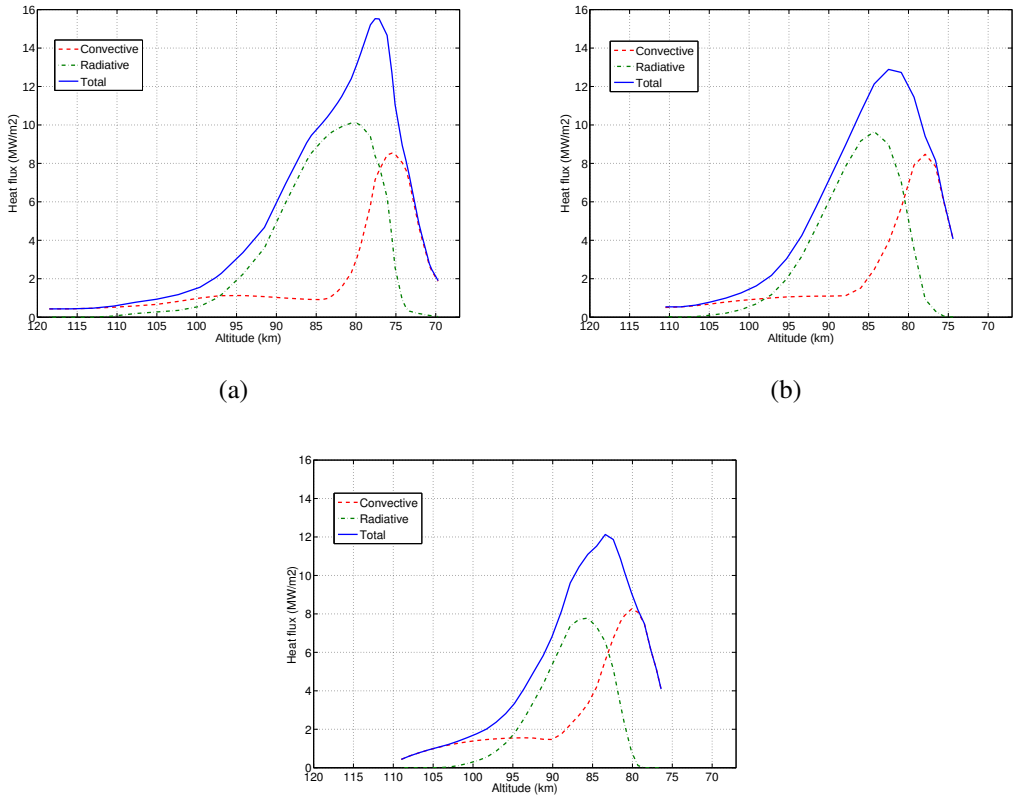

Figure E.11: *Convective and radiative stagnation point heat fluxes as computed by Park and Ahn [149] for the North (a), Night (b) and Day (c) probes, with the blockage effect of pyrolysis gases, using the time-altitude correspondence data from Seiff and Kirk [167]. It should be reminded to that the Night probe profile was not properly validated.*

C^+ (thus a full CO_2 atmosphere). As it has been seen in section E.3.2, it has been experimentally demonstrated that nitrogen is a great contributor of radiative heating in Venus atmosphere, especially in the form of CN, N and in a lower extent N_2. Secondly, they neglected the radiative coupling between the heat flux and the flowfield.

Despite these two unfortunate hypothesis, the thermocouple data they reproduced is in relative good agreement with that recorded during the Pioneer Venus flight. Their results show that whereas the convective heat flux is decreased due to the blockage effect of pyrolysis gases in the stagnation region, it is enhanced in the downstream region due to the promotion of turbulence by the injection of pyrolysis gases. Wall-ward radiative heat flux was also found out to be considerably smaller in the downstream region than at the stagnation point, sometimes even smaller than the shock-ward radiative heat flux.

E.4.5 Tauber et al.

In order to update the stagnation point heating rates correlations, Tauber et al. [186] performed a series of CFD computations for the Sounder probe, the result of which was also briefly introduced in section 4.2.1. As no accurate trajectory data is available for the Sounder probe, they computed it with

the Traj code, developed at NASA Ames Research Centre, for the correct geometry but with a ballistic coefficient of $190\ \mathrm{kg/m^2}$, an entry velocity of $11.584\ \mathrm{km/s}$ and an entry angle of $-31.829\ \mathrm{deg}$, which are all slightly different values from what is found in other sources (see table E.2). The computation were performed for 10 points along that trajectory.

The computations were executed with the Data-Parallel Line Relaxation Methods (DPLR) and NEQAIR codes, both developed at NASA Ames Research Centre, respectively to solve the flowfield and the radiative emission. Finite chemical reaction rates were used. Ablation was not taken into account and the wall was assumed to be cold and fully catalytic. A 16-species $CO_2 - N_2$ mixture was used: CO_2, CO, CO^+, C_2, N_2, O_2, NO, NO^+, CN, C, C^+, N, N^+, O, O^+ and e^-. The difference with Park and Ahn is that while the pyrolysis gas was not taken into account, they included CO^+, O_2, and e^-. The $CO_2 - N_2$ volumetric ratio they used was $96.5 - 3.5\%$, half a percent different from Park and Ahn. The radiative heating at the stagnation point was determined using a tangent slab shock layer approximation. Since DPLR and NEQAIR are uncoupled, the non-adiabatic nature of the flow was accounted for using equation 4.20 with $a = 3$ as derived in [188].

They draw several conclusion from their simulations. First, the low pressure at high altitude causes a greater portion of the flow to be in chemical non-equilibrium, thereby raising the temperature. For the first data point, for example, at $95.22\ \mathrm{km}$ high the pressure is $0.36\ \mathrm{atm}$ and the chemical non-equilibrium extends along 40% of the stagnation line. Second, at the peak heating about 90% of the emission is from atomic species. A secondary pulse can be observed at lower altitude (also for the North probe, see figure E.12) and is likely to result from radiative emission from molecular species, especially CN. The presence of two distinct pulses had already been observed by Edquist [42], who interpreted it the same way.

Those 10 data points were then used to derive approximate expression for the stagnation point radiative heat flux as a function of free-stream velocity v_∞, density ρ_∞, and nose radius. The resulting relation is, for velocities comprised between 10 and $12\ \mathrm{km/s}$ (super-orbital):

$$q_w^r = 8.497 \cdot 10^{-69} R^{0.49} \rho_\infty^{1.2} v_\infty^{18} \tag{E.5}$$

And for velocities smaller than $10\ \mathrm{km/s}$:

$$q_w^r = 2.195 \cdot 10^{-28} R^{0.49} \rho_\infty^{1.2} v_\infty^{7.9} \tag{E.6}$$

This research, however, should be considered with care. It is indeed important to insist on the fact that, unlike the work of Park and Ahn on the small probes, the computations of Tauber et al. make little use of flight data: the trajectory data used was not recorded during flight, and the results were not validated against those of the heat shield experiment. Their result is compared to that obtained by Moss et al. [129], which was a pre-flight attempt to estimate the heating rates. The test cases were not experimentally reproduced either.

In order to have a point of reference for actual flight validated data, one can compare the approximate relations used by Tauber et al. and the rebuilding of Park and Ahn. The result is depicted in

figure E.12 for the North probe, and in table E.3. Qualitatively, the approximate relations give a rather good results: the onset and end of the stagnation point radiative heating are correctly predicted, as is the altitude of its peak. However, at lower altitude, and therefore lower velocity and higher density, they underestimate its magnitude, which is concerning as the result is thus not on the safe side. The stagnation point, in particular, is underestimated by $\sim 20\%$. The peak radiative heating were tabulated in table E.3 together with those obtained by Park and Ahn. Those approximate relations give obviously better results than those used by Dutta et al. [40] (see table E.2), but they could nevertheless benefit from greater accuracy, and do anyway not account for the blockage effect of pyrolysis gas.

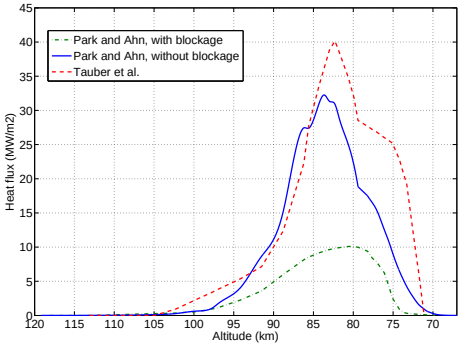

Figure E.12: *Radiative stagnation point heat flux obtained using the approximate expression of Tauber et al. [186] compared to those computed by Park and Ahn with and without the blockage effect of ablation [149] for the North probe.*

q_w^r $[\mathrm{MW/m^2}]$	Park and Ahn 1999 [149]	Tauber et al. 2010 [186]	Relative error [%]	Park and Ahn 1999 [149]	Edquist 1974 [42]	Relative error [%]
Ablation?	no	no		yes	yes[a]	
Sounder	$\sim 26^b$	24.50	5.77	$\sim 10^b$	7.87	21.30
North	$\sim 40^b$	32.25	19.37	10.10	11.56	14.46
Night	$\sim 29^b$	22.70	21.72	9.65	7.55	21.76
Day	$\sim 14^b$	13.25	5.43	7.78	4.38	43.70

Table E.3: *Peak radiative heat heating at the stagnation point, q_r^{stag} in $\mathrm{MW/m^2}$, for Pioneer Venus probes as obtained by the flight validated rebuilding of Park and Ahn and with two different correlations.*

[a] Blockage effect of pyrolysis gases was considered negligible.
[b] Visual estimation from graph in [149].

E.5 Preliminary shock layer analysis

A preliminary numerical analysis was performed to investigate the chemistry in the shock layer. Two features were more specifically looked at: the equilibrium composition and its sensitivity to the free-stream composition (i.e. the ratio between CO_2 and N_2), and the nonequilibrium layer thickness.

The figures of this appendix describing parameters along the probe's trajectory are expressed as a function of the shock velocity. The reader interested in converting them in flight time or altitude should refer to the tables of [167], or to the velocity-altitude map depicted in figure E.9. The velocity range considered includes the radiative heating phase and the peak convective heating, as obtained by [149] and depicted in figure E.11 (c); from $100\ \mathrm{km}$ down to $75\ \mathrm{km}$.

E.5.1 Post-shock equilibrium mixture composition

The post-shock equilibrium conditions corresponding to the Pioneer Venus Day probe have been investigated, so as to have an idea of the expected radiators. These were obtained with CEA, for a normal shock moving at the same velocity as the probe's flight velocity in a $97\%\ CO_2$, $3\%\ N_2$ volumetric mixture at the same static pressure as the one encountered in flight. The result is depicted in figure E.13 (a) for atomic and molecular species and (b) for ionic and electronic species.

It appears that:

- The atomic compounds O, C, and N are present in relatively high concentrations throughout the entire velocity range.
- Free electrons and ions of the main atomic species (C^+, O^+, and N^+) are increasingly important as velocity increases. There is also a notable concentration of CO^+ in the medium to lower range of velocities and, in a lesser extent, NO^+ at low velocities. More complex ionic species are present, but in low concentrations ($> 3 \cdot 10^{-5}\%$).
- Inversly, molecular species are increasingly important towards the lower velocity end, and especially CO which reaches up to $\sim 40\%$. Other species such as N_2, O_2, NO, CN and C_2 top at around $\sim 10^{-3}\%$. The presence of CN is interesting as it is known to be a particularly good radiator, even in small quantities.

These results are consistent with those obtained by Cruden et al. discussed in section E.3.2. The features of CO 4^{th} positive system, CN and the C_2 Swan system, usually expected for Mars entry, are less visible for Venus entry. Inversely, background radiation and atomic features should be increasingly important as velocity increases.

As it has been covered in section E.4, many studies use slightly different mixture of $CO_2 - N_2$ for Venus atmosphere: $90-10\%$ for the preliminary studies of the Pioneer Venus probes, $96.5-3.5\%$ for Tauber et al. and Cruden et al., $97-3\%$ for Park and Ahn and Ediquist, or even full CO_2 for Takahashi and Sawada. The ratio of $97\%\ CO_2$, $3\%\ N_2$ will be retained for the present study. However, another set of computation was performed with CEA in order to have a qualitative idea of how the spectrum might change due to variations in mixture composition. Figure E.14 (a) and (b) are the analogues of figure E.13 but respectively for a $90 - 10\%\ CO_2 - N_2$ mixture and a full CO_2 atmosphere.

The concentration of species that were present in concentration larger than 1% remain almost the same, with the relative amounts of major components varying according to the free-stream mixture:

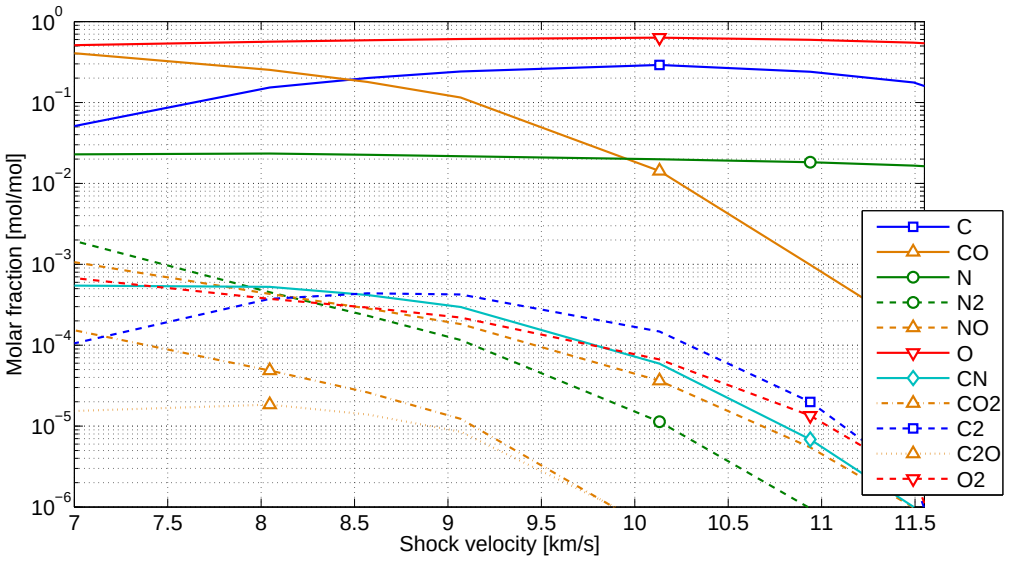

(a)

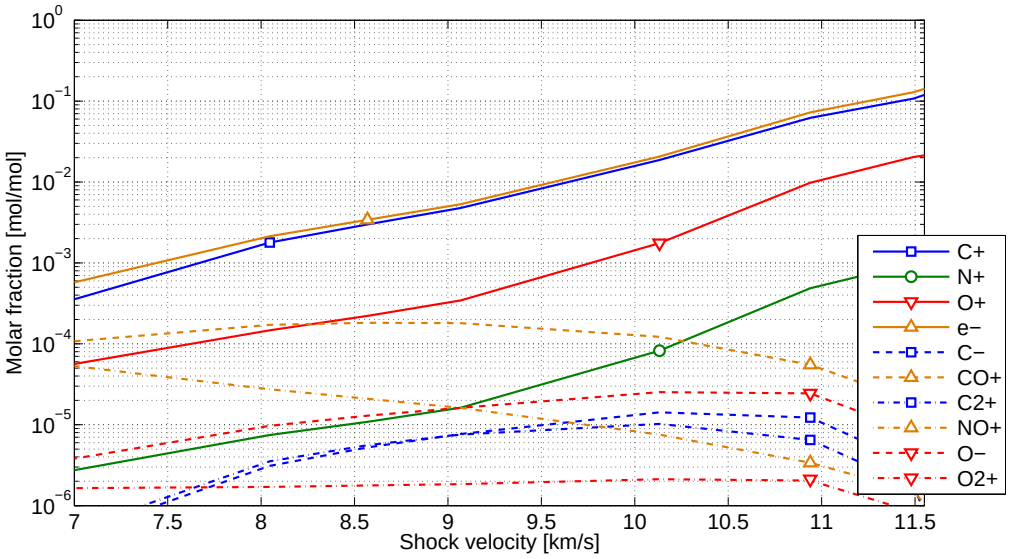

(b)

Figure E.13: *Post-shock equilibrium mixture composition for atomic and molecular species (a) and ionic and electronic species (b), for the Pioneer Venus Day probe trajectory in a* $97\%\ CO_2$ *,* $3\%\ N_2$ *volumetric mixture at a free-stream temperature of* 300 K*, as approximated with CEA. The molar fraction is plotted as a logarithmic scale.*

i.e. an increase in N_2 will create more N_2, NO and N^+. None of these, and other important radiators such as CN, are present for the full CO_2 mixture.

E.5.2 Nonequilibrium

An important parameter needed to explore the post-shock flow features is the shock stand-off distance δ. The different existing correlations were discussed in section 3.2.1. Using the work of Hornung [81]

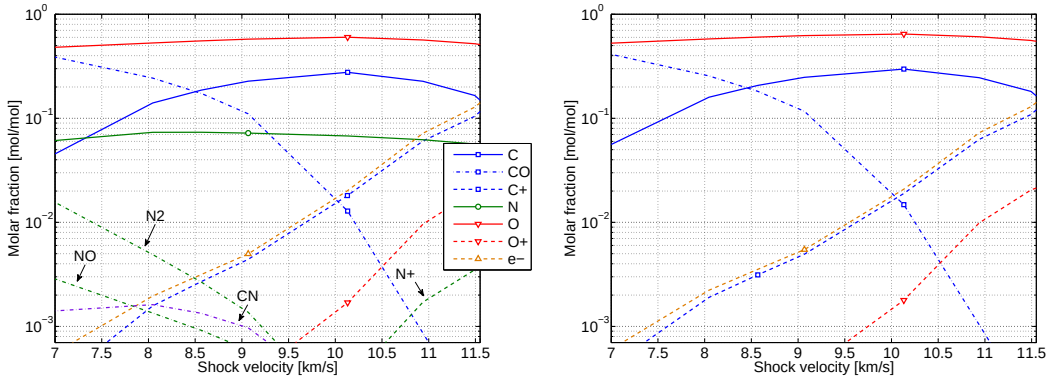

Figure E.14: *Post-shock equilibrium conditions for the Pioneer Venus Day probe trajectory in a* $90 - 10\%$ $CO_2 - N_2$ *(a) volumetric mixture and full* CO_2 *mixture (b) at a free-stream temperature of* 300 K*, as approximated with CEA. The molar fraction is plotted as a logarithmic scale.*

for spheres, as it was done for cylinders in equation E.7, one obtains:

$$\frac{\Delta}{R} = 0.78\frac{\rho_\infty}{\rho_{\text{fr}}} \tag{E.7}$$

and thus $\Delta = 7.7 - 9.3$ mm, the lowest value being for the highest altitude.

Simulations were performed with Poshax for three specific points: the on-set of radiative heating ($t = 68,151.61$ s), the peak radiative heating ($t = 68,154.53$ s), and the end of radiative heating ($t = 68,155.99$ s).

The result is depicted in figure E.15. There is a great deal of nonequilibrium at high altitude ($\sim 16\%$ of the stagnation line, depending on the correlation) and somewhat also at low altitude ($\sim 4\%$). Around the peak radiative heat flux, however, the flow in the vicinity of the stagnation line can be considered as in equilibrium.

That equilibrium 'peak' was expected: the flow temperature is the highest in the vicinity of the peak radiative heating, leading to a higher reaction rate constant and a thicker shock layer, and therefore a higher Damkhöler number. The flow is closer to equilibrium at low velocity than at high velocity because the effect of the post-shock velocity, which follows the same trend with free-stream velocity as the temperature, takes it over.

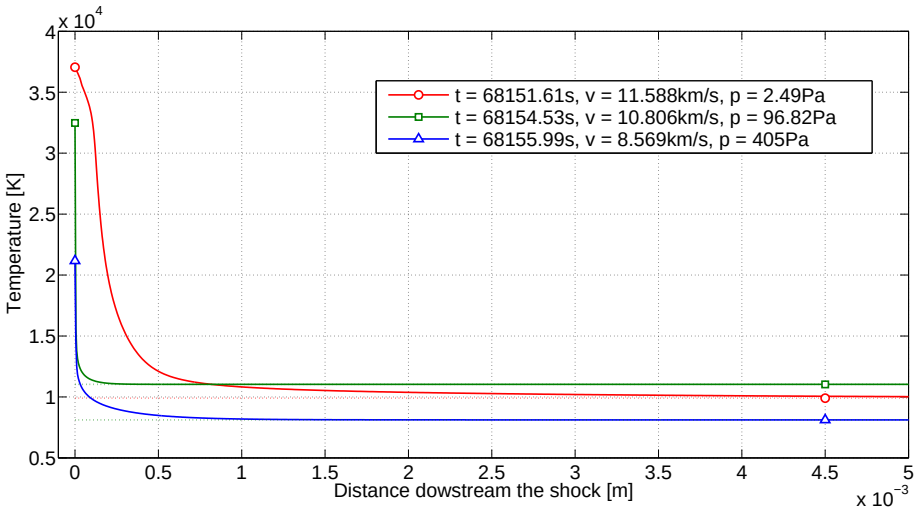

Figure E.15: *Post-shock temperature distribution as obtained with Poshax for a normal shock in flow conditions equivalent to the peak radiative heating of Pioneer Venus, and a free-stream temperature of* 300 K.

Appendix F

X2 test flow design methodology

The overall strategy applied when designing new test conditions is depicted in figure F.1. The target flow conditions are first defined. A preliminary numerical study is then conducted to determine what flow conditions should be achievable. The main intention is to gain a qualitative idea of how the flow is evolving depending on the values assigned to the fill pressure of the different sections. An experimental Pitot survey is then performed in order to determine how accurate that numerical study is. If the flow conditions do not match the target one, an iteration is needed, updating the numerical code with the experimental results. Once a match is found, the quality of the flow is assessed. The main quality driver is to have a test flow that is stable and repeatable over a duration long enough to obtain measurements. If so, and depending on the needs of the experimenter, a more accurate numerical simulation can be performed to determine the test flow conditions with more precision.

F.1 Preliminary numerical design

The numerical design of the test conditions is performed in two steps. The target fill conditions are first roughly estimated by solving numerically the idealized tube model presented in section 6.1.1, assuming equilibrium chemistry. This is done using a solver called Pitot developed by C. James [94]. Practically, the fill pressure of the different sections of the tube are specified. The solver then runs through the different sections of the tube; first it determines the shock speed in the section, then with the fill pressure it matches the velocity and pressure across the interface between the section's gas and the expanding gas from the previous section. Finally, the passage of the gas through the nozzle is simply computed as a steady expansion. The equilibrium properties of the gas are obtained from CEA. However, CEA does not give solutions below $800\ \mathrm{K}$ for gases mixtures including CO_2, for which values compelled in Cengel and Boles' thermodynamics text book are used [31].

Despite its limitations, Pitot has the advantage of computing a solution in a matter of minutes. It is thus possible to perform a quick optimization and obtain a ball park figure for the fill conditions. That figure is then used as an initial solution for a finer numerical simulation with L1D, a quasi-one-dimensional Lagrangian solver, with engineering correlations for viscous effects and point-mass dynamics for piston motions [90, 91]. In the set-up file, the geometrical description of the facility is

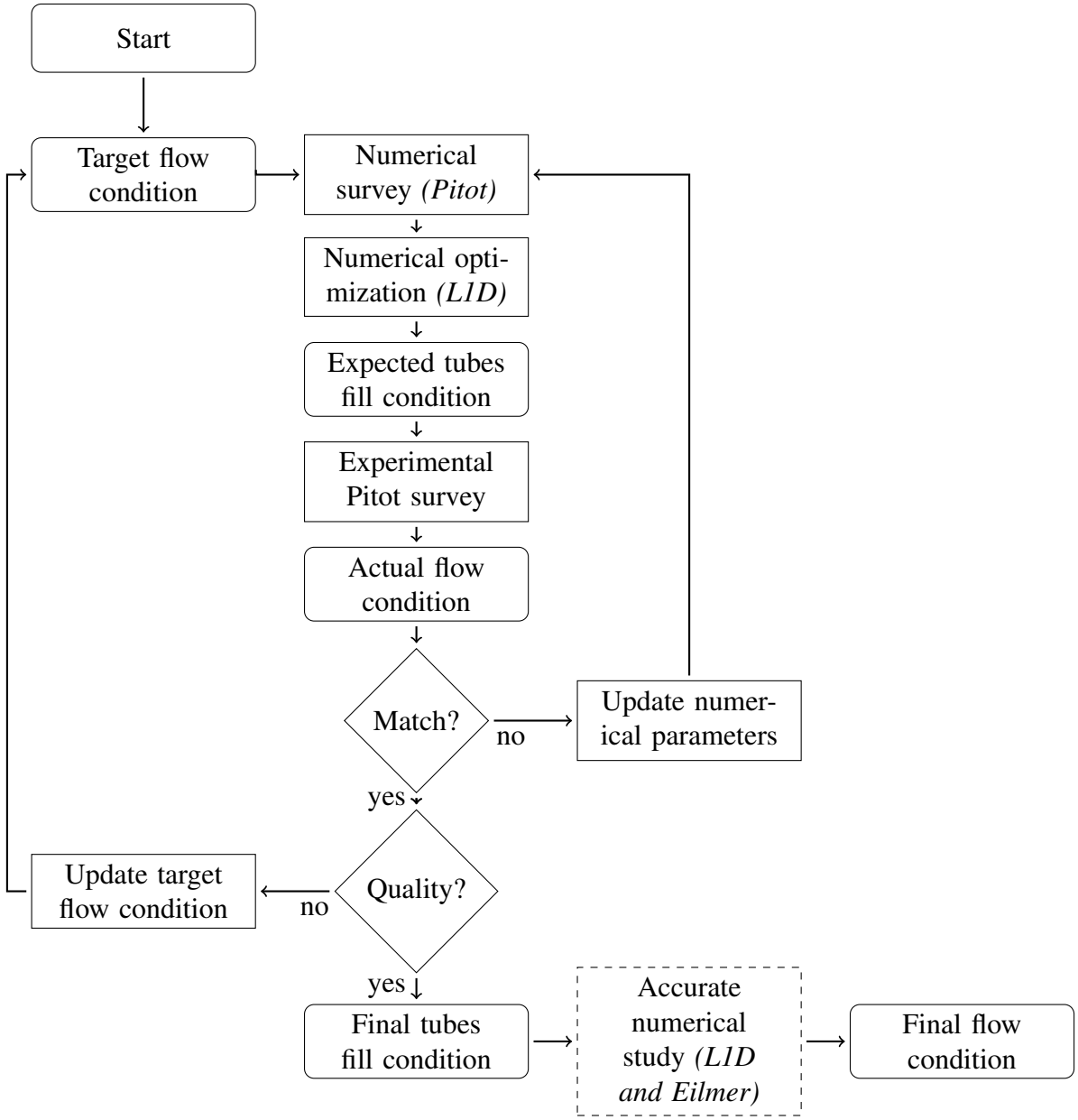

Figure F.1: *Methodology applied for the design of new test conditions; the right balance of numerical simulations and experiments.*

based on the most recent and accurate measurements provided by Gildfind in his Ph.D. thesis [62]. The evolution of different flow variables with respect to time are retrieved for different locations along the tube, which correspond to the pressure transducer that are physically present on X2. This allows for future comparison with experimental data.

F.2 Experimental Pitot survey

The only instrumentation needed to perform experimental characterization of the flow are pressure transducers. Indeed, a series of transducers along the tube will allow to measure the velocity of the shock, thus inferring the enthalpy of the test gas. Measuring the dynamic pressure in the test section is then sufficient to infer the density of the test gas.

The transducers traditionally used for this type of application are PCB® piezoelectric pressure sensor. These especially designed to measure small pressure fluctuations at high static pressure levels and resist to temperatures up to $135\ \mathrm{deg}$. As an additional protection, all sensors are covered with a thin layer of mylar.

Depending on the model used, the maximum range of the transducers used is 50 or $100\ \mathrm{psi}$, which corresponds to 344.74 and $689.48\ \mathrm{kPa}$. A large pressure range is needed to ensure that the transducer resists to the passage of the high-pressure driver gas. The actual pressure measured by the transducers is in the order of $5 - 15\ \mathrm{kPa}$. The calibration process, which is done on a dynamic pressure test rig, is thus performed using more points in the low pressure range. From the calibration, the uncertainty on the pressure measurement is 2.50%.

The tunnel is equipped with 3 pressure transducers along the shock tube, and 6 along the acceleration tube (figure 6.1). The passage of the shock wave corresponds to an abrupt pressure rise that is identified by visual inspection with an accuracy of $\Delta t \sim 0.2\ \mu s$. Their relative position is typically $250 \pm 2.5\ \mathrm{mm}$. The velocity of the shock is simply obtained by retrieving the time of pressure rise at two different positions close to the tube exit, and computing the ratio of the distance that separates them and the difference of time dt by dy; $v = dy/dt$. The relative uncertainty on velocity $\Delta v/v$ is then obtained as:

$$\frac{\Delta v}{v} = \sqrt{\left(\frac{\Delta dy}{dy}\right)^2 + \left(\frac{\Delta dt}{dt}\right)^2} \tag{F.1}$$

where $\Delta dy/dy \simeq 2\%$ and, for a typical velocity of $12.5\ \mathrm{km/s}$, $\Delta dt/dt \simeq 1\%$. The overall uncertainty on the measured velocity is therefore $\sim 2.25\%$.

For flow characterization campaigns, the test section is equipped with a rake of 9 pressure transducers, each of them covered with a $15\ \mathrm{deg}$ nose cone. The tips of the cones are $10 \pm 2\ \mathrm{mm}$ downstream of the nozzle exit plane. The axis of the cones are separated from each other by a vertical distance of $17.5\ \mathrm{mm}$, covering a total of $140\ \mathrm{mm}$. The axis of the central cone is aligned with the centerline of the core flow with an accuracy of $\pm 5\ \mathrm{mm}$. The experiment is recorded with a Shimadzu HPV-1 Hypervision high speed CCD camera, capable of recording 102 images at a maximum frame rate of

1MHz.

The increase in luminosity due to shock arrival is captured by a photodiode directed at the test section at an angle of approximately $30\,\mathrm{deg}$. This signal is used as the trigger for the data recording systems. Upon trigger, both the pressure transducers and the camera record data, including a set of pre-trigger samples (the data is cycled in a buffer and can be recorded for a certain amount of time). The traces from the PCB transducers allows identifying what part of the flow corresponds to the passage of the test gas, which can be confirmed with the high-speed video if necessary. The signals from all the PCB transducers are then averaged during that period of time.

The post-processing is also performed with the numerical code Pitot. The fill pressures and the shock velocities in the different sections of the tube are specified, and the nozzle area ratio, which depends on boundary layer growth, is then varied until the total pressure measured by the cone probe transducers in the test flow is matched. The viscous effects in the nozzle are thus implicitly taken into account, removing one of the major shortcomings of Pitot. The velocity of the flow entering the nozzle is assumed to be equal to that of the normal shock [123].

Once all the test gas properties are known, the free-stream enthalpy is computed according to equation 3.10. The kinetic part is usually the largest contributor to the total enthalpy. However, because of the very high temperatures to which the test gas is brought in expansion tubes, the sensible component is small but non-negligible. The kinetic enthalpy is directly obtained once the velocity is measured (as described earlier), the sensible enthalpy is obtained from CEA assuming equilibrium conditions, and the work is simply obtained as:

$$\int_{\text{rest}}^{\text{test}} pdV = \left[\frac{p}{\rho}\right]_{\text{rest}}^{\text{test}} \tag{F.2}$$

In flight, the sensible enthalpy of the free-stream is largely negligible compared to its kinetic counterpart. In the facility, however, both need to be accounted for. Therefore, the flight velocity is matched in the laboratory to the flight equivalent velocity v_e expressed as:

$$v_{\infty,\text{flight}} = v_e = \sqrt{2h_\infty} \tag{F.3}$$

Fast flight conditions are obtained not only by bringing the test gas it to high velocity, but also by heating it up.

If enough resources are available, the final flow conditions can then be verified numerically. A preferred approach for that last step is to perform a first simulation with L1D up to the secondary diaphragm, and use that solution for a second simulation with Eilmer[1], a three-dimensional compressible CFD code [92, 93].[2]

[1] Eilmer was named after Eilmer of Malmesbury, a 11^{th} century English Benedictine mink known for an early attempt at gliding flight.

[2] These simulations being computationally expensive, they can be simplified using with look-up-tables for the equilibrium gas properties.

Appendix G

Venus atmospheric entry in a non-reflected shock tube

For the sake of comprehensiveness, a preliminary study was performed with L1D in order to determine whether Venus atmospheric entry could be obtained using X2 as a shock tube instead of an expansion tube. The only variable to retrieve is the shock velocity, the static pressure being the fill pressure of the test gas, a parameter fixed in the set-up file. The achievable test conditions were investigated for a set-up both without and with a secondary driver. As for the expansion tube set-up, it was found out that an optimum secondary driver fill pressure exists for each shock tube fill pressure. Four distinctive shock tube fill pressure covering the test range were therefore studied so as to determine to what extent the optimum was evolving. Similarly to the expansion tube configuration, that optimum secondary driver fill pressure proved to vary very little with the shock tube fill pressure; it remains around $10 - 20\,\mathrm{kPa}$. The result is depicted in figure G.1. The data points obtained in EAST (see section E.3.2) are also represented. From both the curve of the facility without secondary driver, in green circles, and with a secondary driver at the optimum fill pressure, in red squares, it appears that there exist a logarithmic relation between the static pressure and the shock velocity. The same kind of logarithmic relation was observed between the free-stream density and velocity for the facility operated as an expansion tube.

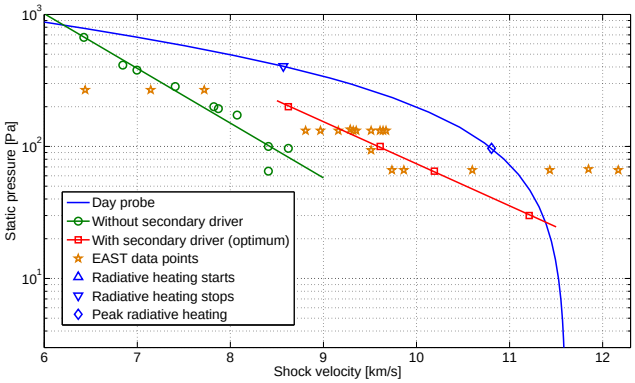

Figure G.1: *Preliminary results on achievable test conditions in shock tube mode obtained with L1d respect to the actual Pioneer Venus Day probe trajectory as well as the data points obtained in EAST (section E.3.2, [38]).*

This mode of operation is indeed interesting regarding the type of data it would allow to obtain. In particular, it could serve as a point of comparison with previous campaigns performed in EAST. However, the target flow conditions would requires a secondary driver, which considerably increases the complexity of the facility's operation. Furthermore, the scope of investigations offered by the non-reflected shock tube mode is considerably smaller than that of the expansion tube mode.

Appendix H

Experimental data of the test campaign conducted in the Plasmatron

Experimental results for the Plasmatron test campaign described in chapter 5: free-stream conditions and measured heat fluxes. The free-stream conditions are defined in terms enthalpy and density. These are then translated in static pressure and heat flux measured at the small probe, two directly measurable quantities in the Plasmatron. Once the desired free-stream flow is obtained, the large probe is injected and the heat flux measured. The dynamic pressure is finally obtained based on a polynomial fit on those measured quantities.

Test ID	h_∞ [MJ/kg]	ρ_∞ [g/m^3]	p_{stat} [mbar]	$q_{w,\text{small}}$ [kW/m^2]	σ_{meas}	q_w [kW/m^2]	σ_{meas}	p_{dyn} [Pa]
1	20	1.0	23	1224	16	598	10	135
2	20	1.0	23	1239	14	572	9	135
ref	20	4.0	96	–	–	1230	–	27
3	25	1.0	27	1638	29	851	12	147
4	25	1.0	27	1670	21	811	10	147
ref	25	4.0	117	–	–	1835	–	36
5	30	1.0	32	2127	25	1075	16	151
6	30	1.0	32	2115	17	1067	15	151
ref	30	4.0	138	–	–	2575	–	51
7	35	0.5	17	1978	34	936	10	252
8	35	0.5	17	1968	16	997	11	252
ref	35	2.0	64	–	–	2360	–	76
9	35	1.0	38	2760	36	1259	11	149
ref	35	4.0	159	–	–	3350	–	65
10	35	1.6	49	2276	29	1078	16	111
11	35	1.6	49	2262	41	1073	11	111
ref	35	6.0	210	–	–	2300	–	20

Appendix I

Experimental data of the Pitot survey conducted in X2

Experimental results of the Pitot survey performed in X2 and described in section 6.2. Different fill pressures were used for the shock tube p_{st} and acceleration tube p_{at}, resulting in different shock velocities v_{st} and v_{at} and cone pressure p_{cone}.

Shot ID	t	p_{st}	p_{at}	v_{st}	v_{at}	p_{cone}
	[mm]	[Pa]		[km/s]		[kPa]
$x2s2481$	1.2	1500	2	4.57	8.88	12.56
$x2s2480$	1.2	1800	2	4.41	9.00	10.85
$x2s2482$	1.2	1800	2	4.46	9.00	11.91
$x2s2496$	1.2	1800	2	4.43	9.09	9.13
$x2s2491$	2.0	3600	15	5.16	9.92	21.78
$x2s2475$	2.0	3600	15	5.32	9.87	25.21
$x2s2474$	2.0	3600	25	5.37	9.55	40.77
$x2s2488$	2.0	3600	40	5.18	9.16	35.33
$x2s2489$	2.0	3600	40	5.25	9.43	34.64
$x2s2500$	2.0	3600	40	5.32	9.28	35.42
$x2s2477$	2.5	4600	23	5.60	10.16	36.45
$x2s2476$	2.5	4600	39	5.60	9.70	46.04
$x2s2494$	2.5	4600	39	5.50	9.71	47.85
$x2s2492$	2.5	4600	100	5.68	8.60	66.41
$x2s2493$	2.5	4600	100	5.52	8.89	61.41
$x2s2501$	2.5	4600	100	5.50	8.89	69.84

Appendix J

Experimental data of the binary scaling test campaign conducted in X2

Experimental results of the binary scaling test campaign performed in X2. The shock velocity in the shock tube v_{st} and in the acceleration tube v_{at} are obtained as described in section F.2. The total stagnation point heat flux q_w and shock standoff Δ/R are measured according to the methodology outlined in chapters 8 and 7. In some instances, the largest probe (i.e. $t = 1.2$ mm) was equipped with two thermocouples, allowing to perform two heat flux measurements at once. The shock standoff could only be measured when record high-speed video from the side rather than from the top.

Shot ID	t [mm]	v_{st} [km/s]	v_{at} [km/s]	q_w [MW/m^2]	$\sigma_{\text{meas}} q_w$ [MW/m^2]	Δ/R [−]
$x2s2687$	1.2	4.45	9.08	56.65	5.97	/
$x2s2688$	1.2	4.45	9.29	/	/	/
$x2s2689$	1.2	4.70	9.66	40.85	3.99	/
$x2s2691$	1.2	4.52	9.16	33.32	1.86	/
$x2s2703$	1.2	4.55	9.30	/	/	0.2134
$x2s2704$	1.2	4.59	9.10	34.57	1.43	0.2020
$x2s2705$	1.2	4.46	9.12	48.46 34.20	3.40 2.82	/
$x2s2706$	1.2	4.51	9.10	48.95	4.58	0.2098
$x2s2707$	1.2	4.42	9.17	58.71	1.21	0.2080
$x2s2708$	1.2	4.44	9.06	48.46 32.25	3.40 1.27	0.2169
$x2s2709$	1.2	/	/	67.08	11.48	/
$x2s2710$	1.2	4.44	9.23	39.33	4.89	0.2004
$x2s2711$	1.2	4.51	9.05	32.77 24.82	1.20 3.93	0.2032
$x2s2664$	2.0	5.61	9.55	/	/	/
$x2s2665$	2.0	/	/	/	/	/
$x2s2666$	2.0	5.72	9.84	/	/	/

$x2s2667$	2.0	5.66	9.55	/	/	/
$x2s2668$	2.0	/	/	/	/	/
$x2s2669$	2.0	5.55	9.27	/	/	/
$x2s2670$	2.0	5.66	9.70	189.28	7.91	/
$x2s2671$	2.0	5.71	9.83	162.84	50.20	/
$x2s2672$	2.0	5.71	9.86	/	/	/
$x2s2673$	2.0	5.65	9.27	148.33	16.82	/
$x2s2674$	2.0	5.60	9.41	/	/	/
$x2s2675$	2.0	5.66	9.42	/	/	/
$x2s2676$	2.0	5.60	9.44	/	/	/
$x2s2712$	2.0	/	/	/	/	/
$x2s2713$	2.0	5.50	9.25	183.91	9.06	/
$x2s2714$	2.0	5.55	9.10	144.61	4.88	/
$x2s2715$	2.0	5.60	8.91	199.45	21.41	/
$x2s2716$	2.0	5.60	9.66	191.56	10.78	/
$x2s2717$	2.0	5.55	9.30	230.74	30.73	0.2750
$x2s2718$	2.0	5.60	9.30	210.17	10.27	0.2887
$x2s2719$	2.0	5.71	9.11	/	/	0.2987
$x2s2720$	2.0	5.55	9.17	168.01	17.87	0.2760
$x2s2730$	2.0	5.55	9.44	/	/	0.2654
$x2s2731$	2.0	5.60	9.17	/	/	0.2719
$x2s2677$	2.5	5.76	9.03	/	/	/
$x2s2678$	2.5	5.65	9.14	/	/	/
$x2s2679$	2.5	5.83	9.27	221.39	30.59	/
$x2s2680$	2.5	5.64	9.14	265.33	44.99	/
$x2s2681$	2.5	5.78	9.40	299.98	74.95	/
$x2s2682$	2.5	5.77	9.42	218.79	17.79	/
$x2s2683$	2.5	5.71	8.89	214.06	42.23	/
$x2s2684$	2.5	5.65	9.02	224.08	42.49	/
$x2s2685$	2.5	5.65	9.14	/	/	/
$x2s2721$	2.5	5.66	8.85	/	/	/
$x2s2722$	2.5	5.66	8.91	207.89	19.52	0.4050
$x2s2723$	2.5	5.71	8.92	305.76	41.08	/
$x2s2724$	2.5	5.61	9.37	280.68	27.72	0.4162
$x2s2725$	2.5	5.50	9.23	275.62	50.37	0.4147
$x2s2726$	2.5	5.66	8.79	281.81	101.12	0.3926
$x2s2727$	2.5	5.66	9.18	271.13	29.99	0.3611
$x2s2728$	2.5	5.66	9.04	272.26	56.68	0.4695
$x2s2729$	2.5	5.66	8.98	221.76	15.51	0.3462